

A STUDY OF HELICOPTER AERODYNAMICS IN GROUND EFFECT

DISSERTATION

Presented in Partial Fulfillment of the Requirements for
the Degree Doctor of Philosophy in the
Graduate School of The Ohio State University

By

Devi Prasad Pulla, B.E., M.S.

* * * * *

The Ohio State University

2006

Dissertation Committee:

A.T. Conlisk, Adviser

S.Mazumder

John Yu

Igor Adamovich

Approved by

Adviser

Graduate Program in
Mechanical Engineering

ABSTRACT

The flow around a helicopter is very complex; it becomes much more complex when it comes close to the ground. The presence of the ground changes the aerodynamic characteristics of the rotor and the flow environment becomes much more complex compared with that of flight out-of-ground effect (OGE) and hence the behavior of the rotor wake in the vicinity of the ground is challenging to predict. Under in-ground-effect(IGE) conditions, the wake collides with the ground and causes a significant perturbation to the flow near the blade. Significant interactions between the main rotor wake and the ground have been associated with the formation and passage of the ground vortex in forward flight. The presence of a ground vortex affects the handling qualities of the helicopter. The aim of this research is to capture the physics of the flow features and dynamics of ground effect flows around a rotorcraft, provide an understanding of the rotor wake/vortices near the ground, and generate rigorous models to accurately predict handling qualities, loads and moments acting on the rotor and the power requirements.

A free vortex method is used to model the flowfield. The presence of the ground is modeled using the method of images and the lifting-surface theory is used to model each rotor blade. An initial wake geometry is assumed which is allowed to develop in time until the flowfield becomes periodic. The rotor wake is assumed to consist of only the tip

vortices and the inboard sheet and the root vortex are neglected. The solution is stepped in time using an Adams-Moulton scheme with a Runge-Kutta starting formula.

The wake structure after periodicity is reached is obtained for hover and different forward flight speeds. Also, the nature of the flowfield, as well as the formation of the ground vortex, is understood by obtaining the velocity contours on a longitudinal plane containing the rotor blade after periodicity is obtained. The unsteadiness in the velocities is quantified by obtaining the RMS deviation in velocities on different planes containing the tail rotor around the rotor disk simulating the various kinds of flight. Thrust and power requirements on the rotor disk have been predicted and have been successfully validated by comparison with experimental results obtained from Georgia Institute of Technology. A tail rotor has also been included in the current model to understand its implications on the wake structure and loads. The computational results have been validated against experimental results obtained at Georgia Institute of Technology and Empey and Ormiston.

ACKNOWLEDGMENTS

Personal gratitude is extended to Professor A.T. Conlisk whose patience and guidance is greatly appreciated. I would also like to thank Mr. Alan Egolf for his helpful input regarding my research.

This work is supported under Task 9.1.2 of the NASA/NTRC Rotorcraft Center of Excellence at Georgia Institute of Technology.

VITA

August 6, 1981	Born - Visakhapatnam, India
July 2002	B.E. Mechanical Engineering Regional Engineering College Suratkal, India
December 2004	M.S. Mechanical Engineering The Ohio State University Columbus, OH
September 2002-present	Graduate Research Associate The Ohio State University Columbus, OH

PUBLICATIONS

Research Publications

Saijo, T., Ganesh, B.A., Huang, A.B., Komerath, N.M., Bhattacharya, S., Pulla, D.P., Conlisk, A.T, “Development of Unsteadiness in the Wake of a Rotor in Ground Effect”, Proceedings of the American Helicopter Society Forum, Pheonix, AZ, May 2003.

Pulla, D.P., Bhattacharyya, S., Conlisk, A.T., “Structure of the Rotor Wake in Ground effect”, Annual meeting of the Division of Fluid Dynamics, APS, Meadowlands, NJ ,November , 2003.

Pulla, D.P., Conlisk, A.T., “The Long Time Structure of the Rotor Wake in Ground effect”, 43rd AIAA Aerospace Sciences Meeting, Reno, Nevada AIAA 2005-1408, January 10-13 2005.

Ganesh, B., Komerath, N.M., Pulla, D.P., Conlisk, A.T., “Unsteady Aerodynamics of Rotorcraft in Ground Effect”, 43rd AIAA Aerospace Sciences Meeting, Reno, Nevada AIAA 2005-1407, January 10-13 2005.

Pulla, D.P., A.T.Conlisk., “The Unsteady Rotor Wake in Ground Effect”, Annual meeting of the Division of Fluid Dynamics, APS, Chicago, IL ,November , 2005.

Pulla D.P., Vishwanath Godavarthy, Burgraff, O.R., Conlisk, A.T., “An Inviscid Model of the Formation of a Rotor Tip-Vortex”, accepted for publication by the AIAA Journal.

FIELDS OF STUDY

Major Field: Mechanical Engineering

Studies in Fluid Mechanics: Professor A.T. Conlisk

TABLE OF CONTENTS

	Page
Abstract	ii
Acknowledgments	iv
Vita	v
List of Tables	x
List of Figures	xi
Chapters:	
1. Introduction	1
1.1 Background	1
1.2 Overview of Helicopter Aerodynamics	3
1.3 Rotor Wake	7
1.4 Wake Models	9
1.5 Effect of the Ground on the Rotor Flow Field	11
1.6 The Current Work	16
2. Numerical Model for the Blade	18
2.1 Introduction	18
2.2 Lifting Line Theory	19
2.3 Lifting Surface Model	24
2.4 IGE Wake Model	35
2.5 Summary	42

3.	Results - Lifting Line	46
3.1	Introduction	46
3.2	Results - Lifting Line Theory	47
3.2.1	OGE Hover for Comparison with IGE Results	47
3.2.2	IGE Hover Lifting Line Results	50
3.2.3	IGE Forward Flight - Single-Bladed Rotor Flow Field Results	58
3.2.4	IGE Forward Flight - Two-Bladed Rotor	64
3.2.5	Comparison with Experiments	72
3.3	RMS Velocity Variations	78
3.4	Summary	92
4.	Results - Lifting Surface Model	95
4.1	Introduction	95
4.2	Results - Lifting Surface	96
4.2.1	Results - Single-Bladed Hover Lifting Surface	96
4.2.2	Results - Two-Bladed Hover Lifting Surface	100
4.2.3	Results - Single-Bladed Forward Flight Lifting surface	101
4.2.4	Results - Two-Bladed Forward Flight Lifting Surface	111
4.2.5	Comparison with Experiments	115
4.3	Transient Velocity Variations	123
4.4	Summary	142
5.	Loads	144
5.1	Introduction	144
5.2	Computation of Loads Using Lifting Line Theory in Hover	146
5.3	Computation of Loads Using the Lifting Surface Theory	154
5.4	Results - Lifting Line Theory	156
5.4.1	Results in Hover	156
5.4.2	Results - Forward Flight	160
5.5	Results - Lifting Surface Theory	162
5.5.1	Results - Hover	163
5.5.2	Results - Forward Flight	166
5.5.3	Comparison of Lifting Line and Lifting Surface Models	167
5.6	Summary	170

6.	Main Rotor - Tail Rotor Interactions	171
6.1	Introduction	171
6.2	Numerical Model	173
6.3	Results	174
6.3.1	Flow field	174
6.3.2	Loads	175
6.4	Summary	185
7.	Overview and Future Work	187
7.1	Summary	187
7.2	Future Work	190
Appendices:		
A.	Vortex Ring Computation	192
Bibliography		195

LIST OF TABLES

Table	Page
3.1 Experimental Parameters in Caradonna <i>et al.</i> [32] experiments.	50
3.2 Experimental parameters in Light [17] experiments.	50
3.3 Comparison of ground vortex coordinates in computation and experiment; $h/R = 0.72$, two-bladed rotor, $\mu = 0.03$	72
4.1 Comparison of ground vortex coordinates in computation and experiment; $h/R = 0.72$, two-bladed rotor, $\mu = 0.03$	121
4.2 Comparison of ground vortex coordinates in computations obtained using lifting surface and lifting line models; $h/R = 0.72$, two-bladed rotor, $\mu =$ 0.03	123

LIST OF FIGURES

Figure	Page
1.1 A summary of specific flow problems involving helicopter aerodynamics. From [1].	4
1.2 A single bladed rotor in forward flight; a top view (a)Advancing and re- treating sides of the rotor disk. (b) Definition of lag and flap angles. (b) Lift and drag in forward flight.	6
1.3 Trailed and shed vorticity in rotor wake(Johnson [3]).	7
1.4 Sketch of a helicopter rotor wake for a single blade. From Gray [4].	8
1.5 Comparison of partial and total ground effects.	12
2.1 Lifting line model for a fixed wing ; the dark areas indicate the magnitude of bound circulation; circulation has an elliptical distribution in the fixed wing case.	20
2.2 Velocity induced by the segments of a typical horseshoe element.	22
2.3 Horseshoe vortex model of a rotary wing.	26
2.4 Horseshoe-vortex panel implementation of a semi-infinite wing. The panel width is non-uniform in the spanwise direction, as discussed in the text. The velocity boundary condition is applied at the three-quarter chord line at the midspan point of each panel. (a) Definition of the local panel coordi- nates. (b) Definition of the global coordinates.	28

2.5	Schematic of the trailing vortex system. Open circles denote the quarter-chord location of each panel (bound vortices), solid circles denote panel edges. Arrows denote the normal direction at the panel three-quarter chord line (normal-velocity boundary condition) [26].	30
2.6	Bound circulation distribution along the blade in hover IGE, $h/R = 0.5$ and OGE; $A = 6$, $\alpha_0 = 10^\circ$	32
2.7	Comparison of the dimensionless tip-vortex circulations for lifting line and lifting surface models in hover, $h/R = 0.5$	33
2.8	Dimensionless tip-vortex circulation as a function of the aspect ratio in hover, $h/R = 0.5$	34
2.9	Model for the wake of a rotor in ground effect.	35
2.10	Coordinate system; the azimuthal angle (not shown) is the angle between the positive y (dimensionless) direction and the reference blade (blade 1), positive in the counter clockwise sense.	36
2.11	Tip-vortex discretization using advance points and straight line vortex filaments.	40
2.12	Comparison of the downwash values obtained using 1600 and 3200 nodes for the tip-vortex in hover for a single bladed rotor; $h/R = 0.5$, $y = 0.5$, $x = 0$, $z = 0.15$	42
2.13	Comparison of the downwash values obtained using 1600 and 3200 nodes for the tip-vortex in hover for a two bladed rotor; $h/R = 0.5$, $y = 0.5$, $x = 0$, $z = 0.15$	43
2.14	Radial and axial trajectories of a single point on the wake starting at the blade tip at $t=0$ for different spatial and time steps. Case 1: $\Delta\psi = 1^\circ$, $\Delta t = 1^\circ$, Case 2: $\Delta\psi = 2^\circ$, $\Delta t = 2^\circ$, Case 3: $\Delta\psi = 4^\circ$, $\Delta t = 4^\circ$, Case 4: $\Delta\psi = 8^\circ$, $\Delta t = 8^\circ$. (a) Radial trajectory (b) Axial trajectory.	44
3.1	Wake structure for a two-bladed rotor (a) OGE (b) IGE Solid line: blade - 1. Dotted line: blade - 2; $h/R = 3.6$	48

3.2	Comparison of experimental and computational trajectories (r and z) of the tip-vortex. Experimental data of Caradonna et al. [32] is represented by ‘o’ and computational data by ‘*’. (a) blade - 1 (b) blade - 2.	49
3.3	Comparison of experimental and computational trajectories (r/R and z/R) of the tip-vortices. Experimental data of Light [17] is represented by the boxes and computational data by a solid line; $h/R = 0.84$	51
3.4	Top view of the trajectory of the tip-vortex of a single-bladed rotor in ground effect in hover after (a) 10 revolutions (b) 30 revolutions (c) 50 revolutions (d) 70 revolutions (e) 90 revolutions (f) 100 revolutions; $h/R = 0.5$	53
3.5	Tip-vortex circulation for a single-bladed rotor in hover and forward flight $\mu = 0.03$ for $h/R = 0.5$ as a function of time.	54
3.6	Downwash distribution along the blade for a single-bladed rotor in hover for $h/R = 0.5$ after 100 revolutions.	55
3.7	Downwash contours in longitudinal cross section for a single-bladed rotor in hover for $h/R = 0.5$ after one hundred revolutions.	55
3.8	Top view of the trajectory of the tip-vortex of a two-bladed rotor in ground effect in hover for $h/R = 0.5$ after (a) 10 revolutions, (b) 30 revolutions, (c) 50 revolutions, (d) 70 revolutions, (e) 90 revolutions, (f) 100 revolutions.	57
3.9	Side view of the wake structure for a two-bladed rotor in hover for $h/R = 0.5$ after 100 revolutions.	58
3.10	Downwash distribution along the blade for a two-bladed rotor in hover for $h/R = 0.5$ after 100 revolutions.	59
3.11	Downwash contours in longitudinal cross section for a two-bladed rotor in hover for $h/R = 0.5$ after one hundred revolutions.	59
3.12	Top view of the trajectory of the tip-vortex of a single-bladed rotor in ground effect in forward flight for $\mu = 0.01$ after (a) 10 revolutions (b) 30 revolutions (c) 50 revolutions (d) 70 revolutions (e) 90 revolutions (f) 100 revolutions; $h/R = 0.5$	60

3.13	Downwash distribution along the blade for a single-bladed rotor for $\mu = 0.01$ for $h/R = 0.5$ after 100 revolutions.	62
3.14	Downwash contours in longitudinal cross section for a single-bladed rotor for $\mu = 0.01$ for $h/R = 0.5$ after one hundred revolutions.	62
3.15	Top view of the trajectory of the tip-vortex of a single-bladed rotor in ground effect ($h/R = 0.5$) in forward flight for $\mu = 0.03$ after (a) 10 revolutions (b) 30 revolutions (c) 50 revolutions (d) 70 r evolutions (e) 90 revolutions (f) 100 revolutions.	63
3.16	Downwash distribution along the blade for a single-bladed rotor for $\mu = 0.03$ for $h/R = 0.5$ after 100 revolutions.	64
3.17	Downwash contours in longitudinal cross section for a single-bladed rotor for $\mu = 0.03$ for $h/R = 0.5$ after one hundred revolutions.	65
3.18	Top view of the trajectory of the tip-vortex of a two-bladed rotor in ground effect in forward flight $\mu = 0.01$ for $h/R = 0.5$ after (a) 10 revolutions, (b) 30 revolutions, (c) 50 revolutions, (d) 70 revolutions, (e) 90 revolutions, (f) 100 revolutions.	66
3.19	Downwash distribution along the blade for a two-bladed rotor for $\mu = 0.01$ for $h/R = 0.5$ after 100 revolutions.	67
3.20	Downwash contours in longitudinal cross section for a two-bladed rotor for $\mu = 0.01$ for $h/R = 0.5$ after one hundred revolutions.	67
3.21	Top view of the trajectory of the tip-vortex of a two-bladed rotor in ground effect in forward flight $\mu = 0.03$ for $h/R = 0.5$ after (a) 10 revolutions, (b) 30 revolutions, (c) 50 revolutions, (d) 70 revolutions, (e) 90 revolutions, (f) 100 revolutions.	69
3.22	Downwash distribution along the blade for a two-bladed rotor for $\mu = 0.03$ for $h/R = 0.5$ after 100 revolutions.	70
3.23	Downwash contours in longitudinal cross section for a two-bladed rotor for $\mu = 0.03$ for $h/R = 0.5$ after one hundred revolutions.	70

3.24	Rotor wake recirculation phenomenon at $\mu = 0.03$, $h/R=0.72$, two-bladed rotor, tilt = 10° , (a) Computational Result (b) Experimental result.	71
3.25	Downwash distribution along the blade, $h/R = 0.72$, two-bladed rotor, tilt = 10°	73
3.26	Rotor wake recirculation phenomenon at $\mu = 0.04$, $h/R = 0.72$, two-bladed rotor, tilt = 10° , (a) Computational Result (b) Experimental result. . .	75
3.27	Downwash power frequency spectrum IGE, $\mu = 0.03$, lifting line model computed at the location $y = -1$, $z = 0.831$, $x = 0$; (a) Computational results (b) Experimental results.	76
3.28	Comparison of the results obtained from the current work with those of Kang and Sun [21] for a four-bladed rotor when $h/R = 0.46$, $\mu = 0.03$ using lifting line model; (a) Kang and Sun [21] results (b) Current work results.	77
3.29	RMS swirl contours for hover at azimuthal locations (a) 0 degrees (b) 15 degrees (c) 30 degrees (d) 45 degrees; $h/R = 0.72$, all four plots are identical as required in hover.	79
3.30	RMS swirl contours for forward flight $\mu = 0.01$ on the advancing side at azimuthal locations (a) 0 degrees (b) 15 degrees (c) 30 degrees (d) 45 degrees (e) 60 degrees (f) 75 degrees (g) 90 degrees, $h/R = 0.72$	82
3.31	RMS swirl contours forward flight $\mu = 0.01$ on the retreating side at azimuthal locations (a) 0 degrees (b) 15 degrees (c) 30 degrees (d) 45 degrees (e) 60 degrees (f) 75 degrees (g) 90 degrees, $h/R = 0.72$	84
3.32	RMS downwash contours for forward flight $\mu = 0.01$ on the advancing side at azimuthal locations (a) 0 degrees (b) 15 degrees (c) 30 degrees (d) 45 degrees (e) 60 degrees (f) 75 degrees (g) 90 degrees, $h/R = 0.72$	85
3.33	RMS downwash contours forward flight $\mu = 0.01$ on the retreating side at azimuthal locations (a) 0 degrees (b) 15 degrees (c) 30 degrees (d) 45 degrees (e) 60 degrees (f) 75 degrees (f) 90 degrees, $h/R = 0.72$	88

3.34	RMS swirl contours for forward flight $\mu = 0.03$ on the advancing side at azimuthal locations (a) 0 degrees (b) 15 degrees (c) 30 degrees (d) 45 degrees (e) 60 degrees (f) 75 degrees (g) 90 degrees, $h/R = 0.72$	90
3.35	RMS swirl contours in forward flight $\mu = 0.03$ on the retreating side at azimuthal locations (a) 0 degrees (b) 15 degrees (c) 30 degrees (d) 45 degrees (e) 60 degrees (f) 75 degrees (g) 90 degrees, $h/R = 0.72$	91
3.36	RMS downwash contours for forward flight $\mu = 0.03$ on the advancing side at azimuthal locations (a) 0 degrees (b) 15 degrees (c) 30 degrees (d) 45 degrees (e) 60 degrees (f) 75 degrees (g) 90 degrees, $h/R = 0.72$	94
4.1	Top view of the tip-vortex trajectory of a single-bladed rotor in ground effect in hover after (a) 10 revolutions (b) 30 revolutions (c) 50 revolutions (d) 70 revolutions (e) 90 revolutions (f) 100 revolutions, $A = 6$, $\alpha_0 = 10^\circ$, $h/R = 0.5$	97
4.2	Comparison in wake structure after 100 revolutions between (a) lifting surface model, $A = 6$, $\alpha = 10^\circ$, $h/R = 0.5$, (b) lifting line model.	98
4.3	Downwash distribution along the blade for a single-bladed rotor in hover for $h/R = 0.5$ after one hundred revolutions; (a) lifting surface model, $\alpha_0 = 10^\circ$, $A = 6$, $h/R = 0.5$, (b) lifting line model.	99
4.4	Downwash contours in longitudinal cross section for a single-bladed rotor in hover for $h/R = 0.5$ after one hundred revolutions; (a) lifting surface model, $\alpha_0 = 10^\circ$, $A = 6$, $h/R = 0.5$, (b) lifting line model.	100
4.5	Top view of the tip-vortex trajectory of a two-bladed rotor in ground effect in hover $h/R = 0.5$ after (a) 10 revolutions, (b) 30 revolutions, (c) 50 revolutions, (d) 70 revolutions, (e) 90 revolutions, (f) 100 revolutions; $\alpha_0 = 10^\circ$, $A = 6$, $h/R = 0.5$	102
4.6	Side view of the wake structure for a two-bladed rotor in hover for $h/R = 0.5$ after 100 revolutions; $\alpha_0 = 10^\circ$, $A = 6$, $h/R = 0.5$	103
4.7	Downwash distribution along the blade for a two-bladed rotor in hover for $h/R = 0.5$ after 100 revolutions (a) lifting surface model, $\alpha_0 = 10^\circ$, $A = 6$, $h/R = 0.5$, (b) lifting line model.	104

4.8	Downwash contours in longitudinal cross section for a two-bladed rotor in hover for $h/R = 0.5$ after one hundred revolutions; (a) lifting surface model, $\alpha_0=10^\circ$, $A = 6$, $h/R = 0.5$, (b) lifting line model.	105
4.9	Top view of the tip-vortex trajectory of a single-bladed rotor in ground effect for $\mu = 0.01$ after (a) 10 revolutions (b) 30 revolutions (c) 50 revolutions (d) 70 revolutions (e) 90 revolutions (f) 100 revolutions, $\alpha_0=10^\circ$, $A=6$, $h/R = 0.5$	106
4.10	Comparison in wake structure after 100 revolutions for $\mu = 0.01$ between (a) lifting surface model, $\alpha_0=10^\circ$, $A = 6$, $h/R = 0.5$, (b) lifting line model.	107
4.11	Downwash distribution along the blade for a single-bladed rotor in forward flight $\mu = 0.01$ for $h/R = 0.5$ after one hundred revolutions; (a) lifting surface model, $\alpha_0= 10^\circ$, $A = 6$, $h/R = 0.5$, (b) lifting line model.	108
4.12	Downwash contours in longitudinal cross section for a single-bladed rotor for $\mu = 0.01$ for $h/R = 0.5$ after one hundred revolutions; (a) lifting surface model, $\alpha_0= 10^\circ$, $A = 6$, $h/R = 0.5$, (b) lifting line model.	109
4.13	Top view of the tip-vortex trajectory of a single-bladed rotor in ground effect for $\mu = 0.03$ after (a) 10 revolutions (b) 30 revolutions (c) 50 revolutions (d) 70 revolutions (e) 90 revolutions (f) 100 revolutions, $\alpha_0=10^\circ$, $A = 6$, $h/R = 0.5$	110
4.14	Comparison in wake structure after 100 revolutions for $\mu = 0.03$ between (a) lifting surface model, $\alpha_0=10^\circ$, $A = 6$, $h/R = 0.5$, (b) lifting line model.	110
4.15	Downwash distribution along the blade for a single-bladed rotor in forward flight $\mu = 0.03$ for $h/R = 0.5$ after one hundred revolutions; (a) lifting surface model, $\alpha_0= 10^\circ$, $A = 6$, $h/R = 0.5$, (b) lifting line model.	112
4.16	Downwash contours in longitudinal cross section for a single-bladed rotor for $\mu = 0.03$ for $h/R = 0.5$ after one hundred revolutions; (a) lifting surface model, $\alpha_0= 10^\circ$, $A = 6$, $h/R = 0.5$, (b) lifting line model.	113
4.17	Top view of the tip-vortex trajectory of a two-bladed rotor in ground effect in forward flight $\mu = 0.01$ for $h/R = 0.5$ after (a) 10 revolutions, (b) 30 revolutions, (c) 50 revolutions, (d) 70 revolutions, (e) 90 revolutions, (f) 100 revolutions, $\alpha_0=10^\circ$, $A = 6$, $h/R = 0.5$	114

4.18	Downwash distribution along the blade for a two-bladed rotor for $\mu = 0.01$ for $h/R = 0.5$ after 100 revolutions; (a) lifting surface model, $\alpha_0=10^\circ$, $A = 6$, $h/R = 0.5$, (b) lifting line model.	116
4.19	Downwash contours in longitudinal cross section for a two-bladed rotor for $\mu = 0.01$ for $h/R = 0.5$ after one hundred revolutions; (a) lifting surface model, $\alpha_0=10^\circ$, $A = 6$, $h/R = 0.5$, (b) lifting line model.	117
4.20	Top view of the tip-vortex trajectory of a two-bladed rotor in ground effect in forward flight $\mu = 0.03$ for $h/R = 0.5$ after (a) 10 revolutions, (b) 30 revolutions, (c) 50 revolutions, (d) 70 revolutions, (e) 90 revolutions, (f) 100 revolutions, $\alpha_0=10^\circ$, $A = 6$, $h/R = 0.5$	118
4.21	Downwash distribution along the blade for a two-bladed rotor for $\mu = 0.03$ for $h/R = 0.5$ after 100 revolutions; (a) lifting surface model, $\alpha_0=10^\circ$, $A = 6$, $h/R = 0.5$, (b) lifting line model.	119
4.22	Downwash contours in longitudinal cross section for a two-bladed rotor for $\mu = 0.03$ for $h/R = 0.5$ after one hundred revolutions; (a) lifting surface model, $\alpha_0=10^\circ$, $A = 6$, $h/R = 0.5$, (b) lifting line model.	120
4.23	Rotor wake recirculation phenomenon at $\mu = 0.03$, $h/R = 0.72$, two-bladed rotor (a) Computational Result (b) Experimental result.	122
4.24	Downwash distribution along the blade for the experimental parameters at $\mu = 0.03$, $A = 5.33$, $h/R = 0.72$, two-bladed rotor, tilt = 10°	124
4.25	Rotor wake recirculation phenomenon at $\mu = 0.04$, $h/R = 0.72$, two-bladed rotor (a) Computational Result (b) Experimental result.	125
4.26	Downwash power frequency spectrum IGE, $\mu = 0.03$, lifting surface model, $y = -1$, $z = 0.831$, $x = 0$, (a) Computational results (b) Experimental results.	126
4.27	Comparison of the downwash power frequency spectrum obtained at $y = -1$, $z = 0.831$, $x = 0$, using (a) lifting surface model (b) lifting line model.	127

4.28	RMS swirl contours for hover on the advancing side at azimuthal locations (a) 0 degrees (b) 15 degrees (c) 30 degrees (d) 45 degrees, $h/R = 0.72$, $A = 6$, $\alpha_0 = 10^\circ$	128
4.29	RMS swirl contours for forward flight $\mu = 0.01$ on the advancing side at azimuthal locations (a) 0 degrees (b) 15 degrees (c) 30 degrees (d) 45 degrees (e) 60 degrees (f) 75 degrees (g) 90 degrees, $h/R = 0.72$, $A = 6$, $\alpha_0 = 10^\circ$	130
4.30	RMS swirl contours for forward flight $\mu = 0.01$ on the retreating side at azimuthal locations (a) 0 degrees (b) 15 degrees (c) 30 degrees (d) 45 degrees (e) 60 degrees (f) 75 degrees (g) 90 degrees, $h/R = 0.72$, $A = 6$, $\alpha_0 = 10^\circ$	131
4.31	RMS downwash contours for forward flight $\mu = 0.01$ on the advancing side at azimuthal locations (a) 0 degrees (b) 15 degrees (c) 30 degrees (d) 45 degrees (e) 60 degrees (f) 75 degrees (g) 90 degrees, $h/R = 0.72$, $A = 6$, $\alpha_0 = 10^\circ$	132
4.32	RMS downwash contours for forward flight $\mu = 0.01$ on the retreating side at azimuthal locations (a) 0 degrees (b) 15 degrees (c) 30 degrees (d) 45 degrees (e) 60 degrees (f) 75 degrees (g) 90 degrees, $h/R = 0.72$, $A = 6$, $\alpha_0 = 10^\circ$	135
4.33	RMS swirl contours for forward flight $\mu = 0.03$ on the advancing side at azimuthal locations (a) 0 degrees (b) 15 degrees (c) 30 degrees (d) 45 degrees (e) 60 degrees (f) 75 degrees (g) 90 degrees, $h/R = 0.72$, $A = 6$, $\alpha_0 = 10^\circ$	138
4.34	RMS swirl contours for forward flight $\mu = 0.03$ on the retreating side at azimuthal locations (a) 0 degrees (b) 15 degrees (c) 30 degrees (d) 45 degrees (e) 60 degrees (f) 75 degrees (g) 90 degrees, $h/R = 0.72$, $A = 6$, $\alpha_0 = 10^\circ$	139
4.35	RMS downwash contours for forward flight $\mu = 0.03$ on the advancing side at azimuthal locations (a) 0 degrees (b) 15 degrees (c) 30 degrees (d) 45 degrees (e) 60 degrees (f) 75 degrees (g) 90 degrees, $h/R = 0.72$, $A = 6$, $\alpha_0 = 10^\circ$	140

4.36	RMS downwash contours for forward flight $\mu = 0.03$ on the retreating side at azimuthal locations (a) 0 degrees (b) 15 degrees (c) 30 degrees (d) 45 degrees (e) 60 degrees (f) 75 degrees (g) 90 degrees, $h/R = 0.72$, $A = 6$, $\alpha_0 = 10^\circ$	142
5.1	Incident velocities and aerodynamic environment at a typical blade element (a) Top view (b) Blade element [33]	147
5.2	Blade element at a distance r_k from the root of the blade.	154
5.3	Thrust coefficient for single and two-bladed rotors in hover as a function of h/R ratio IGE using lifting line theory.	158
5.4	Induced Drag coefficient for single and two-bladed rotors in hover as a function of the h/R ratio IGE using lifting line theory.	159
5.5	Induced power coefficient for single and two-bladed rotors in hover as a function of h/R ratio IGE using lifting line theory.	160
5.6	Induced drag coefficient for single and two-bladed rotors in hover as a function of the forward flight speed IGE using lifting line theory, $h/R = 0.5$. . .	161
5.7	Induced power coefficient for single and two-bladed rotors in hover as a function of the forward flight speed IGE using lifting line theory, $h/R = 0.5$. . .	162
5.8	Induced drag coefficient for single and two-bladed rotors in hover as a function of the h/R ratio using lifting surface theory, $\alpha_0 = 10^\circ$, $A = 6$	164
5.9	Induced power coefficient for single and two-bladed rotors in hover as a function of the h/R ratio using lifting surface theory, $\alpha_0 = 10^\circ$, $A = 6$. . .	165
5.10	Thrust coefficient for single and two-bladed rotors in hover as a function of the h/R ratio using lifting surface theory, $\alpha_0 = 10^\circ$, $A = 6$	166
5.11	Induced drag coefficient for a single and two-bladed rotors as a function of the forward flight speed IGE using lifting surface theory, $\alpha_0 = 10^\circ$, $A = 6$. .	167
5.12	Induced power coefficient for single and two-bladed rotors as a function of the forward flight speed IGE using lifting surface theory, $\alpha_0 = 10^\circ$, $A = 6$. .	168

5.13	Comparison of the induced drag coefficient obtained by (a) lifting surface model, $\alpha_0 = 10^\circ$, $A = 6$, (b) lifting line model in hover.	169
5.14	Comparison of the induced power coefficient obtained by (a) lifting surface model, $\alpha_0 = 10^\circ$, $A = 6$, (b) lifting line model in hover.	169
6.1	Top and side views of the main rotor-tail rotor configuration.	172
6.2	Comparison of the tip-vortex trajectory (a) with the tail rotor included (b) without the tail rotor included in hover; $h/R = 0.5$, $A = 6$, $\alpha_0=10^\circ$	175
6.3	Comparison of downwash profiles in hover for (a) Model without the tail rotor (b) Model with the tail rotor included; $A = 6$, $\alpha_0=10^\circ$, $h/R = 0.5$	176
6.4	Comparison of downwash profiles at $\mu = 0.01$ for (a) Model without the tail rotor (b) Model with the tail rotor included; $A = 6$, $\alpha_0=10^\circ$, $h/R = 0.5$	177
6.5	Comparison of downwash profiles at $\mu = 0.03$ for (a) Model without the tail rotor (b) Model with the tail rotor included; $A = 6$, $\alpha_0=10^\circ$, $h/R = 0.5$	178
6.6	Comparison of induced drag coefficient for a single bladed rotor in hover as a function of h/R ratio between model without the tail rotor and model with the tail rotor included; $A = 6$, $\alpha_0=10^\circ$, $h/R = 0.5$	179
6.7	Comparison of induced drag coefficient for a two bladed rotor in hover as a function of h/R ratio for a Model without the tail rotor and Model with the tail rotor included; $A = 6$, $\alpha_0=10^\circ$, $h/R = 0.5$	180
6.8	Comparison of induced power coefficient for a single bladed rotor in hover as a function of h/R ratio between a model without the tail rotor and a model with the tail rotor included; $A = 6$, $\alpha_0=10^\circ$, $h/R = 0.5$	181
6.9	Comparison of induced power coefficient for a two bladed rotor in hover as a function of h/R ratio between a model without the tail rotor and a model with the tail rotor included; $A = 6$, $\alpha_0=10^\circ$, $h/R = 0.5$	182
6.10	Comparison of induced drag coefficient for a single bladed rotor at $h/R = 0.5$ as a function of advance ratio between a model without the tail rotor and a model with the tail rotor included; $A = 6$, $\alpha_0=10^\circ$, $h/R = 0.5$	182

6.11	Comparison of induced drag coefficient for a two bladed rotor at $h/R = 0.5$ as a function of advance ratio between a model without the tail rotor and a model with the tail rotor included; $A = 6$, $\alpha_0 = 10^\circ$, $h/R = 0.5$	183
6.12	Comparison of induced power coefficient for a single bladed rotor at $h/R = 0.5$ as a function of advance ratio between a model without the tail rotor and a model with the tail rotor included; $A = 6$, $\alpha_0 = 10^\circ$, $h/R = 0.5$	184
6.13	Comparison of induced power coefficient for a two bladed rotor at $h/R = 0.5$ as a function of advance ratio between a model without the tail rotor and a model with the tail rotor included; $A = 6$, $\alpha_0 = 10^\circ$, $h/R = 0.5$	184
6.14	Comparison of the variation of the stagnation point position with free stream velocity between computations and experimental results from Empey and Ormiston [8]; $h/R = 0.53$, two-bladed rotor, $A = 9.78$	186
A.1	Discretization of the vortex ring using straight line vortex filaments.	193

CHAPTER 1

Introduction

1.1 Background

Recent advances in computational power have encouraged modeling in the rotor wake sector. Traditionally, vortex methods with a Lagrangian approach have been used to simulate the rotor wake. The main advantage of these methods is the relatively small amount of computational power required which is just a fraction of the power required for computational fluid dynamics (CFD) methods involving finite difference or finite volume schemes. With the recent advances in computers, vortex methods have become feasible for routine computations involving helicopter design problems. The predictions obtained using these methods provide good qualitative and quantitative approximations for various rotor problems.

The flow field in the case of a rotary wing aircraft is much more complicated when compared to that of a fixed wing aircraft because the influence of the wake in the case of a rotary wing is quite far reaching. The computational domain required for a Euler/Navier-Stokes computation would be quite large and this is the most important factor that deters people from using these methods for rotor calculations. Another major factor is the enormous

amount of computational time required for a Navier-Stokes solver. In a Navier-Stokes computation there is a significant amount of numerical diffusion so that a large number of points is required the tip vortex strength from approaching zero within one revolution. Vortex methods in general and this work in particular can compute the solution for the tip-vortex trajectory up to several hundred revolutions without serious loss in accuracy.

The behavior of the rotor wake in the vicinity of the ground is challenging to predict. Under in ground effect(IGE) conditions, the wake collides with the ground and causes a significant perturbation to the flow near the blade. Significant interactions between the main rotor wake and the ground have been associated with the formation and passage of the ground vortex in forward flight. When the helicopter encounters a ground vortex, the stability of the the aircraft is degraded.

The aim of this research is to capture the physics of the flow features and dynamics of ground-effect flows around rotorcraft, provide an understanding of the rotor wakes/vortices near the ground and generate rigorous models to predict handling qualities, loads and moments acting on the rotor and the power requirements. Specific issues expected to be encountered in the modeling process are

- Non-linear aerodynamics - iterative numerical simulations involved.
- Some components rotate at high speed while others remain fixed.
- Modification of rotor inflow due to wake distortion and ground.
- Deflection of wake due to a fuselage and ground.
- Vortex-vortex interactions and blade-vortex interactions.

The objectives of this research, all of which have been met are to

- Develop physically-based models for the behavior of rotor wakes in ground effect.
- Understand the unsteadiness near the main and tail rotors and determine if they can be attributed to the presence of the ground.
- Determine the effect of the tail rotor and the fuselage on the rotor wake.
- Determine the influence of the ground on the loads and moments induced on the rotor disk as well as the power requirements.

1.2 Overview of Helicopter Aerodynamics

There are a wide variety of different fluid dynamics problems associated with rotorcraft and the problems normally encountered are depicted in Figure 1.1(from [1]). Due to the rapid rotation of the blades, the flow in the vicinity of the blades is compressible with the Mach number reaching near one and beyond; thus shock waves may form which will likely influence the local flow field. On the other hand, in the wake shed by the blades the local Mach number is small, and the flow is essentially incompressible.

A variety of problems are illustrated in Figure 1.1. The vortex shed from the rotating blades tends to interact with the following blades. This phenomenon is called blade-vortex interaction(BVI). The collision of the vortex with the airframe is also a very complex phenomenon. Also there is the tail-rotor, main-rotor vortex interaction which is a major issue in the industry today. When the helicopter is in forward flight, because of the translational motion, the blade on the advancing side has a higher relative velocity than the retreating side. On the retreating side, because of the necessity to balance the moments, the angle of attack must be greater than that on the advancing side. This phenomenon is clearly depicted in Figure 1.2 (a). The process of balancing moments on the rotor is called trim. Due

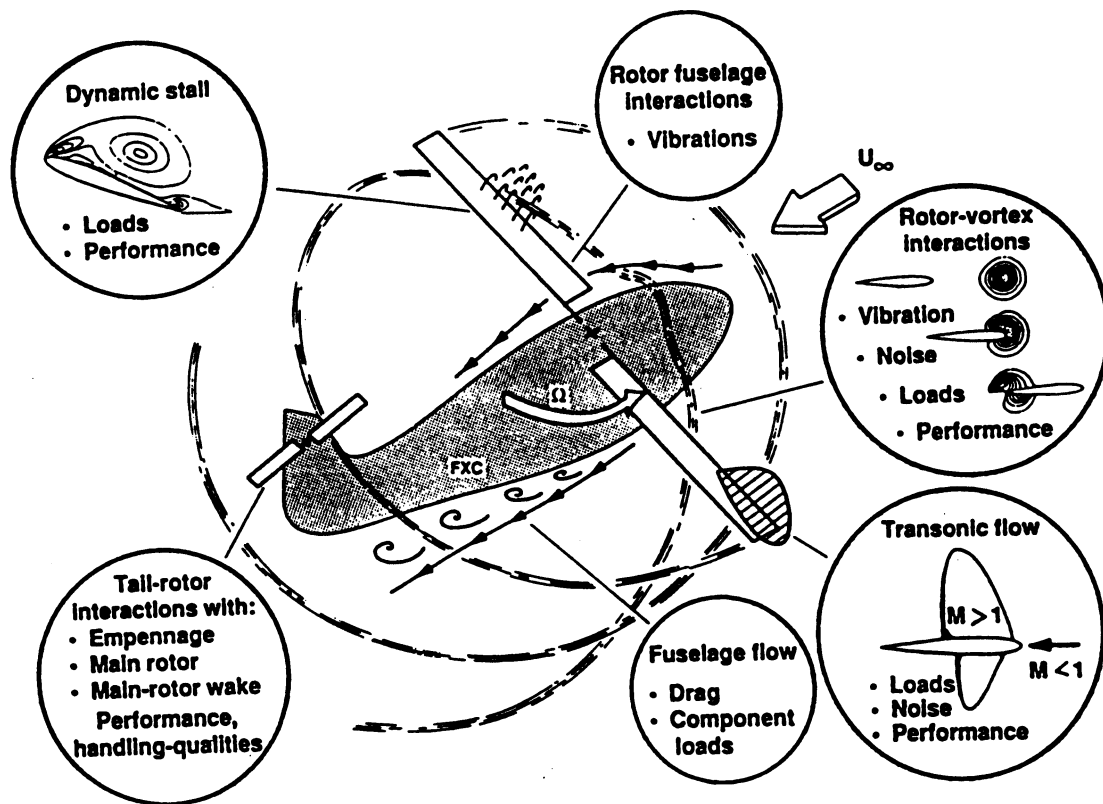
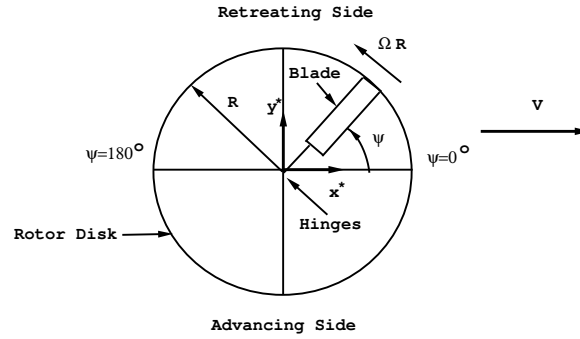


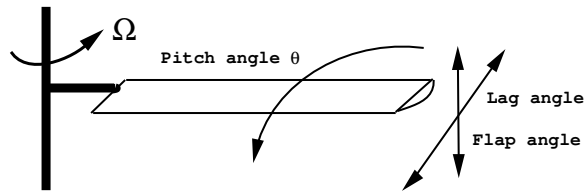
Figure 1.1: A summary of specific flow problems involving helicopter aerodynamics. From [1].

to this the flow may be separated and viscous forces are important in the creation of the stall vortex which is the vortex generated on the wing surface due to the adverse pressure gradient on the wing surface during stall. Stall is a condition in which an excessive angle of attack causes a massive increase in drag and a loss of lift due to flow separation. To provide trim capability and for aeroelastic stress relief, helicopter rotors are often hinged in the sense that the rotor blades must be permitted to bend out of the rotor disk plane as well as pitch to satisfy trim requirements. There are two modes in which the rotor is hinged; the lead-lag hinge permits the motion of the blade within the rotor-disk plane. The flapping hinge permits the flapping motion of the blades out of the rotor-disk plane. A rotor having both types of hinges is said to be fully articulated. Rotor blades have a large span-to-chord ratio and thus severe stresses can be communicated to the hub if the blades are not permitted to flap. However if the blades are aeroelastically soft, then hub stresses can be kept to a minimum and both types of hinges can be eliminated. In such cases the rotor is said to be hingeless.

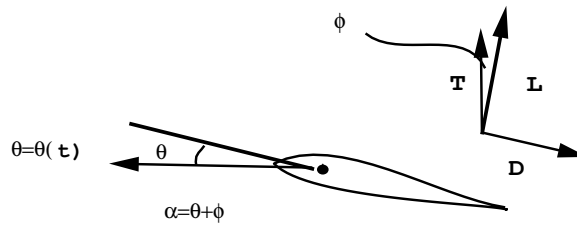
Also, as described by Conlisk [2], the flow past a helicopter is particularly complicated due to the non-linear nature of the flow. In any flight regime, the helicopter operates in or very near its own wake which is three-dimensional and highly unsteady and thus the rotor wake affects the rotor blade aerodynamics. The non-linearity arises from the fact that the strength of the vortex system shed from the rotor depends on the flow field and at the same time, the vortex system itself affects the flow field. Thus, the flow over a rotary wing is unlike the flow over a fixed wing which can often be analyzed by linearized aerodynamics at low angle of attack.



(a)



(b)



(c)

Figure 1.2: A single bladed rotor in forward flight; a top view (a) Advancing and retreating sides of the rotor disk. (b) Definition of lag and flap angles. (b) Lift and drag in forward flight.

1.3 Rotor Wake

On a three-dimensional rotor blade, conservation of vorticity requires that some bound circulation be shed into the wake from the tip to the root. The trailed vorticity γ_t is generated owing to the radial variation of the bound circulation and is normal to the trailing edge of the rotor blade. Near the tip and root, the trailing vortices roll over each other and form the root and tip-vortex; while in the inboard portion of the blade, there is a vortex sheet as shown in Figure 1.3. The trailing vorticity induced by variations in bound vorticity is defined in Johnson [3] in dimensional form as

$$\gamma_t = \frac{\partial \Gamma}{\partial r}$$

where Γ is the bound circulation and r is the radial position on the blade.

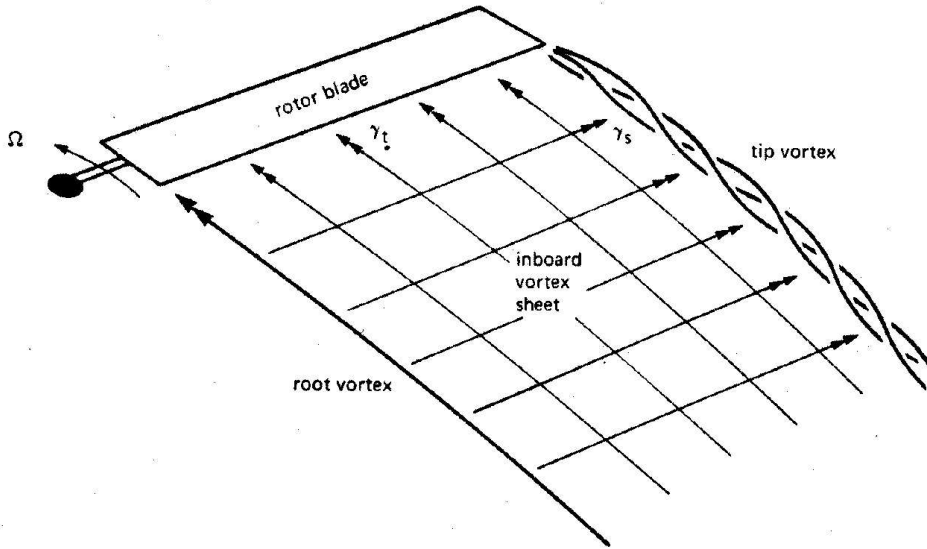


Figure 1.3: Trailed and shed vorticity in rotor wake(Johnson [3]).

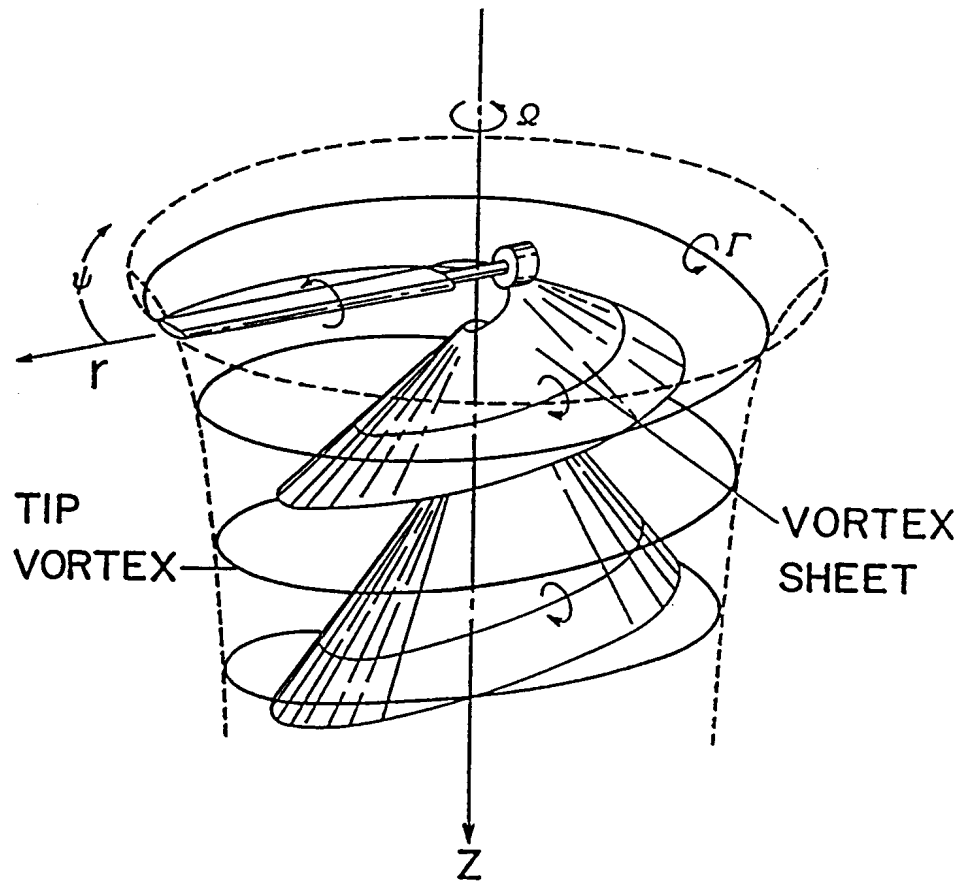


Figure 1.4: Sketch of a helicopter rotor wake for a single blade. From Gray [4].

As described by Johnson [3], owing to the rotation of the blade, the lift and the corresponding circulation are concentrated at the tip. In the tip region, the circulation drops quickly to zero over a finite distance. Owing to the high rate of change in the circulation, the strength of the shed vorticity is very strong, which causes the shed vortices to quickly roll up into a strong single tip-vortex. In the inboard portion of the blade, the bound circulation drops off gradually to zero at the root. Hence there is an inboard sheet of trailed vorticity in the wake with the opposite sign to the tip-vortex. Since the radial variation of the bound circulation is small away from the rotor-tip, the inboard sheet is generally much weaker and more diffuse than the tip-vortex. Figure 1.4 depicts the complexity of the shed wake of a single bladed rotor from Gray [4].

From the viewpoint of pressure, the tip region contains a complex three-dimensional viscous flow field which results from the pressure difference on the upper and lower surfaces on a lifting airfoil. Because at the wing tip, a pressure discontinuity is not possible, the pressure difference on the blade is gradually relieved towards the tip and finally the pressure difference is zero at the wing tip. Associated with this pressure field, near the wing tip, the fluid particles roll up and form the tip-vortex which is convected downstream by the local streamwise velocity.

1.4 Wake Models

Wake prediction models have evolved over the years from simple one-dimensional momentum theory of the 19th century [3] to the highly complex free wake models of today. This development took place as a consequence of the demand for more accurate predictions of helicopter performance, such as lift, drag and blade loading which would help in the design of blades and rotors. Wake models developed over the years can be classified

into three categories: (1) Rigid Wake Models (2) Prescribed Wake Models (3) Free Wake Models. A good review of the development of the wake model from the prescribed wake model to free wake model is given by Conlisk [5].

(1) Rigid Wake Model: The rigid wake model assumes that the wake consists of a series of vortex lines. Each vortex line forms a skewed helix, whose geometry is set by the forward speed of the helicopter and the mean inflow velocity through the tip path plane. The wake is not allowed to deform. The problem in using this wake is that the wake does not contract or expand and therefore, the results do not agree with the experiments. However it is the simplest model, requiring a very small amount of computation. If the flight condition is such that the wake is convected away from the disk, like in high climb rates, and hence there is no significant vortex-blade interaction, then a rigid wake model is a satisfactory model.

(2) Prescribed Wake Model: The prescribed wake model overcomes this disadvantage by utilizing experimental data to predict the wake geometry including the tip-vortex and the inboard vortex sheets. But this model is not truly predictive because it requires experimental data. The use of this model is limited by the necessity of performing experiments for the required rotor and flight condition.

(3) Free Wake Model: A free-wake model allows the wake to develop under the influence of all the components, that is the free stream velocity, the self-induced velocity and the effect of the blade. This is now the industry standard to calculate the wake and the blade loads.

1.5 Effect of the Ground on the Rotor Flow Field

When the helicopter is operating close to the ground, the major influence of the ground can be viewed as a reduction of the average induced velocity at the rotor disk. The reduction in velocity is because the wake is constrained by the ground and is forced to expand in the radial direction. The wake impinges on the ground and then rolls up under the influence of the incoming flow. The presence of the ground acts as a hindrance to the advancement of the wake and since the wake is constrained in the downward axial direction, it expands radially outward as it approaches the ground. This in turn leads to a change in the aerodynamic characteristics of the rotor, including the strength of the tip-vortex and the forces and moments on the rotor. The wake near the ground rolls up in front of the rotor blade resulting in the formation of the ground vortex. The presence of the ground vortex further complicates the flow field leading to instabilities in the wake. The ground vortex creates handling problems, disrupts the trim schedule and leads to imbalance in moments.

Moreover, the presence of the ground plane makes the computation more complicated. In the case where there is no ground plane and the wake is thus unbounded, Kini [6] showed that a far boundary condition consisting of semi-infinite sheet of vorticity, having an analytical representation at the location of the tip-vortex was sufficient to describe the far wake. However, in the ground effect case, such a far boundary condition is not possible. Nevertheless, image techniques are used here to satisfy the boundary condition on the ground plane and the details of these methods are described in Chapter 2.

When a rotor hovers or is in forward flight near the ground, its wake impinges on the ground and then rolls up under the influence of the incoming flow. The presence of the ground changes the aerodynamic characteristics of the rotor and the flow environment

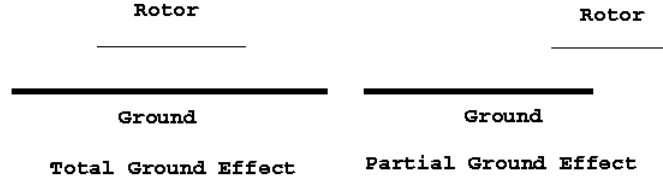


Figure 1.5: Comparison of partial and total ground effects.

becomes much more complex compared with that of flight out-of-ground effect (OGE). An extensive set of references on wake calculations in OGE may be found in the review by Conlisk [2].

Several analytical, empirical and experimental efforts have been made to predict helicopter performance in ground effect (IGE). Yeager *et al.* [7] and Empey and Ormiston [8] have conducted wind tunnel tests to study the impact of the ground vortex on helicopter performance close to the ground. Yeager *et al.* [7] experimentally investigated the effect of various parameters like wind velocity, wind azimuth and tail rotor collective pitch on helicopter directional control in ground effect. Empey and Ormiston [8] experimentally showed that the ground vortex and trailing vortex systems of the main rotor flow field produced tail rotor thrust perturbations that are due to rotational and axial interference with the tail rotor. Weisner and Kohler [9] conducted wind tunnel tests to investigate the characteristics of tail rotor performance in the presence of a main rotor for various conditions including the presence of the ground as well as that of sideward flight. Lynn *et al.*, [10] showed that the major aerodynamic tail rotor problems encountered have occurred in left sideward flight and these problems relate primarily to the helicopter's directional control characteristics which is confirmed by the current work.

Hayden [11] developed a simplified empirical model from a large set of flight test data. His method was based on developing a correction to the induced power due to the presence of the ground. An experimental investigation on the aerodynamic characteristics of a rotor at low advance ratio near the ground was made by Curtiss *et al.* [12]. This study found that a horseshoe vortex forms under a rotor in forward flight near a ground which is termed the ground vortex. Xin *et al.* [13] produced results for the case of a rotor in partial and total ground effect using a finite state dynamic inflow model for the rotor wake structure. A qualitative picture comparing total and partial ground effects can be seen in Figure 1.5. Hanker and Smith [14] conducted ground effect experiments at the Princeton Dynamic Model Track and found that the recirculation occurs until an advance ratio of 0.058, and that the ground vortex disappeared at an advance ratio of about 0.125. Sun [15] used a free vortex wake model combined with prescribed position of ground vortex from experiments to compute the inflow of a rotor in ground effect. Cimbala *et al* [16] studied the unsteady behavior of the ground vortex, and noted that the ground vortex had a low frequency pulsing behavior.

Light [17] conducted an extensive set of experiments using the wide-field shadowgraph method to photograph the tip-vortices of a hovering rotor IGE. He observed variations in the descent and contraction rates of the tip-vortices and interaction between tip-vortices in the far wake. Landgrebe *et al* [18] studied the wake characteristics of the helicopter in hover and low speed forward flight in ground effect. They noted that while hovering, tip-vortices are transported downward, whereas in low speed forward flight the tip-vortices travel inboard and slightly above the rotor and are then transported down through the rotor

disk. They found that the flow velocity at each flow field point varies with time, due to the rotation of the blades and the periodic passage of the tip-vortices.

Kucab *et al.* [19] developed a hybrid code to predict the rotor flows in ground effect. There they solved the Euler/ Navier-Stokes equations to resolve the flow structure near the ground. Kang and Sun [20] numerically simulated the flow field of a single rotor in ground effect. An actuator disk model has been used to model the wake and Navier-Stokes equations in steady state have been used to solve for the flow field. Subsequently Kang and Sun [21] studied the flow fields of the tandem, side-by-side, and co-axial rotor configurations in ground effect at low flight speeds.

Typically a substantial number of revolutions are needed to establish periodic state in hover and low-speed forward flight. This is very difficult using a Navier Stokes/Euler solver because of the large number of points required to resolve the flow for a relatively large number of time steps. With the passage of time, the strength of the tip-vortex as well as the inboard sheet is much weaker than that seen in the experiments due to numerical diffusion. This is especially true at the high disk loadings required in the industry today. For this reason both Euler and Navier-Stokes calculations of the rotor wake are at this point research codes.

Complicating the computation is the need to trim the rotor. Many of the Navier-Stokes computations are only partially trimmed using an external comprehensive rotor design code. At the present time, computational time limitations prevent adding a full trim module to the codes. But there are also certain advantages to the Navier-Stokes solvers compared to the vortex methods. The Navier-Stokes equations contain the physics for vorticity generation at a surface and subsequent convection into the wake. In addition, the viscous drag

on the blade can also be determined for use in computing performance variables such as the thrust and power coefficients whereas with vortex methods, airfoil lookup tables or some other model is required to calculate drag. Two reviews have been published on the use of these methods; Landgrebe [22] outlines the primary contributions of Navier-Stokes and Euler calculations in the United States and Srinivasan and Sankar [23] have discussed possible new methodologies. The capabilities of a European Euler solver have also been presented in [24].

The rotor wake is dominated primarily by a strong tip-vortex which arises from the rapid rolling up of the portions of the vortex sheet shed from the tip region of the blade. In order to understand the flow physics and the performance of a helicopter near the ground, a detailed study on the structure of the tip vortex is required. The literature suggests that a general understanding of the rotor wake IGE is lacking and there has been little modeling work in the literature on helicopter aerodynamics in ground effect since 1990. Most of the work has been of experimental nature and even the modeling work done involves solving Navier-Stokes/Euler equations requiring considerable computational time and cannot be used for design of helicopter blades. Modeling the rotor wake is a small part of the helicopter design process and should take a small amount of computational time and the industry needs to be able to do routine computations.

Helicopters flying close to the ground encounter many handling qualities problems. Large unsteady forces near the main and tail rotors are considered a major cause for these problems. The present research also investigates the role played by the presence of the ground plane in the generation of these large unsteady forces.

1.6 The Current Work

The flow field of a rotor in ground effect takes a large number of revolutions to completely evolve and reach a periodic state. The current work is able to achieve this objective without requiring much computational power. Periodicity is attained after 20-40 revolutions depending on the number of blades in the rotor. When more than one blade is used in the rotor, there are vortex-vortex interactions which make the flow field very complicated and more number of revolutions are needed to attain periodic state.

Rotor wake codes in the world today often make use of lifting line theory to model the blade where the aspect ratio of the blade is assumed to be very large with $1/A \rightarrow 0$. The main disadvantage of using this theory is its inability to model finite aspect ratio blades. Although all rotor blades currently being used in the industry today are high aspect ratio blades, it is very difficult and dangerous to conduct experiments using such blades. Hence it is imperative that a finite aspect ratio blade be modeled to be able to compare the computational results with the existing experimental data. In Chapter 2, the numerical model used to model the blade, wake and the ground has been discussed. The current work makes use of the lifting surface theory to model a finite aspect ratio blade. In this model, the blade is assumed to be flat surface and is divided into a number of panels with each panel being represented by a horseshoe vortex. The solid wall boundary condition is satisfied on the blade to obtain the tip-vortex circulation. Results have also been obtained using the lifting line theory for comparison with lifting surface theory.

Chapters 3 and 4 deal with the representation of the flow field using the wake structure and the downwash profiles. The evolution of the tip-vortex structure with time is presented in both hover and forward flight. Results for single and two-bladed rotors are presented.

The formation of the ground vortex is investigated by looking at the downwash profiles along the blade at various heights from the ground as well as their contours. The flow field results have been compared qualitatively with those obtained from the experimental work being conducted at Georgia Institute of Technology. The results obtained using lifting line theory are compared with those obtained using lifting surface theory. An application concerning the directional control characteristics is studied by looking at the unsteadiness in velocities on and around the tail rotor disk which is believed to be the main reason for the handling qualities problems being encountered by the pilots in ground effect. Various kinds of sideward flight have been considered to investigate the kind of flight experiencing the maximum unsteadiness.

Chapter 5 deals with the effect of the ground on the thrust generated as well as on the power requirements. The values of the thrust coefficient, induced drag coefficient and the induced power coefficient have been obtained both single and two-bladed rotors at various heights above the ground as well as at various advance ratios. The power requirements have been compared with the experimental data obtained from Georgia Institute of Technology. In Chapter 6, a tail rotor has been incorporated into the current model to investigate the effects on the flow field as well as the loads. The impact of the tail rotor on the velocities induced as well as the loads and power requirements on the rotor disk has been studied. The model has been validated by comparison with experimental data obtained from Empey and Ormiston [8] and the comparisons are very good. Chapter 7 summarizes the current work and suggests future extensions of this research.

CHAPTER 2

Numerical Model for the Blade

2.1 Introduction

In the current work, both lifting line and lifting surface models have been used to model the blade. Results obtained using these two models have been compared. The presence of the ground is modeled using the method of images.

The basic assumption of lifting-line theory is that the wing has a high aspect ratio and this is almost always satisfied with a rotor blade. However, as explained by Johnson [3] a more accurate specification of the requirement for validity of lifting line theory is that there be no spanwise change in the aerodynamic environment of the blade; this does not always hold true with the helicopter blade even though the geometric aspect ratio is large. There are two important cases where this requirement is not satisfied on a rotor blade: at the blade tip, and near a vortex-blade interaction. In the present work, we will not be concerned about vortex-blade interaction as much as with the flow-field around a blade tip. The loading near a blade tip must drop to zero in a finite distance. On a rotor blade, where the loading is concentrated at the tip because of higher velocities there, the gradient of the lift at the tip is particularly large, and any small distortion of the loading due to three-dimensional flow effects is very important.

In certain flight conditions the rotor blade passes quite close to a tip-vortex from a preceding blade and substantial time-varying loads are produced. The vortex-induced velocity gradients at the blade will be large for such close passages, and the lifting-line theory significantly overestimates the loading produced [25]. It is for these reasons that the tip-vortex circulation cannot be estimated from lifting-line theory alone. Since the circulation directly influences the subsequent position of the tip-vortex and the intensity of the subsequent interactions with other components of the wake, it is important to determine circulation as accurately as possible.

2.2 Lifting Line Theory

In this work, lifting line [6] and lifting surface [25] theories have been used to model the blade and obtain the value of the bound and tip circulations. Lifting line analysis which is valid as the span to chord of the rotor blade becomes large, has been investigated in earlier work by Li [25]. In this model, consistent with two-dimensional airfoil aerodynamics, the blade is modeled as a single bound vortex line located at the 1/4 chord position and an associated shed vortex sheet [26].

To understand lifting line theory, a knowledge of the Biot-Savart law is essential. The velocity induced by a vortex segment is calculated using the Biot-Savart law given by,

$$\vec{U}_V(\vec{X}, t) = -\frac{\Gamma}{4\pi} \int_C \frac{(\vec{X} - \vec{X}') \times d\vec{X}'}{(|\vec{X} - \vec{X}'|^2 + \mu_c^2)^{3/2}} \quad (2.1)$$

where $\vec{X} = (x, y, z)$ is the field point and $\vec{X}' = (x', y', z')$ the position vector of a point on the vortex and C denotes the space curve occupied by the vortex.

The lifting line model as applied to the fixed wing case [26] is first described here briefly then is later extended to the rotary wing case. As can be seen from Figure 2.1, a

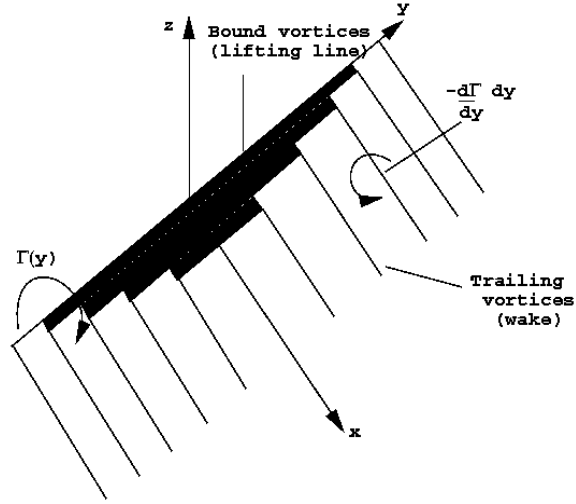


Figure 2.1: Lifting line model for a fixed wing ; the dark areas indicate the magnitude of bound circulation; circulation has an elliptical distribution in the fixed wing case.

straight bound vortex of strength $\Gamma(y)$ is placed along the y -axis in the spanwise direction of the blade. Since there is a variation in the circulation along the bound vortex, trailing vortices of strength $d\Gamma(y) = \frac{d\Gamma(y)}{dy}dy$ are shed along the length of the blade. The boundary condition requiring no flow across the blade would be

$$w_b + w_i + U_\infty \sin\alpha = 0 \quad (2.2)$$

where w_b is the normal velocity induced by the bound vortex and w_i is the sum of the normal velocities induced by the trailing vortices, U_∞ is the free stream velocity and α is the angle of attack. The velocity component induced by the lifting line on the section with a chord $c(y)$ can be estimated by using the lumped-vortex model with the downwash calculated at the collocation point located at the 3/4 chord (2D airfoil aerodynamics [26]) where the solid wall boundary condition is satisfied as can be seen from Figure 2.2. The velocity induced by the complete bound vortex (evaluated at y using the Biot-Savart law) is

given by,

$$w_b = \frac{-\Gamma(y)}{\pi c(y)}. \quad (2.3)$$

The sum of the normal velocities induced by the trailing vortices is given by,

$$w_i = \frac{1}{4\pi} \int_{-b/2}^{b/2} \left(\frac{d\Gamma}{dy} \frac{dy_0}{y - y_0} \right) \quad (2.4)$$

Substituting Equations (2.3) and (2.4) in Equation (2.2), we have,

$$\Gamma(y) = \frac{mc}{2} \left(U_\infty \sin\alpha - \frac{1}{4\pi} \int_{-\frac{b}{2}}^{\frac{b}{2}} \frac{d\Gamma}{dy} \frac{dy_0}{y - y_0} \right) \quad (2.5)$$

where Γ is the circulation, α is the angle of attack, U_∞ is the speed far from the wing, b is the span of the wing, and c is the local value of the chord. Here m is a constant equivalent to the lift-curve slope which is airfoil dependent. For a flat plate, $m = 2\pi$. Equation (2.5) is a non-linear singular integral Equation for $\Gamma(y)$.

It is important to understand the assumptions associated with the derivation of this Equation. Of principal importance for our purposes are

- the trailing wake is assumed to remain in the plane of the wing $z = 0$ for all time, or equivalently in linearized theory, in the cross-plane containing the free stream velocity vector; and
- the pressure difference between the bottom and the top of the wing must approach zero at the tip, and so $\Gamma = 0$ there also.

However, for a rotary wing, the trailing vortices are driven downward away from the rotor-tip path plane and form a nearly helical wake. Therefore, the assumption that trailing vortices remain in the rotor-tip path plane as for the fixed wing is not valid and the lifting line Equation (2.5) cannot be applied to the rotor-tip directly. Including the influence of

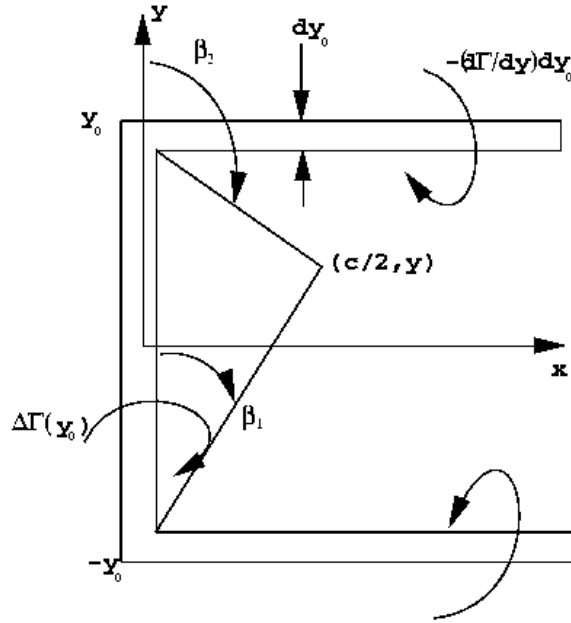


Figure 2.2: Velocity induced by the segments of a typical horseshoe element.

the helical rotor wake, it is shown here that in the tip region, to leading order, the bound circulation of the rotary wing has a solution similar to that of a fixed wing, although the rotary wing analysis involves a parameter dependent on the aspect ratio, the angle of attack and the number of blades.

For the case of the rotor blade in hover, two modifications to the lifting line Equation must be made [25]:

- the true free stream in wing theory is replaced by the angular velocity of rotation of the blade, and
- the trailing vortices of the rotor follow a nearly helical path.

Unlike the bound circulation on the fixed wing, the bound circulation on a rotary wing increases approximately linearly with span and the lifting line equation for a rotary wing is obtained by setting $U_\infty = \Omega r$ where r is the radial location of the blade,

$$\Gamma(r) = \frac{mc}{2} \left(\Omega r \sin \alpha - \frac{1}{4\pi} \int_0^R \frac{d\Gamma}{dr} \frac{dr_0}{r - r_0} \right). \quad (2.6)$$

However, the angle of attack must now be viewed as including the effect of the downwash induced by the wake ,

$$\alpha = \alpha_0 - \alpha_i = \alpha_0 - \frac{w_i(r)}{\Omega r}, \quad (2.7)$$

where α_0 is the pitch angle of attack, α_i is the induced angle of attack and w_i is the induced downwash. The term inside the integral in Equation (2.6) is of the order of $\frac{1}{A}$ where A is the aspect ratio of the rotor blade. For very large aspect ratios, the Equation becomes,

$$\Gamma(r) = \frac{m}{2} c \Omega r \left(\sin \left(\alpha_0 - \frac{w_i(r)}{\Omega r} \right) \right). \quad (2.8)$$

In earlier work on OGE [6], the maximum bound circulation has been assumed to be equal to the tip-vortex circulation which is used here to obtain a few preliminary results. This assumption is based on the Betz theory [27] which states

$$\Gamma_{tip} = \int_0^{r_{max}} \frac{d\Gamma_b}{dr} dr = \Gamma_{b,max} \quad (2.9)$$

where r_{max} is the distance from the tip of the blade to the maximum bound circulation location. Since the maximum bound circulation is used as the tip circulation, the tip- circulation is given by Equation 2.8 evaluated at $r = R$ so that,

$$\Gamma_{tip} = \frac{m}{2} c \Omega R \left(\sin \left(\alpha_0 - \frac{W}{\Omega R} \right) \right) \quad (2.10)$$

where W is the induced downwash at the tip and R is the radial location of the tip. For the case of forward flight this Equation becomes

$$\Gamma_{tip} \sim \frac{m}{2} c(\Omega R + V_f \sin \psi) \sin \left(\alpha_0 - \frac{W}{\Omega R} \right) \quad (2.11)$$

where V_f is the forward flight velocity and ψ is the angle traversed by the blade from its initial position at rest.

2.3 Lifting Surface Model

Lifting line theory is simple and fast computationally; however lifting line theory will fail if large spanwise variations in velocity on the blade occur. In the lifting surface model, the blade is replaced by a single flat surface. This model is expected to capture the wake dynamics close to the blade more accurately than a lifting line model.

In the current work, lifting surface theory is applied to the flow near the blade by using panel methods. The solution to many potential flow problems is obtained using analytical techniques only after major simplifications in the surface geometry and boundary conditions are made. However, the application of panel methods allows the treatment of more realistic geometries, and the fulfillment of the boundary conditions on the actual surface. These methods are based on the surface distribution of singularity elements such as a source, doublet, or vortex, which is a logical extension of the analytical methods to deal with complicated surface geometries. By applying panel methods, the solution to the potential flow problem is reduced to finding the strength of the singularity elements distributed on the body's surface. Once the singularity strengths have been determined, the velocity field and other parameters can be computed. It seems more efficient from a computational perspective to use this method rather than other numerical methods such as

finite-difference methods which are used in solving the more complicated flow fields where compressibility and viscous effects come into the picture. The application of this method to two-dimensional airfoil problems and three-dimensional wings can be referred to from earlier work by Li [25].

Consider a horseshoe-vortex element which is a three-dimensional singularity element that has been used to represent the lifting-wing surface in the current work. A horseshoe vortex is a simplified case of the vortex ring. It consists of a straight bound vortex segment along the panel quarter-chord line that models the lifting properties, and two trailing vortices lying along the panel edges and extending to infinity downstream and which model the wake. The boundary condition of zero normal velocity on the wing surface is satisfied at the three-quarter chord point on the centerline of each panel collocation point and the trailing vortices emanate from the panel quarter-chord line (see Figure 2.3). Actually, this model is based on the two-dimensional “lumped vortex” element model. By placing the leading vortex segment of the horseshoe vortex at the quarter chord line of the panel, the two-dimensional Kutta condition is satisfied along the chord and it is assumed that the two-dimensional Kutta condition satisfactorily accounts for the three-dimensional Kutta condition. The Kutta condition states that for bodies with sharp trailing edges which are at small angles of attack to the free stream, the flow will adjust itself in such a way that the rear stagnation point coincides with the trailing edge.

In this model the blade is modeled by a number of panels. Each panel consists of a horseshoe vortex with a bound vortex and two trailing vortices extending downstream to infinity. The bound vortex is located at the quarter chord line (applying 2-d airfoil theory). For a two-dimensional symmetric airfoil, the center of pressure is at the $1/4$ chord. The

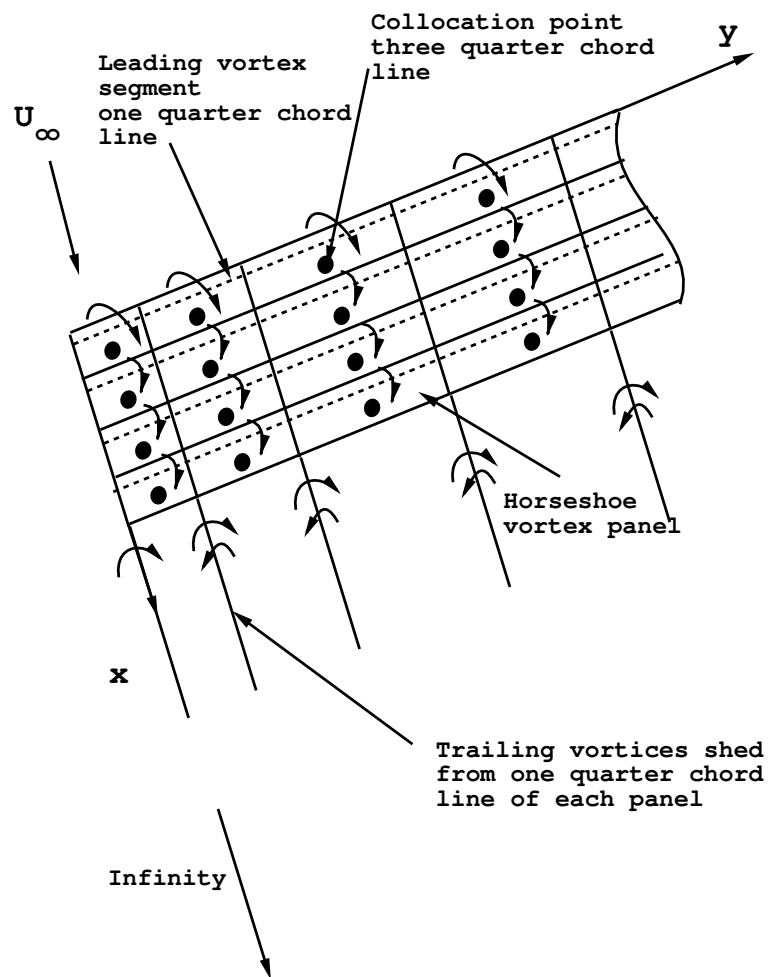


Figure 2.3: Horseshoe vortex model of a rotary wing.

common trailing vortex between adjacent bound vortices has a circulation equal to the difference between the circulations of the two bound vortices to satisfy the laws of vortex theory. To obtain the circulation of each panel a zero normal velocity boundary condition is applied at the three quarter chord location of each panel(2-d airfoil theory). Note that the placement of the collocation point at the 3/4 chord line gives the proper lift for a single vortex placed at the 1/4 chord line as demonstrated for two dimensions.

We now define local panel-based coordinates; define the x -axis to be oriented in the chordwise direction, the y -axis spanwise, and the z -axis vertical as shown in Figure 2.4 (a). x and y are measured from the midpoint of the selected panel, and z from the plane of the wing. The panel-width dimensions are $2a$ by $2b$ in the chordwise and spanwise directions respectively. Then the velocity induced by each unit bound-vortex segment is evaluated using Biot-Savart law in local panel coordinates as [25]

$$\begin{aligned}
 u_B(x, y, z) &= \frac{1}{4\pi} \frac{z}{(x + \frac{a}{2})^2 + z^2} \times \\
 &\quad \left[\frac{y + b}{\sqrt{(x + \frac{a}{2})^2 + (y + b)^2 + z^2}} \right. \\
 &\quad \left. - \frac{y - b}{\sqrt{(x + \frac{a}{2})^2 + (y - b)^2 + z^2}} \right] \\
 w_B(x, y, z) &= -\frac{1}{4\pi} \frac{x + \frac{a}{2}}{(x + \frac{a}{2})^2 + z^2} \times \\
 &\quad \left[\frac{y + b}{\sqrt{(x + \frac{a}{2})^2 + (y + b)^2 + z^2}} \right. \\
 &\quad \left. - \frac{y - b}{\sqrt{(x + \frac{a}{2})^2 + (y - b)^2 + z^2}} \right]
 \end{aligned}$$

while the two unit trailing vortices produce the contributions

$$v_{T1}(x, y, z) = \frac{1}{4\pi} \frac{z}{(y + b)^2 + z^2} \times$$

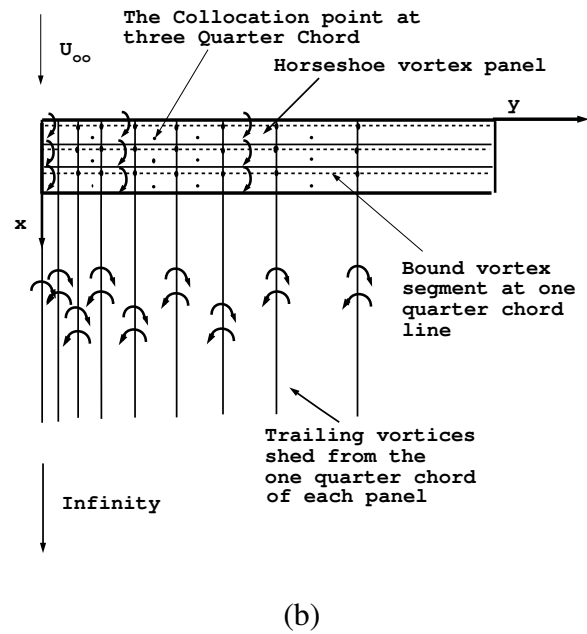
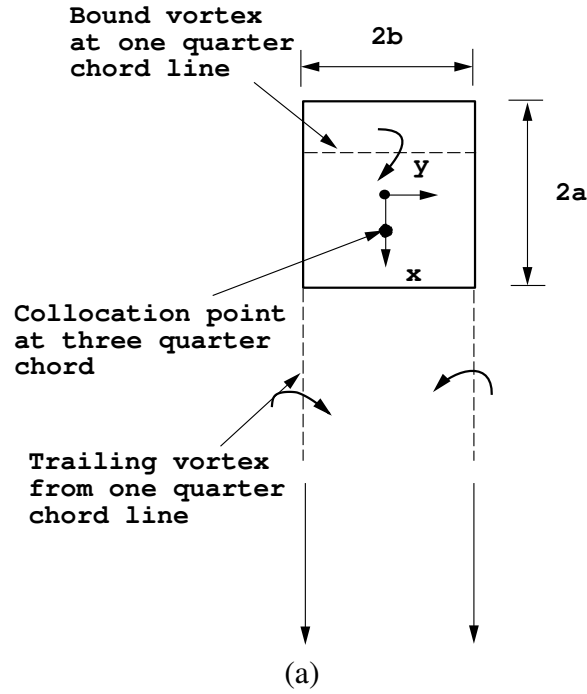


Figure 2.4: Horseshoe-vortex panel implementation of a semi-infinite wing. The panel width is non-uniform in the spanwise direction, as discussed in the text. The velocity boundary condition is applied at the three-quarter chord line at the midspan point of each panel. (a) Definition of the local panel coordinates. (b) Definition of the global coordinates.

$$w_{T_1}(x, y, z) = \frac{-1}{4\pi} \frac{y+b}{(y+b)^2 + z^2} \times \left[\frac{x + \frac{a}{2}}{\sqrt{(x + \frac{a}{2})^2 + (y+b)^2 + z^2}} + 1 \right]$$

and

$$v_{T_2}(x, y, z) = \frac{-1}{4\pi} \frac{z}{(y-b)^2 + z^2} \times \left[\frac{x + \frac{a}{2}}{\sqrt{(x + \frac{a}{2})^2 + (y-b)^2 + z^2}} + 1 \right]$$

$$w_{T_2}(x, y, z) = \frac{1}{4\pi} \frac{y-b}{(y-b)^2 + z^2} \times \left[\frac{x + \frac{a}{2}}{\sqrt{(x + \frac{a}{2})^2 + (y-b)^2 + z^2}} + 1 \right]$$

where u , v and w are the x , y and z components respectively. Subscript B designates the bound-vortex segment and T_1 , T_2 designate the two trailing vortices.

We now consider the global coordinates; define the x -axis to be oriented in the chord-wise direction, originating at the leading edge of the wing, the y -axis spanwise, originating at the wing-tip, and the z -axis vertical, as shown on Figure 2.4 (b). The panel influence coefficients A_{jk} are given by the normal velocity induced in the plane of the wing at the $3/4$ chord position on panel k due to the horseshoe vortex of unit circulation with the bound vortex at the $1/4$ chord position on panel j , as

$$A_{jk} = w_b(x_{jk}, y_{jk}, 0) + w_{T_1}(x_{jk}, y_{jk}, 0) + w_{T_2}(x_{jk}, y_{jk}, 0)$$

where

$$x_{jk} = x_k - x_j + \frac{a}{2}$$

and

$$y_{jk} = y_k - y_j$$

Here, x_k, x_j, y_k, y_j are the global variables and x_{jk}, y_{jk} are the local variables. The boundary condition of zero normal velocity on the wing surface is satisfied at the three-quarter chord point on the centerline of each panel, as in Schlichting and Thomas [28], and the vortices emanate from the panel quarter-chord line and extend through the trailing edge of the wing to infinity downstream (see Figure 2.5). The coordinate along the rotary wing is now y in the lifting surface model.

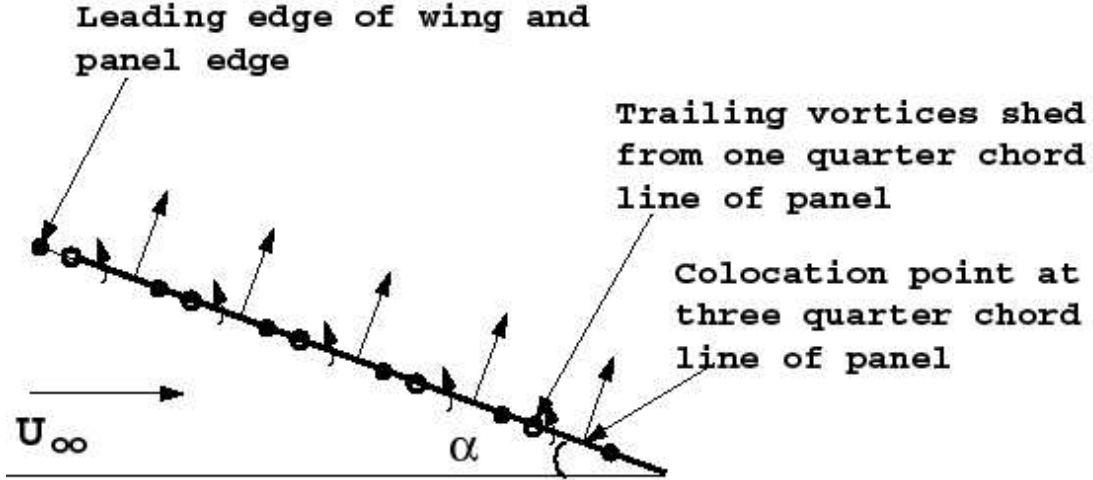


Figure 2.5: Schematic of the trailing vortex system. Open circles denote the quarter-chord location of each panel (bound vortices), solid circles denote panel edges. Arrows denote the normal direction at the panel three-quarter chord line (normal-velocity boundary condition) [26].

Thus the panel circulations $\Gamma_k, k = 1, \dots, m$ may be evaluated from the surface boundary condition, expressed as a set of m linear Equations for Γ_k

$$\sum_{k=1}^m A_{jk} \Gamma_k = -\alpha_0(1 - w_{i,j}) \quad j = 1, \dots, m \quad (2.12)$$

where $w_{i,j}$ is the dimensionless induced downwash due to the presence of the wake at the j th panel. The set of equations is numerically solved by Gaussian elimination using LINPACK routines.

The trailing vortices near the tip roll up to form the tip-vortex. Hence, the strength of the tip-vortex equals the sum of the circulations of the roll over trailing vortices. The amount of trailing circulation is determined by the derivative of the bound circulation and in discrete form the trailing circulation at a fixed radial location is given by

$$\Gamma_t = -\frac{d\Gamma}{dy}$$

where Γ is the bound circulation and y -axis is the coordinate along the blade. The variation of bound circulation in the spanwise direction of the blade in hover IGE and OGE can be seen in Figure 2.6. There is a gradual increase in the value of circulation as we move from the root to near the tip of the blade but there is a steep decrease in its value as we move towards the tip where it reaches zero. The steep decrease in the bound circulation near the tip is the reason behind the high strength of the tip vortex. The magnitude of the bound circulation is higher in ground effect as seen in Figure 2.6.

The values of tip-circulation obtained by the lifting surface model are compared with those obtained from the lifting line model in hover in ground effect obtained from Equation 2.10. An aspect ratio of $A = 6$, near the value used in experiments (see Chapter 4) has been used for the lifting surface model. Figure 2.7 shows the comparison between the tip

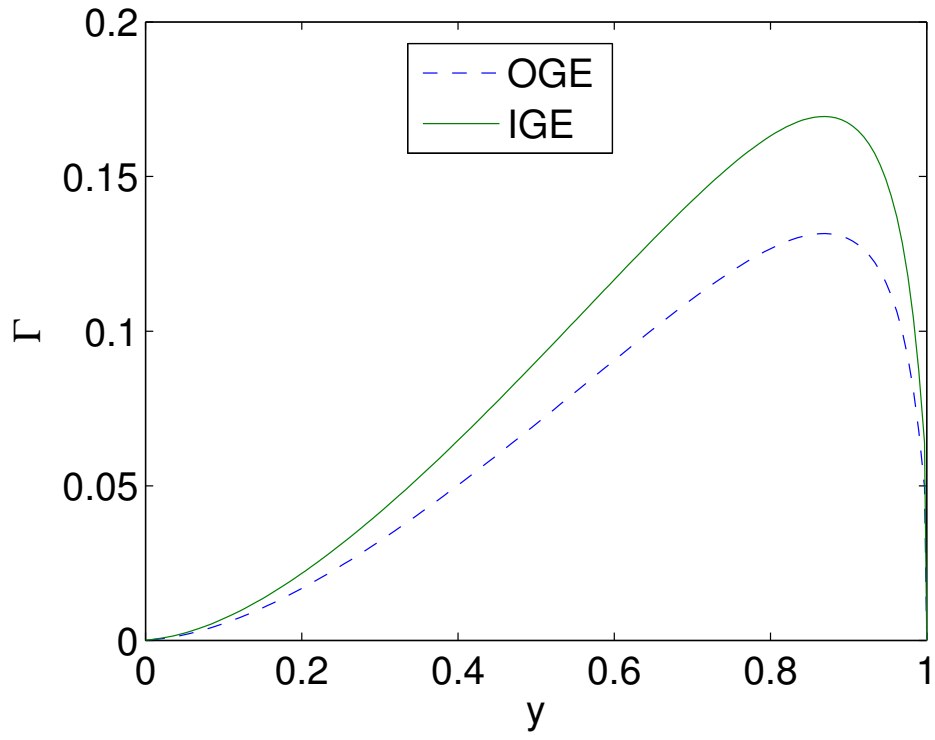


Figure 2.6: Bound circulation distribution along the blade in hover IGE, $h/R = 0.5$ and OGE; $A = 6$, $\alpha_0 = 10^\circ$.

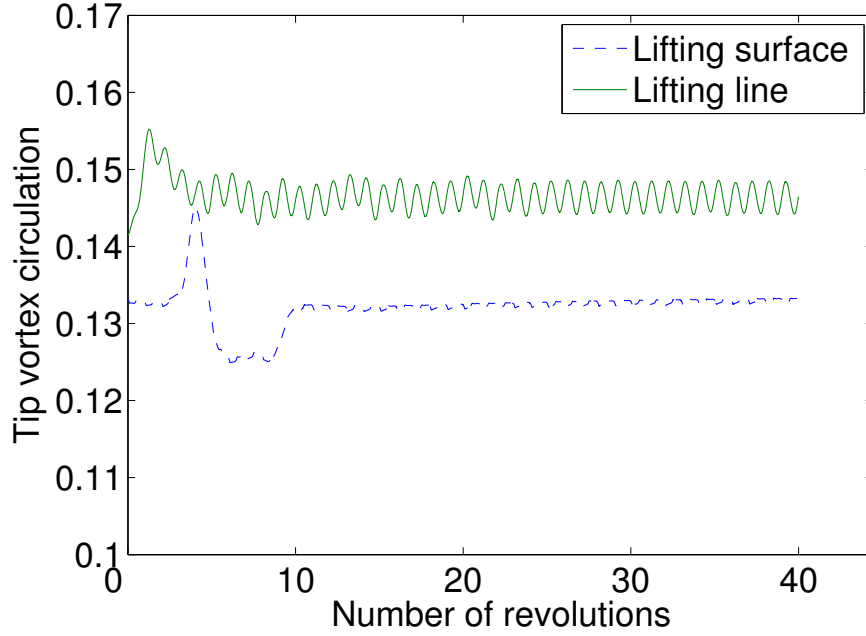


Figure 2.7: Comparison of the dimensionless tip-vortex circulations for lifting line and lifting surface models in hover, $h/R = 0.5$.

circulation values. It can be seen that the lifting line model overestimates the value of tip-circulation for the case of hover. The reason behind this could be because of the fact that we are using maximum bound circulation for the tip circulation for the lifting line case.

The tip-vortex circulations at various aspect ratios have been presented in Figure 2.8. It can be seen that the value of the tip-vortex circulation increases with aspect ratio. It increases from about 0.132 at $A = 6$ to 0.148 at $A = 40$. It can be seen that the tip-circulation obtained from the lifting surface model reaches the lifting line limit at $A = 20$.

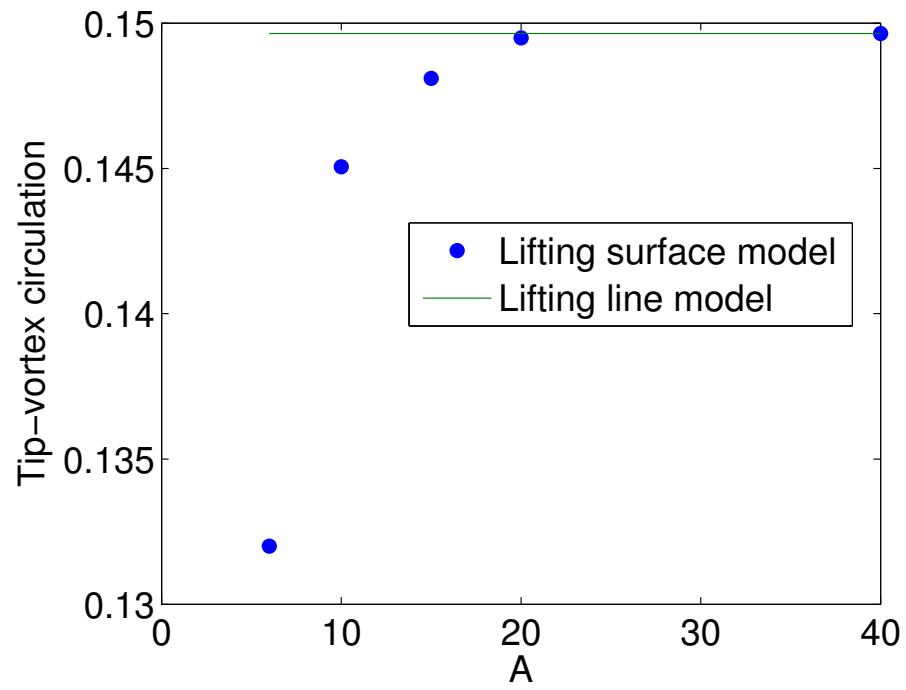


Figure 2.8: Dimensionless tip-vortex circulation as a function of the aspect ratio in hover, $h/R = 0.5$.

2.4 IGE Wake Model

The presence of a ground plane below a helicopter rotor introduces the requirement that the velocity component normal to the ground be zero. As the fluid flow is assumed to be inviscid and incompressible, employing the Method of Images automatically satisfies this boundary condition. The model is depicted in Figure 2.9.

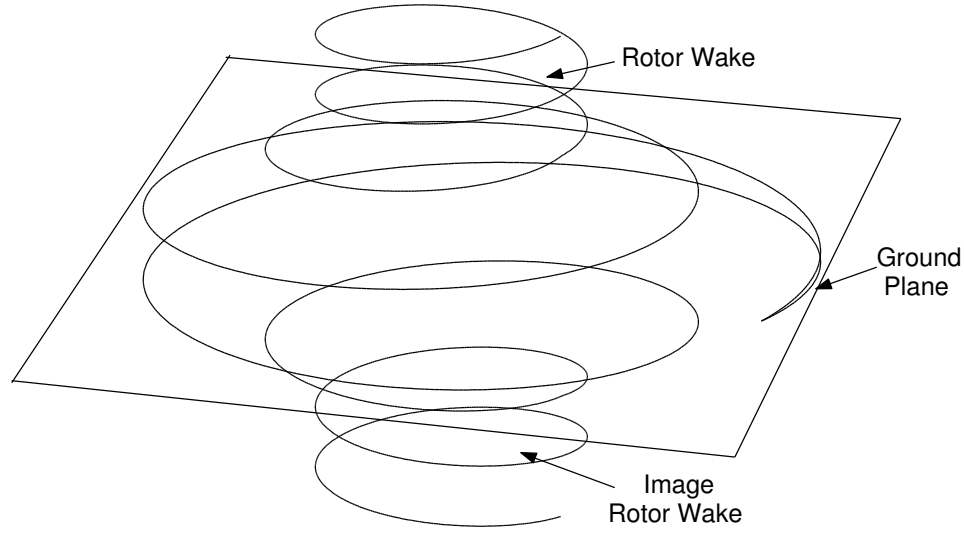


Figure 2.9: Model for the wake of a rotor in ground effect.

An orthogonal right handed non-rotating system of coordinates is used here as shown in Figure 2.10. The blade moves in the $x - y$ plane and the z axis points along the direction of downwash. The azimuth ψ , (not shown in figure) is measured from the positive y axis in the counter clockwise sense.

All lengths are non-dimensionalised by the rotor radius R and the velocity components are non-dimensionalised by $\frac{\Omega R}{2\pi}$, where Ω is the angular velocity of the blade. The time is

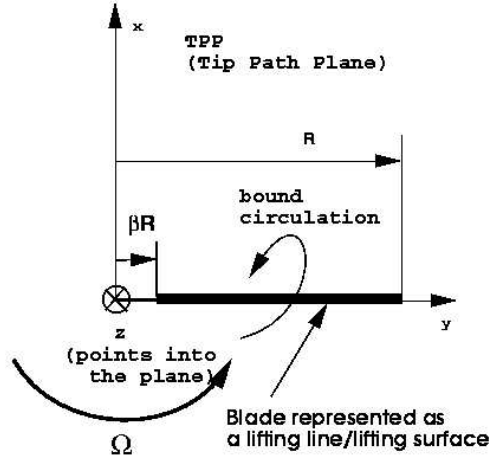


Figure 2.10: Coordinate system; the azimuthal angle (not shown) is the angle between the positive y (dimensionless) direction and the reference blade (blade 1), positive in the counter clockwise sense.

non-dimensionalised by $\frac{\Omega}{2\pi}$. Thus the dimensionless circulation is $\Gamma = 2\pi\Gamma^*/\Omega R^2$ where Γ^* is the dimensional circulation.

The rotor wake is assumed to consist of only the tip-vortex and the influence of the inboard sheet and the root vortex are neglected. In the numerical scheme, the tip-vortex is composed of straight line vortex segments of equal strength and the initial condition employed is a smoothly expanding helical assembly of vortices. The following Equations which describe an expanding helix set up the initial wake geometry for a rotor in ground effect

$$\begin{aligned}
 z_{vj,r}^0 &= \frac{j}{N_p} z_{grpl} \\
 x_{vj,r}^0 &= -f_e \times \sin(j\Delta\psi) \\
 y_{vj,r}^0 &= f_e \times \cos(j\Delta\psi)
 \end{aligned} \tag{2.13}$$

where the wake expansion factor, f_e is initially assumed to be equal to $1.0 + j/N_p$ based on initial trial runs as suggested by Kini and Conlisk [6]. $\Delta\psi$ is the spatial step size and z_{grpl} is the distance between the rotor and the ground plane. The superscript '0' refers to the position at time $t=0$ and $(x_{vj,r}^0, y_{vj,r}^0, z_{vj,r}^0)$ are made dimensionless by the rotor radius. Here, $j = 0, \dots, N_p$ where N_p is the total number of advance points in the real wake. $x_{vj,r}^0, y_{vj,r}^0, z_{vj,r}^0$ are the coordinates of the vortex nodes in the real wake. The rotor is located at the $z = 0$ plane and the image wake is then set up using the following set of Equations

$$\begin{aligned} z_{vj,i}^0 &= 2 \times z_{grpl} - z_{vj,r}^0 \\ x_{vj,i}^0 &= x_{vj,r}^0 \\ y_{vj,i}^0 &= y_{vj,r}^0 \end{aligned} \quad (2.14)$$

$x_{vj,i}^0, y_{vj,i}^0, z_{vj,i}^0$ are the coordinates of the vortex nodes in the imaginary wake below the ground. The subscripts r and i in the above two sets of Equations stand respectively for the real and image wake points.

We assume an inviscid model in which the vorticity evolves as material elements of the fluid, convecting with the local fluid velocity in a Lagrangian sense. At any field point the velocity induced by the tip-vortex is calculated using the Biot-Savart law with a smoothing parameter given by,

$$\vec{U}_V(\vec{X}, t) = -\frac{\Gamma}{4\pi} \int_C \frac{(\vec{X} - \vec{X}') \times d\vec{X}'}{(|\vec{X} - \vec{X}'|^2 + \mu_c^2)^{3/2}} \quad (2.15)$$

where $\vec{X} = (x, y, z)$ is the field point and $\vec{X}' = (x', y', z')$ the position vector of a point on the vortex and C denotes the space curve occupied by the tip-vortices. The flow in the vortex is assumed to be a Rankine vortex with radius a_v . The smoothing parameter based on a Rankine core has been shown by Affes *et al.* [29] to be $\mu_c = a_v e^{-3/4}$.

Each point on the tip-vortex is advanced in time by solving

$$\frac{d\vec{X}_v}{dt} = \vec{U} \quad (2.16)$$

where \vec{X}_v is the position vector of a point on the vortex and \vec{U} is the total velocity induced at that point. Thus \vec{U} is the sum of the velocity induced by the helical tip-vortex, \vec{U}_V (Equation (2.15)), the velocity induced by the bound circulation of each blade, \vec{U}_{blade} and the non-dimensional forward flight speed along the positive y - *axis* , V_f . Thus,

$$\vec{U} = \vec{U}_V + \vec{U}_{blade} + \vec{U}_{V,i} + \vec{U}_{blade,i} + 2\pi V_f \quad (2.17)$$

where the subscript i stands for the image wake velocity contribution. Here the advance ratio is $\mu = V_f$.

While carrying out the computations, it is not necessary to calculate the velocities induced at the nodes in the image wake. The velocities induced by both the wakes are computed at all nodes in the real wake alone and these points are then stepped in time to their new positions in the next time step. The new image wake is then obtained as a mirror image of this new real wake. To solve Equation (2.16) numerically the continuous helical tip vortex represented by Equation 2.13 is discretized into straight line vortex filaments of constant circulation. The length vector of any segment of each vortex in space is defined as,

$$\vec{l}(j) = (x_{v,j+1} - x_{v,j})\hat{i} + (y_{v,j+1} - y_{v,j})\hat{j} + (z_{v,j+1} - z_{v,j})\hat{k} \quad (2.18)$$

where \hat{i} , \hat{j} and \hat{k} are the unit vectors in the x , y and z directions respectively. Thus Equation (2.16) is solved for each j and each Θ as,

$$\frac{d\vec{x}_{vj}}{dt} = \vec{U}_{vj} \quad j = 0, \dots, nm - 1 \quad (2.19)$$

with the initial condition

$$\vec{x}_{vj} = \vec{x}_{vj}^0 \text{ at } t = 0 \quad (2.20)$$

where $\vec{x}_{vj} = (x_{vj}, y_{vj}, z_{vj})$ and $\vec{x}_{vj}^0 = (x_{vj}^0, y_{vj}^0, z_{vj}^0)$ is given by Equation (2.13). The right hand side of Equation (2.19) is evaluated according to Equation (2.17).

Figure 2.11 shows the discretization of the tip-vortex near an advance point, P_A . All velocity integrals are evaluated at integration points which lie midway between adjacent advance points or at the center of a vortex filament as shown in Figure 2.11. The total vortex induced velocity is computed by adding the velocity contributions of all the vortex segments. The velocity contribution due to each tip-vortex segment is computed using the analytical formula given by [2] for a straight line vortex

$$\vec{U}_v = \frac{\Gamma_a}{4\pi} \left\{ \left[\frac{(|\vec{a}| + |\vec{b}|)(|\vec{a}||\vec{b}| - \vec{a} \cdot \vec{b})}{|\vec{a}||\vec{b}||\vec{a} \times \vec{b}|^2} \right] \right\} \quad (2.21)$$

where \vec{b} is the vector connecting the point P and $x_{va,j+1}$ while \vec{a} connects P to $x_{va,j}$. Γ_a is the value of circulation of the vortex segment connecting $x_{va,j}$ and $x_{va,j+1}$. The evaluation point in the figure is shown as $x_{ve,j}$. The evaluation point is obtained as

$$x_{ve,j} = \frac{1}{2}(x_{va,j} + x_{va,j+1})$$

The velocity induced at the advance points is obtained using linear interpolation.

The solution is stepped in time using an Adams-Moulton scheme with a Runge-Kutta starting formula. The integral on the right hand side of Equation (2.16) is evaluated at advance points, while the integration of the first order system of ODE Equation (2.16) is carried out using integration points. The integration points are located at the mid-point of each straight-line vortex segment [6]. After every time step, each of the advance points is

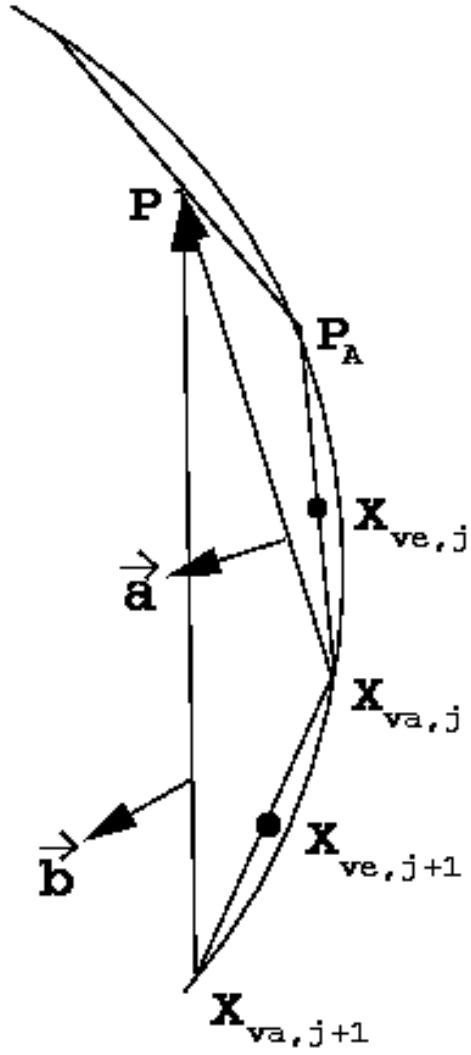


Figure 2.11: Tip-vortex discretization using advance points and straight line vortex filaments.

moved to its new location. This method is observed to give better results than where the advance points and integration points coincide [30]. An initial wake geometry has to be specified for the time-marching scheme which is then allowed to evolve in time. The initial geometry of the wake is taken to be helical corresponding to a prescribed wake.

In this scheme, the vortex segment closest to the ground is removed after every time step and a segment is added near the blade. The contribution of this removed segment to the velocity of any point in the wake will be very small since its effect is almost canceled by its image vortex segment below the ground. To model the removed points, since the tip vortices possess a nearly circular structure near the ground, a vortex ring is introduced close to the ground. The strength of the vortex ring is equal to the tip circulation at each time step. A more detailed discussion of the vortex has been included in Appendix A. Each tip-vortex is represented by 1600 nodes based on numerical accuracy issues. The downwash obtained using 1600 and 3200 nodes for a single bladed rotor in hover for $h/R = 0.5$ at $y = 0.5, x = 0, z = 0.15$ has been compared in Figure 2.12. The downwash in both the cases is the same. The above computation has been repeated for a two-bladed rotor and the results can be seen in Figure 2.13. Hence 1600 nodes is sufficient to model the tip-vortex of each blade.

The accuracy of the numerical scheme was verified by varying the initial spatial step size and time step from $\Delta\psi = 8^\circ$ down to $\Delta\psi = 1^\circ$. The radial and axial trajectories of a single point on the wake starting at the blade tip at $t=0$ for different spatial and time steps are depicted in Figure 2.14. We find that the spatial step $\Delta\psi = 2^\circ$ and time step $\Delta t = 2^\circ$ insure accuracy up to three decimal places in the computed vortex trajectories. Figure 2.14 shows the tip-vortex trajectories(radial and axial) for different spatial and time

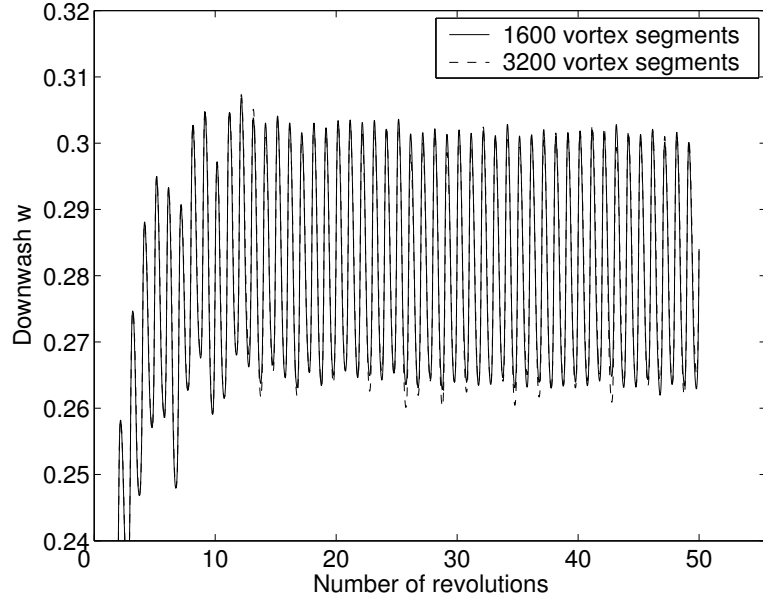


Figure 2.12: Comparison of the downwash values obtained using 1600 and 3200 nodes for the tip-vortex in hover for a single bladed rotor; $h/R = 0.5$, $y = 0.5$, $x = 0$, $z = 0.15$.

steps. Figure 2.14 (a) shows the radial trajectory while (b) shows the axial trajectory. It is evident that as we reduce $\Delta\psi$ from 8° to 1° , the trajectories come closer together indicating the convergence.

2.5 Summary

In this chapter, the lifting line and lifting surface models have been discussed. It has been shown that the lifting line model overestimates the circulation compared the lifting surface model for aspect ratio $A = 6$. The variation of circulation within each revolution is also lesser compared with the lifting surface model. The model has been numerically verified. The lifting surface model serves to simulate low aspect ratio blades which are used mostly in the experiments. On the other hand, the lifting line model is a good approximation

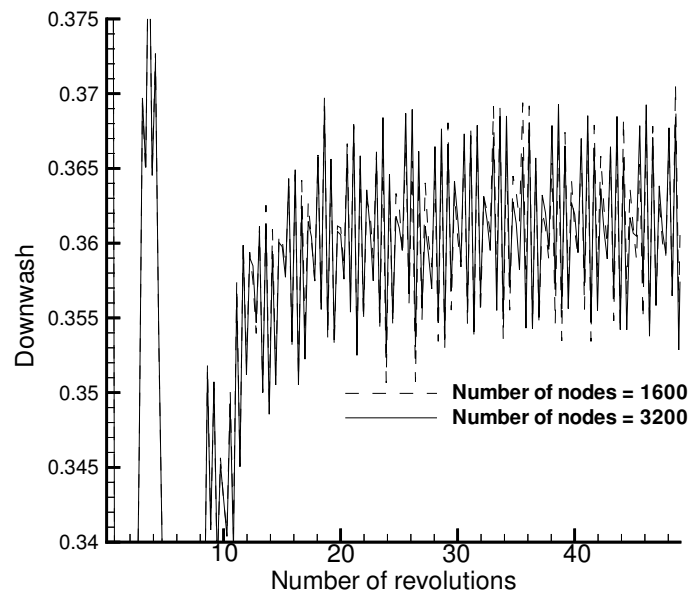
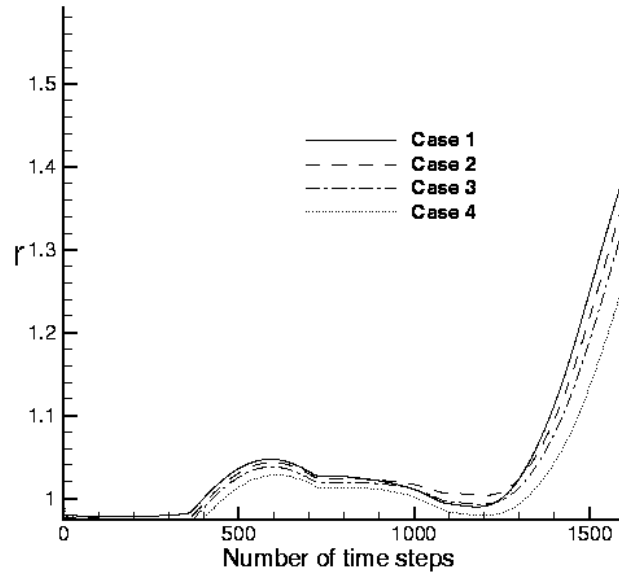
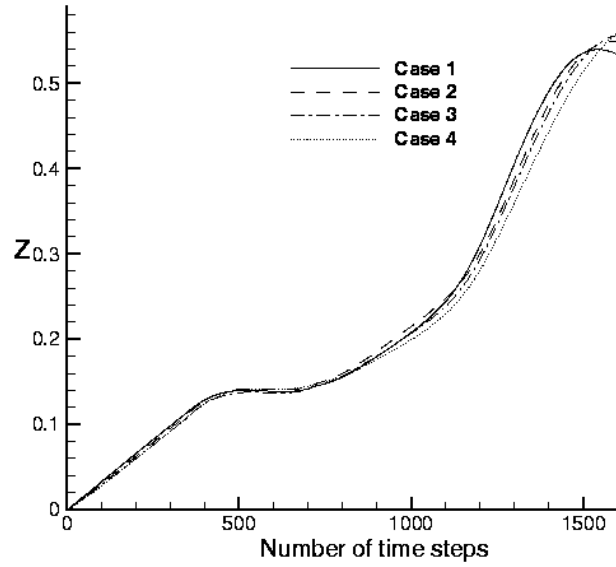


Figure 2.13: Comparison of the downwash values obtained using 1600 and 3200 nodes for the tip-vortex in hover for a two bladed rotor; $h/R = 0.5$, $y = 0.5$, $x = 0$, $z = 0.15$.



(a)



(b)

Figure 2.14: Radial and axial trajectories of a single point on the wake starting at the blade tip at $t=0$ for different spatial and time steps. Case 1: $\Delta\psi = 1^\circ$, $\Delta t = 1^\circ$, Case 2: $\Delta\psi = 2^\circ$, $\Delta t = 2^\circ$, Case 3: $\Delta\psi = 4^\circ$, $\Delta t = 4^\circ$, Case 4: $\Delta\psi = 8^\circ$, $\Delta t = 8^\circ$. (a) Radial trajectory (b) Axial trajectory.

to model the actual full scale blade since actual helicopter blades typically have aspect ratios of around 15-20. Nevertheless, there are certain other disadvantages associated with the lifting line model like modeling the shape of the blade is not possible and also the blade-vortex interactions cannot be accounted for. These problems do not occur with the lifting surface model. The computational time required for the lifting surface model is only slightly higher than the lifting line model since just twenty panels are enough to model the blade. Hence, judging by all these factors, the lifting surface model is the better choice for most cases.

CHAPTER 3

Results - Lifting Line

3.1 Introduction

The flow field around the rotor blade has been obtained using the lifting line model described in Chapter 2. The basic assumption underlining the lifting line theory is that the aspect ratio of the blade is very large and $1/A \rightarrow 0$ and the spanwise variations are very less. The tip-vortex structure has been depicted at various times showing the progression to periodicity. The velocity contours of a longitudinal cross-section of the flow field containing the blade when it is at its initial position of rest have been shown to understand the formation of the recirculations and the ground vortex. The velocity profiles have been presented to depict the formation of the ground vortex. RMS deviations of the axial and swirl components of velocities have been obtained on different planes around the rotor disk (plane containing the hypothetical tail rotor) simulating different kinds of flight to understand the unsteadiness in velocities and their handling qualities implications.

Periodicity is attained at a larger number of revolutions for a two-bladed rotor ($\sim 40 - 50$) compared to that of a single-bladed rotor ($\sim 20 - 25$). Also, there is considerable vortex-vortex interaction in the two-bladed rotor wake. The formation of ground vortex is

observed in hover and low speed forward flight cases considered in the current work and with an increase in the advance ratio, the ground vortex moves under the rotor disk. The flow field obtained in the computations has been qualitatively compared with experimental data obtained from Georgia Institute of Technology and the comparisons are very good.

The unsteadiness on a hypothetical tail rotor plane has been quantified and it has been determined that the sideward flight at an angle of 45 degrees experiences maximum unsteadiness in the tail rotor inflow. In this Chapter, the tip-vortex trajectories for single and two-bladed rotors at various times have been presented followed by the downwash profiles after 100 revolutions. The experimental comparisons with results obtained from experiments at Georgia Institute of Technology are then presented. The RMS velocity variations on a hypothetical tail rotor plane around the rotor disk are then presented in the following section.

3.2 Results - Lifting Line Theory

Results have been obtained in both hover and forward flight. Most of the results have been obtained for a rotor at a non-dimensional height of $h/R = 0.5$ and also at $h/R = 0.72$ to compare with the experiments being conducted at the Georgia Institute of Technology [31]. The typical dimensional values corresponding to the non-dimensional parameters being used in the computations are an angular speed of 2100 rpm, main rotor diameter of about 15m, and a ground to rotor disk distance of 7.5m.

3.2.1 OGE Hover for Comparison with IGE Results

Figure 3.1 compares the structure of the tip-vortex of a two-bladed rotor in hover for OGE [6] with that in the case of IGE for $h/R = 3.6$ which is a large value of this parameter

that allows a comparison with a similar number of turns OGE. Note that the first several turns of the wake(OGE) are helical in structure but below this the wake is irregular. A discussion of this phenomena and the connection with early experimental work showing this feature is given by Kini and Conlisk [6]. The wake structure in the case of IGE expands as it approaches the ground.

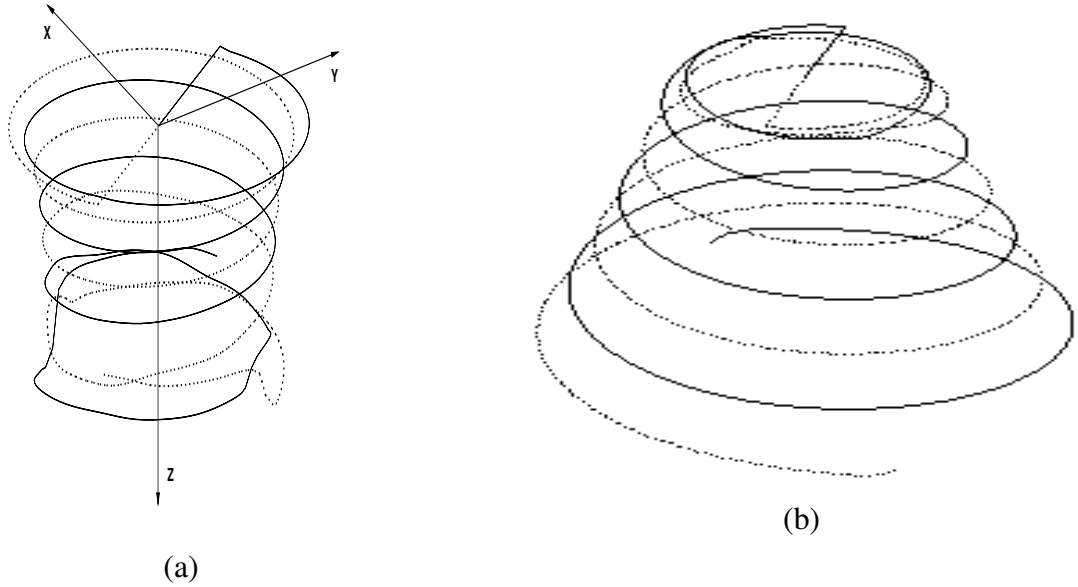


Figure 3.1: Wake structure for a two-bladed rotor (a) OGE (b) IGE Solid line: blade - 1. Dotted line: blade - 2; $h/R = 3.6$.

The computed tip-vortex trajectories for a two-bladed rotor in OGE have been compared with experimental data of Caradonna et al. [32]. The experimental parameters are presented in Table 3.1. Figure 3.2 shows that the computed trajectories (r and z) are in good agreement with the experimental results. The trajectories for the two blades are different because of the fine scale differences in the blade tips due to age.

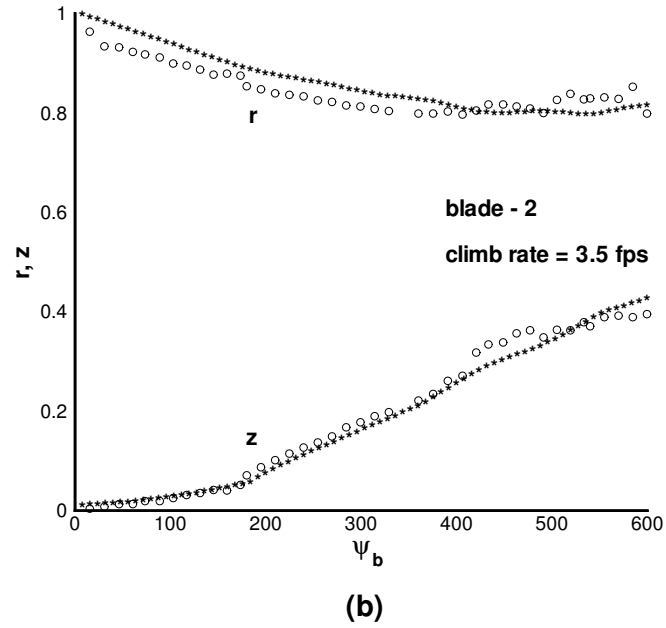
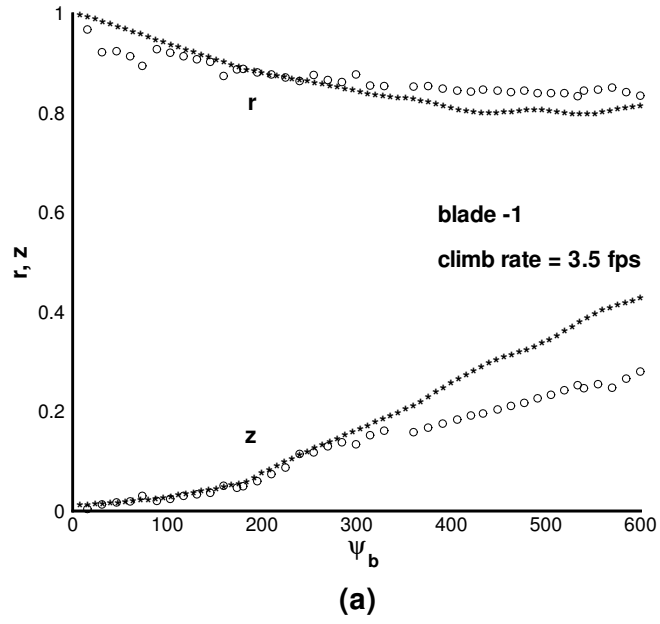


Figure 3.2: Comparison of experimental and computational trajectories (r and z) of the tip-vortex. Experimental data of Caradonna et al. [32] is represented by 'o' and computational data by '*'. (a) blade - 1 (b) blade - 2.

R	$1.04\ m$
Ω	$188.4\ rad/s$
c	$0.076\ m$
N	2
a_v	$0.0127\ m$
Γ^*	$4.0\ m^2/s$

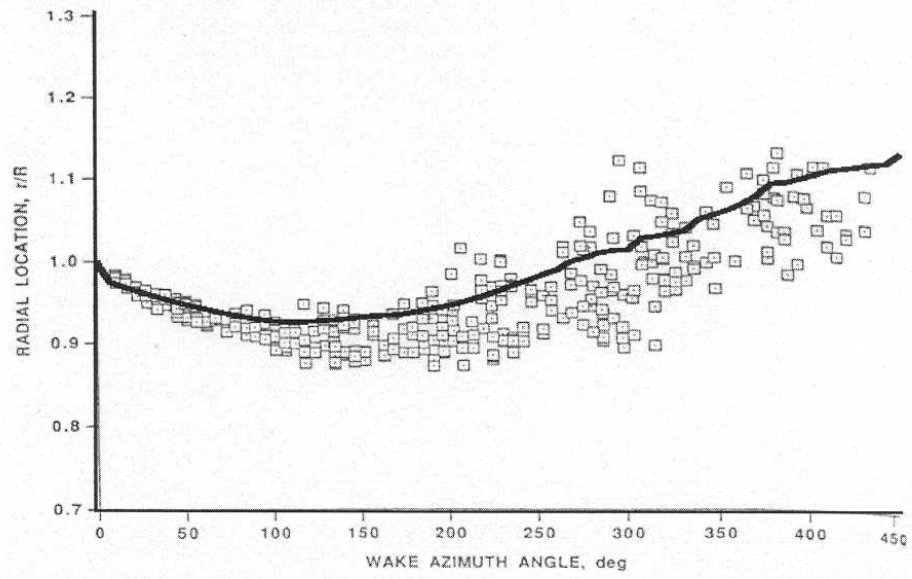
Table 3.1: Experimental Parameters in Caradonna *et al.* [32] experiments.

R	$1.105\ m$
c	$0.18\ m$
N	4
h/R	0.84
C_T/σ	0.071
Tip Mach No.	0.56

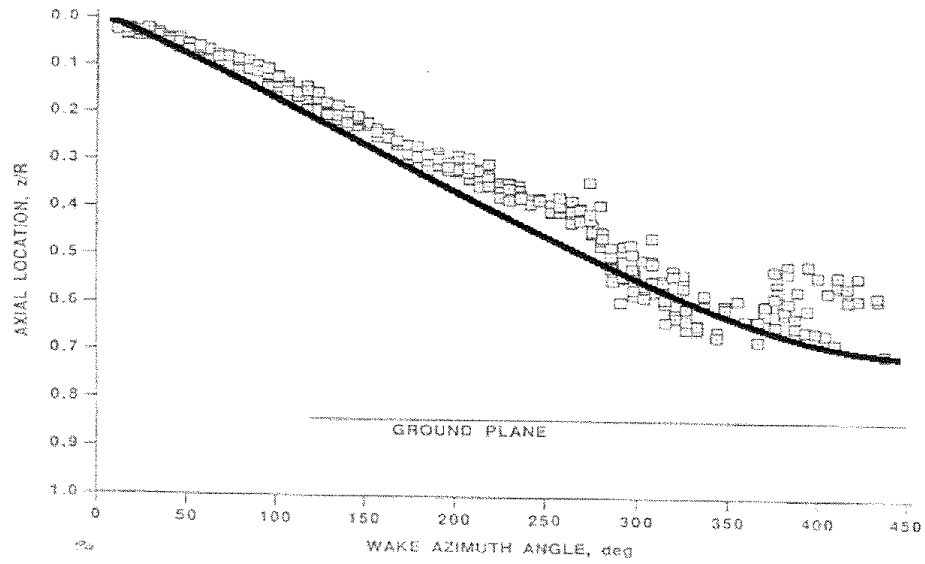
Table 3.2: Experimental parameters in Light [17] experiments.

3.2.2 IGE Hover Lifting Line Results

The r and z trajectories of the rotor wake in ground effect (IGE) have been compared with experimental results of Light [17]. Figure 3.3 shows the comparison between experimental and computed results. The experimental parameters are given in Table 3.2. The comparison is very good given the complexity of the problem. All four tip-vortex trajectories (from 4 blades) are plotted. The computational results are shown as a single solid line because the tip-vortex trajectories are coincident. Note the spread of the wake as indicated by the increasing radial location of the tip-vortices at a larger azimuthal angle. This expansion does not occur in the OGE results.



(a)



(b)

Figure 3.3: Comparison of experimental and computational trajectories (r/R and z/R) of the tip-vortices. Experimental data of Light [17] is represented by the boxes and computational data by a solid line; $h/R = 0.84$.

We have computed tip-vortex trajectories and velocity field for the rotor to ground plane separation distance of $h/R = 0.5$. In hover a typical rotor wake in ground effect expands as it approaches the ground. Near the ground the wake tends to form a ring-like structure which is the ground vortex. Note that the wake expands beyond the radius of the rotor to as far as one and a half times the rotor radius.

All the calculations have been made for a single bladed rotor above the ground at a non dimensional height of $h/R = 0.5$. We have computed the wake structure and the induced downwash for a single bladed rotor in hover to a hundred rotor revolutions. Figure 3.4 shows the structure of the wake for a single bladed rotor after 10, 20, 30, 50, 70 and 100 revolutions. There are some differences between the wake structures after 10 and 20 revolutions but the wakes after 20 and 30 revolutions look quite similar with minor differences. All the other wake structures after 50, 70 and 100 are similar with the only variations occurring in the last vortex turn close to the ground.

The behavior of tip-circulation in hover with time is presented in Figure 3.5. The circulation has been plotted until 40 revolutions. There is some variation in the tip circulation value below 10 revolutions but after that, it becomes periodic and settles down to an average value of 0.146. The behavior of the tip-vortex circulation also indicates that the flow field becomes periodic after the initial transient period.

The induced downwash w is shown in Figure 3.6 below the rotor blade at different heights from the ground after 100 revolutions. The blade coincides with the y -axis at this time. Here the z -axis is taken to be vertically upwards with $z = 0$ along the ground. The velocity distribution below the tip of the blade is similar to a classical Lamb vortex. Two downwash peaks exist upstream of the blade indicating the formation of some recirculation

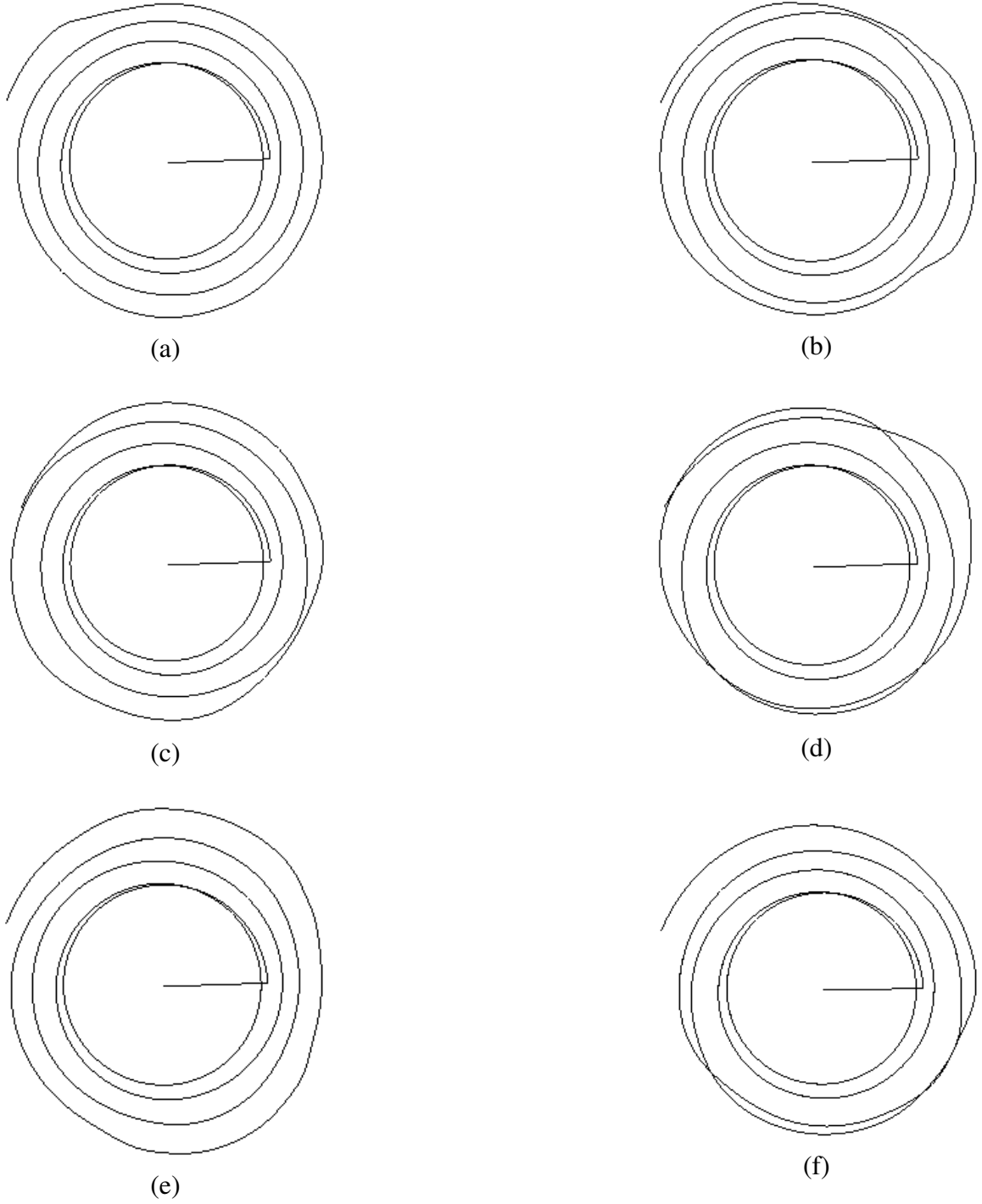


Figure 3.4: Top view of the trajectory of the tip-vortex of a single-bladed rotor in ground effect in hover after (a) 10 revolutions (b) 30 revolutions (c) 50 revolutions (d) 70 revolutions (e) 90 revolutions (f) 100 revolutions; $h/R = 0.5$.

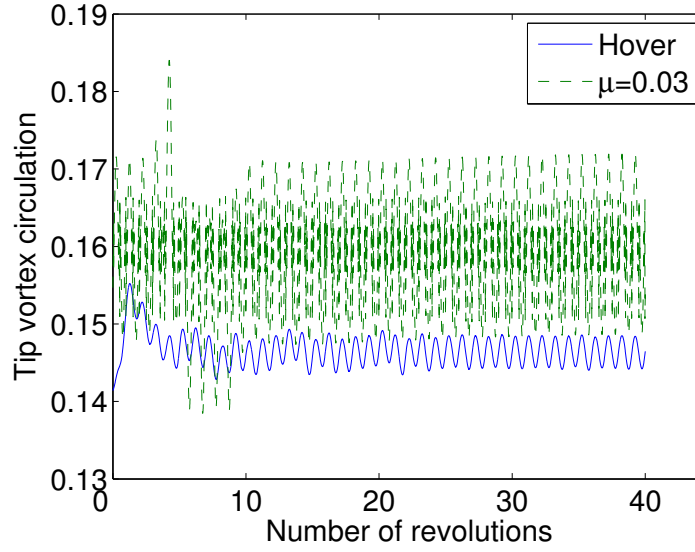


Figure 3.5: Tip-vortex circulation for a single-bladed rotor in hover and forward flight $\mu = 0.03$ for $h/R = 0.5$ as a function of time.

due to the presence of the ground. The downwash curves corresponding to $z = 0.2$ and $z = 0.3$ represent the ground vortex slightly upstream of the rotor.

The velocity field for a single-bladed rotor in hover at $h/R = 0.5$ is presented in Figure 3.7 . The velocity contours are presented in the plane $x = 0$ containing the blade and the ground. We present the results after one hundred complete revolutions of the blade and the blade coincides with the y-axis. It can be noticed that the flow field is symmetric and the formation of the ground vortex can be noticed below and in front of the tip of the blade. There is also formation of recirculation upstream of the blade, due to vortices getting reflected by the ground and moving back towards the blade.

The wake structure after 10, 30, 50, 70, 90 and 100 revolutions for the case of a two-bladed rotor in hover is shown in Figure 3.8 . The structure of the wake is symmetric like

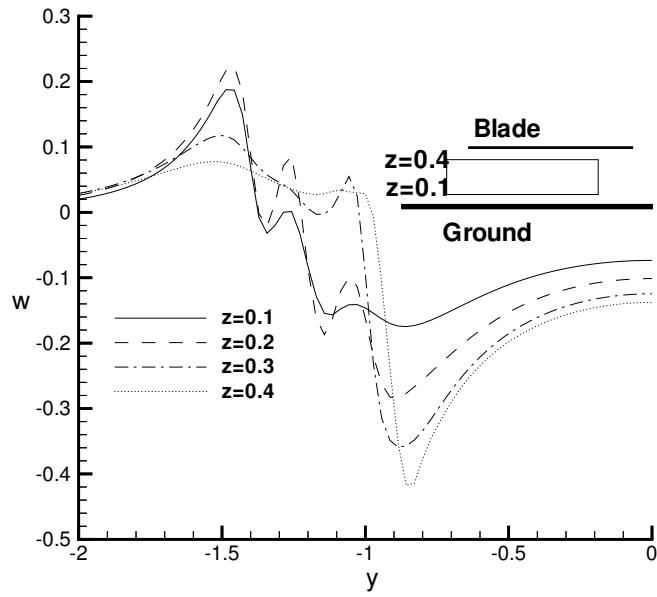


Figure 3.6: Downwash distribution along the blade for a single-bladed rotor in hover for $h/R = 0.5$ after 100 revolutions.

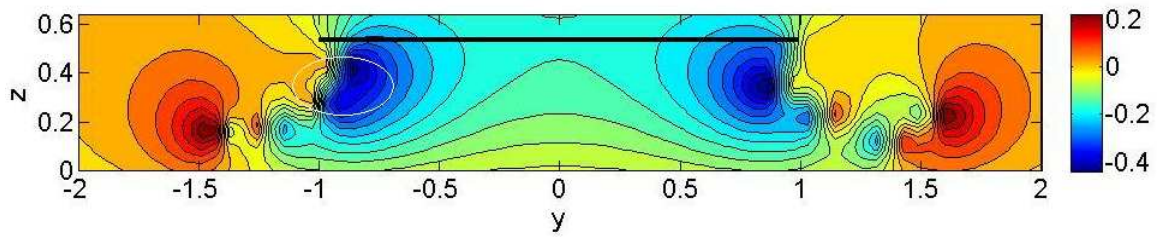


Figure 3.7: Downwash contours in longitudinal cross section for a single-bladed rotor in hover for $h/R = 0.5$ after one hundred revolutions.

in the case of a single bladed rotor. It can be seen from Figure 3.8 that there are two tip-vortices here one emanating from each blade. The wake expands in size as it reaches the ground. The individual vortex turns are not very smooth and there is considerable vortex-vortex interaction near the ground.

The first few turns of the wake structures after 10, 30, 50, 70, 90 and 100 revolutions are very smooth with not much vortex-vortex interaction. The differences near the ground are substantial and exist even near 90-100 revolutions. The wake structure close to the ground doesn't reach a steady state unlike in the case of a single-bladed rotor. The unsteadiness may be caused due to a variety of reasons. It may partly be due to the vortex-vortex interaction between the two tip-vortices. The flow field becomes much more complex than the single bladed rotor case with the two tip-vortices interacting, and then the two blades affecting the vortices and vice versa.

A sideview of the wake structure of the two-bladed rotor in hover after 100 revolutions is presented in Figure 3.9 to look at possible blade-vortex interactions. As can be seen from Figure 3.9, the flow field is very complicated even close to the blade. There seem to be some blade-vortex interactions in this flow field.

The downwash as a function of the distance along the blade for a two-bladed rotor in hover can be seen in Figure 3.10. The downwash profile is quite different when compared to that of the single bladed rotor with higher number of peaks. There also seems to be some recirculation further upstream of the rotor (not shown in the Figure) which was not noticed in the single-bladed case. The flow field here is more complicated with the effect of the rotor wake reaching far upstream of the blade. Again, the downwash profiles at $z = 0.1$

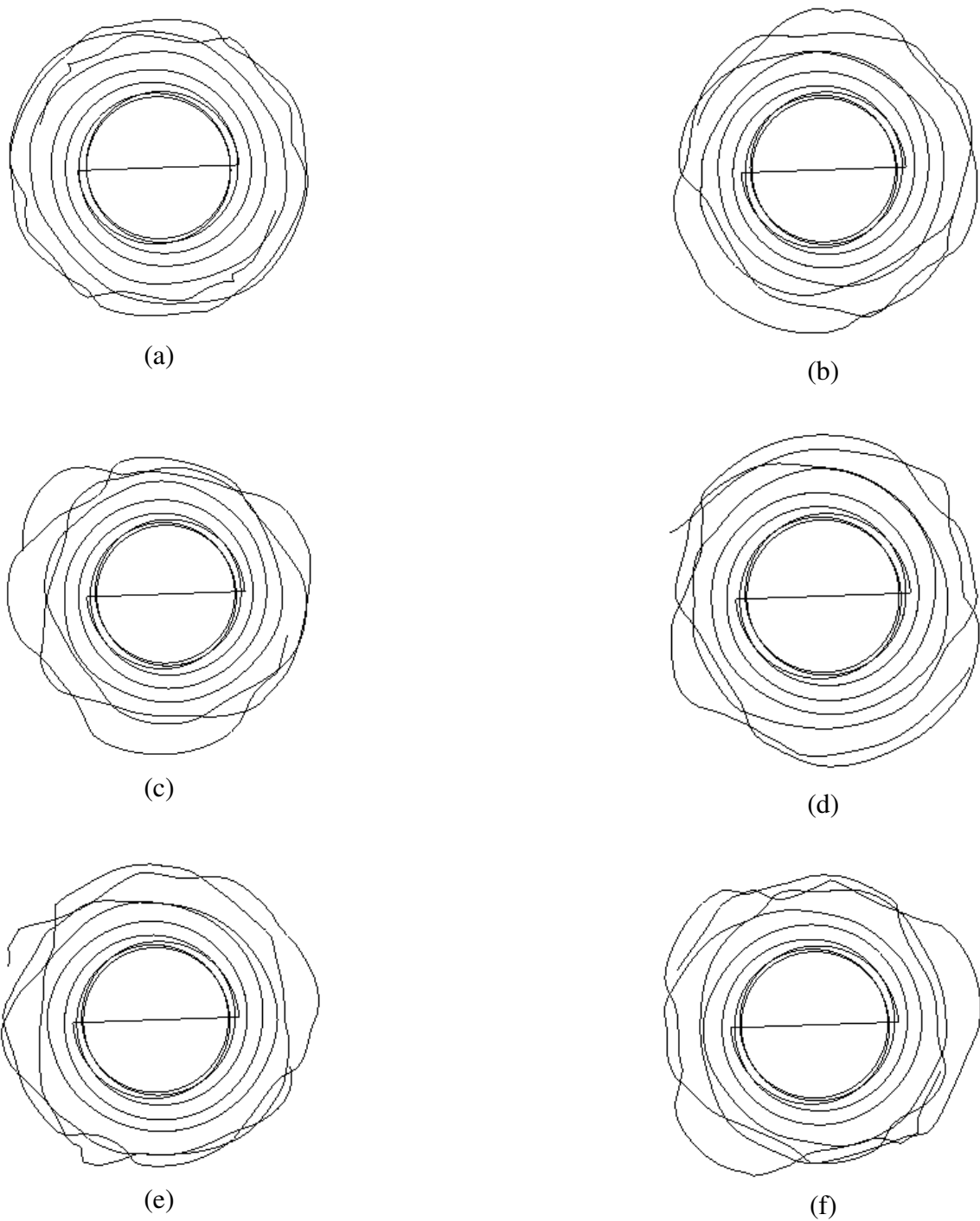


Figure 3.8: Top view of the trajectory of the tip-vortex of a two-bladed rotor in ground effect in hover for $h/R = 0.5$ after (a) 10 revolutions, (b) 30 revolutions, (c) 50 revolutions, (d) 70 revolutions, (e) 90 revolutions, (f) 100 revolutions.



Figure 3.9: Side view of the wake structure for a two-bladed rotor in hover for $h/R = 0.5$ after 100 revolutions.

and $z = 0.2$ represent the ground vortex. The formation of the ground vortex is slightly upstream of the rotor disk.

The complicated flow field can be better visualized by looking at the downwash contours in Figure 3.11. The formation of the ground vortex right below the tip of the blade can be noticed. Also the recirculation of the tip-vortices after the striking the ground can be noticed. As has been mentioned earlier, the effect of tip-vortex is far-reaching as the velocity does not approach zero even at $y = -2$. Like in the single-bladed hover case, the ground vortex is slightly upstream of the rotor disk.

3.2.3 IGE Forward Flight - Single-Bladed Rotor Flow Field Results

The wake structure in the forward flight case ceases to be symmetric. The wake moves under the rotor disk with the maximum shift occurring near the ground. Two cases of forward flight $\mu = 0.01$ and $\mu = 0.03$ have been studied extensively. The wake structure for the case where $\mu = 0.01$ is presented in Figure 3.12. Except for the wake structure after 10 revolutions, all other wake structures have very few differences. The initial few revolutions can be considered the transition period. Since the forward flight speed is very less, there is very little movement of the wake under the rotor disk.

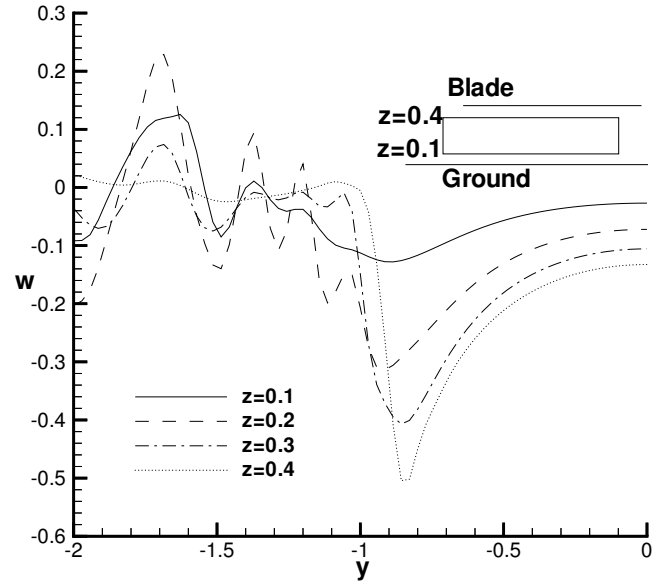


Figure 3.10: Downwash distribution along the blade for a two-bladed rotor in hover for $h/R = 0.5$ after 100 revolutions.

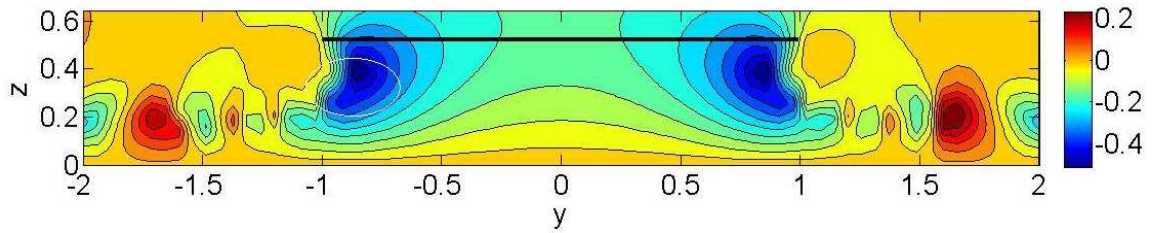


Figure 3.11: Downwash contours in longitudinal cross section for a two-bladed rotor in hover for $h/R = 0.5$ after one hundred revolutions.

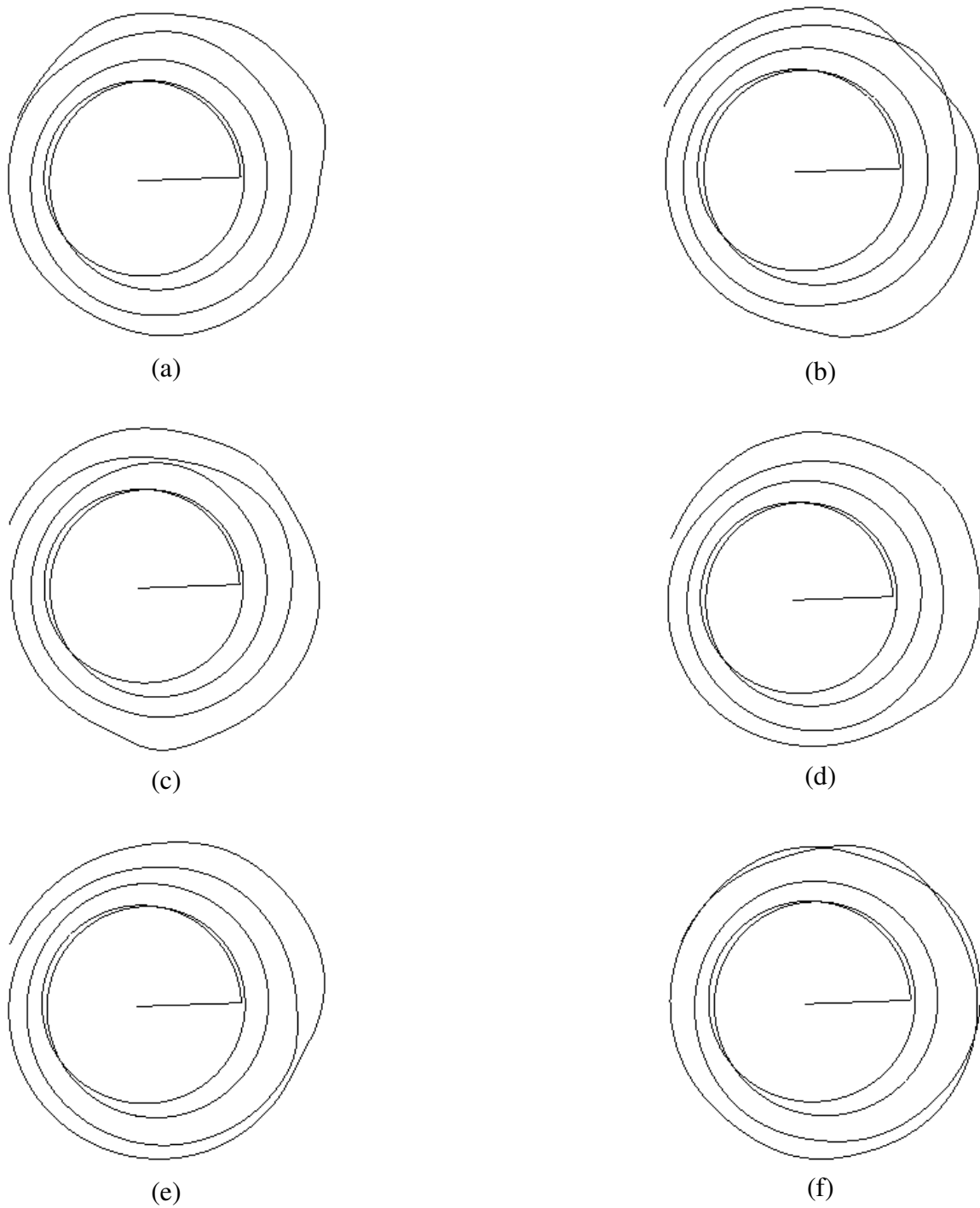


Figure 3.12: Top view of the trajectory of the tip-vortex of a single-bladed rotor in ground effect in forward flight for $\mu = 0.01$ after (a) 10 revolutions (b) 30 revolutions (c) 50 revolutions (d) 70 r revolutions (e) 90 revolutions (f) 100 revolutions; $h/R = 0.5$.

As was done in the case of hover, the downwash for a single bladed rotor after 100 revolutions for $\mu = 0.01$ has been plotted along the blade at different heights from the ground. Figure 3.13 shows the variation of the downwash/vertical velocity along the blade at different heights below the rotor blade for $\mu = 0.01$. The velocity profile at $z = 0.1$ and $z = 0.2$ clearly indicates the formation of a ground vortex just in front of the tip of the blade. There is also some recirculation upstream of the rotor like in the case of hover.

The downwash contours after 100 revolutions on the $x = 0$ plane containing the blade have been plotted in Figure 3.14. Formation of a ground vortex at slightly upstream of the rotor disk can be seen.

Figure 3.15 shows the wake structure of a single-bladed rotor for the advance ratio of 0.03. Due to the increased forward flight advance ratio, the wake moves further under the rotor disk. Figure 3.15 suggests that it takes a little longer than in the case of $\mu = 0.01$ for the wake to stabilize. The tip-vortex structure after 10 revolutions in this case is not as smooth as that of hover or $\mu = 0.01$. But with the increase in the number of revolutions, the irregularities in the wake structure die down.

The behavior of the tip-vortex circulation for a single-bladed rotor in forward flight at $\mu = 0.03$ can be seen in Figure 3.5. It can be noticed that the tip-vortex circulation at $\mu = 0.03$ is higher than that of hover and has more variation in each revolution than in hover. The downwash for $\mu = 0.03$ for a single-bladed rotor after 100 revolutions is shown in Figure 3.16. The profile of the downwash indicates the formation of a vortex midway between the root and the tip of the blade. The ground vortex is represented by the downwash at $z = 0.1$ and $z = 0.2$. There is no recirculation upstream of the rotor. The formation of the ground vortex can be better visualized by Figure 3.17 showing the

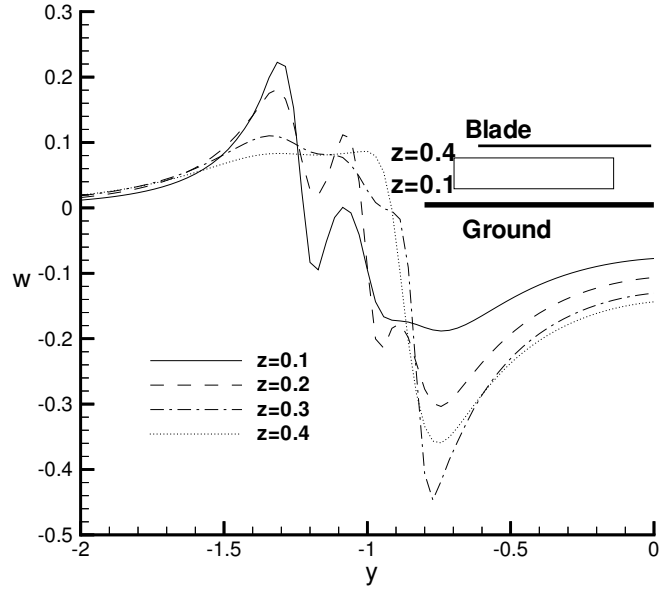


Figure 3.13: Downwash distribution along the blade for a single-bladed rotor for $\mu = 0.01$ for $h/R = 0.5$ after 100 revolutions.

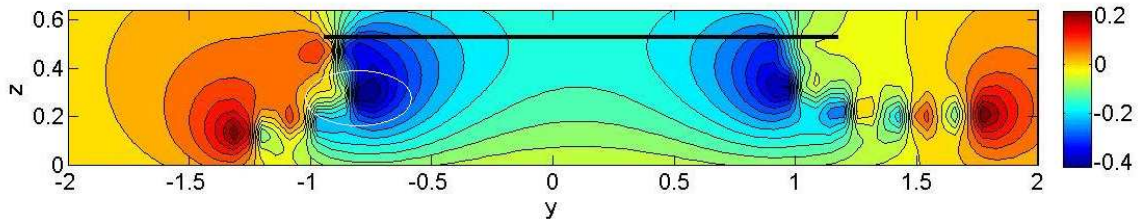


Figure 3.14: Downwash contours in longitudinal cross section for a single-bladed rotor for $\mu = 0.01$ for $h/R = 0.5$ after one hundred revolutions.

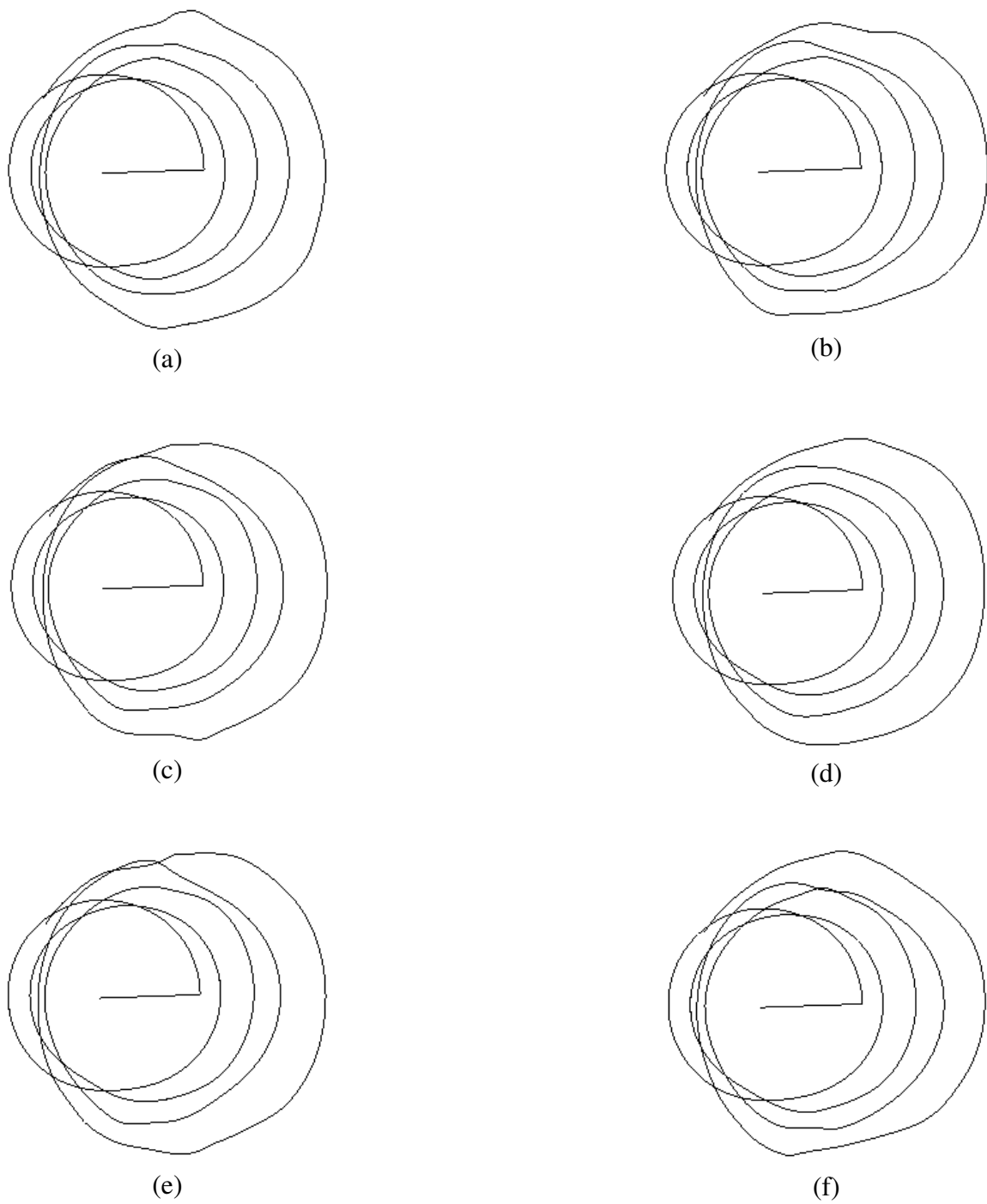


Figure 3.15: Top view of the trajectory of the tip-vortex of a single-bladed rotor in ground effect ($h/R = 0.5$) in forward flight for $\mu = 0.03$ after (a) 10 revolutions (b) 30 revolutions (c) 50 revolutions (d) 70 r evolutions (e) 90 revolutions (f) 100 revolutions.

downwash contours on the $x = 0$ plane where the ground vortex is circled. Compared to $\mu = 0.01$, there is a shift of the ground vortex towards the right and towards the ground.

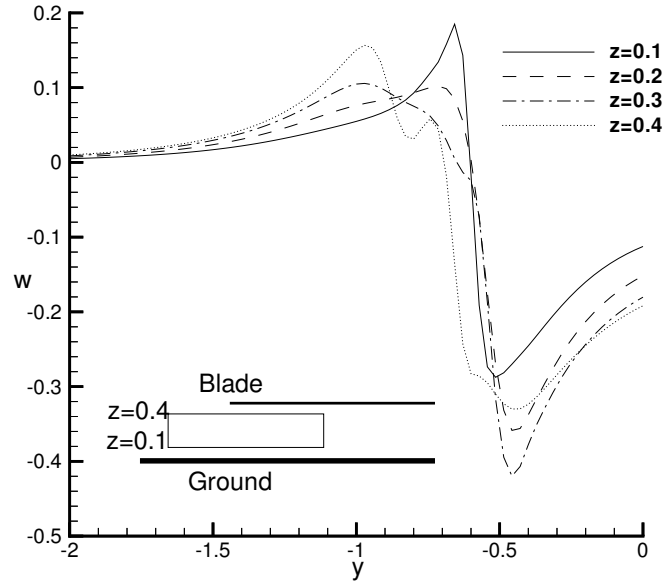


Figure 3.16: Downwash distribution along the blade for a single-bladed rotor for $\mu = 0.03$ for $h/R = 0.5$ after 100 revolutions.

3.2.4 IGE Forward Flight - Two-Bladed Rotor

Figure 3.18 shows the wake structure of a two-bladed rotor moving at an advance ratio $\mu = 0.01$. Like in hover, there is considerable vortex-vortex interaction close to the ground. The irregularities in the wake exist even after 100 revolutions. However, the first few turns at all the times look similar indicating that wake is periodic close to the blade.

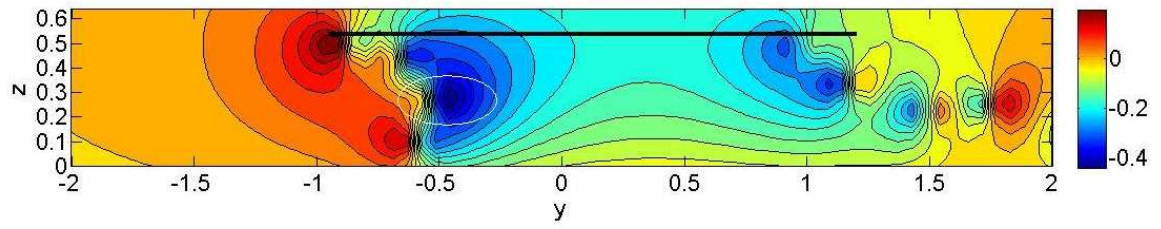


Figure 3.17: Downwash contours in longitudinal cross section for a single-bladed rotor for $\mu = 0.03$ for $h/R = 0.5$ after one hundred revolutions.

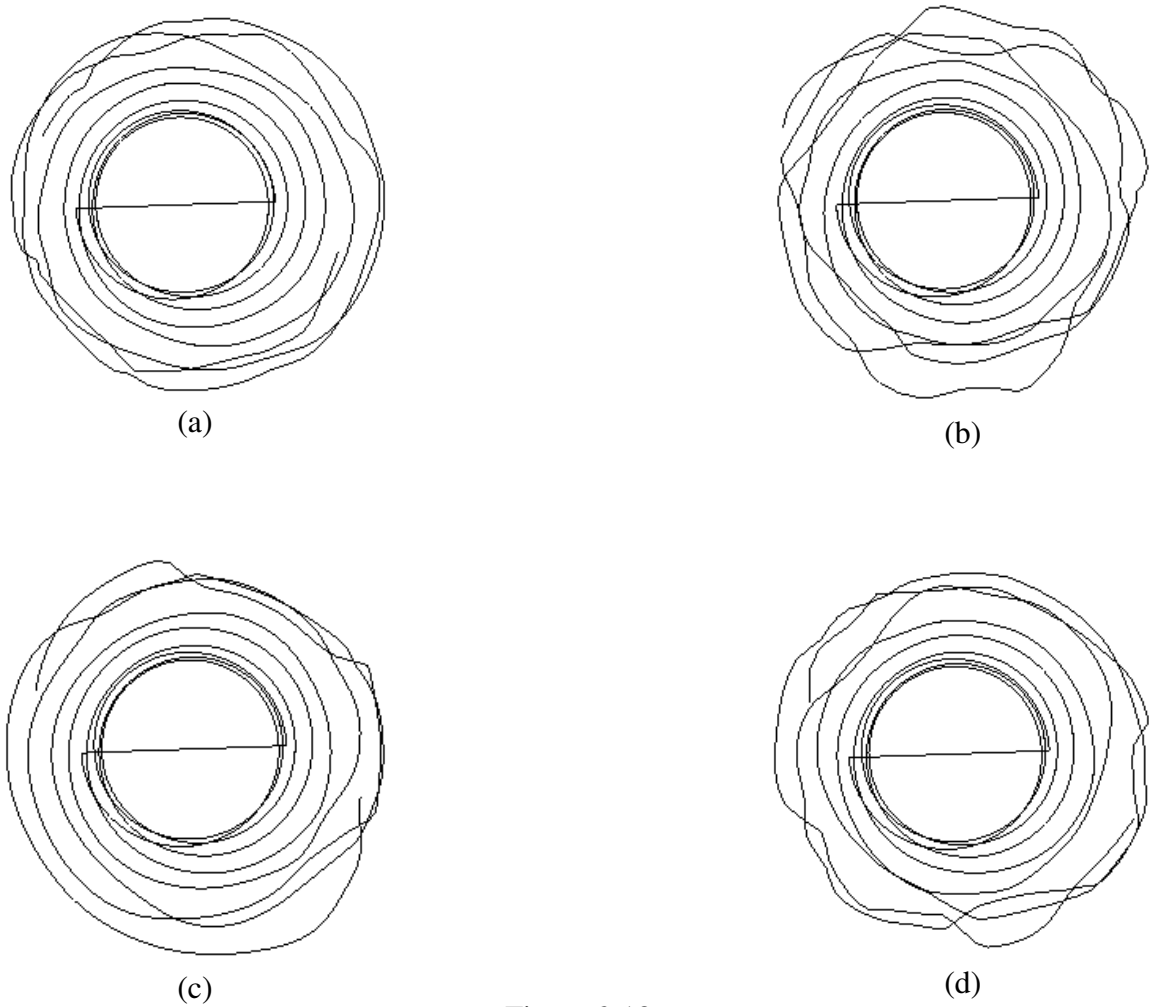


Figure 3.18

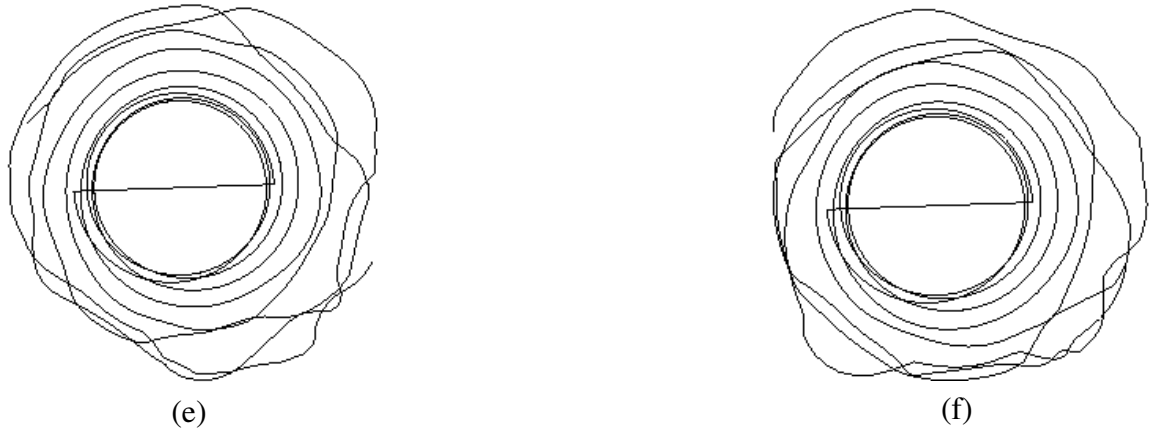


Figure 3.18: Top view of the trajectory of the tip-vortex of a two-bladed rotor in ground effect in forward flight $\mu = 0.01$ for $h/R = 0.5$ after (a) 10 revolutions, (b) 30 revolutions, (c) 50 revolutions, (d) 70 revolutions, (e) 90 revolutions, (f) 100 revolutions.

Figure 3.19 shows the downwash profile along the y -axis for a two-bladed rotor at $\mu = 0.01$. There is a slight shift of the downwash peak under the rotor blade indicating the movement of the ground vortex in the same direction. Qualitatively the profile looks quite similar to that of hover close to and under the blade. There is very little change in the location of the ground vortex compared to that of hover.

The flow field at $\mu = 0.01$ for the two-bladed rotor can be better visualized by looking at the downwash contours in Figure 3.20. The effect of the tip-vortex on the flow field extends to as far as $y = -2$ and beyond as can be seen from Figure 3.20. The position of the ground vortex stays almost the same as in hover.

Figure 3.21 shows the wake structure of a two-bladed rotor for advance ratio $\mu = 0.03$. The blades are kept fixed and the flow due to the advance ratio is allowed to come in at the particular forward flight speed. The wake structure ceases to be symmetric and moves

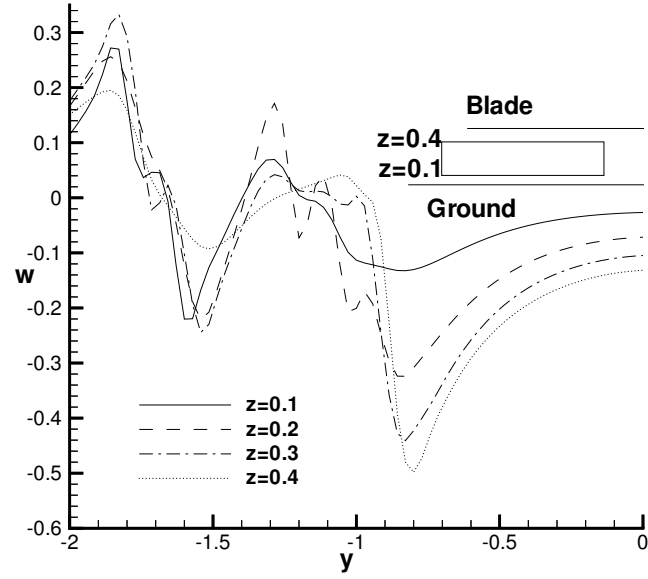


Figure 3.19: Downwash distribution along the blade for a two-bladed rotor for $\mu = 0.01$ for $h/R = 0.5$ after 100 revolutions.

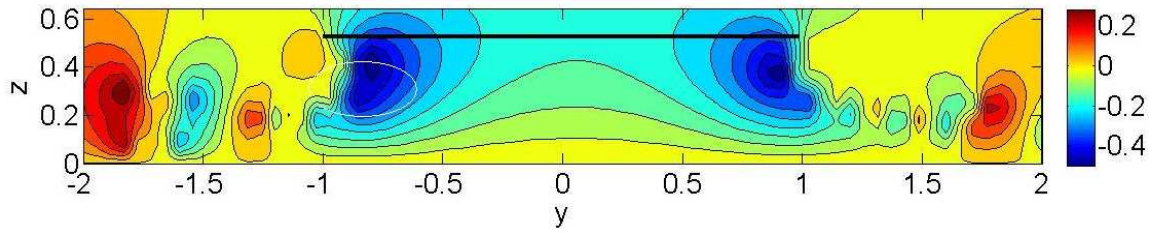


Figure 3.20: Downwash contours in longitudinal cross section for a two-bladed rotor for $\mu = 0.01$ for $h/R = 0.5$ after one hundred revolutions.

under the rotor disk. Similar to what we have seen in the single bladed rotor case, the maximum shift occurs near the ground gradually becoming zero near the blade.

The behavior of the wake structure with time is similar to that of hover and $\mu = 0.01$. The first few vortex turns are very smooth but after that there is considerable disturbance near the ground. There are some differences near the ground between the wake structures after 10 and 30 revolutions. But the wakes after 50 and 70 revolutions look very much alike even near the ground. However at 90 and 100 revolutions, the differences near the ground are quite substantial. Hence, the wake doesn't settle down in to a pattern and is not periodic or steady close to the ground.

The first few turns of the vortex collect upstream of the rotor blade suggesting the formation of a ground vortex. The formation of the ground vortex is a very crucial phenomenon in the flow IGE. It has a considerable effect on the loads acting on the rotor blades and might also lead to an imbalance of moments. Thus the flow field for a two bladed rotor case is more unsteady compared to the single bladed rotor case. The vortex-vortex interaction and the blade-vortex interactions could be possible reasons for this phenomenon.

Figure 3.22 shows the downwash along the y -axis for a two-bladed rotor at an advance ratio $\mu = 0.03$. Four peaks for the downwash can be seen in the Figure. One large vortex which is not the ground vortex upstream of the blade can be noticed, indicative of the fact that the recirculation is very high even upstream of the blade. The downwash profiles at $z = 0.1$ and $z = 0.2$ represent the ground vortex. There is a change in the position of the ground vortex with increase in advance ratio from upstream of the rotor to slightly under the rotor disk.

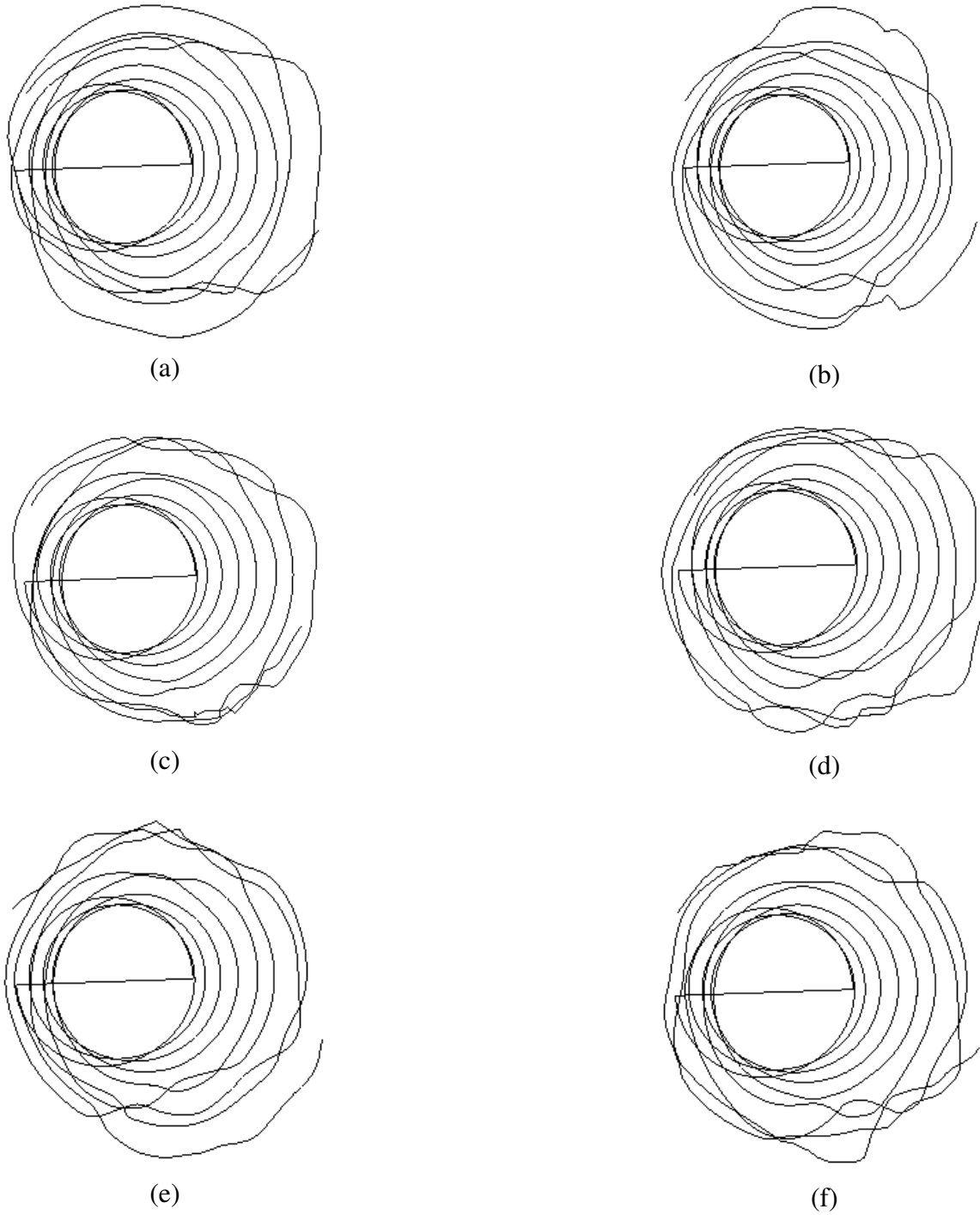


Figure 3.21: Top view of the trajectory of the tip-vortex of a two-bladed rotor in ground effect in forward flight $\mu = 0.03$ for $h/R = 0.5$ after (a) 10 revolutions, (b) 30 revolutions, (c) 50 revolutions, (d) 70 revolutions, (e) 90 revolutions, (f) 100 revolutions.

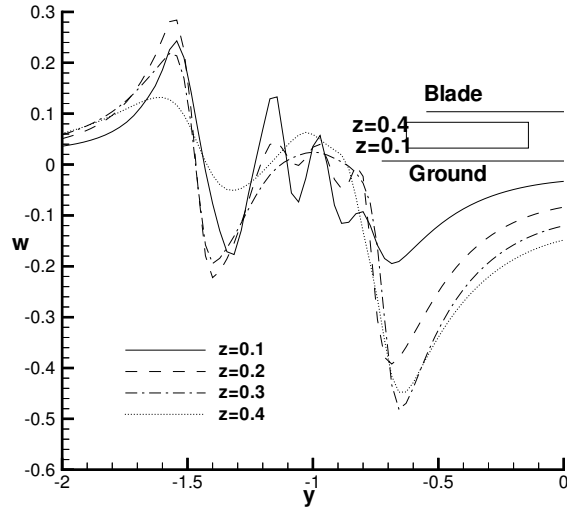


Figure 3.22: Downwash distribution along the blade for a two-bladed rotor for $\mu = 0.03$ for $h/R = 0.5$ after 100 revolutions.

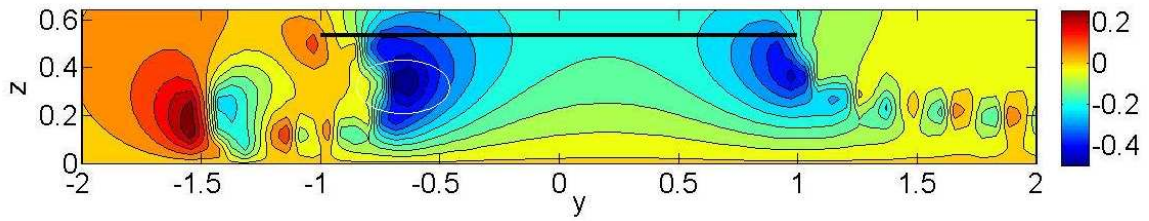
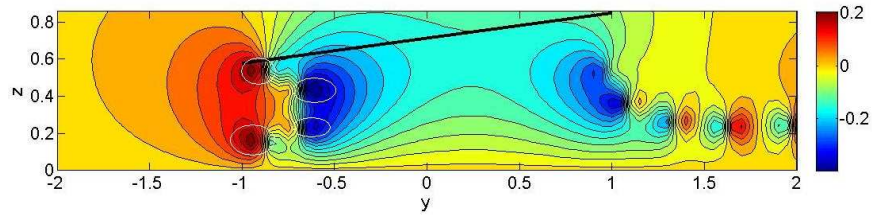
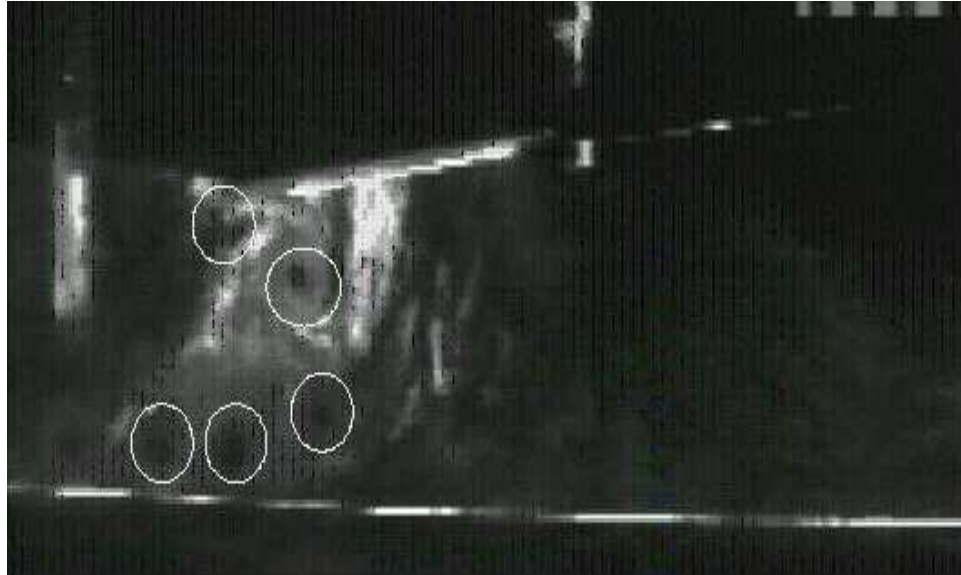


Figure 3.23: Downwash contours in longitudinal cross section for a two-bladed rotor for $\mu = 0.03$ for $h/R = 0.5$ after one hundred revolutions.

The above observation can be confirmed from Figure 3.23 showing the downwash contours at $\mu = 0.03$. The ground vortex can be seen below the blade and the large recirculation that was seen in the other Figure can be noticed upstream of the blade. Hence the rotor moving forward at $\mu = 0.03$ will have to encounter two large vortices upstream. These two vortices will have substantial influence on the loads and power requirements of the rotor.



(a)



(b)

Figure 3.24: Rotor wake recirculation phenomenon at $\mu = 0.03$, $h/R=0.72$, two-bladed rotor, tilt = 10° , (a) Computational Result (b) Experimental result.

Vortex	Expt		Model	
	y	z	y	z
1	-0.945	0.532	-0.960	0.557
2	-0.822	0.444	-0.711	0.459
3	-0.805	0.144	-0.711	0.216
4	-0.987	0.099	-	-
5	-1.051	0.102	-1.11	0.178

Table 3.3: Comparison of ground vortex coordinates in computation and experiment; $h/R = 0.72$, two-bladed rotor, $\mu = 0.03$.

3.2.5 Comparison with Experiments

Figures 3.24 and 3.26 compare the ground vortex phenomenon in the computations and the experimental results obtained from Georgia Institute of Technology for the case of a two-bladed rotor at a non-dimensional height(h/R) of 0.72 above the ground. A tilt of 10° has been used for the rotor in the computations as well as the experiments. Results have been obtained for the advance ratios $\mu = 0.03$ and $\mu = 0.04$. The flow field obtained from the computational results is depicted using contours of the downwash (after periodicity 100 revolutions when the blade is at the zero azimuth) on the longitudinal section plane being compared. The experimental flow field is a snapshot of the flow field after periodicity is attained when the blade is at the zero azimuthal position. Figure 3.24(a) shows the ground vortex formed in the computational results. Figure 3.24 (b) shows the corresponding plot for the experimental results. In the experimental flow field five vortices(circled) can be seen and their position are given in Table 3.3. The corresponding vortices in the computational flow field have been circled. As can be seen from Table 3.3, their positions match adequately but the computations have not been able to capture one vortex as can be seen from

Figure 3.24(a). The vortices can be more clearly observed in Figure 3.25. The downwash profiles at $z = 0.178, 0.216, 0.459$ and 0.557 clearly indicate the formation of Lamb-type vortices under the rotor disk.

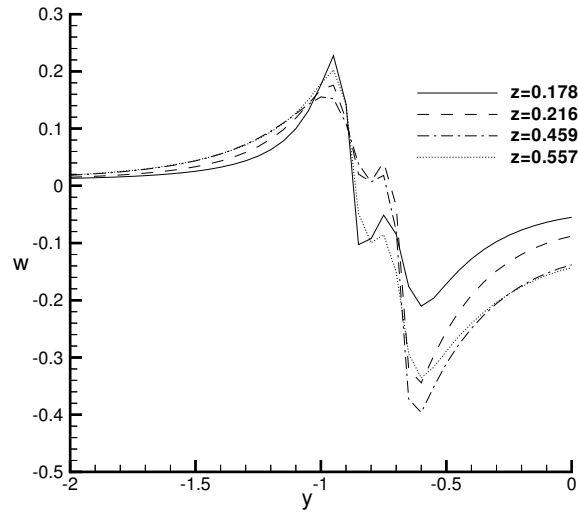


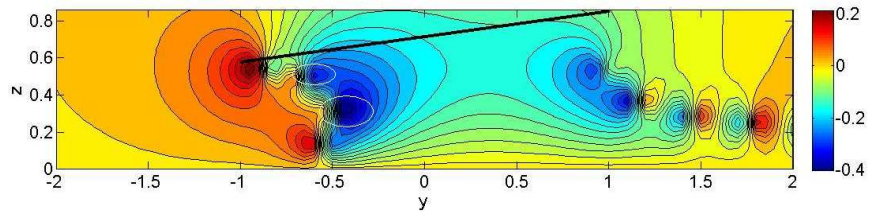
Figure 3.25: Downwash distribution along the blade, $h/R = 0.72$, two-bladed rotor, tilt = 10° .

Figure 3.26 shows the comparison between the ground vortex phenomenon in the computations and the experiments for an advance ratio $\mu = 0.04$. This Figure is quite similar to the one for $\mu = 0.03$ but the positions of the vortices do not match very well with those on the experiments.

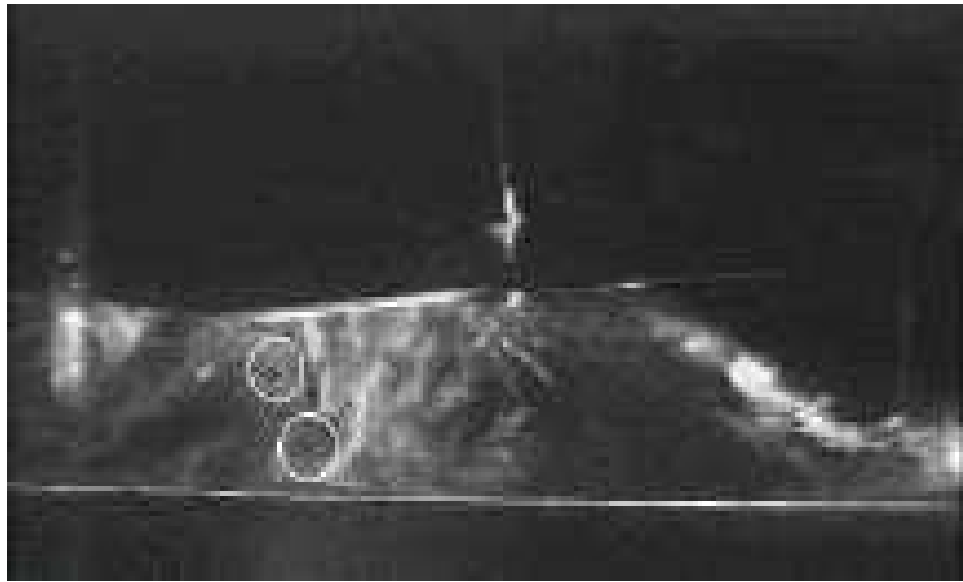
The power spectrum of the downwash has also been compared with the experimental results obtained from Georgia Tech in Figure 3.27. Downwash in the experiments has been obtained at $y = -1, z = 0.831, x = 0$. As can be seen from the Figure, a large

low frequency component can be noticed in both the experimental as well as the computational results indicating certain long time period characteristics of the downwash. The amplitudes of the power in the computations and experiments match very well. The peak at 70Hz corresponds to the time period of one rotor revolution since the angular velocity in the experiments is 2100rpm. The most dominant low frequency component in both experimental and computational results can be seen at around 2Hz indicating a very long time period component perhaps due to the persistent unsteadiness seen in the wake computations. The corresponding power spectrum for the OGE computations has also been presented in Figure 3.27. There is only one peak in the OGE spectrum corresponding to the time period of one revolution which implies it does not have a low frequency component.

We have also compared our results(using average values of the velocities obtained between 50 and 60 revolutions) with those of Kang and Sun [21] who have performed computations for non-dimensional height $h/R = 0.46$ as shown in Figure 3.28 for an advance ratio $\mu = 0.03$ and using a four-bladed rotor. Their Navier-Stokes computations are at steady state with the rotor wake modeled by the inclusion of momentum source terms in the Navier-Stokes equations. Note that this model is significantly different from the present vortex model. Despite this, the results are qualitatively in line with those results although the position of the vortex in the Kang and Sun work [21] is further below the blade tip than in the present case.

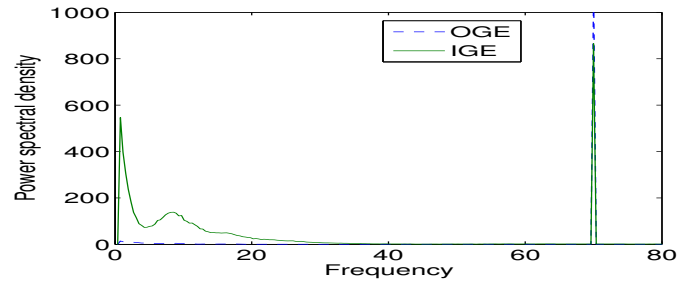


(a)

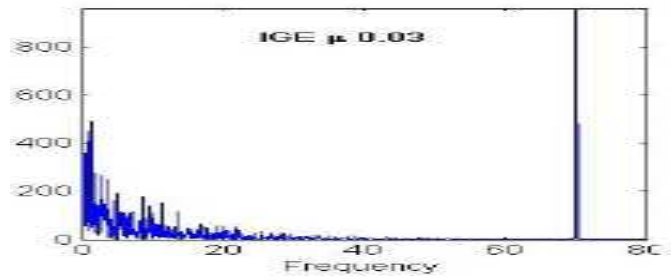


(b)

Figure 3.26: Rotor wake recirculation phenomenon at $\mu = 0.04$, $h/R = 0.72$, two-bladed rotor, tilt = 10° , (a) Computational Result (b) Experimental result.

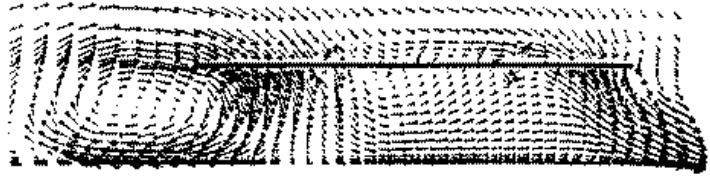


(a)

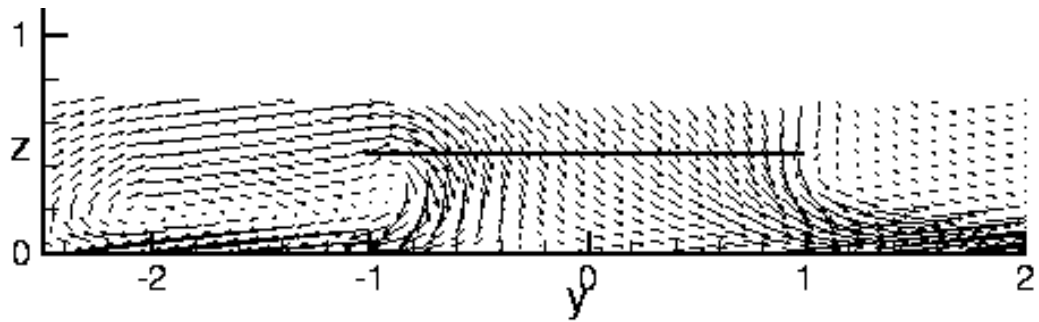


(b)

Figure 3.27: Downwash power frequency spectrum IGE, $\mu = 0.03$, lifting line model computed at the location $y = -1$, $z = 0.831$, $x = 0$; (a) Computational results (b) Experimental results.



(a)



(b)

Figure 3.28: Comparison of the results obtained from the current work with those of Kang and Sun [21] for a four-bladed rotor when $h/R = 0.46$, $\mu = 0.03$ using lifting line model; (a) Kang and Sun [21] results (b) Current work results.

3.3 RMS Velocity Variations

From a handling qualities perspective, it is believed that large unsteady fluctuations in velocities induced at the main and tail rotors can cause large unsteady surface loads at low speed in-ground effect. To understand the unsteadiness near the tail rotor the RMS(a measure of the deviation from the mean) of the axial and the swirl components of the induced velocity has been computed on the plane containing the hypothetical tail rotor for various kinds of flight. Different planes around the rotor disk have been considered to simulate various kinds of flight. This was suggested by Mr. T. Alan Egolf of Sikorsky (private communication). The RMS velocity is given by

$$U_{RMS} = \frac{1}{N} \sqrt{\int_t^{2\pi+t} (U - U_0)^2 dt} \quad (3.1)$$

where N is the number of time steps between t and $2\pi + t$ and U_0 is the average velocity over each revolution. The azimuthal velocity at the hypothetical tail rotor disk is equivalent to the tail rotor inflow. 30 points in the axial direction from -0.3 to 0.3 and 60 points in the radial direction from 0.75 to 1.5 have been taken for the grid on each plane.

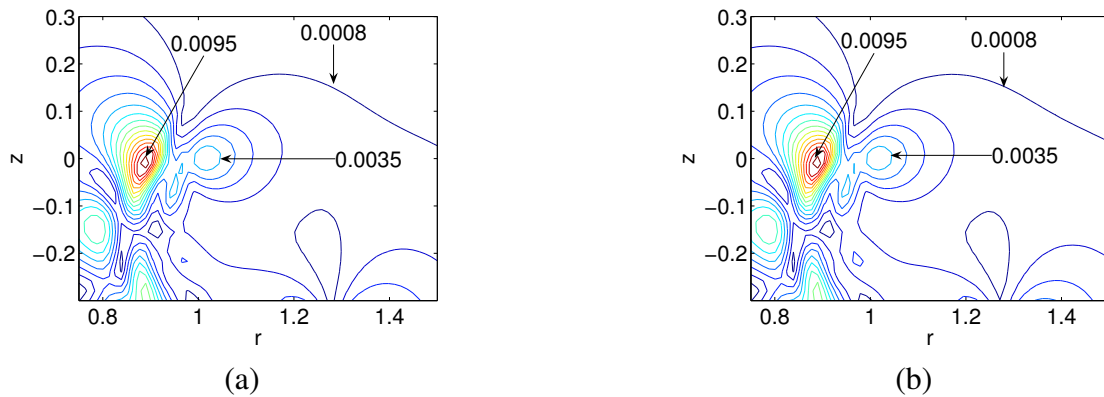


Figure 3.29

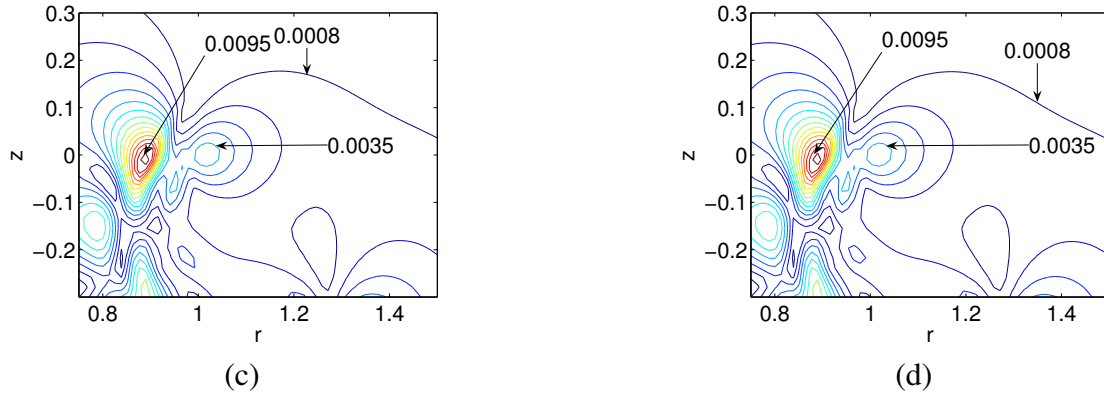


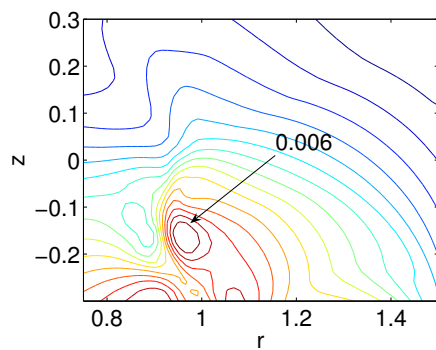
Figure 3.29: RMS swirl contours for hover at azimuthal locations (a) 0 degrees (b) 15 degrees (c) 30 degrees (d) 45 degrees; $h/R = 0.72$, all four plots are identical as required in hover.

RMS swirl velocities have been computed for the cases of hover and low forward flight with advance ratios $\mu = 0.01$ and $\mu = 0.03$. Figure 3.29 shows the contours of the RMS swirl velocities on the planes on the advancing side of the main rotor for the case of hover. Velocities have been obtained on the planes at the azimuthal locations 15° , 30° and 45° respectively. It can be seen from Figure 3.29 that all the plots look identical indicative of the fact that there is no change in the magnitudes with azimuthal location. This is an expected result because of the fact that the wake is radially symmetric in the case of hover and so the average values of the magnitudes of the velocities induced are the same. The maximum of about 0.0095 occurs at around 0.9 radial location on the rotor disk plane. Another local maximum of 0.0035 magnitude occurs at the 1.05 radial location.

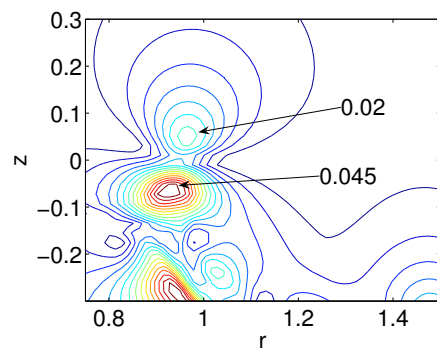
Figure 3.30 shows the swirl contours on different planes around the rotor disk for advance ratio $\mu = 0.01$. On the plane at 0 degrees, it can be seen that the deviation in swirl component is quite small and the maximum is just 0.006 and occurs close to the blade tip

at around $z = -0.15$. At 15° azimuthal location the RMS deviation in the swirl velocity increases considerably with the maximum being 0.045. However most of the swirl is concentrated inboard of the rotor blade with the RMS being close to zero everywhere outboard of the rotor blade. The maximum RMS deviation becomes 0.073 but the location where it occurs remains more or less the same. As we move to 45° azimuthal location, the locations of the RMS maximums stay the same but the magnitude of the maximum near the blade tip at $z = -0.3$ becomes 0.083. As the angle of the plane being considered is increased further, it can be noticed that there is a decrease in the value of the RMS maximums and the locations of these maximums tend to shift further inboard. Hence the maximum RMS swirl deviation occurs at 45° azimuthal location with the maximum occurring close to the blade tip. Thus, the maximum unsteadiness in the inflow on the rotor disk is experienced when the rotor is moving forward at an angle of 45 degrees. This is halfway between the normal straight flight and complete sideward flight. The unsteadiness in the swirl velocity is a measure of the handling difficulties faced and hence the pilot is expected to face the maximum handling qualities problems during sideward flight at an angle of 45 degrees.

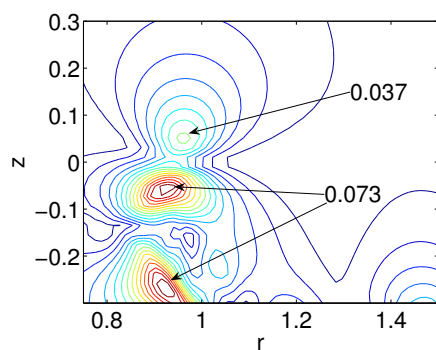
The behavior of the RMS swirl velocities on the retreating side is similar to that on the advancing side with the RMS values increasing monotonically from 0 to 45 degrees and then decreasing as we go from 45 degrees to 90 degrees as can be seen from Figure 3.31. The magnitude of the RMS values here is almost the same as that on the advancing side. Like on advancing side the maximum swirl occurs at 0.9 radial location close to the rotor disk plane. There is a large increase in the maximum RMS swirl from the value at 0° of 0.006 to 0.042 at 15° . With further increase in the angle of the hypothetical tail rotor plane the maximum RMS swirl value almost doubles to 0.082 at 45° . However there is no further



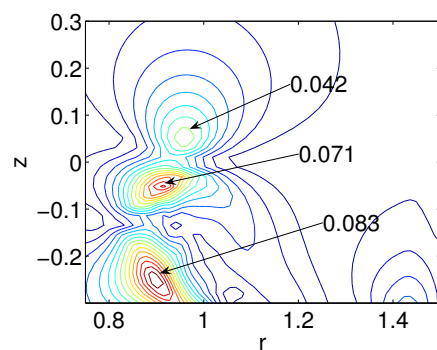
(a)



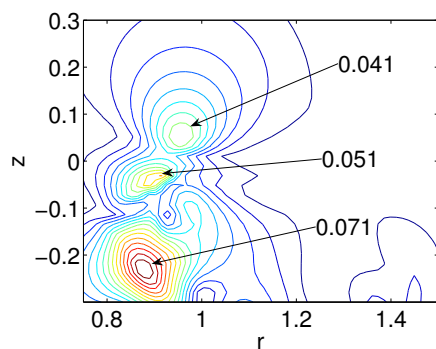
(b)



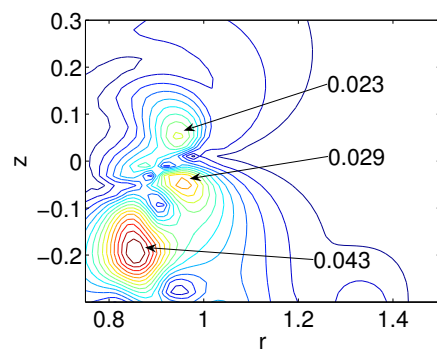
(c)



(d)



(e)



(f)

Figure 3.30

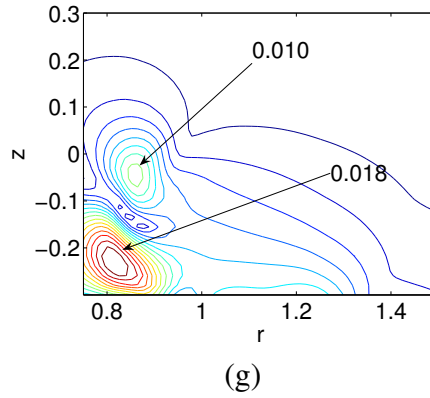
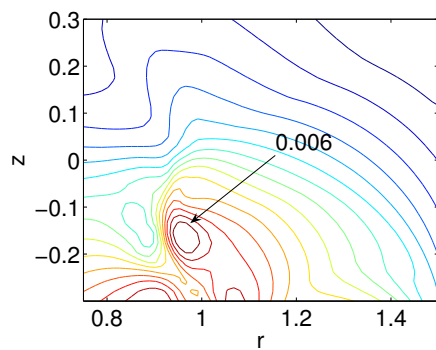


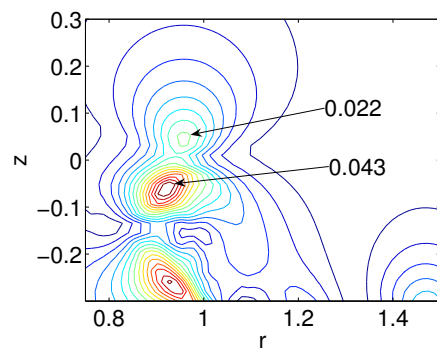
Figure 3.30: RMS swirl contours for forward flight $\mu = 0.01$ on the advancing side at azimuthal locations (a) 0 degrees (b) 15 degrees (c) 30 degrees (d) 45 degrees (e) 60 degrees (f) 75 degrees (g) 90 degrees, $h/R = 0.72$.

increase in the value of the RMS maximum with increase in the angle of the hypothetical tail rotor plane. Hence, like on the advancing side, the maximum RMS swirl occurs on the tail rotor plane at an angle of 45 degrees.

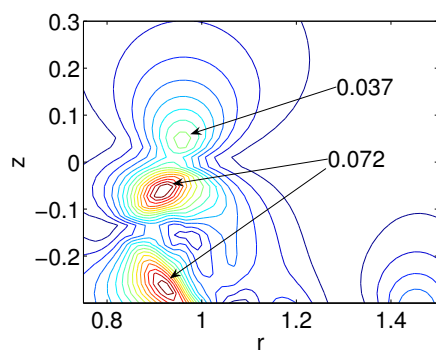
Downwash contours on the advancing side of the rotor disk for forward flight $\mu = 0.01$ can be seen from Figure 3.32. The maximum at the 0 degrees azimuthal location is 0.071. There is a slight increase in this value as we move from 0 to 15 and then from 15 to 30. But as we move from 30 to 45 degrees, there is a substantial increase in the maximum value of the velocity magnitude. A local maximum occurs at 1.05 radial location and this value again steeply increases between 30 and 45 degrees azimuthal locations. There is more increase in the RMS values of velocities as we move from 45 to 60 degrees and then from 60 to 75 degrees. As we move from 75 to 90 degrees, there is a decrease in the deviation in velocities and from these results it can be ascertained that the maximum occurs in the region of the 75 degrees azimuthal plane.



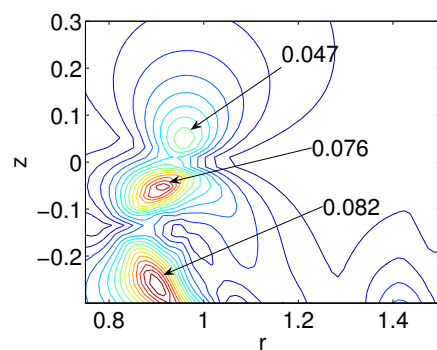
(a)



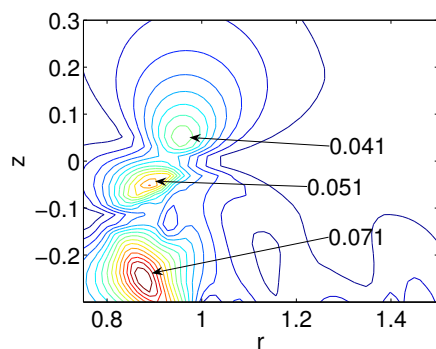
(b)



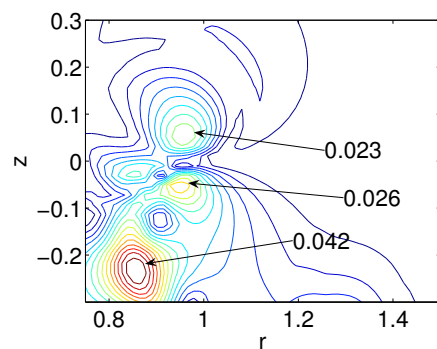
(c)



(d)



(e)



(f)

Figure 3.31

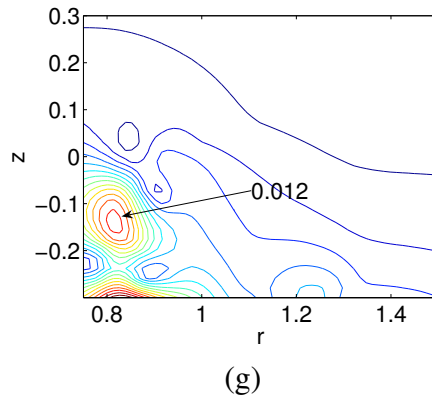


Figure 3.31: RMS swirl contours forward flight $\mu = 0.01$ on the retreating side at azimuthal locations (a) 0 degrees (b) 15 degrees (c) 30 degrees (d) 45 degrees (e) 60 degrees (f) 75 degrees (g) 90 degrees, $h/R = 0.72$.

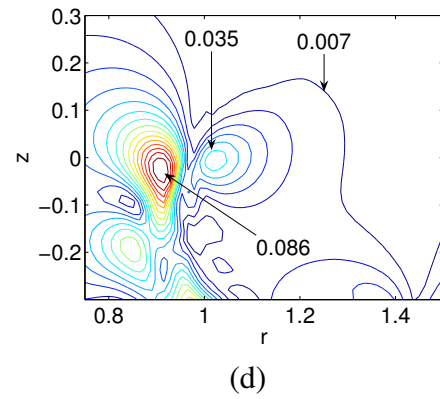
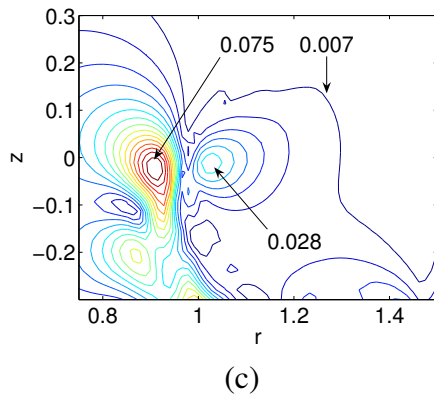
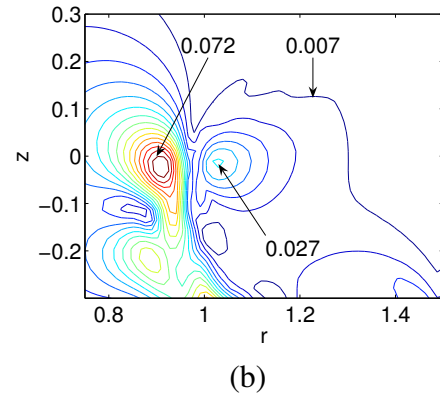
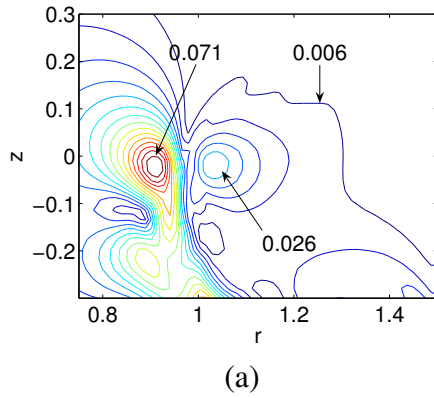
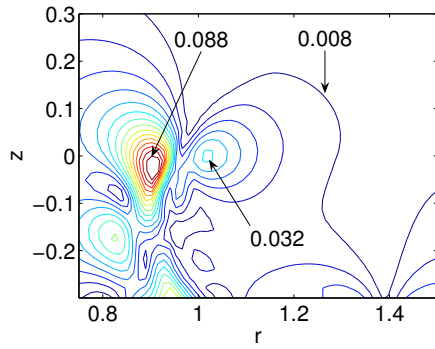
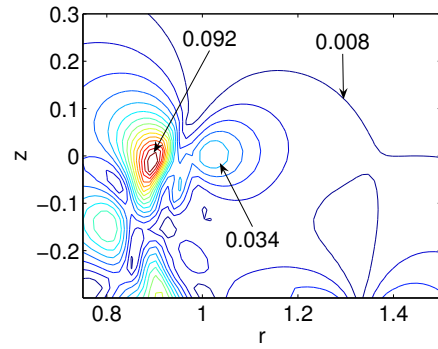


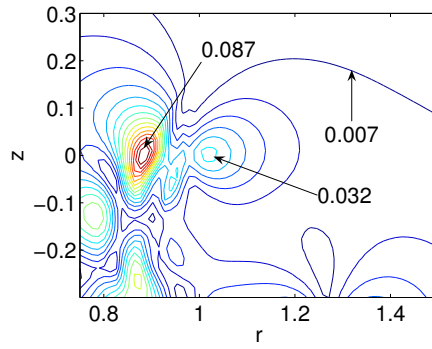
Figure 3.32



(e)



(f)

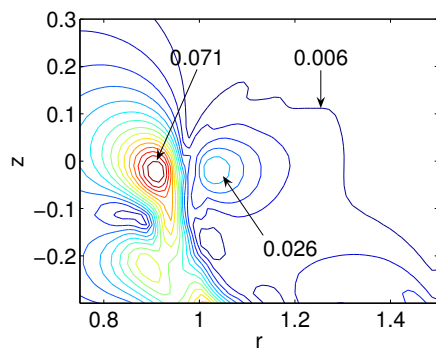


(g)

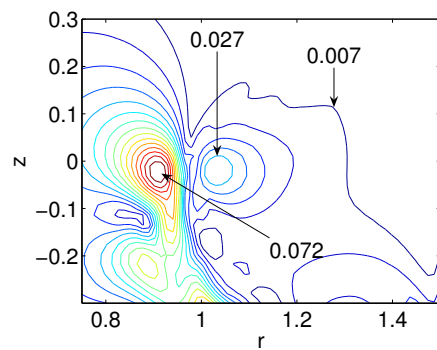
Figure 3.32: RMS downwash contours for forward flight $\mu = 0.01$ on the advancing side at azimuthal locations (a) 0 degrees (b) 15 degrees (c) 30 degrees (d) 45 degrees (e) 60 degrees (f) 75 degrees (g) 90 degrees, $h/R = 0.72$.

Downwash contours on the retreating side of the rotor disk for forward flight $\mu = 0.01$ can be seen in Figure 3.33. Similar to what was seen on the advancing side, the RMS maximum occurs close to the blade tip with another local maximum occurring at $r = 1.05$ on the rotor disk plane. With increase in the angle of the hypothetical tail rotor plane being considered, there is an increase in the maximum value of the RMS as the value of the azimuth is increased from 0 degrees to 45 degrees. The maximum value of the RMS doesn't change as the angle of the plane is increased from 45 to 60 degrees but there is a very slight increase in the value of the local maximum on the hypothetical tail rotor plane. The maximum RMS increases slightly as the azimuth is increased further from 60 to 75 but shows a slight decrease as we move from 75 to 90 degrees. But the changes in the magnitudes between 45 and 90 degrees are very small. All these planes experience similar variations of downwash on the plane being considered. Hence the planes at angles 45 and higher from the initial location of the blade experience higher unsteadiness in downwash than the other planes.

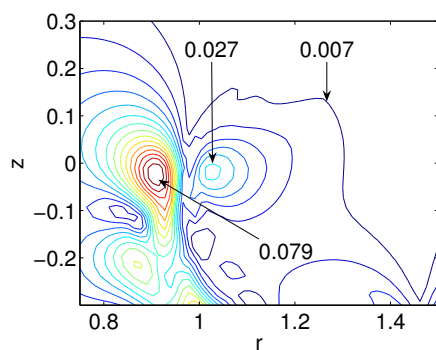
Figure 3.34 shows the contours of the RMS swirl velocities on the advancing side when the non-dimensional forward flight speed is $\mu = 0.03$. The RMS deviation is quite small for the 0 degrees azimuthal location and quantitatively close to the value for the case of hover but there is an increase in this value as we move to 15° azimuthal location. The maximum is near 1 and 1.1 radial location and 0.1 axial location. The maximum also occurs a little below at $z = 0.3$ between $r = 1.1$ and $r = 1.2$. As we move to the 30° azimuthal location, the locations of the RMS deviations move slightly inboard(into the rotor disk) but there is a substantial increase in their magnitudes. At 45° azimuthal location, there is further shift of the locations of the maximums with further increase in



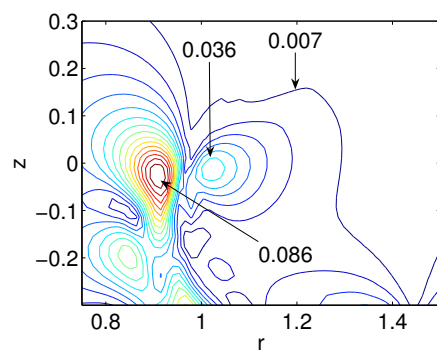
(a)



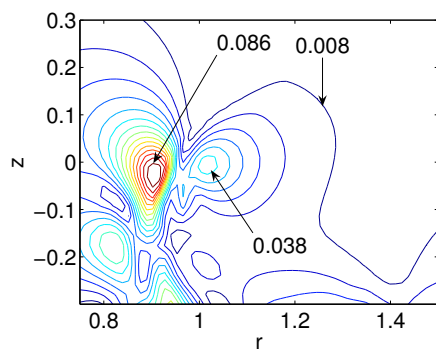
(b)



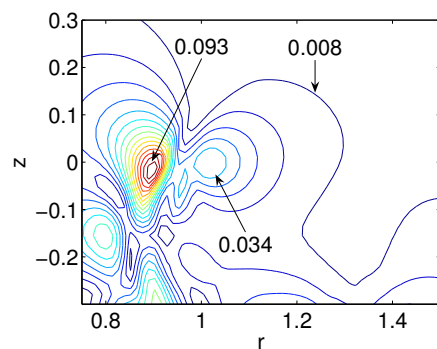
(c)



(d)



(e)



(f)

Figure 3.33

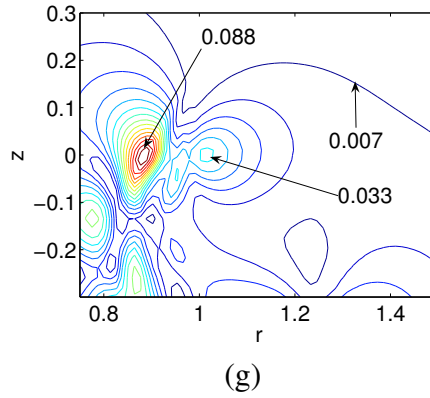
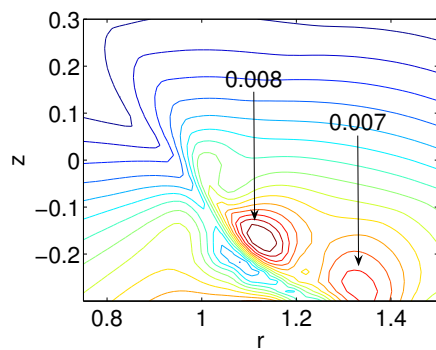


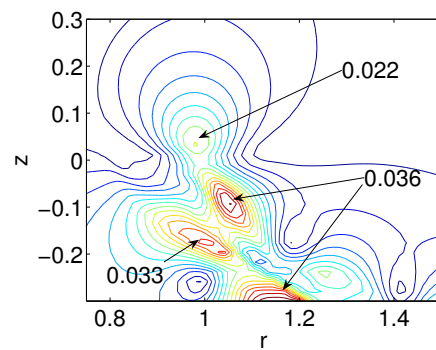
Figure 3.33: RMS downwash contours forward flight $\mu = 0.01$ on the retreating side at azimuthal locations (a) 0 degrees (b) 15 degrees (c) 30 degrees (d) 45 degrees (e) 60 degrees (f) 75 degrees (f) 90 degrees, $h/R = 0.72$.

their magnitudes. At 60° azimuthal location, surprisingly, there is a shift of the maximum value locations in the upward direction with a decrease in the magnitude. At 75° there is a further shift inboard and there is a huge decrease in the maximum values and at 90° , there is a further shift inboard and the deviations on the hypothetical tail rotor containing plane are almost negligible. Again, the RMS deviations in the inflow on the tail rotor disk, have maximum presence and magnitude on the plane at an azimuthal location of 45 degrees. Like at $\mu = 0.01$, the maximum unsteadiness in the inflow on the tail rotor is experienced in sideward flight at an angle of 45 degrees close to the ground.

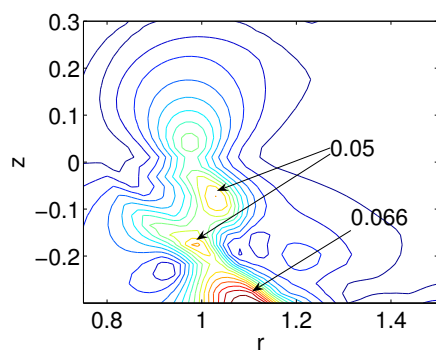
The behavior of the RMS values on the retreating side is similar to that on the advancing side with the RMS values increasing monotonically from 0 to 75 degrees and then decreasing as we go from 75 degrees to 90 degrees as can be seen from Figure 3.35. The magnitude of the RMS values here is almost the same as that on the advancing side.



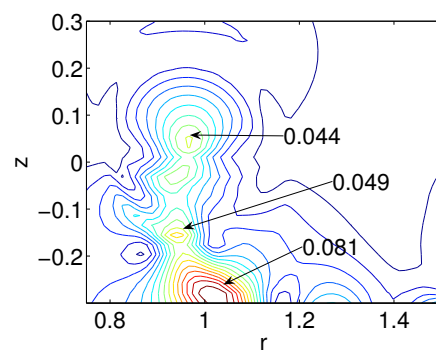
(a)



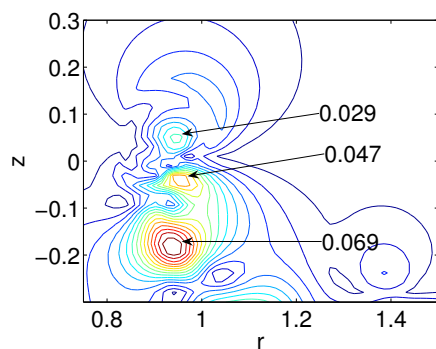
(b)



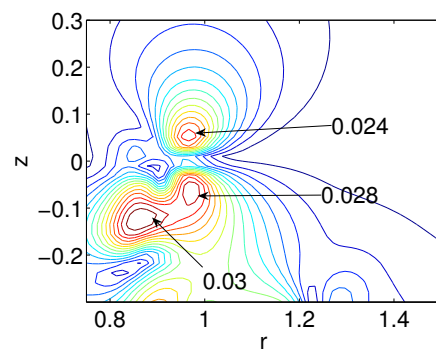
(c)



(d)



(e)



(f)

Figure 3.34

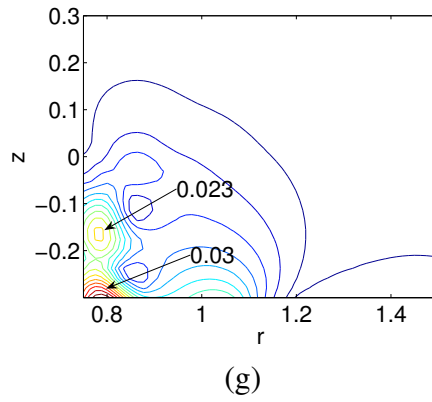


Figure 3.34: RMS swirl contours for forward flight $\mu = 0.03$ on the advancing side at azimuthal locations (a) 0 degrees (b) 15 degrees (c) 30 degrees (d) 45 degrees (e) 60 degrees (f) 75 degrees (g) 90 degrees, $h/R = 0.72$.

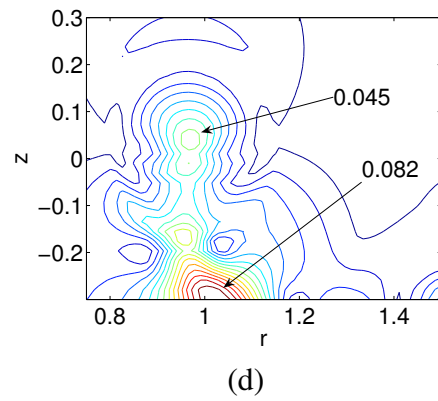
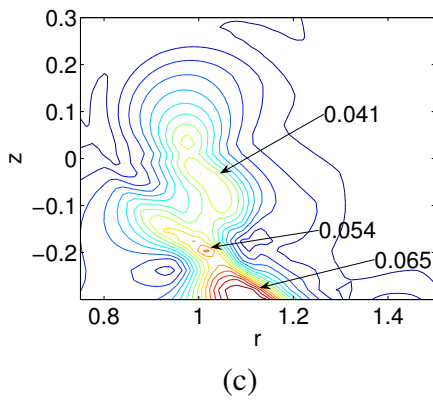
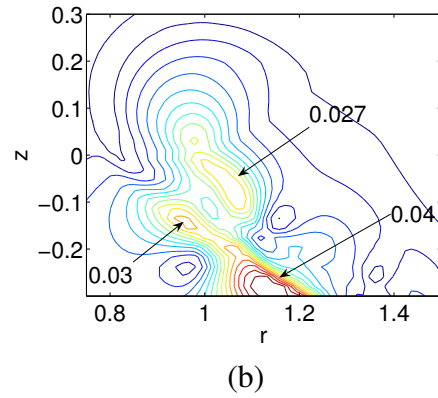
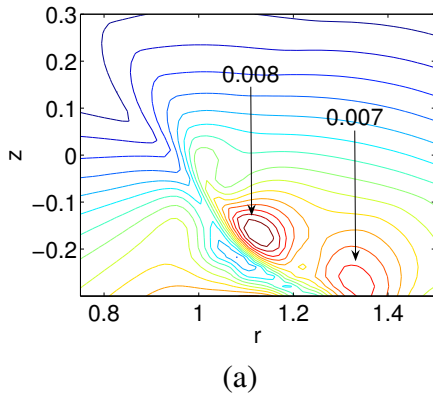
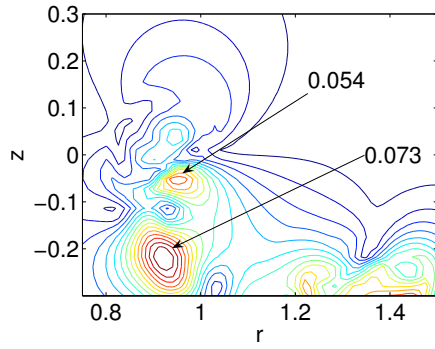
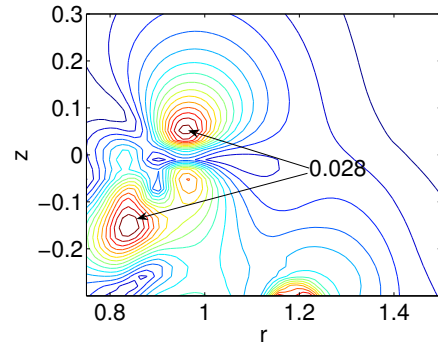


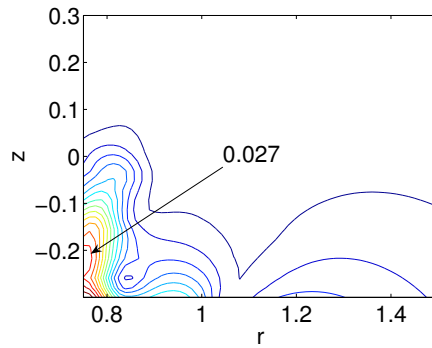
Figure 3.35



(e)



(f)



(g)

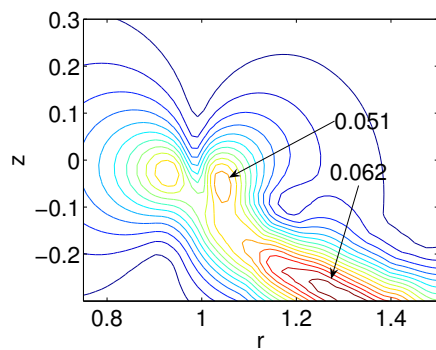
Figure 3.35: RMS swirl contours in forward flight $\mu = 0.03$ on the retreating side at azimuthal locations (a) 0 degrees (b) 15 degrees (c) 30 degrees (d) 45 degrees (e) 60 degrees (f) 75 degrees (g) 90 degrees, $h/R = 0.72$.

Figure 3.36 shows the behavior of the RMS downwash on different planes around the rotor disk. There is very little difference in the magnitudes of the RMS downwash magnitudes between 0 and 45 degrees. The unsteadiness in the RMS downwash increases at 60 degrees but reduces a bit at 75 degrees experiencing further decrease at 90 degrees. The unsteadiness is the maximum after 45 degrees, indicating maximum unsteadiness in downwash is experienced by rotors moving sideward at 60 and 75 degrees.

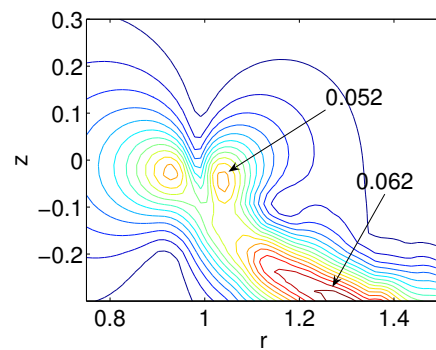
3.4 Summary

The tip-vortex structure is axisymmetric in hover and shifts in the direction of inflow in forward flight. The tip-vortex structure close to the blade reaches a periodic state but there are fine scale differences in the wake structure close to the ground even after 90-100 revolutions. But, overall, the flow field reaches periodicity. The formation of ground vortex is observed in hover and in forward flight. During hover, the position of the ground vortex is right below the tip of the blade while in forward flight, the location of the ground vortex moves under the rotor disk and reaches midway between the root and tip of the blade at $\mu = 0.03$.

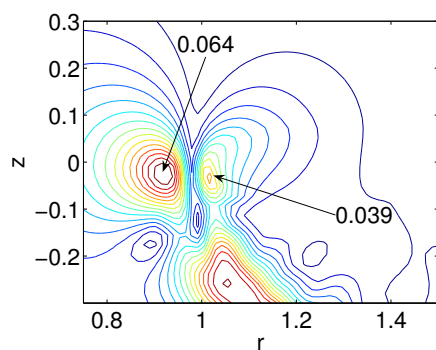
The two bladed rotor wake exhibits much more unsteadiness with the tip-vortex structure not becoming smooth or periodic close to the ground even at 90-100 revolutions. The flow field is periodic but a low frequency/long time period component also has been observed in the inflow of the two-bladed rotor. The unsteadiness in the swirl velocity on and around the hypothetical tail rotor plane is the maximum on the plane making an angle of 45 degrees to initial location of the blade or in other words sideward flight at an angle of



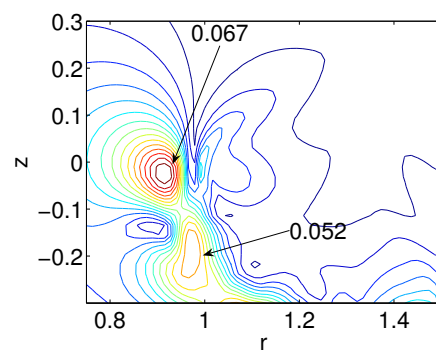
(a)



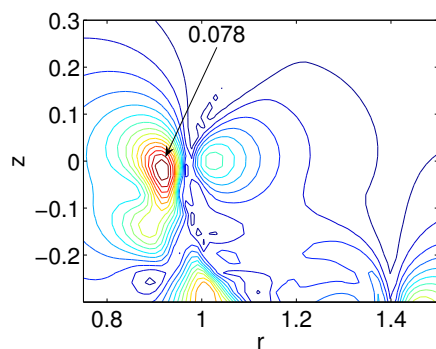
(b)



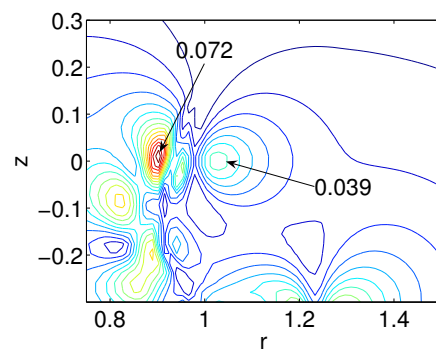
(c)



(d)



(e)



(f)

Figure 3.36

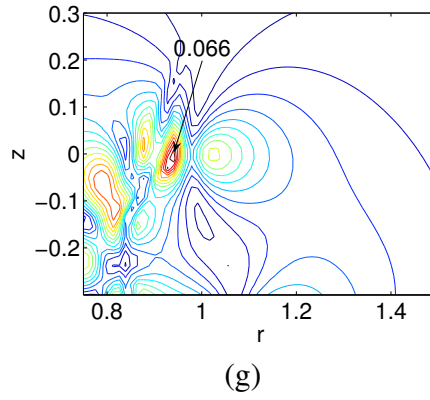


Figure 3.36: RMS downwash contours for forward flight $\mu = 0.03$ on the advancing side at azimuthal locations (a) 0 degrees (b) 15 degrees (c) 30 degrees (d) 45 degrees (e) 60 degrees (f) 75 degrees (g) 90 degrees, $h/R = 0.72$.

45 degrees experiences maximum tail rotor inflow unsteadiness. The axial velocity exhibits slightly different characteristics, with the planes at an angle higher than 45 degrees exhibiting large unsteadiness and no particular maximum exists.

CHAPTER 4

Results - Lifting Surface Model

4.1 Introduction

Results obtained using the lifting surface theory are presented in this chapter. As discussed in Chapter 2, the difference here is in the aspect ratio of the blade. Lifting line theory makes an assumption that aspect ratio is very large and $1/A \rightarrow 0$. As we discussed in Chapter 2, the lifting surface theory reaches the limit of lifting line theory when the aspect ratio is 20. Hence the lifting line theory cannot accurately model any blade whose aspect ratio is less than 20. Although actual helicopters use large aspect ratio blades, it is not feasible to conduct experiments with large aspect ratio blades because it is very dangerous working with high aspect ratio blades. Hence, to validate the computations with experiments a model which can be used to account for the small aspect ratio blade is needed. The lifting surface model does not make the large aspect ratio assumption and small aspect ratio blades can be considered here. An aspect ratio of $A = 6$ and an angle of attack of 10 degrees have been used for the blades. In this Chapter, the tip-vortex structure for single and two-bladed rotors, structure of the ground vortex and the velocity contours are presented. As in the case of the lifting line model in Chapter 3, results have been compared with experimental results obtained from Georgia Institute of Technology. Results have also been

compared with those obtained using the lifting line model. Results for the unsteadiness on the hypothetical tail rotor plane have also been presented.

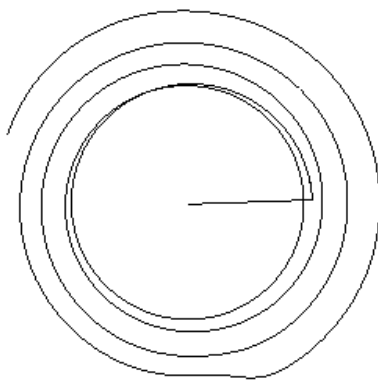
4.2 Results - Lifting Surface

The structure of the tip-vortices at various times has been computed for the rotor in hover and forward flight using the lifting surface theory to model the blade.

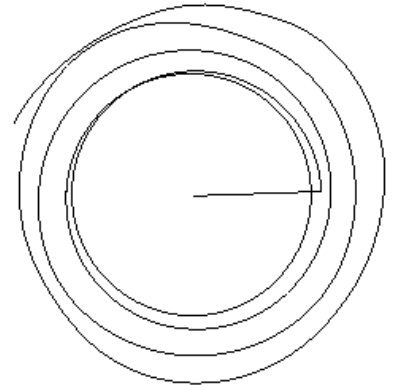
4.2.1 Results - Single-Bladed Hover Lifting Surface

In all of this work, one chordwise panel and twenty spanwise panels are used to describe the blade. Computations using two chordwise and forty spanwise panels (not shown) were also made and the results apart from more chordwise detail are numerically equivalent to the case of one and twenty panels. Figure 4.1 shows the tip-vortex structure as a function of the number of revolutions in hover for a single-bladed rotor. Since the advance ratio is zero, the tip-vortex structure is axisymmetric in nature. The first three turns of the tip-vortex look identical at all times. But there seem to be slight variations in the last two turns of the tip-vortex(close to the ground). Hence the flow field close to the ground hasn't quite attained the periodic state. The rest of the flow field attains periodicity quite early, even near the ground, there exist only fine scale differences.

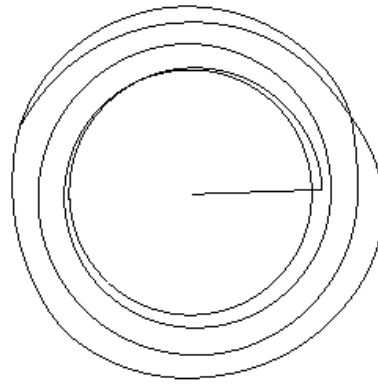
The tip-vortex structure after 100 revolutions in hover has been compared with the lifting line wake structure in Figure 4.2. The first three turns are virtually the same but near the ground there are fine scale differences. The wake structure has a larger radius in the lifting surface model compared to the lifting line model. Also, in the lifting line model, the vortex lines overlap in the top view which does not happen in the lifting surface case.



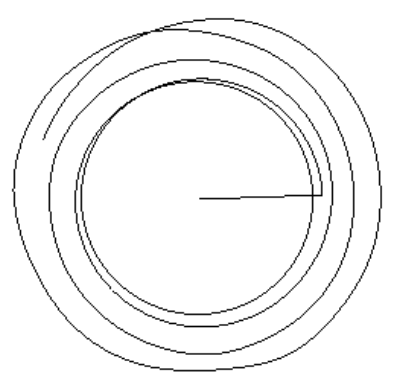
(a)



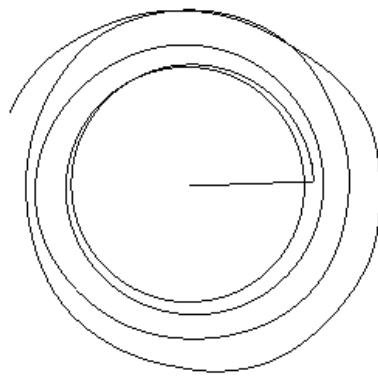
(b)



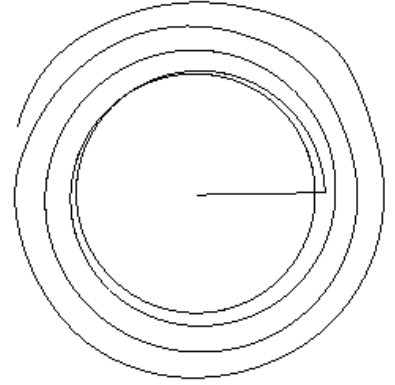
(c)



(d)



(e)



(f)

Figure 4.1: Top view of the tip-vortex trajectory of a single-bladed rotor in ground effect in hover after (a) 10 revolutions (b) 30 revolutions (c) 50 revolutions (d) 70 revolutions (e) 90 revolutions (f) 100 revolutions, $A = 6$, $\alpha_0 = 10^\circ$, $h/R = 0.5$.

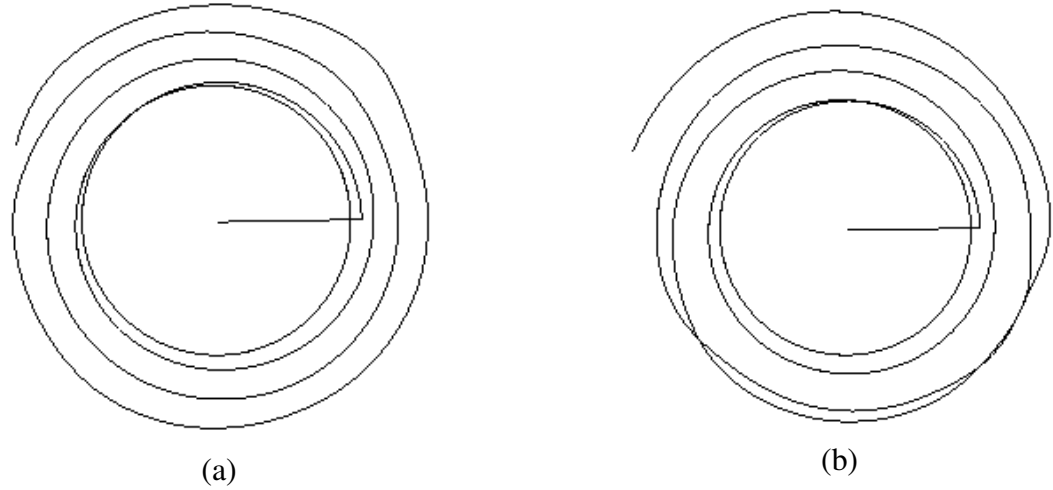
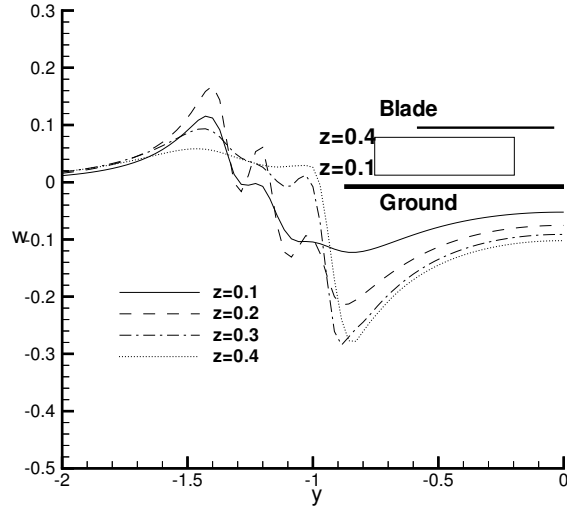


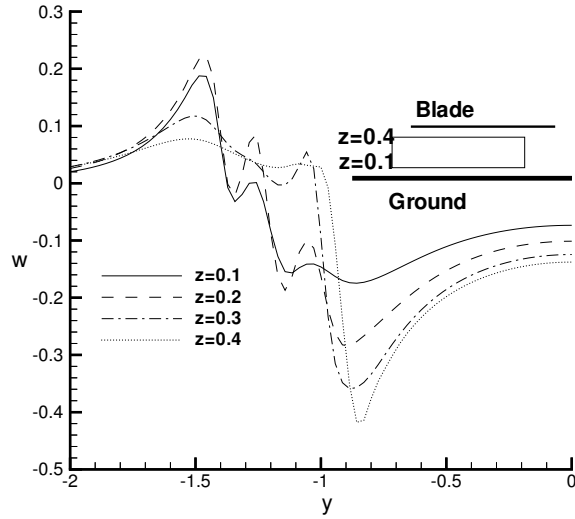
Figure 4.2: Comparison in wake structure after 100 revolutions between (a) lifting surface model, $A = 6$, $\alpha = 10^\circ$, $h/R = 0.5$, (b) lifting line model.

Figure 4.3 shows the downwash as a function of the y coordinate for different heights above the ground in hover. The formation of a ground vortex just in front of the tip of the blade can be seen from the profiles of the downwash at $z = 0.1$ and $z = 0.2$. The plot for the same conditions using the lifting line theory has been presented for comparison. Qualitatively, both the plots look quite similar, but the magnitude of the downwash is higher in the lifting line case indicating formation of a bigger ground vortex.

The flow field in this case is studied using contour plots of the downwash obtained on the longitudinal section below the blade after periodicity is obtained (100 revolutions). Figure 4.4(a) shows the downwash contours below the blade for a single-bladed rotor in hover when the blade is at the zero azimuth position (after 100 revolutions) in hover. The convection of the tip-vortex from the blade to the ground can be seen in the form of small vortices on both sides of the rotor disk. The vortices tend to go up towards the tip of the blade after striking the ground indicating a recirculation. The formation of the ground



(a)



(b)

Figure 4.3: Downwash distribution along the blade for a single-bladed rotor in hover for $h/R = 0.5$ after one hundred revolutions; (a) lifting surface model, $\alpha_0 = 10^\circ$, $A = 6$, $h/R = 0.5$, (b) lifting line model.

vortex can be better visualized here. The downwash contours obtained using the lifting line model can be seen in Figure 4.4(b). There are differences in the size of the vortex near the blade and also in the magnitudes of velocities. The magnitude of the downwash is lesser when the lifting surface model is used. The position of the ground vortex is circled in the Figure.

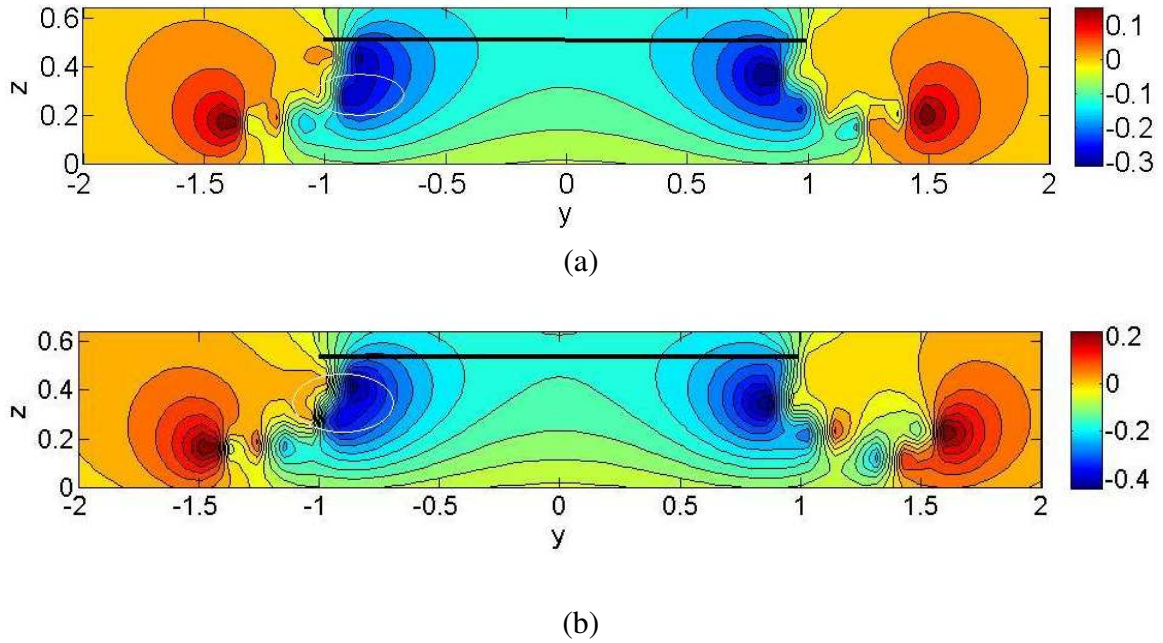


Figure 4.4: Downwash contours in longitudinal cross section for a single-bladed rotor in hover for $h/R = 0.5$ after one hundred revolutions; (a) lifting surface model, $\alpha_0 = 10^\circ$, $A = 6$, $h/R = 0.5$, (b) lifting line model.

4.2.2 Results - Two-Bladed Hover Lifting Surface

Figure 4.5 shows the two-bladed wake structure in hover. Like in the lifting line case, the wake structure for a two-bladed rotor is not as smooth as that of a single-bladed rotor.

It is interesting to note that the wake structure close to the ground is smooth after 10 revolutions but not so much after that. However, the first few turns at all times look identical. The last three turns of the tip-vortex close to the ground, do not quite become smooth and remain unsteady until 100 revolutions. As was discussed in the lifting line chapter, this is most likely due to the vortex-vortex interactions since there are two tip-vortices.

A sideview of the wake structure of the two-bladed rotor in hover after 100 revolutions is presented in Figure 4.6 to look at possible blade-vortex interactions. As can be seen from Figure 3.9, the complications in the flow field exist only close to the ground.

Figure 4.7 shows the behavior of the downwash along the y -axis for a two-bladed rotor in hover and it can be seen that there are more peaks indicating more recirculation compared to the single-bladed rotor. The downwash behavior for the lifting line case has also been presented for comparison. The magnitude of the velocities is slightly lower in the lifting surface case. Also there seem to be differences in the positions of the downwash peaks upstream of the rotor disk.

The downwash contours in hover for the two-bladed rotor can be seen in Figure 4.8. Qualitative differences between the lifting line and lifting surface models can be seen upstream of the rotor blade. The flow field appears to be more complicated in the lifting surface case with vortices even at $y = -2$. Right below the rotor the flow field in both the cases is identical with the formation of a ground vortex slightly upstream of the tip of the blade.

4.2.3 Results - Single-Bladed Forward Flight Lifting surface

Figure 4.9 shows the progression of the tip-vortex structure for a single-bladed rotor in forward flight at $\mu = 0.01$ with time. The wake structure is not axisymmetric because of the

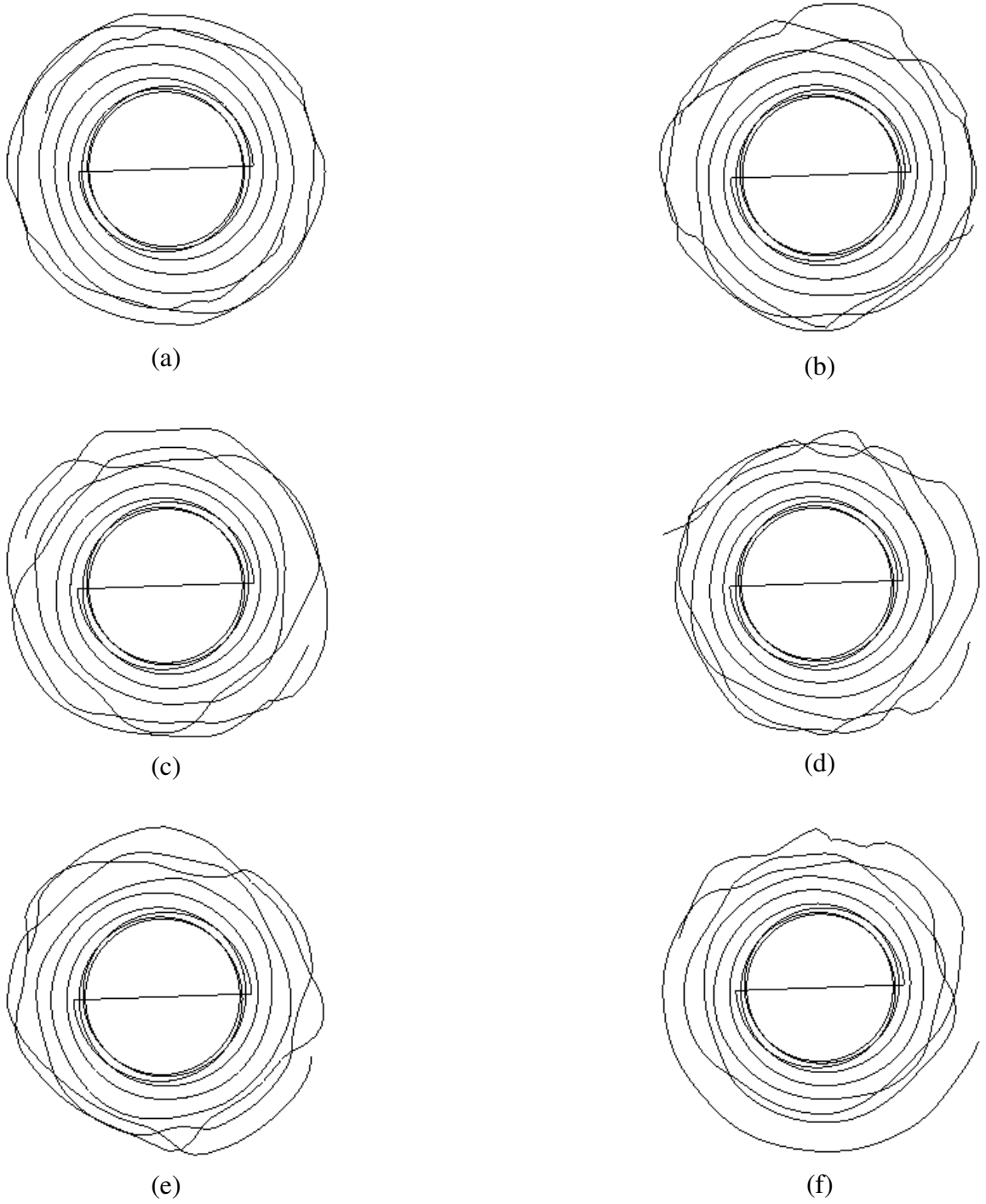


Figure 4.5: Top view of the tip-vortex trajectory of a two-bladed rotor in ground effect in hover $h/R = 0.5$ after (a) 10 revolutions, (b) 30 revolutions, (c) 50 revolutions, (d) 70 revolutions, (e) 90 revolutions, (f) 100 revolutions; $\alpha_0=10^\circ$, $A = 6$, $h/R = 0.5$.

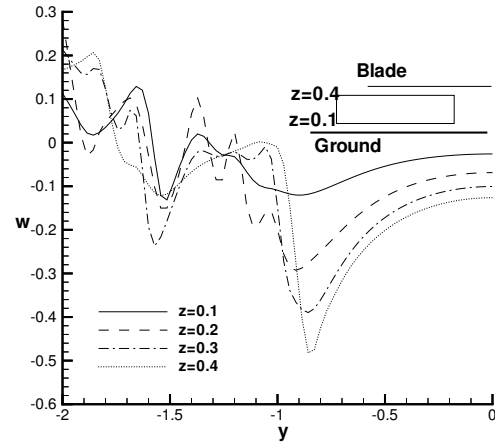


Figure 4.6: Side view of the wake structure for a two-bladed rotor in hover for $h/R = 0.5$ after 100 revolutions; $\alpha_0=10^\circ$, $A = 6$, $h/R = 0.5$.

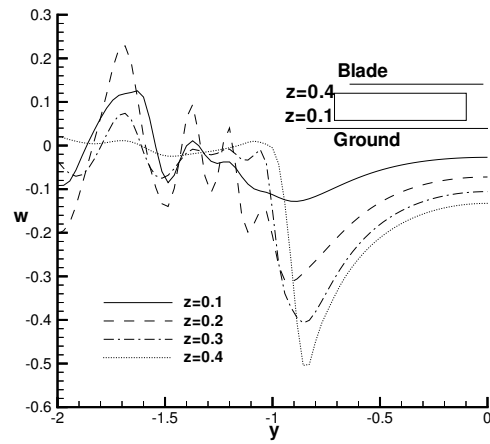
advance ratio. There are slight variations near the ground until about 50 revolutions. After 50 revolutions, it can be seen that the wake structures are quite identical to one another even close to the ground. Hence it can be inferred that the entire flow field attained periodic state after 50 revolutions. It must be noted here that when the lifting line model is used, slight differences near the ground exist even near 90 and 100 revolutions.

The tip-vortex structure after 100 revolutions for $\mu = 0.01$ has been compared with the lifting line wake structure in Figure 4.10. In the lifting line wake, the last two turns overlap but using the lifting surface model, the tip-vortices do not overlap. As has been said earlier, the wake structure obtained using the lifting surface model is periodic even close to the ground while the wake obtained by lifting line model is not.

The downwash for a single-bladed rotor at $\mu = 0.01$ after 100 revolutions as a function of the distance along the blade at different heights from the ground at $\mu = 0.01$ can be seen in Figure 4.11 (a). It has been compared with the downwash profile obtained by the lifting line model. The downwash magnitude in the lifting line model is considerably higher compared to the lifting surface model. Qualitatively both the profiles look similar except at $z = 0.2$ where there seem to be three peaks in the downwash indicative of three vortices



(a)



(b)

Figure 4.7: Downwash distribution along the blade for a two-bladed rotor in hover for $h/R = 0.5$ after 100 revolutions (a) lifting surface model, $\alpha_0=10^\circ$, $A = 6$, $h/R = 0.5$, (b) lifting line model.

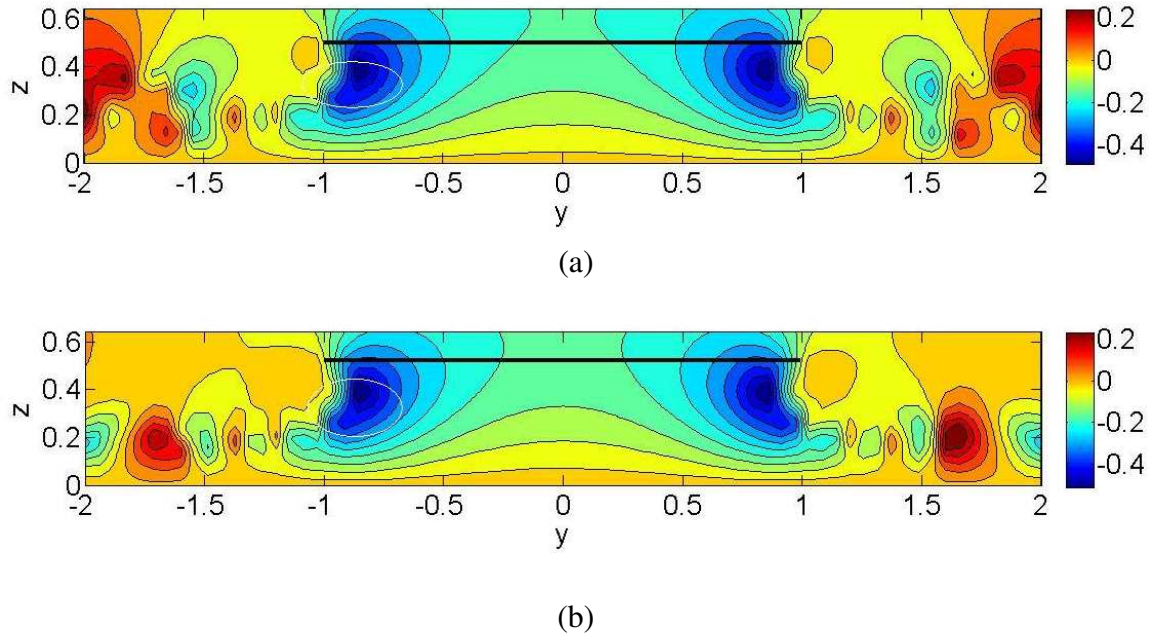


Figure 4.8: Downwash contours in longitudinal cross section for a two-bladed rotor in hover for $h/R = 0.5$ after one hundred revolutions; (a) lifting surface model, $\alpha_0=10^\circ$, $A = 6$, $h/R = 0.5$, (b) lifting line model.



Figure 4.9

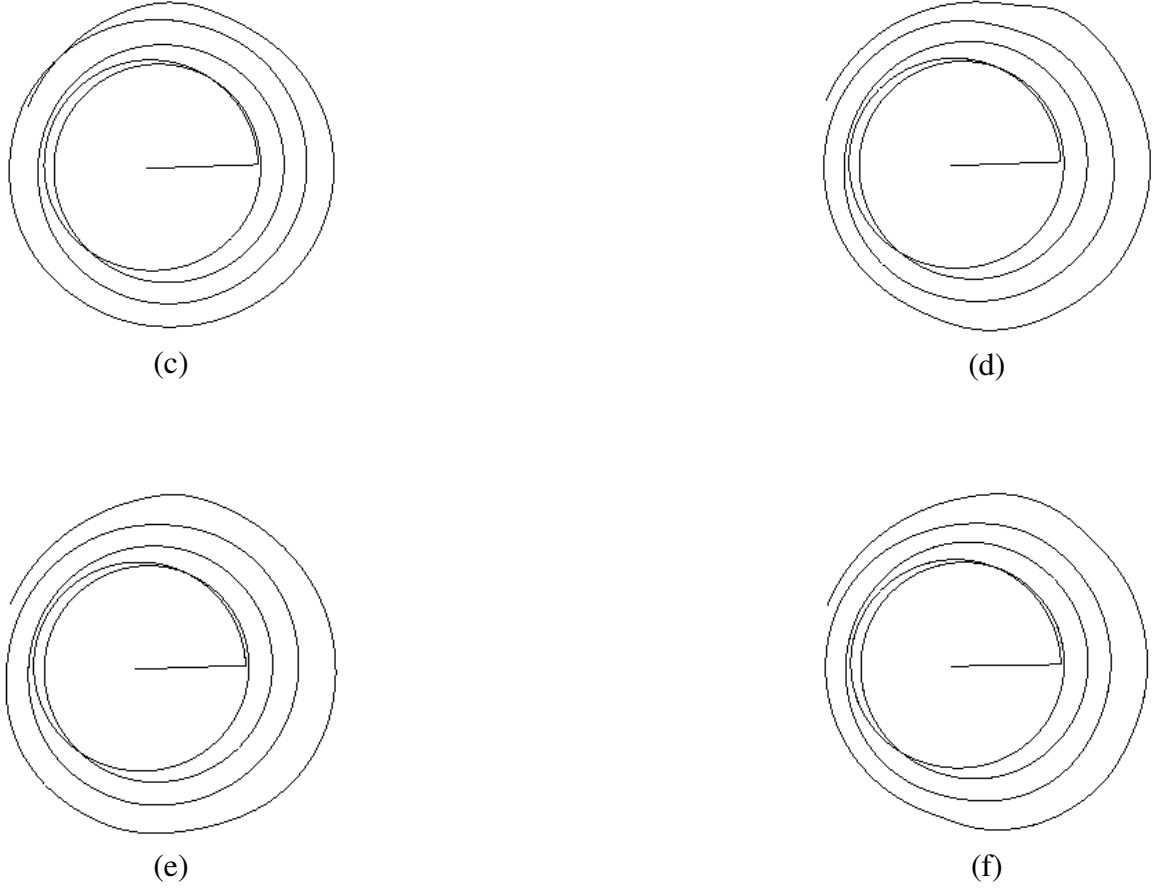


Figure 4.9: Top view of the tip-vortex trajectory of a single-bladed rotor in ground effect for $\mu = 0.01$ after (a) 10 revolutions (b) 30 revolutions (c) 50 revolutions (d) 70 revolutions (e) 90 revolutions (f) 100 revolutions, $\alpha_0=10^\circ$, $A=6$, $h/R = 0.5$.

in the lifting line model, while in the lifting surface model, there are only two peaks. The downwash profiles at $z = 0.1$ and $z = 0.2$ indicate the formation of ground vortex slightly upstream of the rotor disk.

As has been done for the case of hover, the downwash contours for a single-bladed rotor at $\mu = 0.01$ have been obtained across a longitudinal section of the flow field containing the blade after 100 revolutions. Figure 4.12 compares the downwash contours obtained using

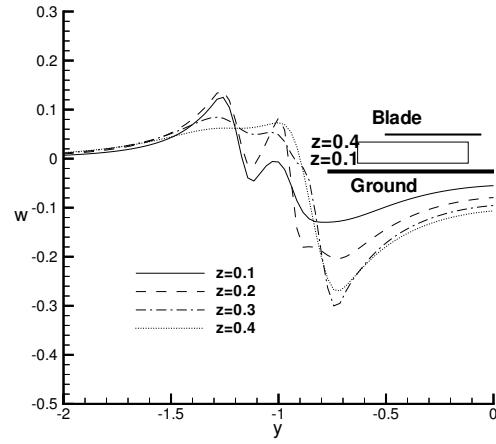


Figure 4.10: Comparison in wake structure after 100 revolutions for $\mu = 0.01$ between (a) lifting surface model, $\alpha_0=10^\circ$, $A = 6$, $h/R = 0.5$, (b) lifting line model.

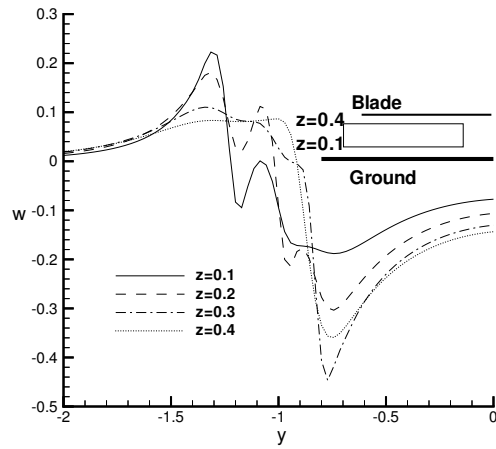
the lifting line and lifting surface models. Qualitatively, the downwash contours obtained from lifting line and lifting surface models look quite similar. The flow field in this case is no longer axisymmetric and there is some recirculation upstream of the rotor. The position of the ground vortex is marked in the Figure.

The tip-vortex structure of a single-bladed rotor when it is moving at an advance ratio $\mu = 0.03$ can be seen in Figure 4.13. There is more shift of the wake under the rotor disk due to increase in magnitude of the advance ratio. There are slight differences between the wake structures after 10 and 30 revolutions close to the ground but after that no differences between the wake structures can be noticed even close to the ground. Note that when the lifting line model has been used, periodicity close to the ground has not been achieved.

The tip-vortex structure after 100 revolutions for $\mu = 0.03$ has been compared with the lifting line wake structure in Figure 4.14. There is substantial difference in the last two turns.



(a)



(b)

Figure 4.11: Downwash distribution along the blade for a single-bladed rotor in forward flight $\mu = 0.01$ for $h/R = 0.5$ after one hundred revolutions; (a) lifting surface model, $\alpha_0 = 10^\circ$, $A = 6$, $h/R = 0.5$, (b) lifting line model.

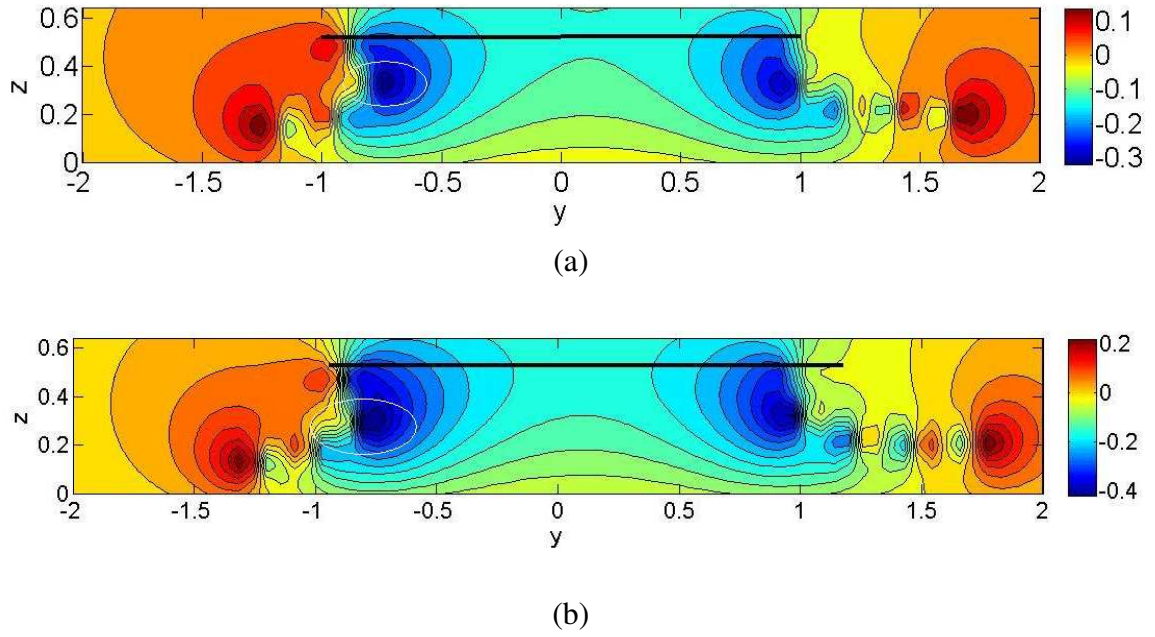


Figure 4.12: Downwash contours in longitudinal cross section for a single-bladed rotor for $\mu = 0.01$ for $h/R = 0.5$ after one hundred revolutions; (a) lifting surface model, $\alpha_0 = 10^\circ$, $A = 6$, $h/R = 0.5$, (b) lifting line model.

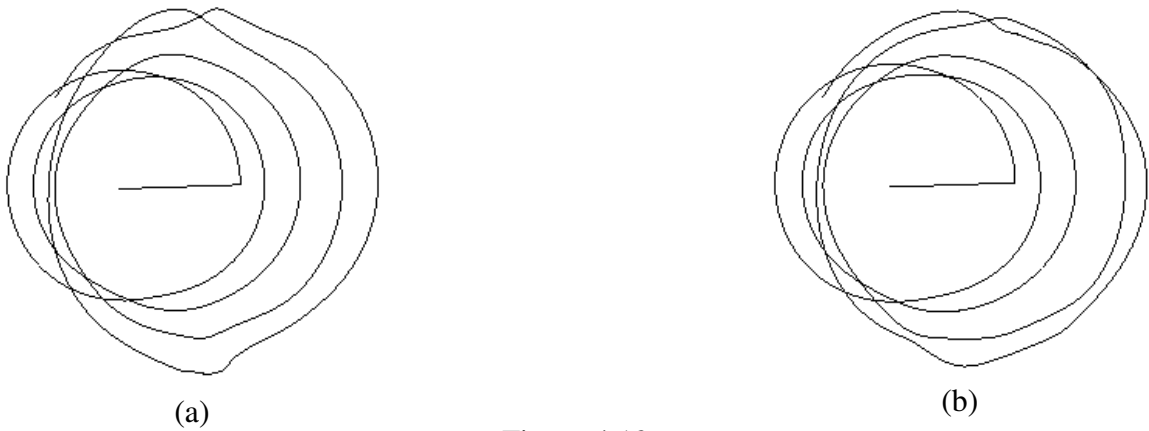
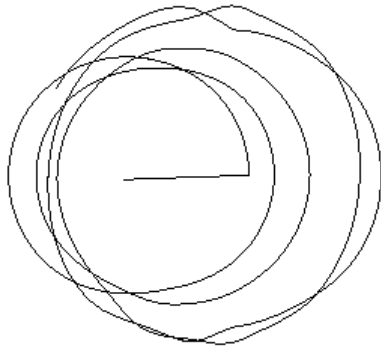
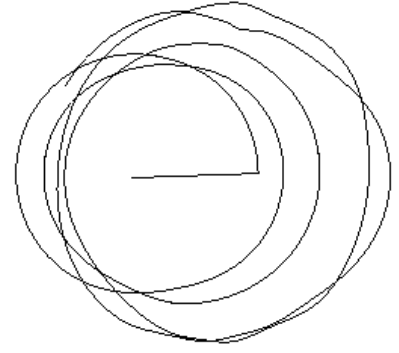


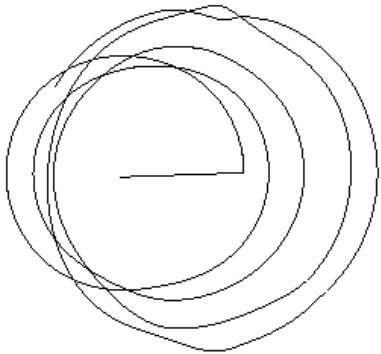
Figure 4.13



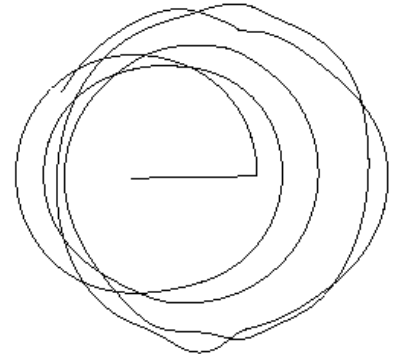
(c)



(d)

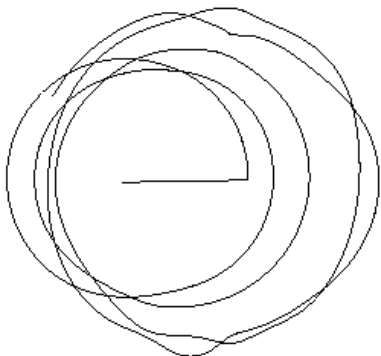


(e)

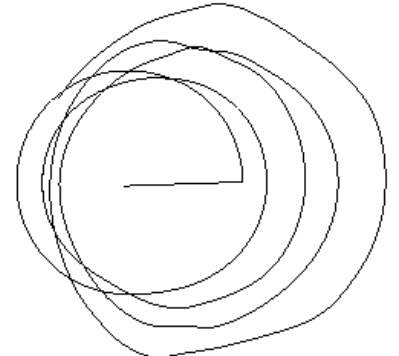


(f)

Figure 4.13: Top view of the tip-vortex trajectory of a single-bladed rotor in ground effect for $\mu = 0.03$ after (a) 10 revolutions (b) 30 revolutions (c) 50 revolutions (d) 70 revolutions (e) 90 revolutions (f) 100 revolutions, $\alpha_0 = 10^\circ$, $A = 6$, $h/R = 0.5$.



(a)



(b)

Figure 4.14: Comparison in wake structure after 100 revolutions for $\mu = 0.03$ between (a) lifting surface model, $\alpha_0 = 10^\circ$, $A = 6$, $h/R = 0.5$, (b) lifting line model.

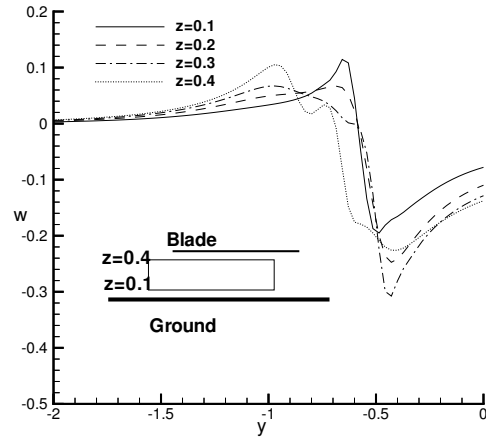
The downwash profile along the length of the blade at different heights from the ground for a single-bladed rotor at $\mu = 0.03$ can be seen in Figure 4.15. As can be seen, there is shift in the peak of the downwash inboard indicating a shift in the ground vortex. Also, only a single peak can be noticed at $z = 0.1, 0.2$ and 0.3 which means the individual peaks seen previously assimilated into the ground vortex. This suggests the formation of a strong ground vortex midway between the root and the tip of the blade.

As has been done for the case of hover and $\mu = 0.01$, the downwash contours have been obtained across a longitudinal section of the flow field containing the blade after 100 revolutions for $\mu = 0.03$ as can be seen from Figure 4.16. The flow field in this case is no longer axisymmetric and there is some recirculation upstream of the rotor. The recirculating vortices come together to form a strong ground vortex midway between the root and tip of the blade.

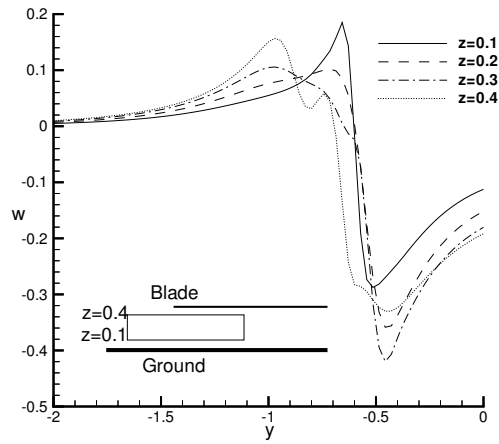
4.2.4 Results - Two-Bladed Forward Flight Lifting Surface

The wake structure for a two-bladed rotor at $\mu = 0.01$ can be seen in Figure 4.17. The behavior of the wake structure with time is quite similar to that of hover, the wake is smooth even close to the ground after 10 revolutions, but after that it is not very smooth close to the ground. The wake close to the ground does not become steady with differences existing even between 90 and 100 revolutions.

The downwash profile as a function of the distance along the blade for a two-bladed rotor at $\mu = 0.01$ can be seen in Figure 4.18. The downwash peak that was not seen in hover(which was probably upstream) moves towards the right due to the advance ratio with a peak appearing close to $y = -2$. There is also a slight shift in the locations of the other downwash peaks downstream. Compared to the lifting line case, the magnitude of



(a)



(b)

Figure 4.15: Downwash distribution along the blade for a single-bladed rotor in forward flight $\mu = 0.03$ for $h/R = 0.5$ after one hundred revolutions; (a) lifting surface model, $\alpha_0 = 10^\circ$, $A = 6$, $h/R = 0.5$, (b) lifting line model.

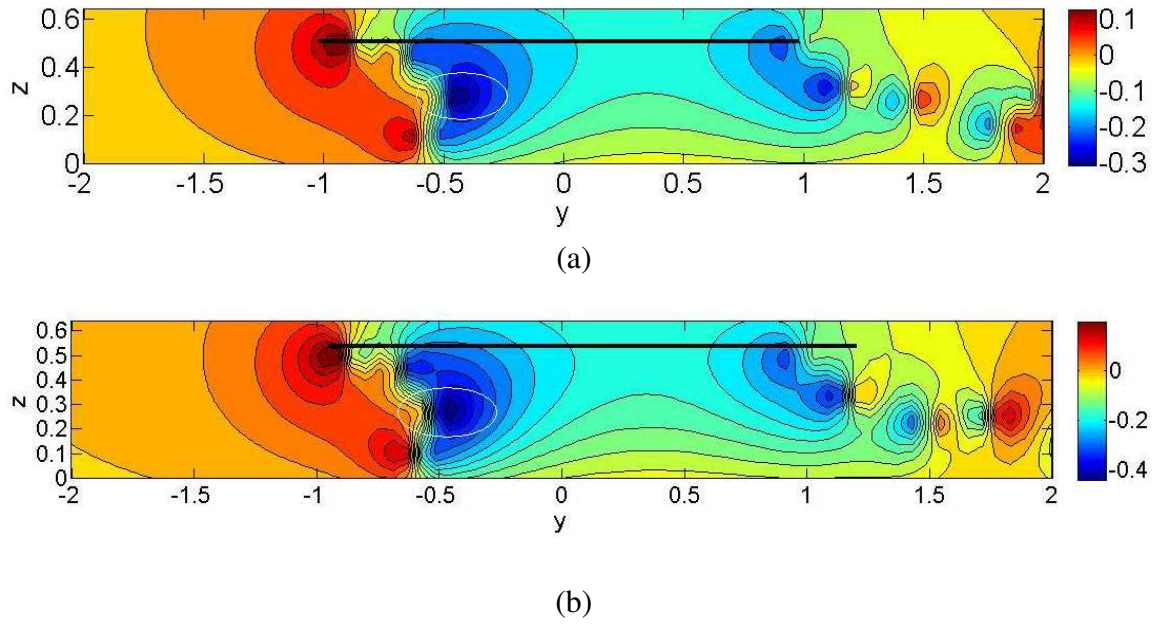


Figure 4.16: Downwash contours in longitudinal cross section for a single-bladed rotor for $\mu = 0.03$ for $h/R = 0.5$ after one hundred revolutions; (a) lifting surface model, $\alpha_0 = 10^\circ$, $A = 6$, $h/R = 0.5$, (b) lifting line model.

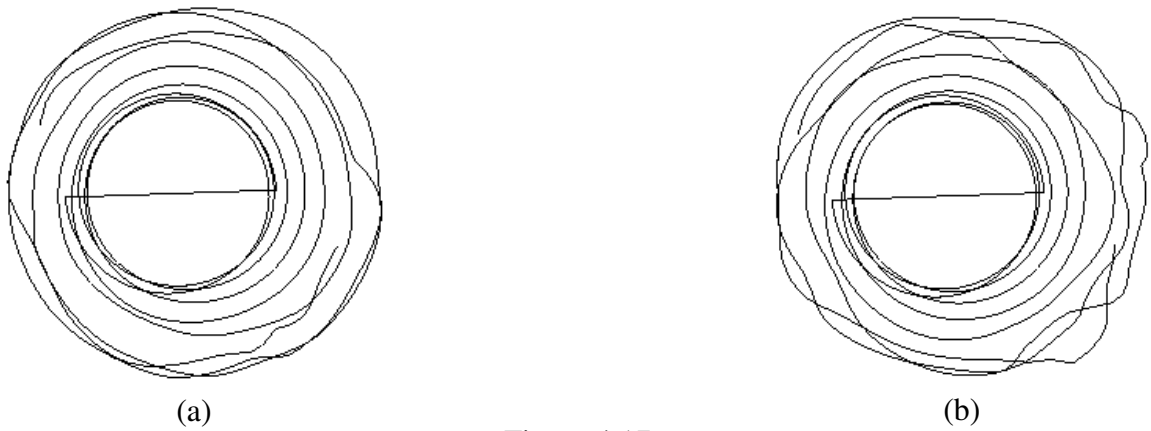


Figure 4.17

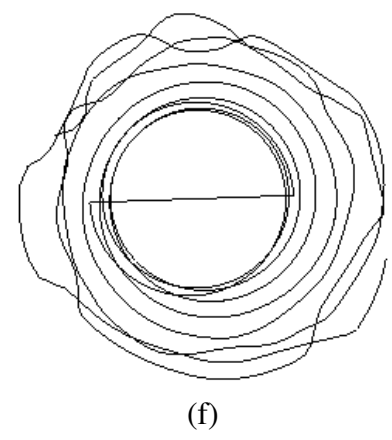
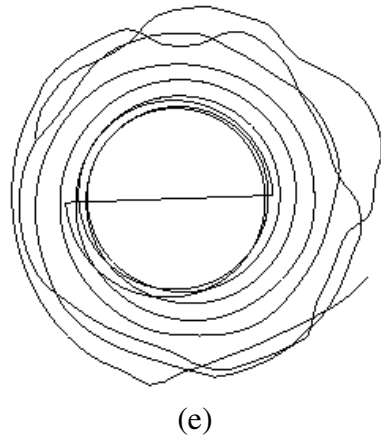
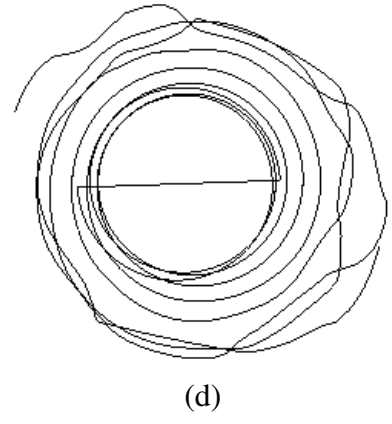
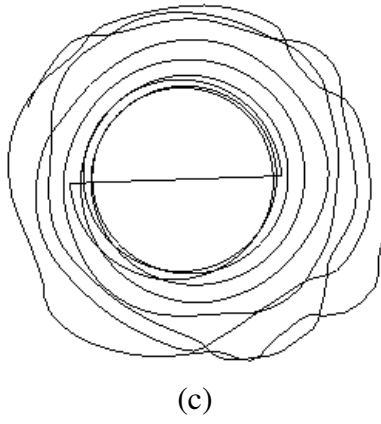


Figure 4.17: Top view of the tip-vortex trajectory of a two-bladed rotor in ground effect in forward flight $\mu = 0.01$ for $h/R = 0.5$ after (a) 10 revolutions, (b) 30 revolutions, (c) 50 revolutions, (d) 70 revolutions, (e) 90 revolutions, (f) 100 revolutions, $\alpha_0=10^\circ$, $A = 6$, $h/R = 0.5$.

the downwash is smaller and the number of peaks is more. This indicates that the ground vortex in the lifting line case is stronger.

The downwash contours for the two-bladed rotor at $\mu = 0.01$ can be seen in Figure 4.19. There is a slight shift of the ground vortex from the tip of the blade further inboard. There are fine scale differences between the lifting line and lifting surface models in the flow field.

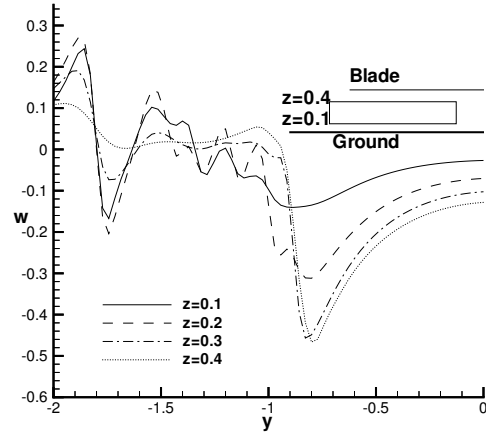
The tip-vortex structure for a two-bladed rotor at $\mu = 0.03$ can be seen in Figure 4.20. Similar to what was noticed in hover and $\mu = 0.01$, the wake structure close to the ground does not become smooth or stable. The unsteadiness close to the ground exists even near 90 and 100 revolutions.

Figure 4.21 compares the downwash profiles for a two-bladed rotor at $\mu = 0.03$ for the lifting surface and lifting line cases. The magnitude of the downwash in the lifting line case is slightly higher again but there more peaks in the lifting surface case. The flow field looks more complicated compared to single-bladed case. The position of the velocity peak(ground vortex) has also moved further under the rotor disk compared to $\mu = 0.01$.

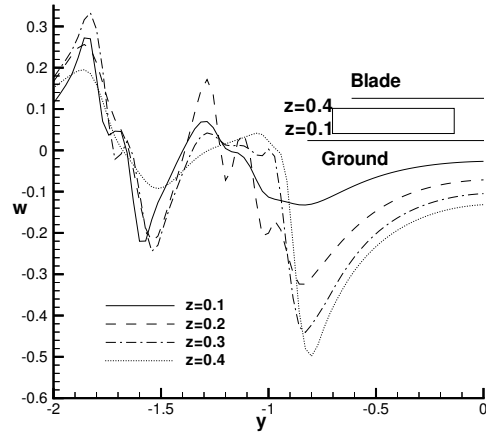
Qualitatively, the flow field in the lifting line and lifting surface models looks the same as can be seen from Figure 4.22.

4.2.5 Comparison with Experiments

Figures 4.23 and 4.25 compare the ground vortex phenomenon in the computations and the experimental results obtained from Georgia Institute of Technology for the case of a two-bladed rotor at a non-dimensional height(h/R) of 0.72 above the ground. The aspect ratio of the blades used in the experiments is $A = 5.33$. Results have been obtained for the advance ratios $\mu = 0.03$ and $\mu = 0.04$. The flow field obtained from the computational

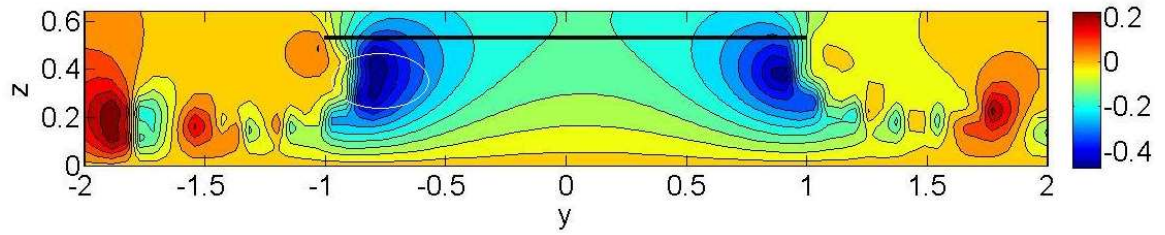


(a)

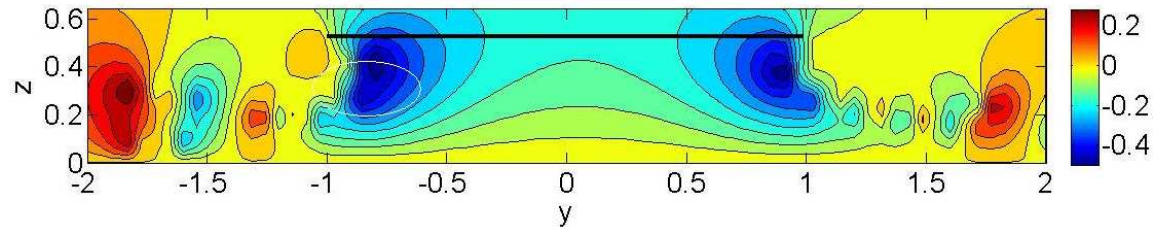


(b)

Figure 4.18: Downwash distribution along the blade for a two-bladed rotor for $\mu = 0.01$ for $h/R = 0.5$ after 100 revolutions; (a) lifting surface model, $\alpha_0=10^\circ$, $A = 6$, $h/R = 0.5$, (b) lifting line model.

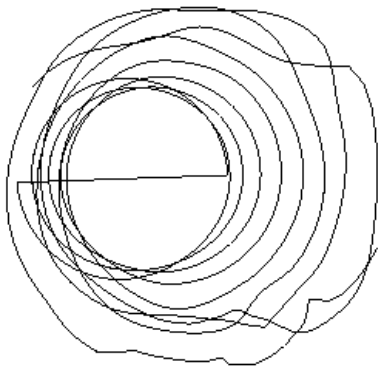


(a)

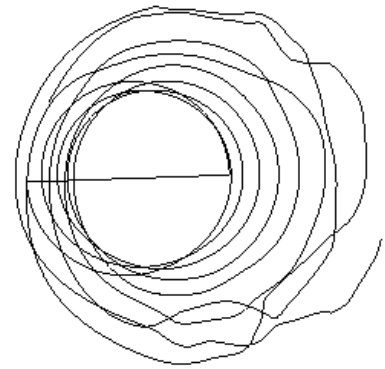


(b)

Figure 4.19: Downwash contours in longitudinal cross section for a two-bladed rotor for $\mu = 0.01$ for $h/R = 0.5$ after one hundred revolutions; (a) lifting surface model, $\alpha_0=10^\circ$, $A = 6$, $h/R = 0.5$, (b) lifting line model.



(a)



(b)

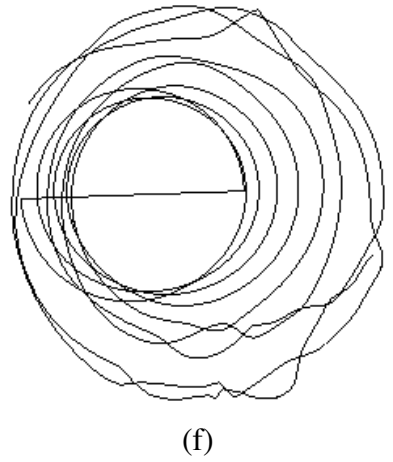
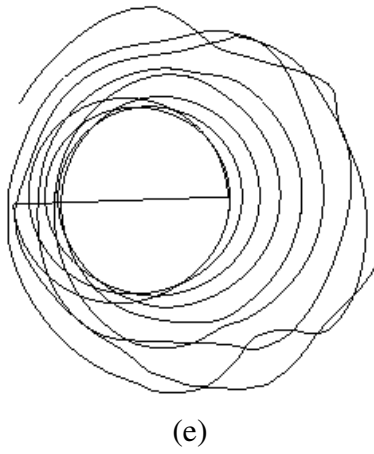
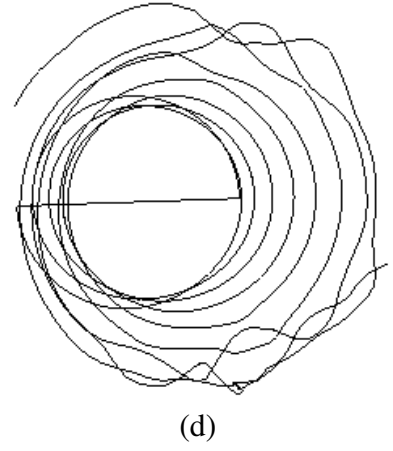
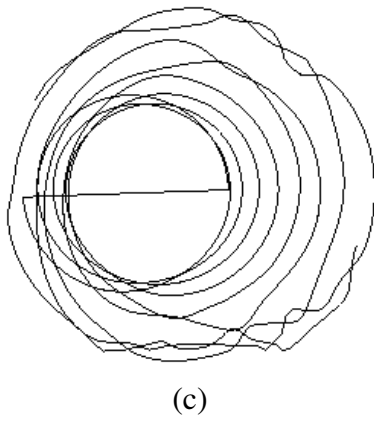
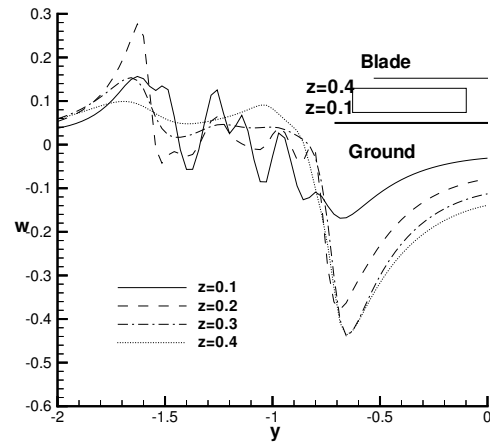
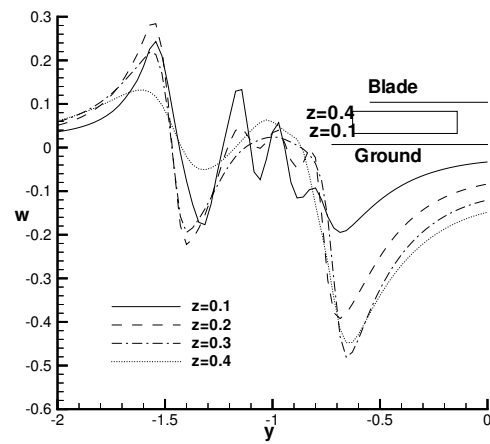


Figure 4.20: Top view of the tip-vortex trajectory of a two-bladed rotor in ground effect in forward flight $\mu = 0.03$ for $h/R = 0.5$ after (a) 10 revolutions, (b) 30 revolutions, (c) 50 revolutions, (d) 70 revolutions, (e) 90 revolutions, (f) 100 revolutions, $\alpha_0=10^\circ$, $A = 6$, $h/R = 0.5$.



(a)



(b)

Figure 4.21: Downwash distribution along the blade for a two-bladed rotor for $\mu = 0.03$ for $h/R = 0.5$ after 100 revolutions; (a) lifting surface model, $\alpha_0=10^\circ$, $A = 6$, $h/R = 0.5$, (b) lifting line model.

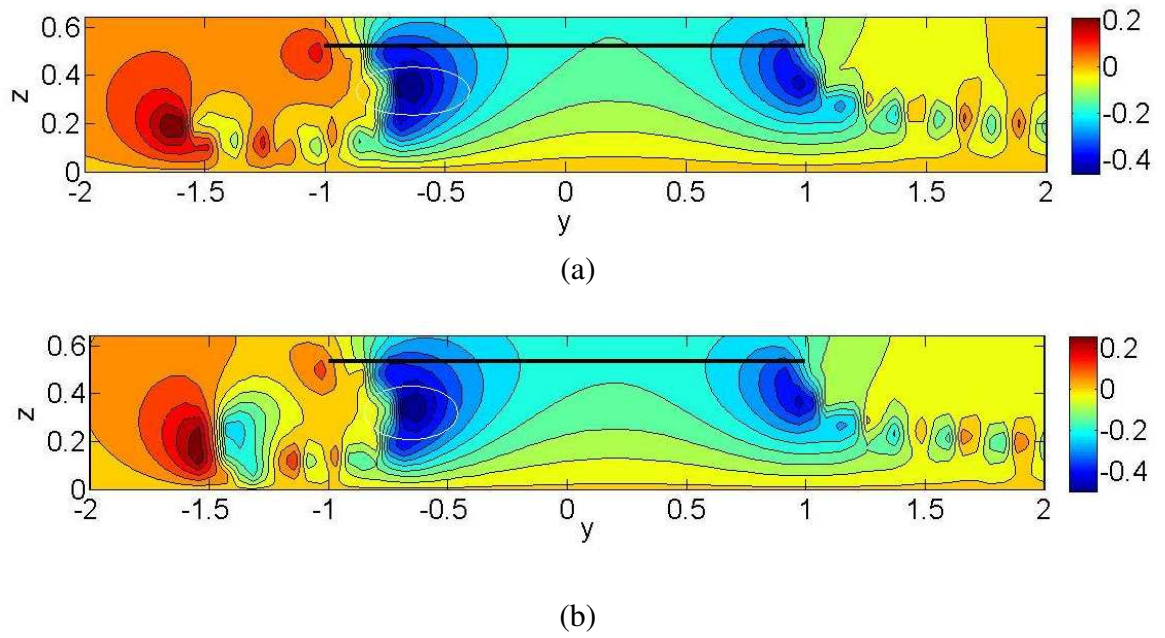


Figure 4.22: Downwash contours in longitudinal cross section for a two-bladed rotor for $\mu = 0.03$ for $h/R = 0.5$ after one hundred revolutions; (a) lifting surface model, $\alpha_0=10^\circ$, $A = 6$, $h/R = 0.5$, (b) lifting line model.

	Expt		Model(LS)	
Vortex	y	z	y	z
1	-0.945	0.532	-0.951	0.578
2	-0.822	0.444	-0.687	0.469
3	-0.805	0.144	-0.722	0.204
4	-0.987	0.099	-	-
5	-1.051	0.102	-1.050	0.138

Table 4.1: Comparison of ground vortex coordinates in computation and experiment; $h/R = 0.72$, two-bladed rotor, $\mu = 0.03$.

results is depicted using contours of the downwash after periodicity (100 revolutions) when the blade is at the zero azimuth on the longitudinal section plane being compared. The experimental flow field is a snapshot of the flow field after periodicity is attained when the blade is at the zero azimuthal position. Figure 4.23(a) shows the ground vortex formed in the computational results. Figure 4.23 (b) shows the corresponding plot for the experimental results. The corresponding vortices in the computational flow field have been circled. As can be seen from the Figure, their positions and sizes match very closely and the comparison looks very good. However, the computations have not been able to obtain one of the vortices.

The positions of the vortices obtained using the lifting line and lifting surface models are compared in Table 4.2. There is not much difference in the values obtained from these two models.

The downwash profile of the flow field for the experimental conditions at $\mu = 0.03$ can be seen in Figure 4.24. The formation of the vortices can be more clearly noticed from this

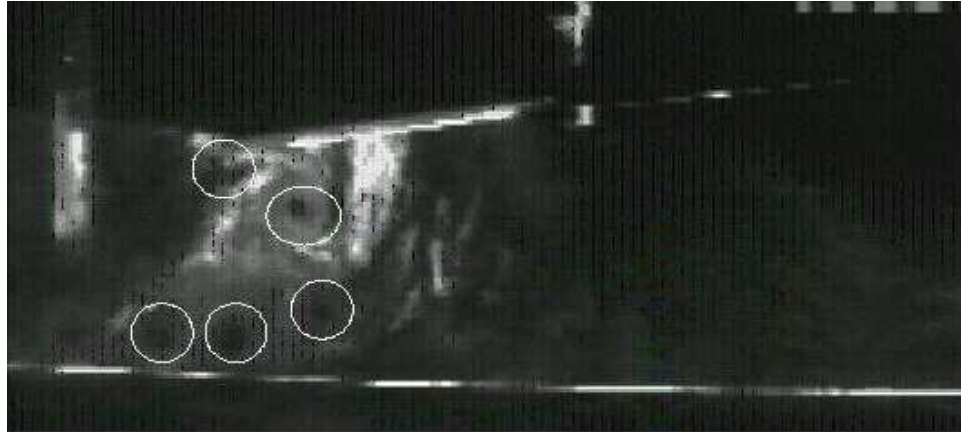
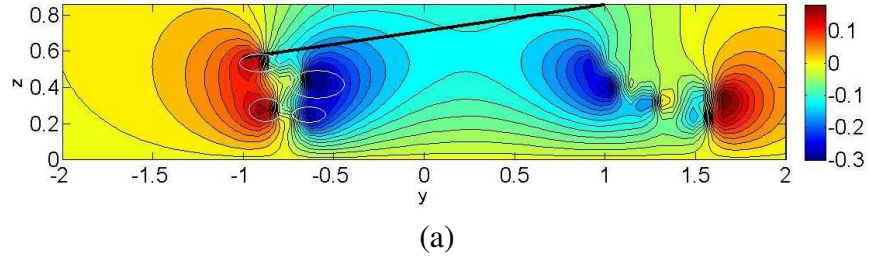


Figure 4.23: Rotor wake recirculation phenomenon at $\mu = 0.03$, $h/R = 0.72$, two-bladed rotor (a) Computational Result (b) Experimental result.

Figure. The vortex positions correspond to the positions midway between the maximum and minimum of the downwash.

Figure 4.25 shows the comparison between the ground vortex phenomenon in the computations and the experiments for an advance ratio $\mu = 0.04$. This Figure is similar to the one for $\mu = 0.03$.

The power frequency spectrum of the downwash has also been compared with the experimental results obtained from Georgia Tech in Figure 4.26. As can be seen from the figure, a large low frequency component can be observed in both the experimental as

	Model(LL)		Model(LS)	
Vortex	y	z	y	z
1	-0.960	0.557	-0.951	0.578
2	-0.711	0.459	-0.687	0.469
3	-0.711	0.216	-0.722	0.204
4	-1.11	0.178	-1.050	0.138

Table 4.2: Comparison of ground vortex coordinates in computations obtained using lifting surface and lifting line models; $h/R = 0.72$, two-bladed rotor, $\mu = 0.03$.

well as the computational results indicating certain long time period characteristics of the downwash which is absent in the OGE calculations. The most dominant low frequency component in both experimental and computational results can be seen as less than 10Hz indicating a very long time period.

The downwash power frequency spectrum obtained by lifting line and lifting surface models has been compared in Figure 4.27. The two Figures look alike qualitatively but there are differences in the magnitude of the power with the power in the lifting surface case being slightly less. A low frequency/long time period component is present in both the results.

4.3 Transient Velocity Variations

RMS Velocity contours have been obtained around the main rotor plane at different azimuthal positions. These computations have been made to identify the plane with the maximum deviation in velocities and thus contributing to the handling qualities problems. 30 points in the axial direction from -0.3 to 0.3 and 60 points in the radial direction from 0.75 to 1.5 have been taken for the grid on each plane.

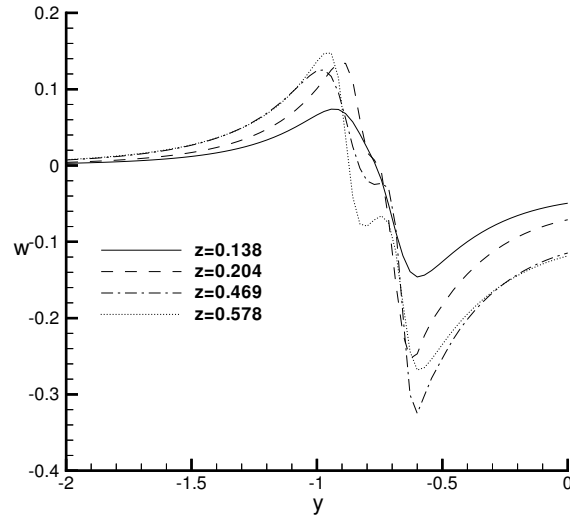


Figure 4.24: Downwash distribution along the blade for the experimental parameters at $\mu = 0.03$, $A = 5.33$, $h/R = 0.72$, two-bladed rotor, tilt = 10° .

Lifting surface model for the blade has been used to compute all the velocities. A single-bladed rotor at a non-dimensional height of 0.72 has been used. Both hover and forward flight results have been obtained. Figure 4.28 shows the RMS values of the velocities (swirl) for the case of hover. Planes at azimuthal locations of 0° , 15° , 30° and 45° on the advancing side of the main rotor disk have been considered. It can be seen that all the contours are identical and the RMS values at all the planes are the same. The reason behind this behavior is the symmetric nature of the wake in the case of a hovering rotor. The maximum non-dimensional RMS velocity value is 0.0094 and occurs on the rotor disk plane at a radial location of around 0.9. Another local maximum occurs at the same height from the ground as the actual maximum but at a radial location of around 1.05. The velocities on the planes on the retreating side of the main rotor as well as on any other azimuthal location

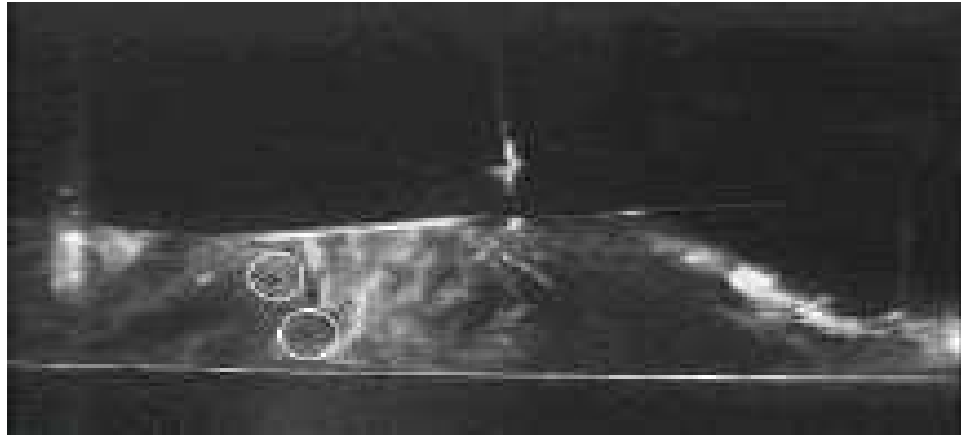
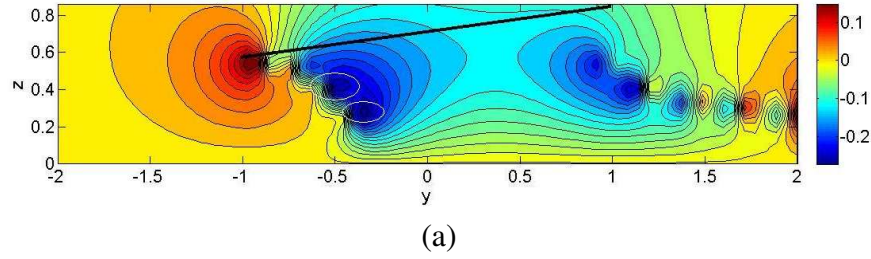
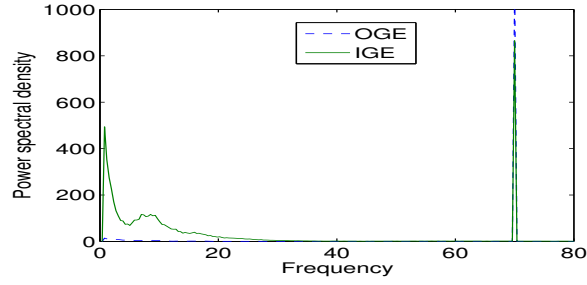


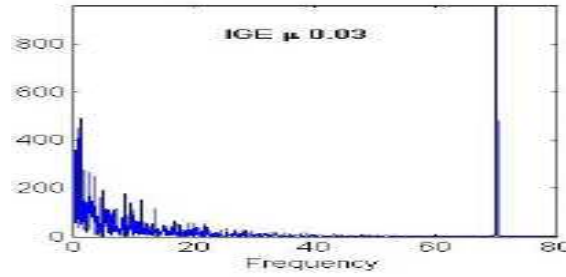
Figure 4.25: Rotor wake recirculation phenomenon at $\mu = 0.04$, $h/R = 0.72$, two-bladed rotor (a) Computational Result (b) Experimental result.

are also expected to exhibit similar behavior. The magnitudes of the RMS swirl velocities obtained using the lifting surface model are almost the same as those obtained using the lifting line model in Figure 3.29.

Figure 4.29 shows the RMS velocity contours(swirl) for the case of low speed forward flight with $\mu = 0.01$ on the advancing side of the rotor disk. The RMS local maxima are located at 0.9 radial location and $z = 0.1$, $z = 0.25$ at the 15° and 30° azimuthal locations. There is an increase in the magnitude of the RMS maxima from 15° to 30° . At 45° azimuthal location there is very slight shift of the locations of the RMS maxima inboard



(a)



(b)

Figure 4.26: Downwash power frequency spectrum IGE, $\mu = 0.03$, lifting surface model, $y = -1$, $z = 0.831$, $x = 0$, (a) Computational results (b) Experimental results.

with an increase in the magnitude. As the angle of the azimuthal plane is further increased to 60° , there is further shift of the maxima locations inboard but this time with a decrease in the magnitudes. As the angle is further increased to 75° and 90° , the magnitude of the RMS swirl further reduces and the location of the maximum moves inboard. Hence the plane at 45° azimuthal location experiences the maximum RMS deviation in swirl. The magnitudes of the RMS swirl velocities obtained using the lifting surface model at $\mu = 0.01$ are slightly higher to the ones obtained using the lifting line model for the same parameters in Figure 3.30.

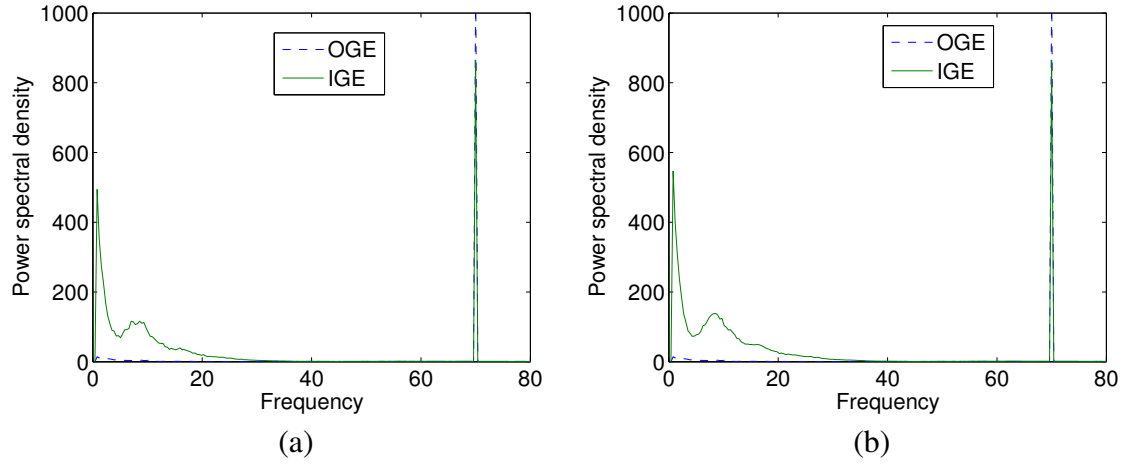
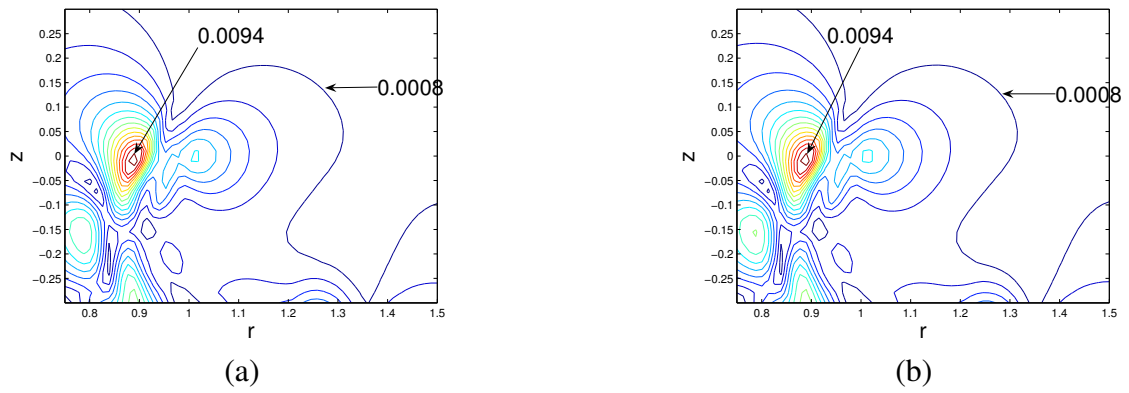


Figure 4.27: Comparison of the downwash power frequency spectrum obtained at $y = -1$, $z = 0.831$, $x = 0$, using (a) lifting surface model (b) lifting line model.



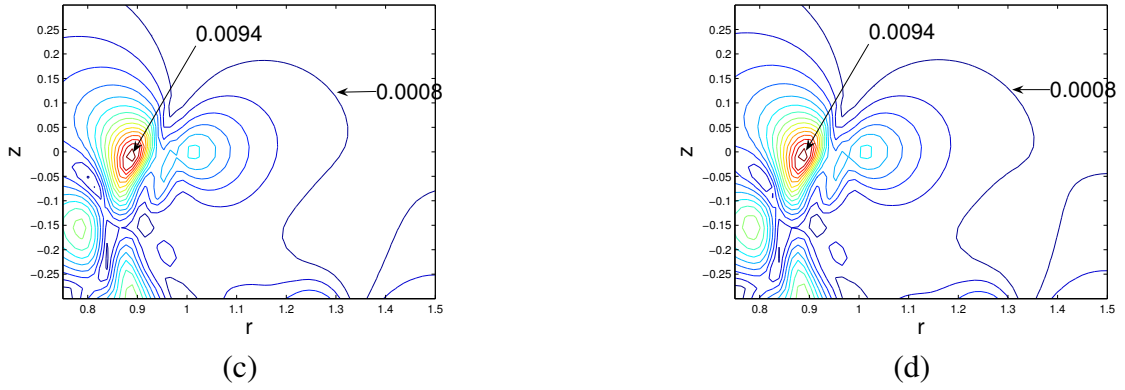
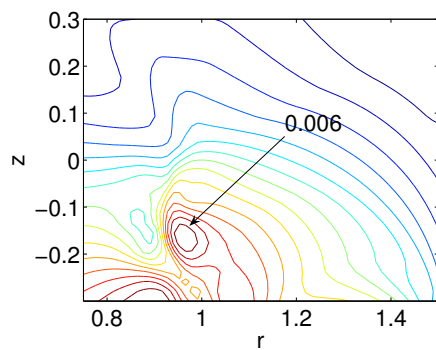


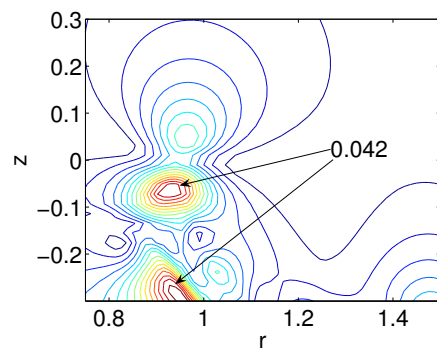
Figure 4.28: RMS swirl contours for hover on the advancing side at azimuthal locations (a) 0 degrees (b) 15 degrees (c) 30 degrees (d) 45 degrees, $h/R = 0.72$, $A = 6$, $\alpha_0 = 10^\circ$.

Figure 4.30 shows the RMS contours(swirl) on the retreating side of the main rotor disk. The behavior of the velocities is similar to that seen on the advancing side. The maximum RMS occurs at the same location as on the advancing side. Until the 45 degrees azimuthal location is reached, the location of the maximum RMS swirl remains the same but after 45 degrees, it starts shifting inboard and reducing in magnitude. At 90 degrees azimuthal location, there is very little deviation on the plane being considered. The magnitudes are almost the same as those on the advancing side.

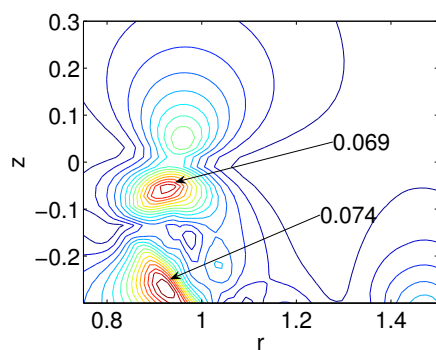
Figure 4.31 shows the RMS deviations of the downwash from the mean on different planes around the rotor disk. As can be seen from Figure 4.31 there are two local maxima at locations $r=0.9, z=0.02$ and $r=0.9, z=0.23$ on all the planes being considered. There is very little change in the location of these local maxima with change in the azimuthal location. But the magnitudes of these maxima increase with increase in the angle associated with the plane from 0° to 75° with a slight decrease as we move from 75° to 90° . The value of the maximum RMS deviation increases from 0.074 at 15° to 0.094 at 75° .



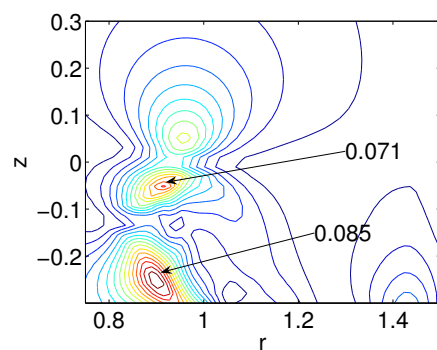
(a)



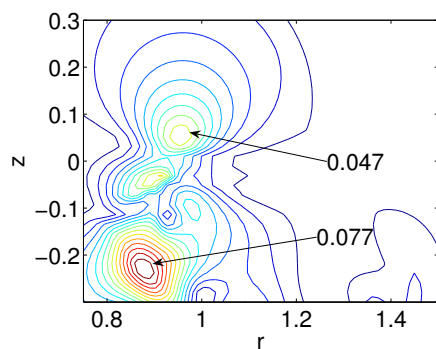
(b)



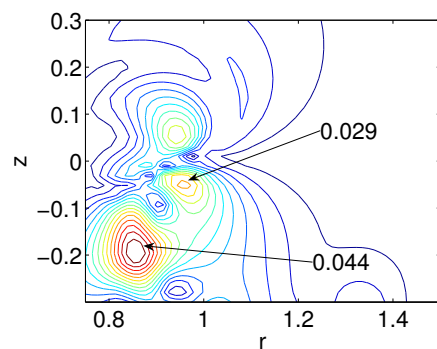
(c)



(d)



(e)



(f)

Figure 4.29

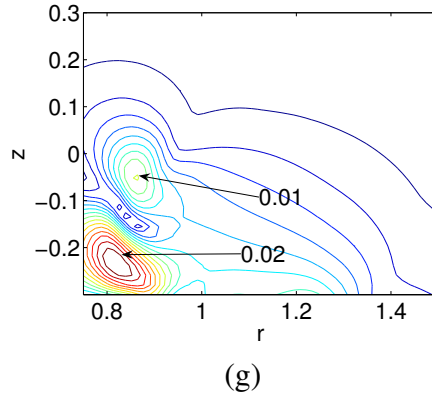


Figure 4.29: RMS swirl contours for forward flight $\mu = 0.01$ on the advancing side at azimuthal locations (a) 0 degrees (b) 15 degrees (c) 30 degrees (d) 45 degrees (e) 60 degrees (f) 75 degrees (g) 90 degrees, $h/R = 0.72$, $A = 6$, $\alpha_0 = 10^\circ$.

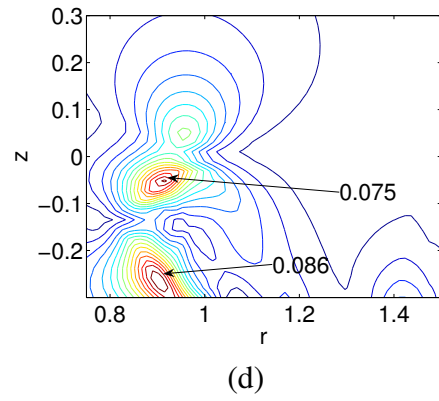
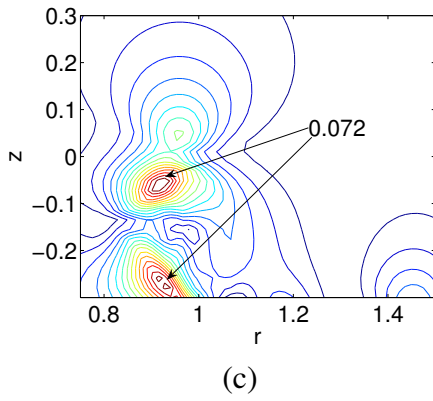
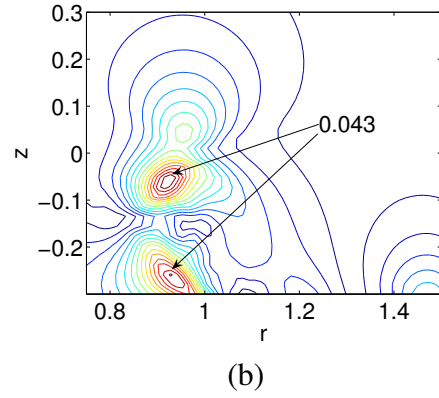
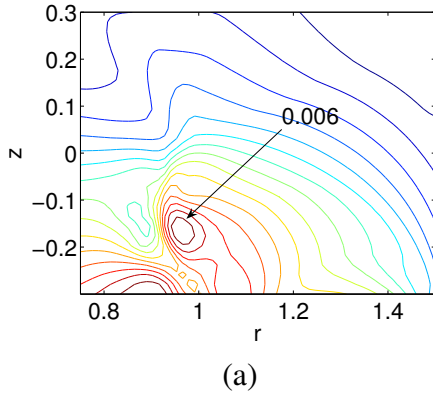
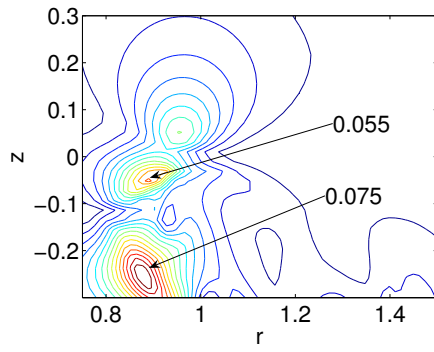
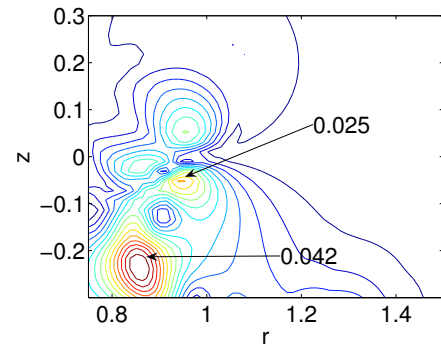


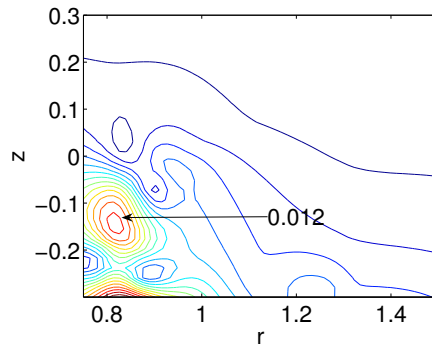
Figure 4.30



(e)

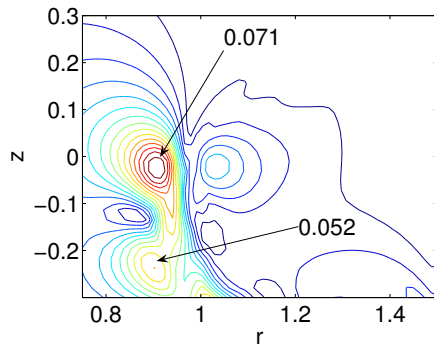


(f)

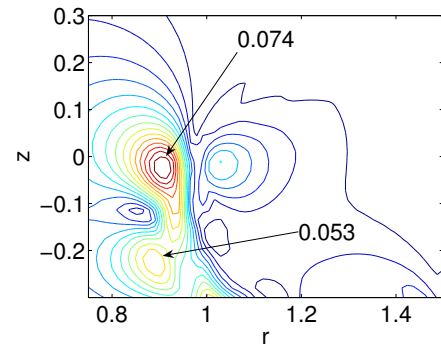


(g)

Figure 4.30: RMS swirl contours for forward flight $\mu = 0.01$ on the retreating side at azimuthal locations (a) 0 degrees (b) 15 degrees (c) 30 degrees (d) 45 degrees (e) 60 degrees (f) 75 degrees (g) 90 degrees, $h/R = 0.72$, $A = 6$, $\alpha_0 = 10^\circ$.

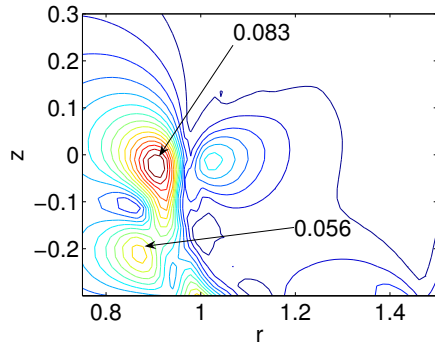


(a)

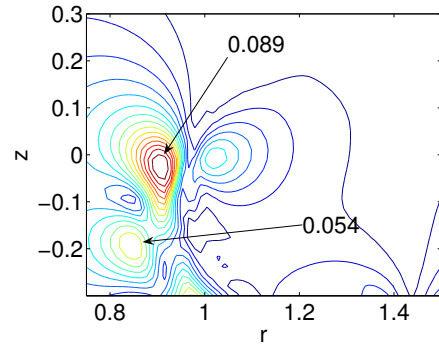


(b)

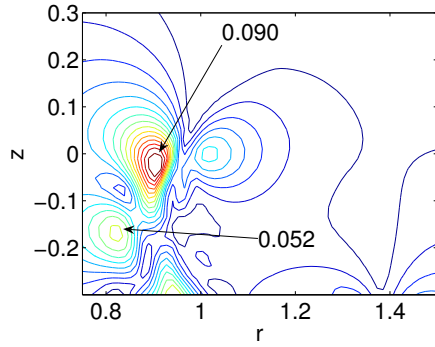
Figure 4.31



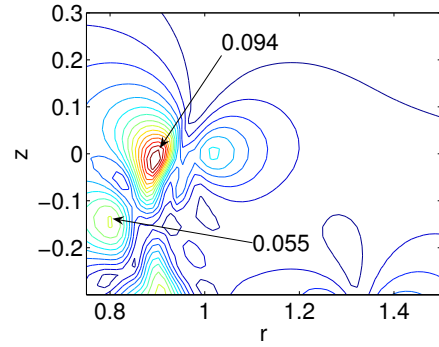
(c)



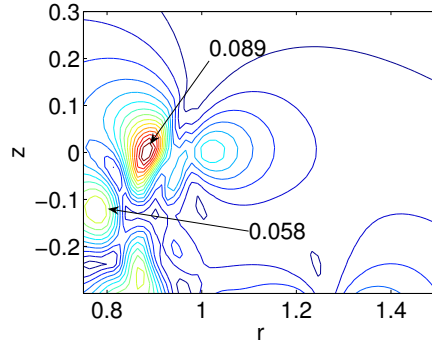
(d)



(e)



(f)

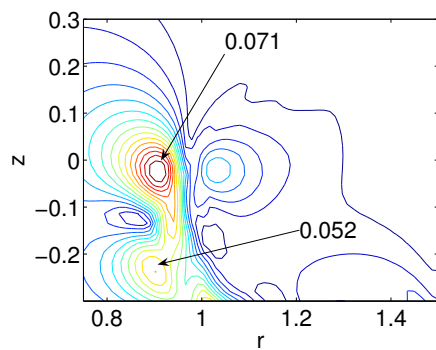


(g)

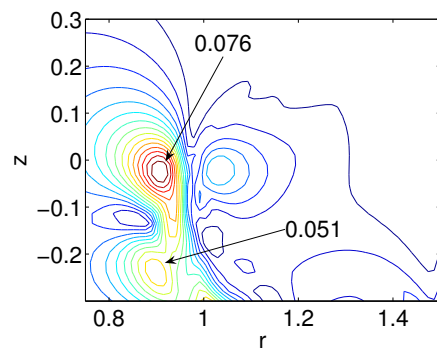
Figure 4.31: RMS downwash contours for forward flight $\mu = 0.01$ on the advancing side at azimuthal locations (a) 0 degrees (b) 15 degrees (c) 30 degrees (d) 45 degrees (e) 60 degrees (f) 75 degrees (g) 90 degrees, $h/R = 0.72$, $A = 6$, $\alpha_0 = 10^\circ$.

Figure 4.32 shows the RMS deviations of downwash on the retreating side of the rotor disk. The deviations in the downwash increase with increase in the angle of the plane being considered until 75 degrees. There is a small decrease from 75 to 90 degrees. The RMS deviation occurs at around $r = 0.9$ close to the rotor disk plane on all the planes being considered. This is interesting considering the fact that the location of the maximum RMS swirl shifts inboard with increase in the angle of the plane.

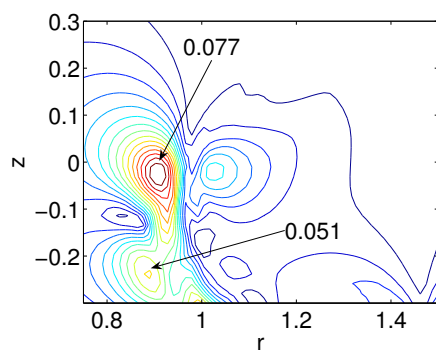
Figure 4.33 shows the RMS contours(swirl) on the advancing side of the main rotor disk. At 0° azimuthal location the RMS deviation is very less and is the maximum at $r = 1.11, z = -0.15$. At 15° , the RMS swirl increases considerably in magnitude and the intensity shifts inboard. The maximum occurs at $r = 1.05$ just below the rotor disk(tail rotor plane) and at $r = 1.15, z = -0.3$. As the angle of azimuthal location is increased to 30° , the magnitude of the RMS swirl increases further with the locations of the maximums remaining almost the same. At 45° azimuthal location, there is more increase in the RMS magnitude to 0.084 occurring at $r = 1.02, z = -0.27$. At 60° , there is slight decrease in the maximum RMS magnitude and there is shift of the maximum RMS location slightly inboard and in the upward direction(towards the rotor disk). On the plane at 75° there is steep decrease in the RMS magnitude and there is further shift of the maximum location inboard. At 90° , the RMS is almost zero on the entire plane except near the rotor disk. Hence it can be inferred that the maximum deviation in the swirl component of velocity occurs on the plane at 45° azimuthal location. This implies that the maximum unsteadiness in swirl is encountered by a helicopter moving at 45° angle(Flight which is right in between a normal straight flight and a complete sideward flight). Again, compared to the lifting



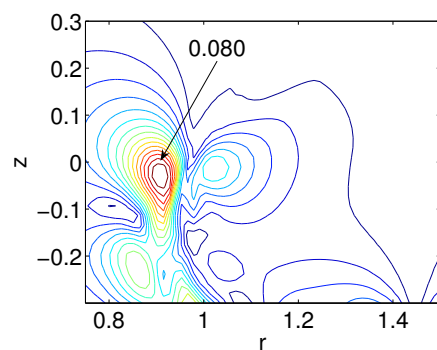
(a)



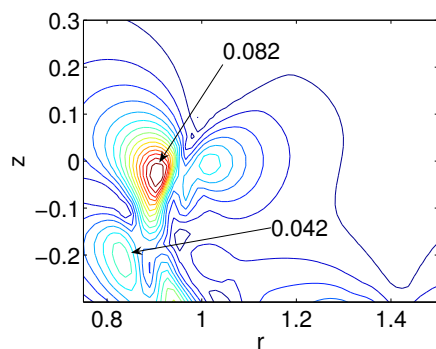
(b)



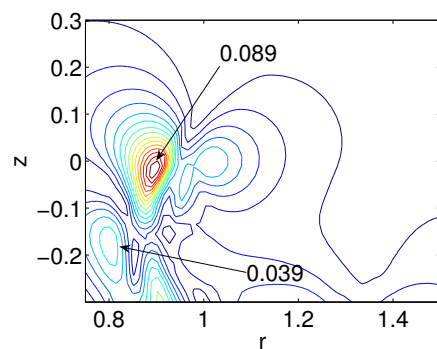
(c)



(d)



(e)



(f)

Figure 4.32

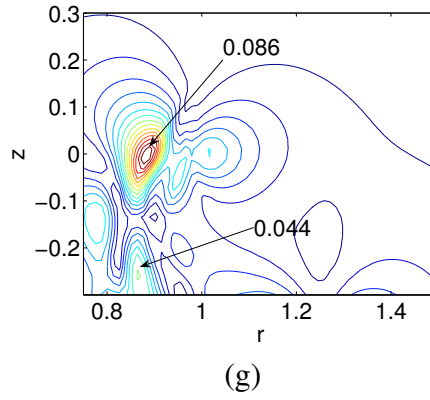


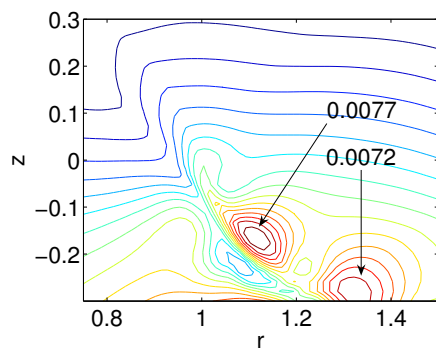
Figure 4.32: RMS downwash contours for forward flight $\mu = 0.01$ on the retreating side at azimuthal locations (a) 0 degrees (b) 15 degrees (c) 30 degrees (d) 45 degrees (e) 60 degrees (f) 75 degrees (g) 90 degrees, $h/R = 0.72$, $A = 6$, $\alpha_0 = 10^\circ$.

line model in Figure 3.34, the magnitudes of the swirl velocities obtained using the lifting surface model are slightly higher.

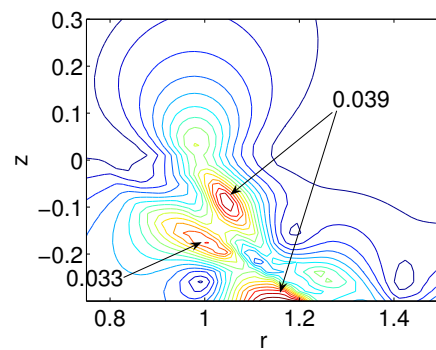
Figure 4.34 shows the RMS contours (swirl) on the retreating side of the main rotor disk. Although the behavior of the RMS swirls with azimuthal angle of the plane is similar to that on the advancing side, there are variations in the locations of the local maxima of the RMS deviations. On the 60° plane, there is a local maxima at $r = 1.4$, and $z = -0.25$ which does not exist on the advancing side. Also the locations of the RMS maxima are slightly outboard on the retreating side.

Figure 4.35 shows the RMS deviation of the downwash from its mean value on different planes around the rotor disk. At 15° azimuthal location, there are two local maxima, one near the blade tip on the rotor disk plane and the other at $r = 1.1$, $z = -0.3$ with magnitudes 0.061 and 0.071 respectively. On the 30° plane, there is a slight shift in the locations of the two local maxima to the left (inboard) and toward the rotor disk. The magnitudes remain almost the same. At 45° location, the locations of the local maxima remain almost the same but the magnitude of the maxima near the blade tip increased to 0.08 while the value of the other maxima reduced to 0.059. As we move further in the direction of the advancing side to 60° , the magnitude of the RMS maximum near the blade tip increases to 0.092. At 75° this value reduces to 0.077 and further reduced to 0.067 at 90° .

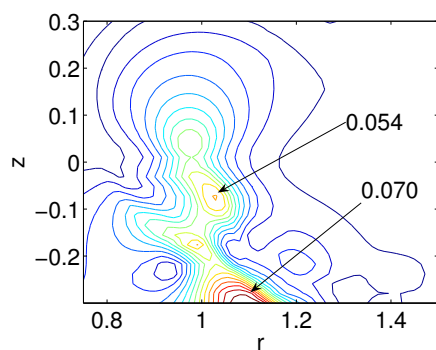
Figure 4.36 shows the RMS deviation of downwash from the mean on the retreating side of the rotor disk. It is interesting to note that there is very little change in the magnitude of the maximum RMS deviation between 0 and 45 degrees. There are changes where the maximum occurs. There is a large increase between 45 and 60 degrees with a slight further increase between 60 and 75 degrees. The RMS maximum again reduces at 90 degrees.



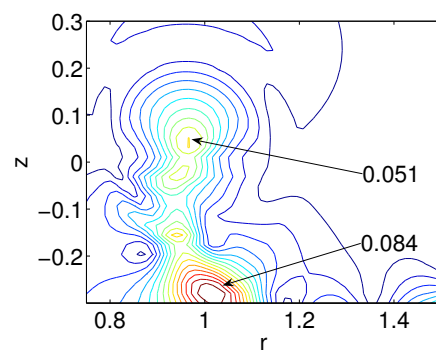
(a)



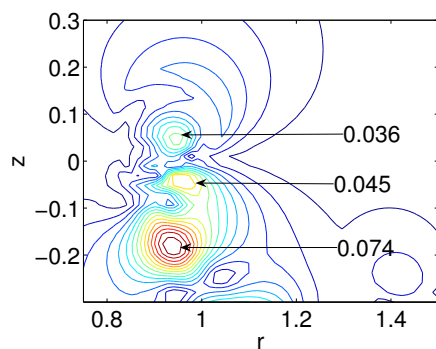
(b)



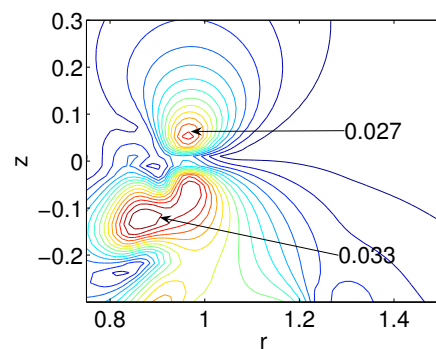
(c)



(d)



(e)



(f)

Figure 4.33

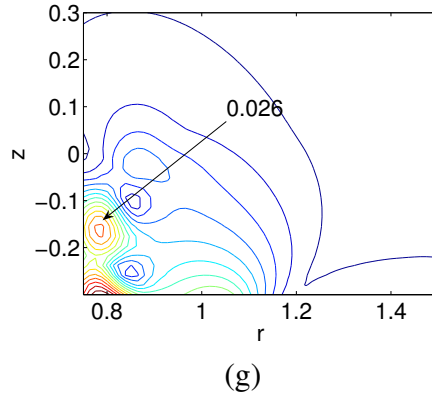


Figure 4.33: RMS swirl contours for forward flight $\mu = 0.03$ on the advancing side at azimuthal locations (a) 0 degrees (b) 15 degrees (c) 30 degrees (d) 45 degrees (e) 60 degrees (f) 75 degrees (g) 90 degrees, $h/R = 0.72$, $A = 6$, $\alpha_0 = 10^\circ$.

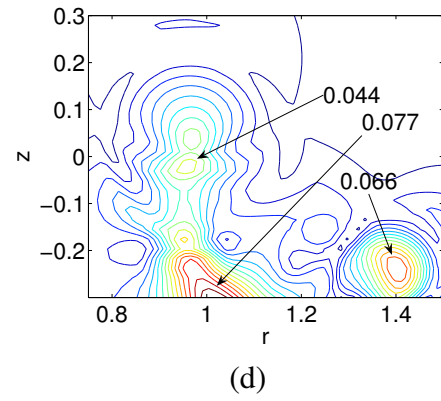
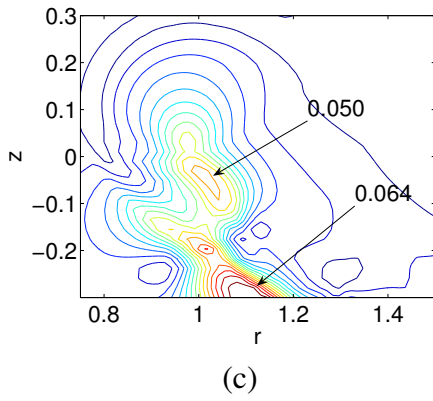
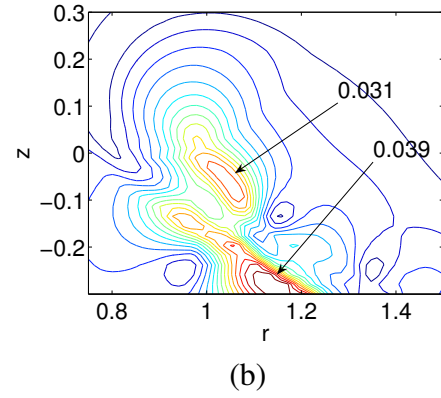
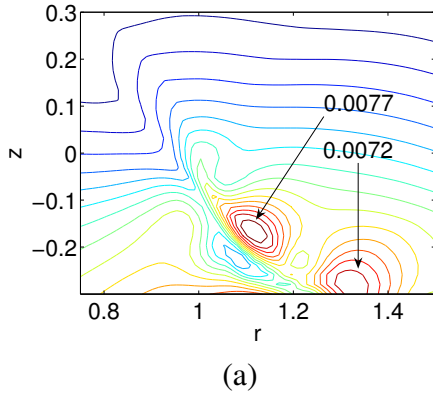


Figure 4.34

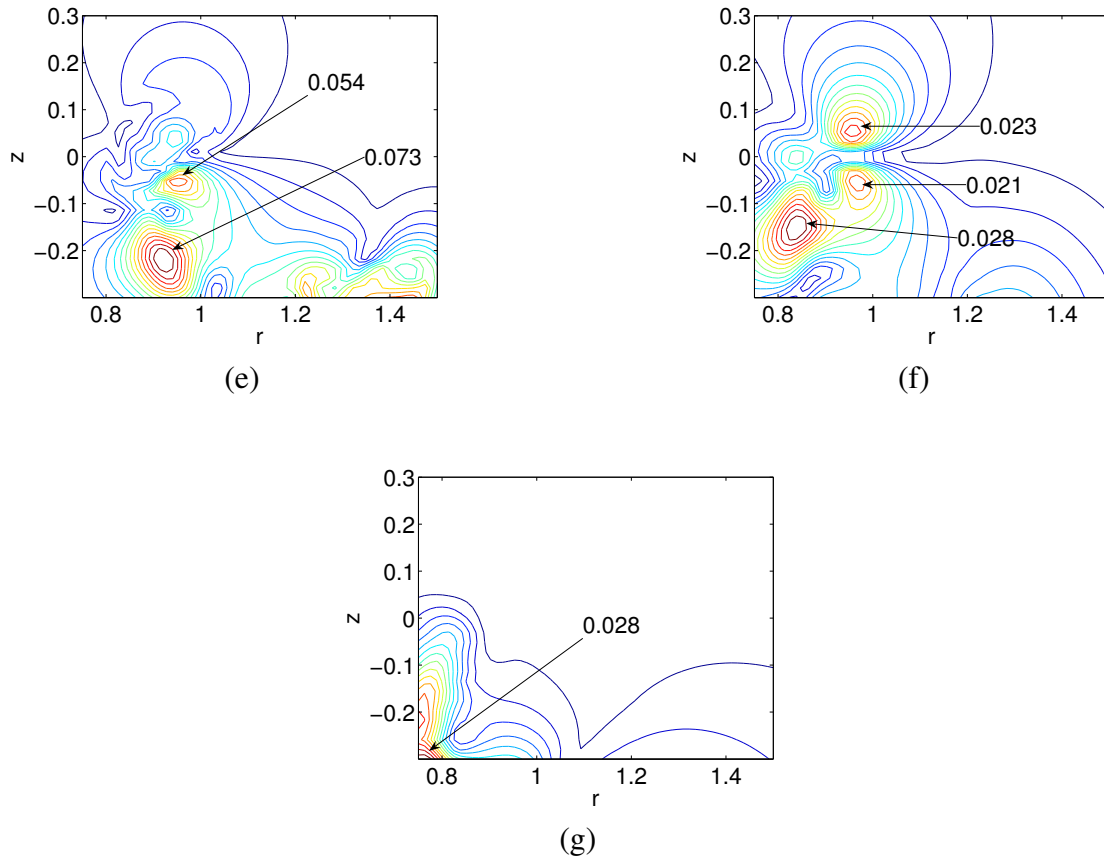


Figure 4.34: RMS swirl contours for forward flight $\mu = 0.03$ on the retreating side at azimuthal locations (a) 0 degrees (b) 15 degrees (c) 30 degrees (d) 45 degrees (e) 60 degrees (f) 75 degrees (g) 90 degrees, $h/R = 0.72$, $A = 6$, $\alpha_0 = 10^\circ$.

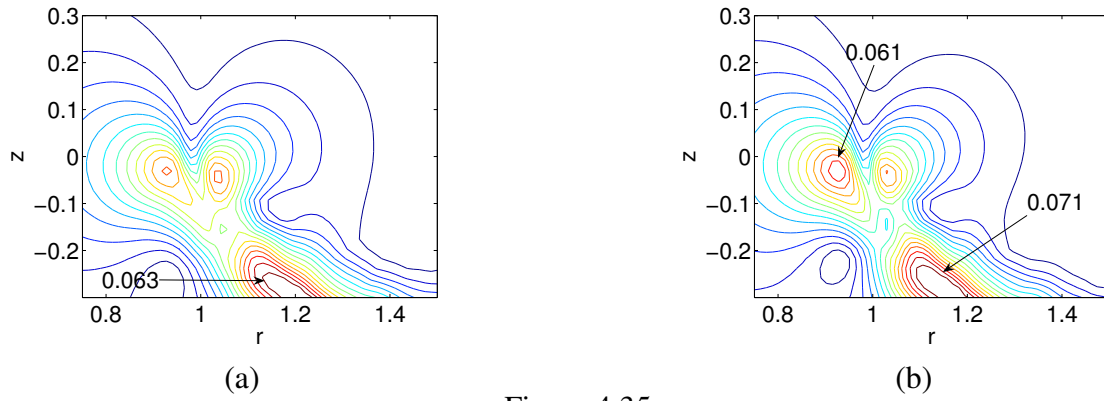


Figure 4.35

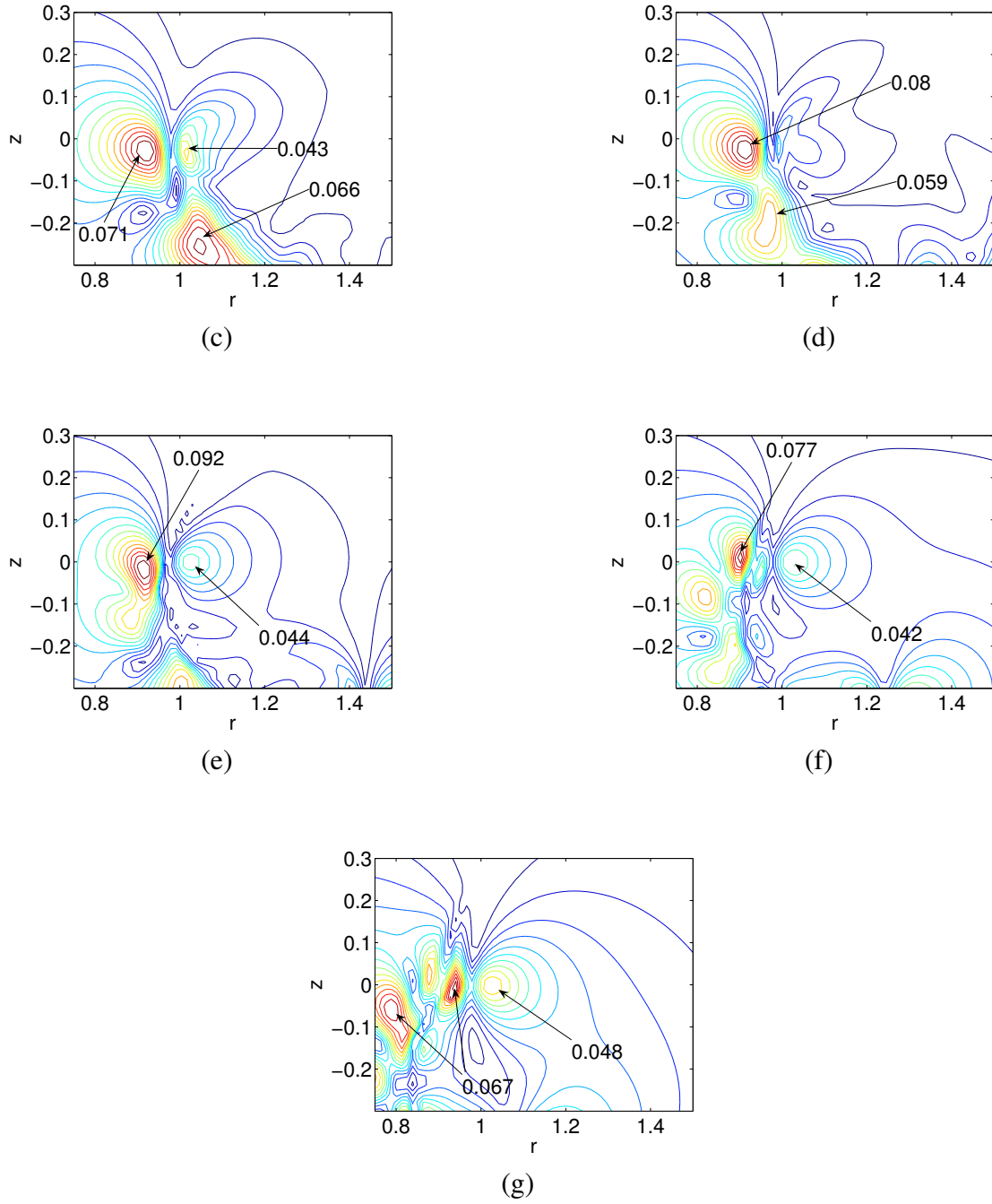
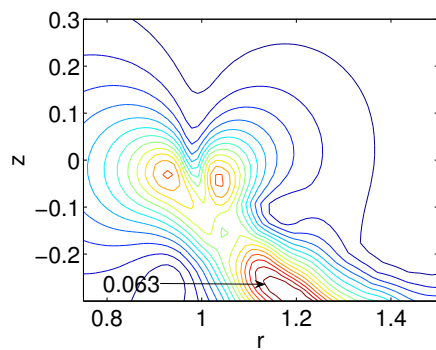
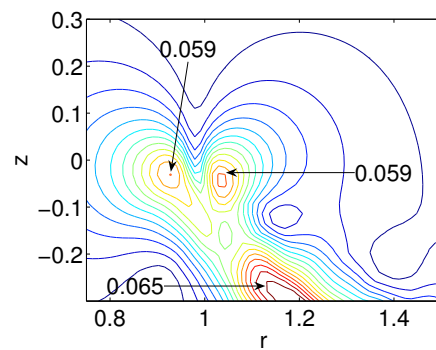


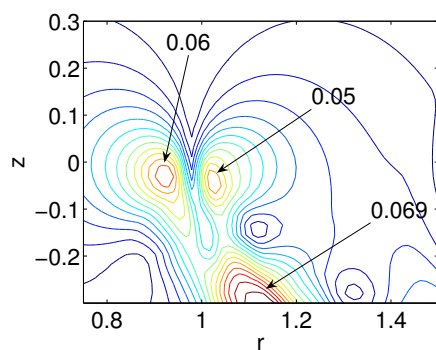
Figure 4.35: RMS downwash contours for forward flight $\mu = 0.03$ on the advancing side at azimuthal locations (a) 0 degrees (b) 15 degrees (c) 30 degrees (d) 45 degrees (e) 60 degrees (f) 75 degrees (g) 90 degrees, $h/R = 0.72$, $A = 6$, $\alpha_0 = 10^\circ$.



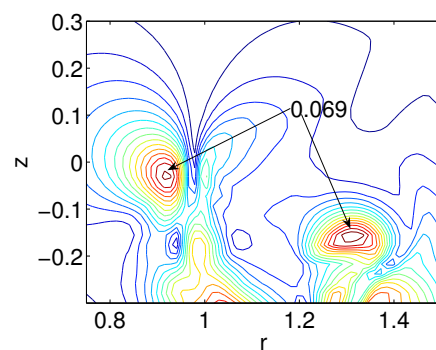
(a)



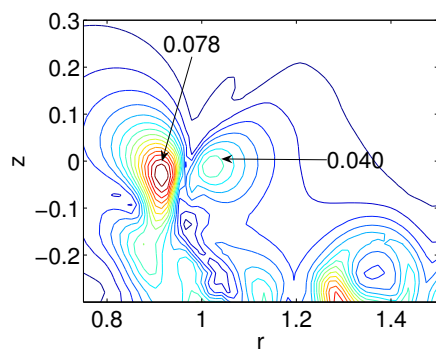
(b)



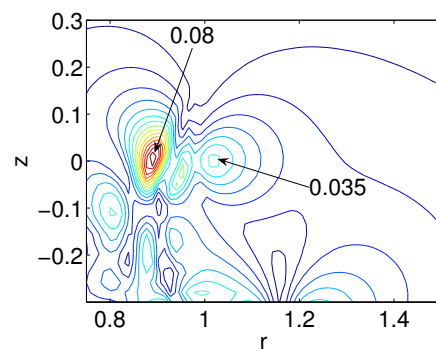
(c)



(d)



(e)



(f)

Figure 4.36

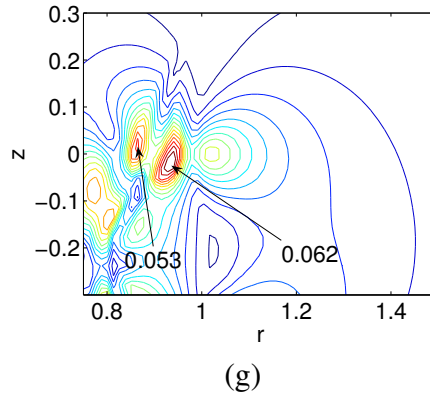


Figure 4.36: RMS downwash contours for forward flight $\mu = 0.03$ on the retreating side at azimuthal locations (a) 0 degrees (b) 15 degrees (c) 30 degrees (d) 45 degrees (e) 60 degrees (f) 75 degrees (g) 90 degrees, $h/R = 0.72$, $A = 6$, $\alpha_0 = 10^\circ$.

4.4 Summary

The velocities induced by the tip-vortex when a lifting surface model is used for the blade are smaller compared to those obtained using the lifting line model. Also, for a single-bladed rotor in low speed forward flight, periodicity is attained even close to the ground while this is not the case with the lifting line model. The size of the ground vortex formed here is slightly smaller here. The magnitudes of unsteadiness in the tail rotor swirl experienced is almost the same as that of the lifting line model. The behavior of the RMS velocities with the azimuth is also similar. The lifting surface models serves to simulate low aspect ratio blades which are used mostly in the experiments. On the other hand, the lifting line model is a good approximation to model the actual full scale blade since actual helicopter blades typically have aspect ratios of around 15-20. Nevertheless, there are certain other disadvantages associated with the lifting line model; the shape of the

blade is a line and blade-vortex interactions cannot be accounted for. These problems do not occur with the lifting surface model. The computational time required for the lifting surface model is only slightly higher than the lifting line model since just twenty panels are enough to model the blade. Hence, judging by all these factors, the lifting surface model is the better choice for most cases.

CHAPTER 5

Loads

5.1 Introduction

This chapter deals with the forces and moments acting on the rotor blade. Both lifting line and lifting surface theories can be used to compute the forces on the rotor disk. When the lifting surface theory is used, since the bound circulation distribution over the entire blade is obtained, the vortex theory alone is enough to compute the loads. For the case of lifting line theory, since only the tip-vortex circulation is calculated in this study, a combination of vortex theory and blade element theory can be used to predict the forces and moments (lifting line theory). The main disadvantage to using the blade element theory alone is that it does not predict the induced velocity near the rotor disk.

Blade element theory provides the necessary means to predict the aerodynamic forces and moments acting on a rotor blade in forward flight. Similar to momentum theory, it is necessary to determine the magnitude and direction of the airflow in the immediate vicinity of the blade element under consideration. Once these velocities are known, the calculation of the forces and moments can be performed using two-dimensional airfoil characteristics. The blade element approach is a powerful tool for the aerodynamic analysis of helicopter

rotors [33]. It forms the basis for nearly all modern computational methods used for performance, air-loads and aeroelastic analysis. The basic ideas consists of representing the airloads along the blade span as two-dimensional sections of the blade and integrating their effect to find the performance of the rotor as a whole. This allows flexibility in the rotor analysis and also allows the effects of airfoil shape to be examined along with some elementary effects associated with nonlinear aerodynamics and stall. Although the induced velocity distribution near the rotor disk can be modeled with a combination of the blade element theory and momentum theory, the induced velocity distribution becomes considerably more complicated in low speed forward flight and in descent and the use of vortex methods provides improved fidelity necessary under these conditions.

The velocity at the inflow boundary to the rotor depends crucially on the structure of the wake flow. Consider the rotation of the blades started from rest. In the initial stages of the motion, the velocity at the inflow rotor-disk depends on the local flow near the rotor blades. As time passes, the vortex sheet and the tip-vortex shed from the rotor blades begin to extend far below the rotor-disk, forming the rotor wake. At this point, the inflow velocity at the rotor-disk becomes critically dependent on the precise placement of the wake. This is why the calculation of the rotor wake is crucial in calculating the loads on the rotor blades. Vortex methods can predict the unsteady effects of the rotor wake on the blades and on the airframe, and this is discussed next.

In this work, to compute the thrust, drag and power coefficients, the wake structure is advanced in time until periodicity is attained. The coefficient that is being computed is taken as the criterion for periodicity. In general, it takes 20 revolutions for a single-bladed

rotor in hover to attain periodicity while it takes 45 revolutions for a two-bladed rotor in hover. In forward flight it takes a slightly higher number of revolutions to attain periodicity.

5.2 Computation of Loads Using Lifting Line Theory in Hover

Since the blade element theory assumes the local flow at a given spanwise location is two dimensional, it is appropriate to discuss forces and moments due to a two-dimensional flow past an airfoil. Figure 5.1 shows a sketch of the flow environment and aerodynamic forces at a representative blade element on the rotor. The aerodynamic forces are assumed to arise solely from the velocity and the angle of attack normal to the leading edge of the blade section. The induced angle of attack, ϕ , arises because of the velocity induced by the rotor and its wake. Therefore, the induced velocity serves to modify the direction of the relative flow velocity vector and therefore, alters the angle of attack at each blade element from its 2-D value. This induced velocity also inclines the local lift vectors, which by definition act perpendicular to the resultant velocity vector at the blade element and, therefore, provide a source of induced drag and the source of induced power required at the rotor shaft.

The resultant local flow velocity at any blade element at a radial distance r from the rotational axis has an out-of-plane component $U_P = W$ where W is the induced velocity component normal to the rotor disk due to the wake and an in-plane component $U_T = \Omega r$ parallel to the rotor because of blade rotation, relative to the disk plane. The resultant velocity at the blade element is, therefore,

$$U = \sqrt{U_T^2 + U_P^2}$$

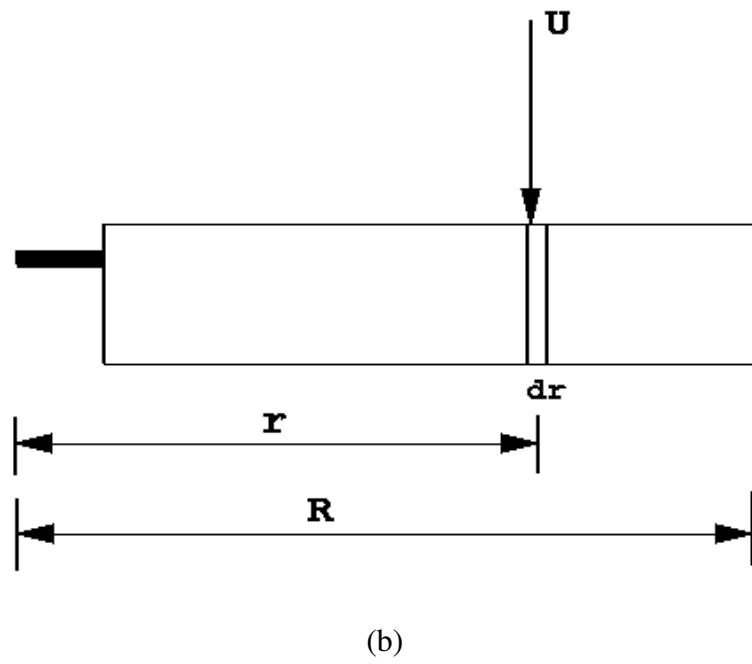
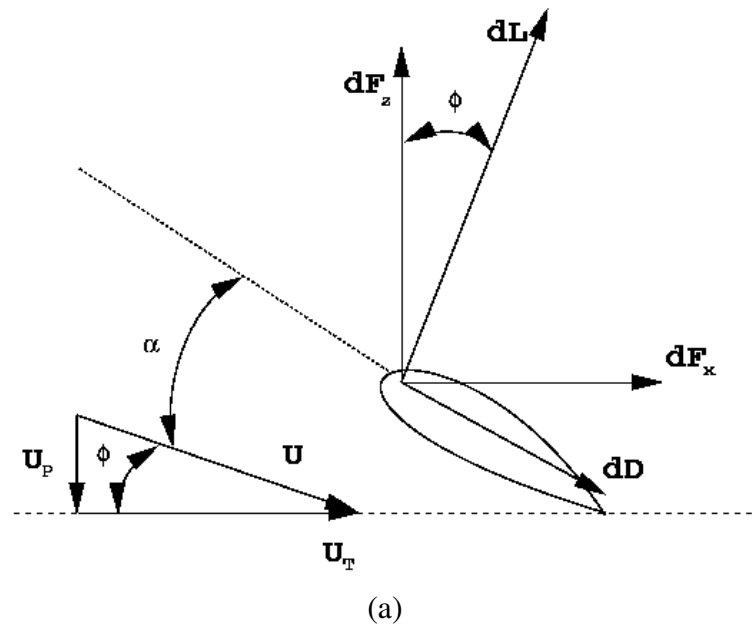


Figure 5.1: Incident velocities and aerodynamic environment at a typical blade element (a) Top view (b) Blade element [33] .

The relative inflow angle at the blade element will be

$$\phi = \tan^{-1} \frac{U_P}{U_T} \sim \frac{U_P}{U_T}$$

Thus the effective angle of attack becomes

$$\alpha = \theta - \phi$$

The resultant incremental lift dL and drag dD per unit span on this blade element are $dL = \frac{1}{2}\rho U^2 c C_l dr$ and $dD = \frac{1}{2}\rho U^2 c C_d dr$, where C_l and C_d are the sectional lift and drag coefficients respectively. The lift dL and drag dD act perpendicular and parallel to the resultant flow respectively. Using Figure 5.1, these forces can be resolved perpendicular and parallel to the rotor disk plane giving

$$dF_z = dL \cos \phi - dD \sin \phi$$

$$dF_x = dL \sin \phi + dD \cos \phi \quad (5.1)$$

Therefore, the contributions to the thrust, torque, and power of the rotor are

$$dT = N_b dF_z, dQ = N_b dF_x r$$

and

$$dP = N_b dF_x \Omega r$$

where N_b is the number of blades comprising the rotor. Substituting the results from dF_x and dF_z from Equation (5.1) gives

$$dT = N_b (dL \cos \phi - dD \sin \phi) \quad (5.2)$$

$$dQ = N_b (dL \sin \phi + dD \cos \phi) r \quad (5.3)$$

$$dP = N_b(dL\sin\phi + dD\cos\phi)\Omega r \quad (5.4)$$

For helicopter rotors, the following simplifying assumptions can be made [33]:

- The out-of-plane velocity U_P is much smaller than the in-plane velocity so that the resultant velocity is approximately equal to U_T .
- The induced angle ϕ is small, so that $\phi = U_P/U_T$.
- The drag is at least one order of magnitude less than the lift, so that the contribution $dD\sin\phi$ is negligible.

Applying these simplifications to the preceding equations results in

$$dT = N_b dL$$

$$dQ = N_b(\phi dL + dD)r$$

$$dP = N_b\Omega(\phi dL + dD)r \quad (5.5)$$

To make things simpler, non-dimensional quantities are introduced by dividing lengths by R and velocities by $\frac{\Omega R}{2\pi}$ where R is the radius of the blade and Ω , the angular velocity and so $y = \frac{r}{R}$ and $\frac{U}{\frac{\Omega R}{2\pi}} = 2\pi y$. The incremental thrust coefficient $dC_T = dT / \rho A (\Omega R)^2$ and the incremental power coefficient $dC_P = \frac{dP}{\rho A (\Omega R)^3}$ where $A = \pi R^2$ is the area of the rotor disk. The incremental thrust coefficient after simplification is given by

$$dC_T = \frac{1}{2} \sigma C_l y^2 dy$$

Similarly, the power coefficient is given by,

$$dC_P = \frac{1}{2} \sigma (\phi C_l + C_d) y^3 dy$$

To find the total thrust coefficient and moment coefficients, the incremental thrust and power quantities derived above must be integrated along the blade from the root to the tip. For a rectangular blade, the thrust coefficient is

$$C_T = \frac{1}{2}\sigma \int_0^1 C_l y^2 dy$$

and the power coefficient is

$$C_P = \frac{1}{2}\sigma \int_0^1 (\phi C_l + C_d) y^3 dy$$

The local blade lift coefficient can be written as

$$C_l = C_{l\alpha}(\theta - \phi)$$

where $C_{l\alpha}$ is the two-dimensional lift-curve slope of the airfoil section comprising the rotor. For an incompressible flow, $C_{l\alpha}$ would have a value close to the thin airfoil result of 2π per radian. Although $C_{l\alpha}$ will take a different value at each blade station because it is a function of local incident Mach number and Reynolds number, an average value can be assumed for the rotor without a serious loss of accuracy. Therefore, the thrust coefficient becomes,

$$C_T = \frac{1}{2}\sigma C_{l\alpha} \int_0^1 (\theta - \phi) y^2 dy$$

The power required is made up of two components, the induced power and profile power. Induced power is the power required to force the air down to keep the rotor flying. Induced power is directly proportional to weight and density altitude. Secondly, we have the profile power requirement to overcome form drag and skin friction that occurs with a rotor blade at a local zero lift condition; in other words, it is the drag of the blade at flat pitch. Look at it as the resistance that results when moving an object through the

air that is producing lift such as rotor blades and vertical or horizontal stabilizers. It is proportional to forward flight speed (squared) and blade pitch. Since we are using an inviscid model, we will only be able to compute the induced power coefficient and not the profile power coefficient. The computation of the profile power requires the knowledge of the drag coefficient which is beyond the scope of this work. Under these assumptions, the induced power coefficient is given by,

$$C_{P,i} = \frac{1}{2} \sigma C_{l\alpha} \int_0^1 \phi(\theta - \phi) y^3 dy$$

Thus to obtain the thrust, drag and power coefficients, the induced angle of attack at various sections of the blade is needed. The induced angle of attack is computed from the value of the downwash induced at various locations on the blade which in turn is computed from the strength of the tip-vortex of the blade. The induced angle of attack ϕ is given by,

$$\phi = \frac{w^*}{\Omega r}$$

where w^* is the dimensional downwash induced at the blade section. Non-dimensionalising by dividing numerator and denominator by $\frac{\Omega R}{2\pi}$ we have,

$$\phi = \frac{w}{2\pi y}$$

where w is the dimensionless downwash induced by the tip-vortex at the blade section and $y = \frac{r}{R}$.

In forward flight, the rotor moves almost edgewise through the air, and the blade sections must encounter a periodic variation in local velocity. The same blade element assumptions and approximations previously used for the axisymmetric flight will also be considered as valid in low speed forward flight. As before, the velocity at the blade element with

a pitch angle θ is decomposed into an out-of-plane(perpendicular) velocity component, U_P , and a tangential(in-plane) component, U_T , perpendicular to the leading edge of the blade, both relative to the rotor disk plane, as shown previously in Figure 5.1. In this case, the out-of-plane velocity component(velocity induced by the wake) will remain the same although the inplane component will be different. The inplane component is now also a function of the forward flight speed of the rotor. The component of the in-plane velocity perpendicular to the blade element will now be $\Omega r + V_f \sin\psi$. The in-plane component tangential to the blade section doesn't account for the lift or thrust or moments. Hence it is the component perpendicular to the blade section that is relevant in this discussion.

The relative inflow angle at the blade section(neglecting the component tangential to the blade section and any inflow due to the rotor tip path plane attitude and flapping velocities) is

$$\phi = \tan^{-1}\left(\frac{U_P}{U_T}\right)$$

Since ϕ is small,

$$\phi = \frac{U_P}{U_T} = \frac{w^*}{\Omega r + \mu \Omega R \sin\psi}$$

where w^* is the dimensional downwash induced on the blade section. Non-dimensionalising by dividing the numerator and denominator by $\frac{\Omega R}{2\pi}$, we have

$$\phi = \frac{w}{2\pi(y + \mu \sin\psi)} \quad (5.6)$$

where w is the non-dimensional downwash induced at the blade section. Therefore, the linearized aerodynamic angle of attack of the blade element is given by

$$\alpha = \theta - \phi = \theta - \frac{w}{2\pi(y + \mu \sin\psi)}$$

Like in the case of hover, the incremental lift dL is given by

$$dL = \frac{1}{2}\rho U^2 c C_l dr$$

and the incremental drag is given by,

$$dD = \frac{1}{2}\rho U^2 c C_d dr$$

The force parallel to the rotor disk is,

$$dF_x = \phi dL + dD$$

The incremental power is

$$dP = N_b \Omega (\phi dL + dD) r$$

so the power coefficient like in the case of hover is

$$\begin{aligned} dC_P &= N_b \Omega r \left(\frac{\frac{1}{2}\rho U_T^2 c C_l dr}{\rho \pi \Omega^3 R^5} + \frac{\frac{1}{2}\rho U_T^2 c C_d dr}{\rho \pi \Omega^3 R^5} \right) \\ dC_P &= \left(\frac{1}{2} \frac{N_b c}{\pi R} \left(\frac{U_T}{\Omega R} \right)^2 C_l \phi + \frac{1}{2} \frac{N_b c}{\pi R} \left(\frac{U_T}{\Omega R} \right)^2 \right) y dy \\ dC_P &= \frac{1}{2} \sigma (\phi C_l + C_d) (y + \mu \sin \psi)^2 y dy \end{aligned} \quad (5.7)$$

The first part in the power coefficient equation involving C_l is the induced power coefficient while the second part is the profile power or the power required to overcome the drag. As has been said for the hover case, the present work is capable of computing only the induced power coefficient. The induced power coefficient is given by,

$$C_P = \frac{1}{2} \sigma C_{l\alpha} \int_0^1 \phi(\theta - \phi) (y + \mu \sin \psi)^2 y dy \quad (5.8)$$

The angle ϕ in this case can be obtained from Equation (5.6).

5.3 Computation of Loads Using the Lifting Surface Theory

If the bound circulation distribution on the entire blade is known, the lift force at a radial location can be computed directly from the magnitude of the free stream velocity and the magnitude of the circulation at that radial location using the Kutta-Joukowski law. Using the lifting surface theory, as we had seen earlier, the bound circulation distribution on the blade is computed and hence the lift force can be directly computed using the strength of the bound vortex. In the same way, the induced drag force can also be computed using the magnitude of the downwash perpendicular to the blade. Figure 5.2 shows a blade element with bound circulation $\Gamma_{r,k}$ and the free stream velocity at that location.

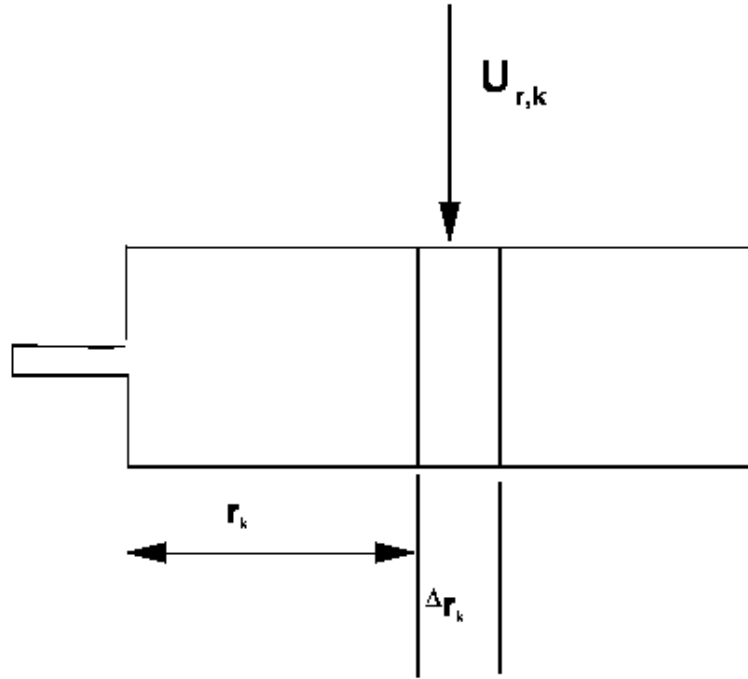


Figure 5.2: Blade element at a distance r_k from the root of the blade.

The lift and the drag can be calculated using the Kutta Joukowsky law which establishes the relation between lift and circulation [5]. The lift per unit span can be obtained using the Kutta-Joukowsky law given by,

$$L = \rho U \Gamma$$

For the lifting surface model, the velocity U perpendicular to the vortex is the sum of the free-stream velocity and the velocity induced by the wake in the θ -direction although the velocity induced by the tip-vortex in the θ -direction will be much smaller compared to the free-stream velocity. The freestream velocity perpendicular to the vortex element (blade element) is Ωr where r is the radial location of the vortex and Ω is the angular velocity of the blade.

In the current work, the blade is divided into a number of panels with each panel being represented by a horseshoe vortex. Each horseshoe vortex consists of a bound vortex segment and two trailing vortices extending downstream. The strength of these vortices is computed using the zero normal velocity boundary condition on the blade as already described. The strength of these bound vortices is now made use of for the computation of loads. The lift generated on a panel (say k^{th} panel, see Figure 5.2) neglecting the velocity induced by the wake in the θ direction, can be computed as [34]

$$L_k = \rho \Gamma_{rk} U_{\infty,k} \Delta r_k \cos \phi$$

where Γ_{rk} is the circulation of the bound vortex on the k^{th} panel, Δr_k is the width of the k^{th} panel, and ϕ is the angle induced by the downwash on the panel like in the lifting line case. Since ϕ is very small, $\cos \phi \sim 1$. Therefore the total lift generated for all the panels would be,

$$L = \rho \sum_{k=1}^n \Gamma_{rk} (U_{\infty,k}) \Delta r_k$$

where n is the number of panels. Hence the thrust coefficient is given by

$$C_T = \frac{N_b L}{\rho(\pi R^2)(\Omega R)^2}$$

The induced drag (drag induced due to the downwash) can also be computed in a similar fashion. The induced drag is given by

$$D_i = -\rho \sum_{k=1}^n \Gamma_{rk} w_k^* \Delta r_k.$$

The induced drag coefficient is given by,

$$C_{D,i} = \frac{D_i}{\rho(\pi R^2)(\Omega R)^2}.$$

The induced drag is the force acting in the plane of the rotor disk. This force multiplied by the distance of the radial location at which the force is acting from the center of the rotor disk would give the value of the generated torque. The product of this torque and the angular velocity would give the induced power required. The induced power is given by

$$P_i = \rho \sum_{k=1}^n \Gamma_{rk} w_k^* \Delta r_k \Omega r_k$$

5.4 Results - Lifting Line Theory

All the results obtained using the lifting line theory have been discussed in the following two subsections.

5.4.1 Results in Hover

A parametric study has been done for thrust coefficients and power coefficients in hover by varying the h/R ratio. Both single and two-bladed rotors have been considered. The

variation of the thrust coefficient as a function of the ground height for both single and two-bladed rotors can be seen in Figure 5.3. The thrust coefficient at $h/R = 0.5$ corresponds to the wake structure seen in Chapter 3 in Figures 3.4 and 3.8. The corresponding circulation can be observed in Figure 3.5 which becomes almost periodic after 10 revolutions. It can be seen that there is a decrease in the thrust coefficient value as the rotor moves farther away from the ground. Results were obtained until the OGE limit was reached. The OGE limit has been checked to a 4-digit accuracy. The OGE limit is reached to a four-digit accuracy at $h/R = 2.5$ in both the cases but becomes less than 5% of the OGE value at $h/R = 1.5$. For the case of the single-bladed rotor, the variation in the thrust coefficient between the h/R values of 0.5 and 1.0 is substantial but after that the decrease is very small. In fact the decrease is so small that the difference in the thrust coefficient magnitudes between $h/R = 0.5$ and $h/R = 1.0$ is greater than the decrease between $h/R = 1.0$ and $h/R = 3.0$.

For the single and two-bladed rotors the h/R ratio is kept constant and the thrust coefficients are compared. The results obtained for the two-bladed rotor are very much similar to the ones obtained using a single-bladed rotor. An interesting feature that can be observed from this graph is that the C_T/σ value for the two-bladed rotor is less than the corresponding value for the single-bladed rotor. This is because of the fact that the downwash increases for the two-bladed rotor and with that the downwash induced angle increases and hence the decrease. Nevertheless, notice that the actual thrust here is higher than the single-bladed rotor because the value of σ for the two-bladed rotor is double that of the single-bladed rotor. But the thrust will not be double the value because of the lower C_T/σ value. Again the decrease is maximum between $h/R = 0.5$ and $h/R = 1.0$ and the thrust coefficient remains almost constant after that.

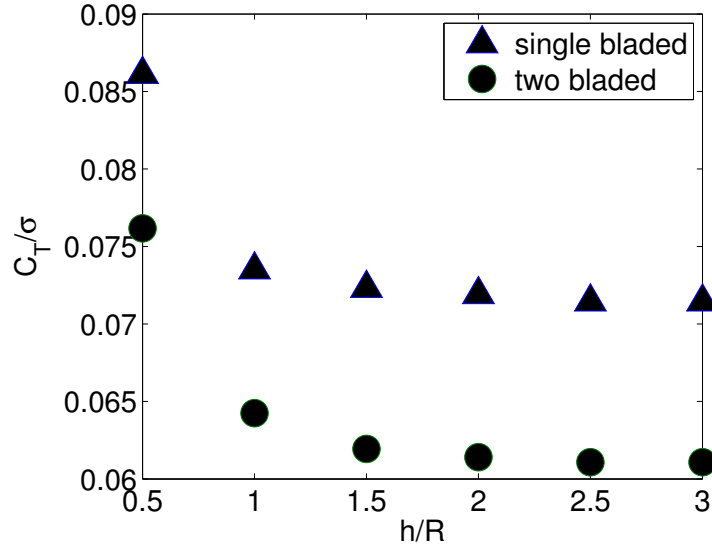


Figure 5.3: Thrust coefficient for single and two-bladed rotors in hover as a function of h/R ratio IGE using lifting line theory.

The induced drag as a function of the h/R ratio for both single and two-bladed rotors is depicted in Figure 5.4. The induced drag coefficient at $h/R = 0.5$ corresponds to the wake structure seen in Chapter 3 in Figures 3.4 and 3.8. The corresponding circulation can be observed in Figure 3.5 which becomes almost periodic after 10 revolutions. The drag increases with increase in the h/R ratio. There is no further change in the value of the induced drag. This is because with increase in the rotor-ground distance, the downwash induced at the rotor increases and hence the induced angle of attack increases and hence the component of the lift contributing to the induced drag increases. In the single-bladed case it increases from 0.0031 at $h/R = 0.5$ to 0.0035 at $h/R = 2.5$.

Similar to the calculation of the thrust coefficient, the h/R ratio is kept the same and the induced drag coefficient for the two-bladed rotor is computed. From the behavior of

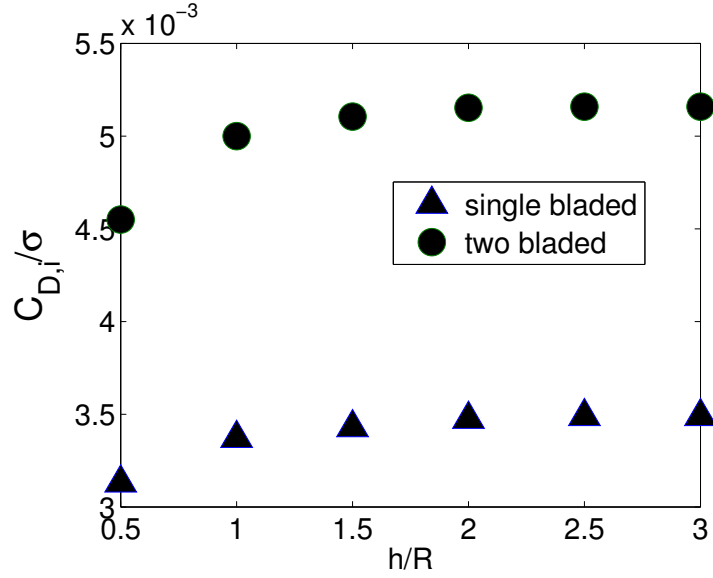


Figure 5.4: Induced Drag coefficient for single and two-bladed rotors in hover as a function of the h/R ratio IGE using lifting line theory.

the induced drag for the two-bladed rotor as a function of the h/R ratio it is interesting to note here that $C_{D,i}/\sigma$ value is higher than that for the single-bladed rotor. More drag is experienced by each blade and hence the total drag is more than double the single-bladed value. As discussed about the behavior of the thrust coefficient, the induced downwash increases for a two-bladed rotor and hence there is an increase in the induced angle of attack which increases the induced drag on each blade. Contrast this with the behavior of the rotor thrust where $\frac{C_T}{\sigma}$ is less than in the two-bladed case. More drag implies less than thrust and vice versa. Thrust and drag are the two components of the same force, increase in one force leads to a decrease in the other.

Results of the power coefficient values have also been obtained at different heights above the ground as can be seen from Figure 5.5. The power coefficient is dependent on

the induced drag since it is the power required to overcome the drag. Hence it is quite natural for us to expect it to behave in the same fashion. The power coefficient increases with increase in the h/R ratio and reaches OGE value at $h/R = 2.5$. Like in the induced drag case, the induced power required to overcome the drag on each blade is higher for the two-bladed rotor than the single-bladed rotor.

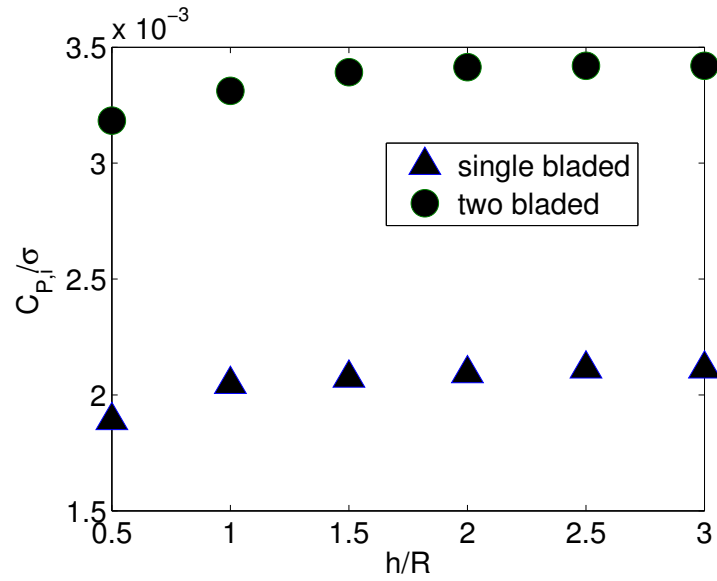


Figure 5.5: Induced power coefficient for single and two-bladed rotors in hover as a function of h/R ratio IGE using lifting line theory.

5.4.2 Results - Forward Flight

The induced drag coefficients for various advance ratios can be seen in Figure 5.6. There is a reduction in the induced drag with increase in the advance ratio because of the reduction in the induced downwash at the rotor with the increase in advance ratio. With the reduction in the induced downwash, the induced angle of attack decreases and

the component of the lift contributing towards the induced drag is reduced and hence the reduction in induced drag.

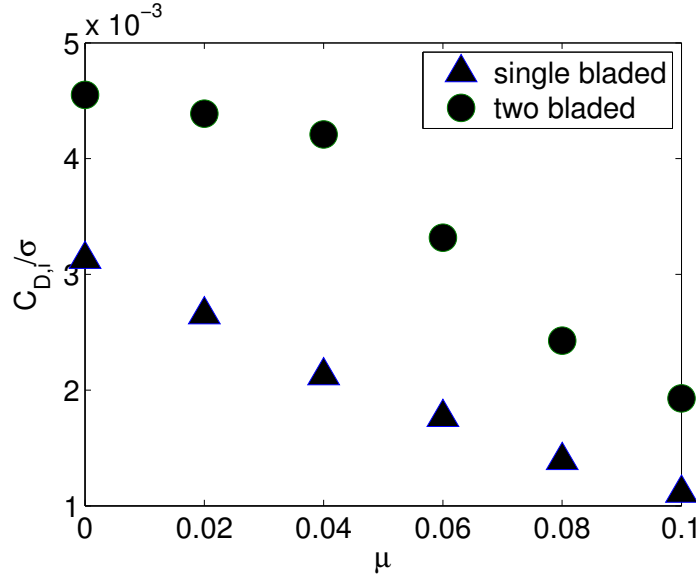


Figure 5.6: Induced drag coefficient for single and two-bladed rotors in hover as a function of the forward flight speed IGE using lifting line theory, $h/R = 0.5$.

In the two-bladed rotor case, there is a reduction in the induced drag with increase in the advance ratio and the $C_{D,i}/\sigma$ value is higher than that of a single-bladed rotor and hence the total induced drag on the rotor will be more than double the single-bladed value.

The power coefficient values for various advance ratios have been obtained for both single-bladed and two-bladed rotors. The behavior of power coefficient with advance ratio can be seen in Figure 5.7. There is a decrease in the value of the power coefficient with increase in the advance ratio. The underlying reason behind this behavior can be seen from the behavior of the induced drag coefficient which causes the induced power. The decrease

is almost linear with advance ratio, and the decrease is quite high. The power coefficient for $\mu = 0.1$ is one-fifth of the corresponding value for hover.

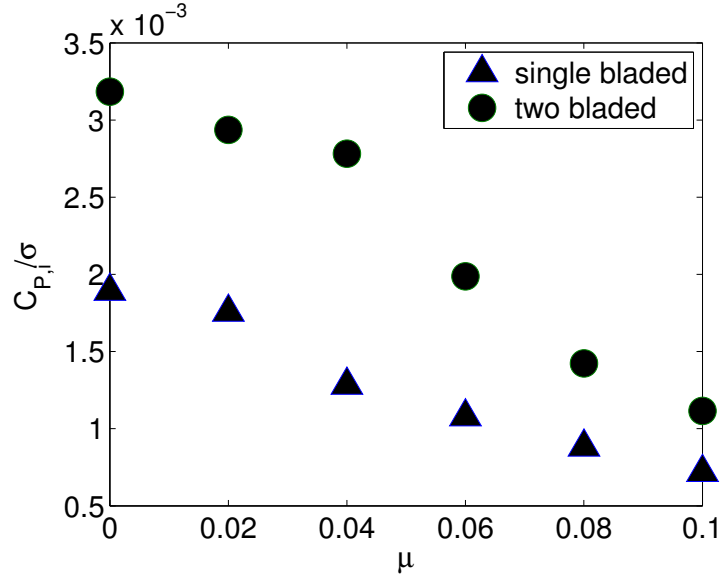


Figure 5.7: Induced power coefficient for single and two-bladed rotors in hover as a function of the forward flight speed IGE using lifting line theory, $h/R = 0.5$.

Even in the two-bladed rotor case, there is a decrease in the magnitude of the power coefficient with increase in the advance ratio but this time it is not linear. The decrease is much less between the advance ratios of 0 and 0.04 but very steep after that from $\mu = 0.04$ to $\mu = 0.1$. Eventually, the power coefficient at $\mu = 0.1$ is 3.5 times lesser than the value at hover. Thus the decrease is kind of lesser here.

5.5 Results - Lifting Surface Theory

All the results obtained using the lifting surface theory have been discussed in the following two subsections. The angle of attack is 10 degrees and the aspect ratio is 6.

5.5.1 Results - Hover

The induced drag coefficient values at different heights above the ground have been obtained for both single and two-bladed rotors. The thrust coefficient at $h/R = 0.5$ corresponds to the wake structure seen in Chapter 4 in Figures 4.1 and 4.5. The corresponding circulation can be observed in Figure 2.7 which becomes almost periodic after 10 revolutions. We know that the induced downwash increases as the distance between the ground and the rotor increases. This increases the induced angle of attack which in turn increases the component of lift contributing to the induced drag and thus the induced drag coefficient is expected to increase with increase in the h/R ratio. This view is supported by the behavior of the drag coefficient obtained using the lifting surface theory. It can be seen from Figure 5.8 that the induced drag coefficient increases with the increase in h/R ratio and the increase is very steep between the h/R values of 0.5 and 1.0. After that the increase is very small. The OGE limit is reached at $h/R = 2.5$.

The above computation has been repeated using a two-bladed rotor by keeping the aspect ratio, angle of attack and h/R ratio the same and the results can be seen in Figure 5.8. The increase in the value of the induced drag coefficient is again the maximum between $h/R = 0.5$ and $h/R = 1.0$ but after that it is almost constant. The increase is much less and the OGE limit is reached at $h/R = 2.5$. Hence the effect of the ground can be felt at $h/R = 0.5$. The magnitude of the induced drag on each blade of the two-bladed rotor is almost one and a half times that for the single-bladed rotor. More downwash is created due to the two blades and hence more induced drag.

The power required to overcome the induced drag for a single-bladed rotor can be seen in Figure 5.9. As expected, the behavior of the induced power is very similar to that of the

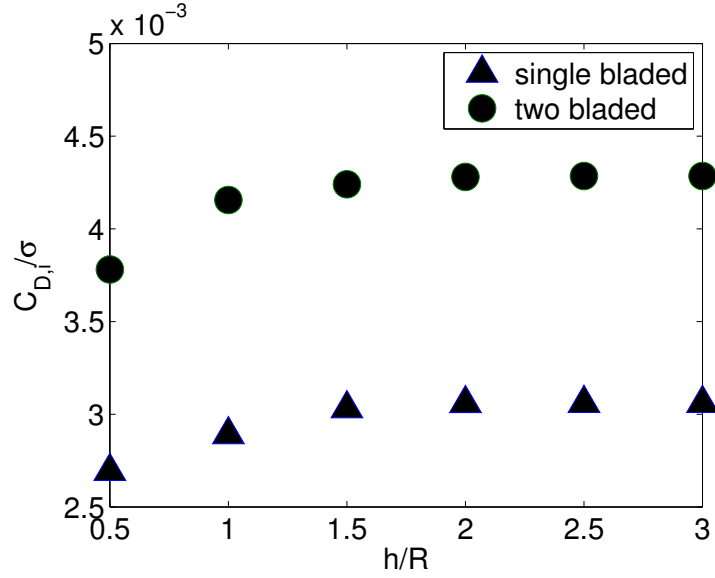


Figure 5.8: Induced drag coefficient for single and two-bladed rotors in hover as a function of the h/R ratio using lifting surface theory, $\alpha_0 = 10^\circ$, $A = 6$.

induced drag with the power required increasing in magnitude as the h/R ratio increases. The effect is most pronounced at $h/R = 0.5$ with the power values at other ground heights remaining very close to one another.

The power required to overcome the induced drag on each blade when a two-bladed rotor is used can also be seen in Figure 5.9. When a two-bladed rotor is used, the induced drag on each blade increases and hence the power required to overcome the drag also increases.

The thrust coefficient as a function of the rotor-ground distance can be seen in Figure 5.10. It is once again clear from this Figure that the effect of the ground is most pronounced at $h/R = 0.5$. The value of C_T/σ is close to 0.075 at $h/R = 0.5$ and it reduces to 0.055

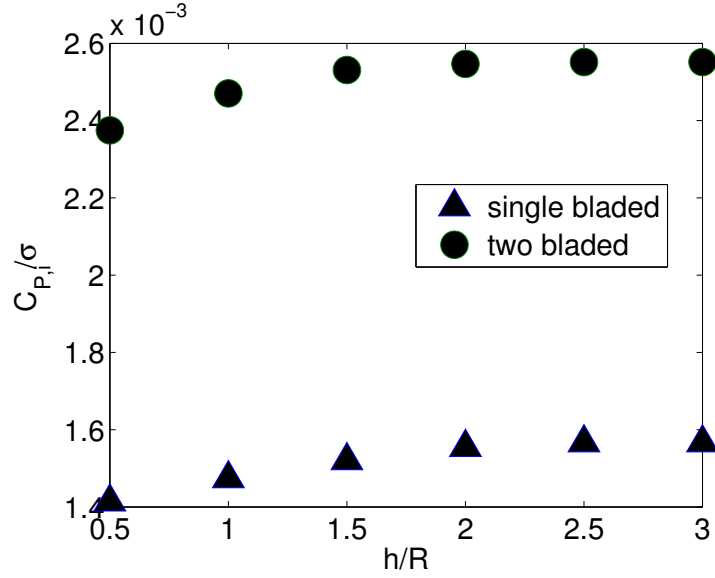


Figure 5.9: Induced power coefficient for single and two-bladed rotors in hover as a function of the h/R ratio using lifting surface theory, $\alpha_0 = 10^\circ$, $A = 6$.

with increase in the ground height. Hence, more thrust is experienced by the rotor when it is close to the ground.

The thrust coefficient for a two-bladed rotor with the same aspect ratio and at the same angle of attack as that of the single-bladed rotor can also be seen in Figure 5.10 and its behavior is very similar to that of the single-bladed rotor qualitatively. The thrust experienced by each blade is lower here than in the single-bladed case. This can be intuitively expected since the induced drag on each blade is higher in the two-bladed case. The C_T/σ value in this case at $h/R = 0.5$ is 0.065 and reduces to an OGE value of 0.046 with increase in ground height. Hence the total thrust on the rotor is less than double the thrust on a single-bladed rotor.

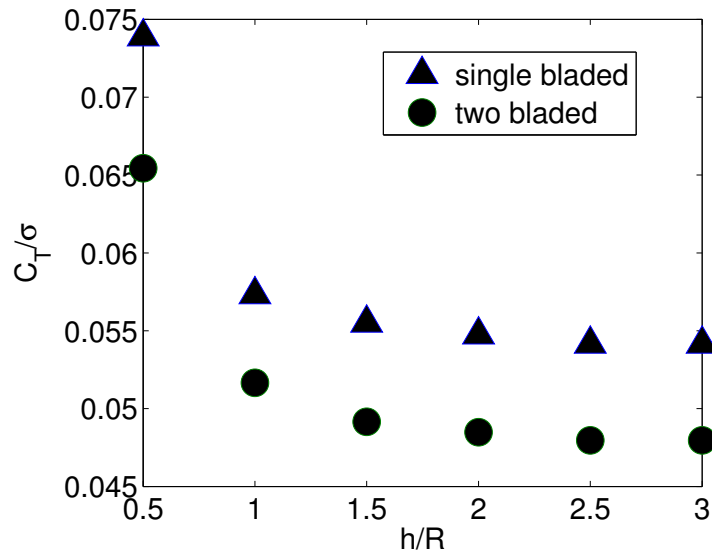


Figure 5.10: Thrust coefficient for single and two-bladed rotors in hover as a function of the h/R ratio using lifting surface theory, $\alpha_0 = 10^\circ$, $A = 6$.

5.5.2 Results - Forward Flight

The induced drag at $h/R = 0.5$ as a function of the advance ratio can be seen in Figure 5.11. It decreases with increase in the advance ratio and the decrease is maximum between hover and $\mu = 0.02$, and after that it is almost linear and less steeper. With increase in the advance ratio, since the wake is swept away by the forward flight, the downwash induced on the rotor disk plane reduces, and hence the magnitude of the induced drag reduces. Hence when the rotor is accelerating, its induced drag keeps reducing.

The induced drag for the two-bladed rotor with the same aspect ratio, angle of attack and h/R ratio exhibits a little different behavior compared to the single-bladed rotor as can be seen from Figure 5.11. The decrease in the induced drag with increase in the advance

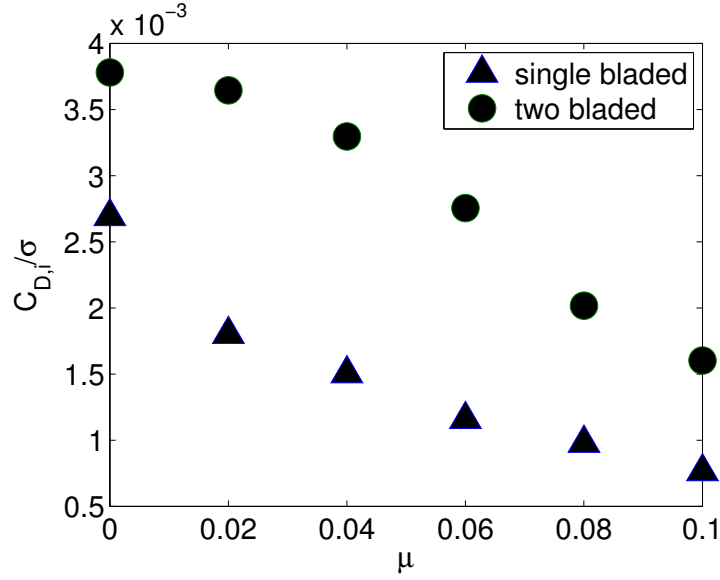


Figure 5.11: Induced drag coefficient for a single and two-bladed rotors as a function of the forward flight speed IGE using lifting surface theory, $\alpha_0 = 10^\circ$, $A = 6$.

ratio is linear throughout. The $C_{D,i}/\sigma$ value reduces from 0.0037 in hover to about 0.0016 at $\mu = 0.1$.

The induced power requirement also reduces with increase in advance ratio for both single and two-bladed rotors as can be seen from Figure 5.12. In the single-bladed case, it reduces from about 0.0014 at hover to 0.0005 at $\mu = 0.1$ while in the two-bladed case it is 0.0024 at hover and becomes 0.0008 at $\mu = 0.1$.

5.5.3 Comparison of Lifting Line and Lifting Surface Models

The induced drag obtained by the lifting line and lifting surface models has been compared. Figure 5.13 compares the induced drag obtained by the lifting line model with that obtained using the lifting surface model. As can be seen from the figure, the induced drag

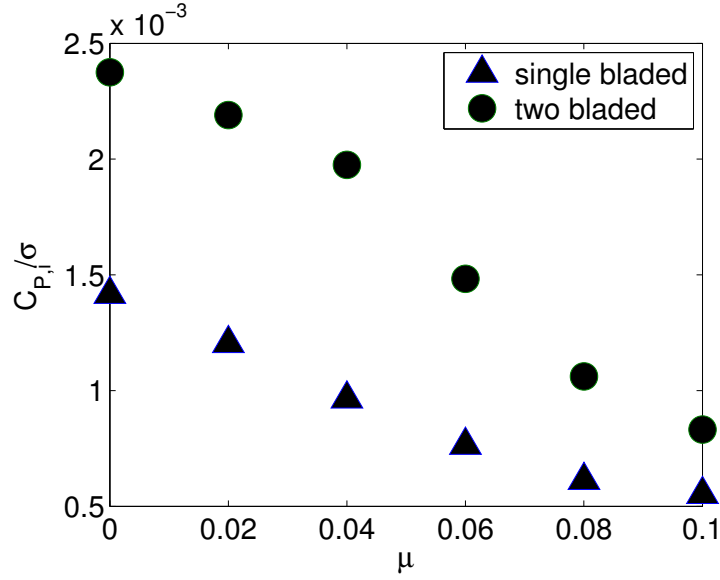


Figure 5.12: Induced power coefficient for single and two-bladed rotors as a function of the forward flight speed IGE using lifting surface theory, $\alpha_0 = 10^\circ$, $A = 6$.

obtained using the lifting line model is 18% higher than that obtained using the lifting surface model. Hence the lifting line model significantly overestimates the induced drag. The reason behind this behavior is higher tip-vortex circulation in the lifting line model which can be seen from Figure 2.7.

The induced power obtained by the lifting line and lifting surface models has also been compared. Figure 5.14 compares the induced drag obtained by the lifting line model with that obtained using the lifting surface models. As can be seen from the Figure, the induced power obtained by the the lifting line model is higher than that obtained by the lifting surface model. The comparison has been done only in hover because the same difference in magnitude exists even in forward flight.

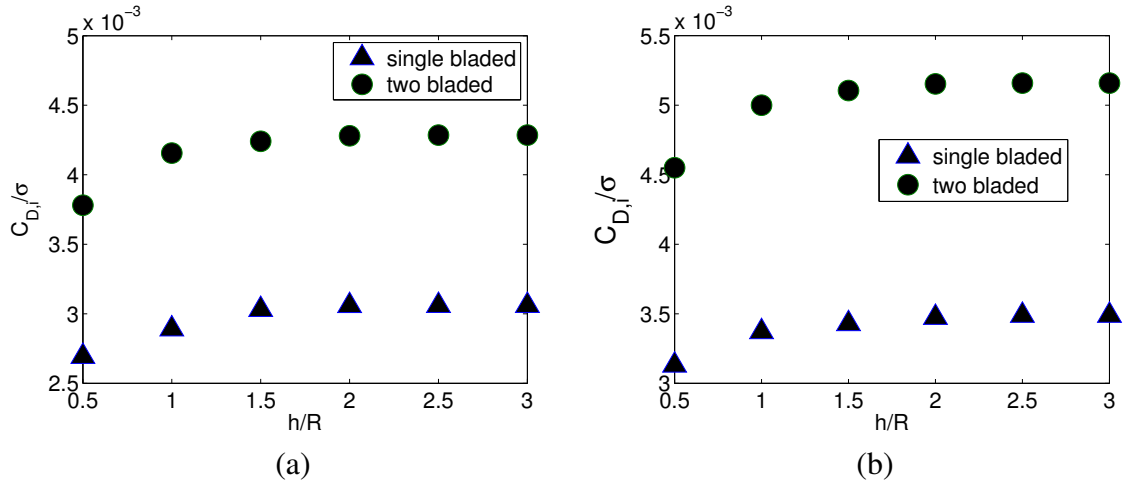


Figure 5.13: Comparison of the induced drag coefficient obtained by (a) lifting surface model, $\alpha_0 = 10^\circ$, $A = 6$, (b) lifting line model in hover.

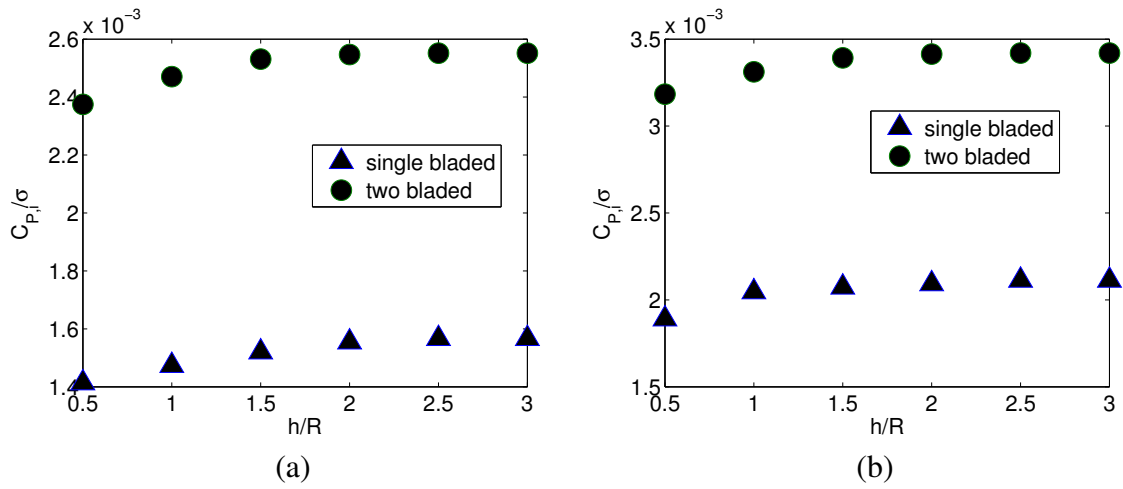


Figure 5.14: Comparison of the induced power coefficient obtained by (a) lifting surface model, $\alpha_0 = 10^\circ$, $A = 6$, (b) lifting line model in hover.

5.6 Summary

The magnitude of the downwash induced at the rotor reduces when rotor comes close to the ground. Due to this reason, the thrust and drag on the rotor are different from the OGE values. Because of the reduction in downwash, the component of the lift contributing to the thrust increases and hence more thrust is generated on the rotor IGE. Again, for the same reason, the induced drag on the rotor reduced when it comes close to the ground. The effect of the ground is most felt at $h/R = 0.5$, it becomes almost negligible at $h/R = 1.0$. A two-bladed rotor experiences less than double the thrust experienced by a single-bladed rotor while it experiences more than twice the drag experienced by a single-bladed rotor. As the advance ratio increases, the rotor experiences a decrease in the induced drag due to reduction in the induced downwash on the rotor disk and hence reduced power requirement to overcome the drag. The lifting line model substantially overestimates the induced drag and power compared to the lifting surface model.

CHAPTER 6

Main Rotor - Tail Rotor Interactions

6.1 Introduction

In this chapter, a tail rotor has also been included in the current configuration and its effect on the flow field and the power requirements has been computed. The wake structures due to two blades at different positions are considered and they are then advanced in time by their self-induced velocity as well as the velocity induced due to the other wake structure. The main rotor-tail rotor configuration is separated by a distance $1.05R + R_t$ where R is the main rotor radius and R_t is the tail rotor radius. This arrangement corresponds to that of a Sikorsky BlackHawk. The top view and side view of the main rotor-tail rotor arrangement can be seen in Figure 6.1.

The same principle that has been used previously is applied to include the tail rotor in the current configuration. The tail rotor is assumed to have a wake which is dominated again by the tip-vortex. The influence of this tail rotor tip-vortex on the main rotor tip-vortex is obtained, by including the velocity induced by the tail rotor tip-vortex in the velocity expression.

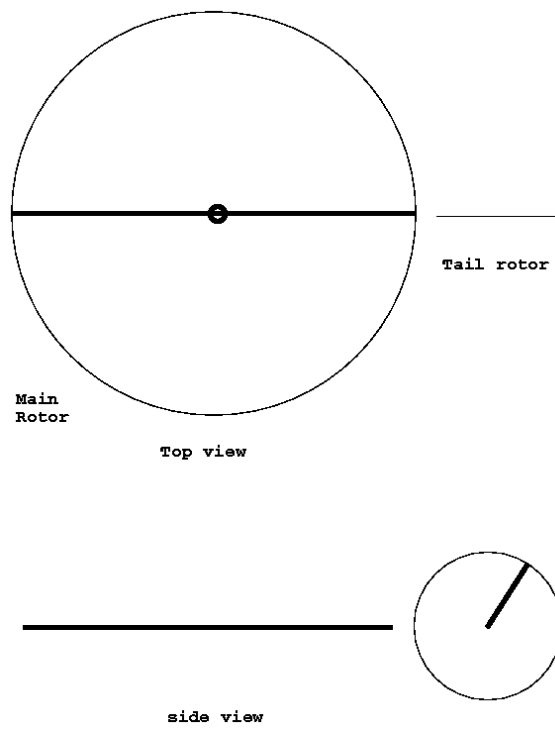


Figure 6.1: Top and side views of the main rotor-tail rotor configuration.

6.2 Numerical Model

The initial wake structure for the tail rotor wake is taken to be a perfect helix. The helical structure for the tail rotor wake is maintained for six turns and after that it is replaced by an infinitely long cylinder coaxial with the tail rotor. The advance velocity for the main rotor tip-vortex with the tail rotor included in the model is given by

$$U = U_V + U_{V,i} + U_b + U_{b,i} + 2\pi V_f + U_{tr} + U_{tr,i} \quad (6.1)$$

where $U_V, U_{V,i}$ are the velocities induced by the main rotor tip-vortex and its corresponding image wake, $U_b, U_{b,i}$ are the velocities induced by the main rotor blade and its image, V_f is the forward flight advance ratio, and $U_{tr}, U_{tr,i}$ are the velocities induced by the tail rotor wake including the blade. The velocity induced by the tail rotor vortex is calculated in a similar fashion to that of the main rotor tip-vortex. The tip-vortex is discretised into a number of straight line vortex segments with a constant circulation. The rotational speed of the tail rotor is three times that of the main rotor. The radius of the tail rotor blade is one fifth the radius of the main rotor. These ratios are typical of the helicopters used in the industry today. A non-dimensional main rotor to ground height of $h/R = 0.5$ is used and an aspect ratio of $A = 6$ is used for both the main and tail rotors. A single-bladed tail rotor is used. The typical dimensional parameters corresponding to these non-dimensional values are a main rotor radius of $15m$, tail rotor radius of $3m$, main rotor angular speed of 2100 rpm and a tail rotor angular speed of 6300 rpm. The typical rotor to ground height on the field is $7.5m$.

6.3 Results

The flow field has been obtained with the tail rotor included for the cases of hover and forward flight with advance ratios $\mu = 0.01$ and $\mu = 0.03$. The induced power and drag requirements have also been obtained with this model. In the following subsections the results obtained with this model have been compared with the results obtained using the model without the tail rotor.

6.3.1 Flow field

The wake structure obtained with the tail rotor included in the model in hover IGE at $h/R = 0.5$ has been depicted in Figure 6.2(a). When the tail rotor is included, it takes around 20 revolutions to attain periodic state for a single-bladed rotor in hover. The wake structure obtained without the tail rotor included in the model has also been shown for comparison. It can be seen that there are fine scale differences in the wake structure with the tail rotor included but not much can be concluded from this comparison.

The downwash profile along the y -axis after periodicity is attained in hover at $h/R = 0.5$ for the models with and without the tail rotor can be seen in Figure 6.3. In the model where no tail rotor is present, it can be seen that there are three small pockets of recirculation while in the model without the tail rotor included, only two recirculation zones are seen. The downwash values are higher when no recirculation is present.

Figure 6.4 compares the downwash profiles in the models with and without the tail rotor at advance ratio $\mu = 0.01$ for $h/R = 0.5$. When the tail rotor is not included formation of two large ground vortices can be noticed. With the inclusion of the tail rotor, the profile completely changes with the vortices becoming considerably smaller in size but increase

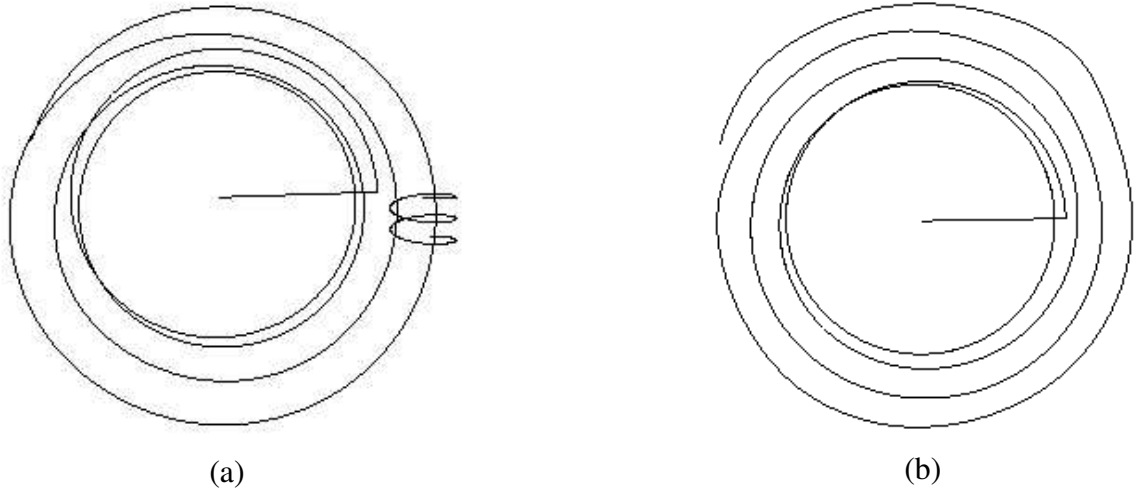


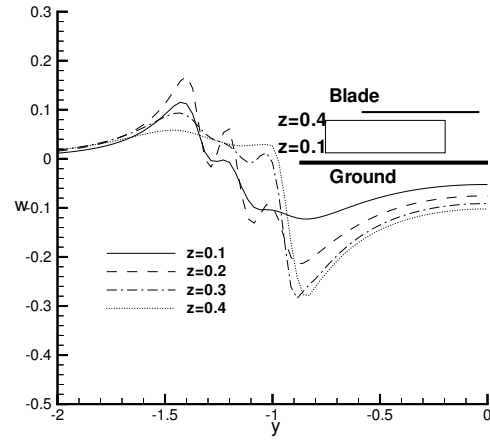
Figure 6.2: Comparison of the tip-vortex trajectory (a) with the tail rotor included (b) without the tail rotor included in hover; $h/R = 0.5$, $A = 6$, $\alpha_0 = 10^\circ$.

in number to three. The magnitude of the downwash is comparatively lesser when the tail rotor is included.

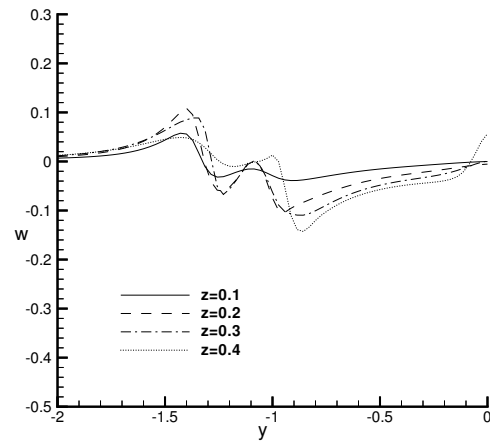
Figure 6.5 shows the above described comparison when the advance ratio is $\mu = 0.03$ for $h/R = 0.5$. There is very little difference qualitatively in the downwash profiles between the models with and without the tail rotor. But the difference is quite substantial in the magnitudes.

6.3.2 Loads

The induced drag and the power requirements have also been compared. Figure 6.6 compares the induced drag coefficient plotted as function of the h/R ratio obtained from the model without the tail rotor included and with the tail rotor included. In both the cases, there is an increase in the induced drag coefficient with increase in the h/R ratio but in the model with the tail rotor included, the magnitude of the induced drag is slightly lesser

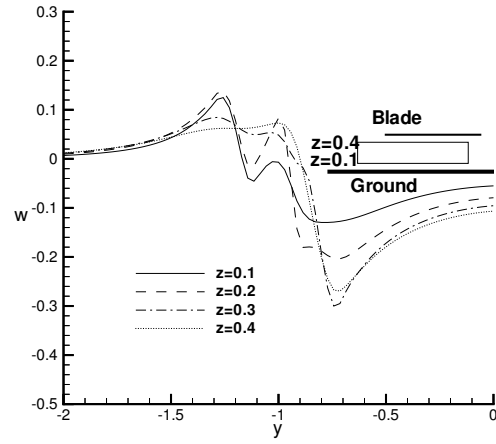


(a)

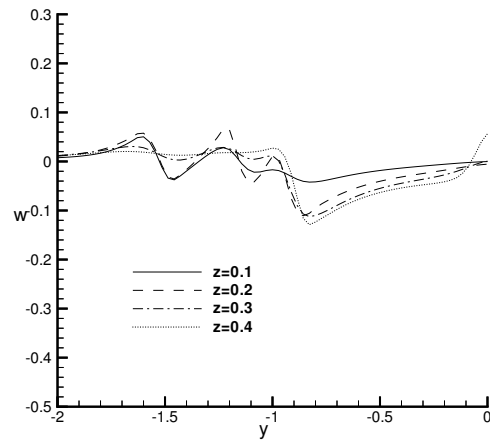


(b)

Figure 6.3: Comparison of downwash profiles in hover for (a) Model without the tail rotor (b) Model with the tail rotor included; $A = 6$, $\alpha_0 = 10^\circ$, $h/R = 0.5$.

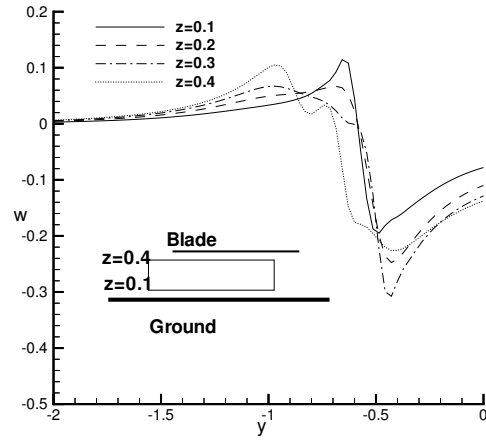


(a)

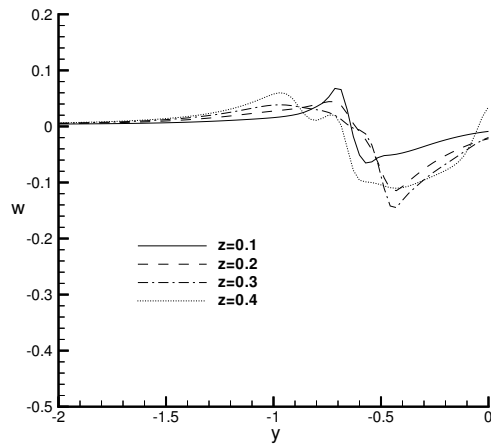


(b)

Figure 6.4: Comparison of downwash profiles at $\mu = 0.01$ for (a) Model without the tail rotor (b) Model with the tail rotor included; $A = 6$, $\alpha_0 = 10^\circ$, $h/R = 0.5$.



(a)



(b)

Figure 6.5: Comparison of downwash profiles at $\mu = 0.03$ for (a) Model without the tail rotor (b) Model with the tail rotor included; $A = 6$, $\alpha_0 = 10^\circ$, $h/R = 0.5$.

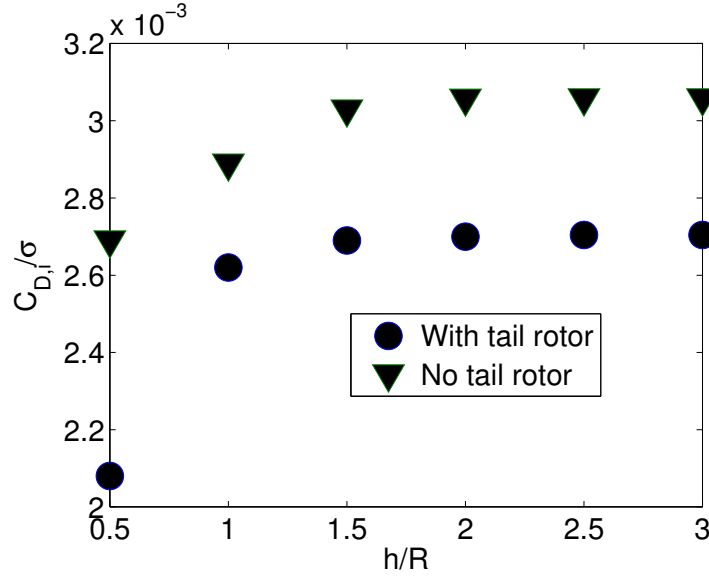


Figure 6.6: Comparison of induced drag coefficient for a single bladed rotor in hover as a function of h/R ratio between model without the tail rotor and model with the tail rotor included; $A = 6$, $\alpha_0 = 10^\circ$, $h/R = 0.5$.

compared to the model without the tail rotor. In the model without the tail rotor, the induced drag coefficient, $\frac{C_D}{\sigma}$ value is 0.0027 while that in the model including the tail rotor is around 0.0021 when $h/R = 0.5$. The increase in the drag with increase in the rotor distance from the the ground is steeper with the tail rotor included in the model. This implies that the tail rotor wake is affecting the main rotor wake/flow field in a way that is causing a decrease in the downwash which is responsible for the induced drag. Hence, in the model without the tail rotor, the induced drag is being over predicted slightly.

Figure 6.7 shows the comparison between the models with and without the tail rotor for a two-bladed rotor. Qualitatively both the plots look similar but the magnitude of the induced drag is lesser when the tail rotor is included in the model. The increase in the induced drag with h/R ratio is very smooth and gradual in both the cases.

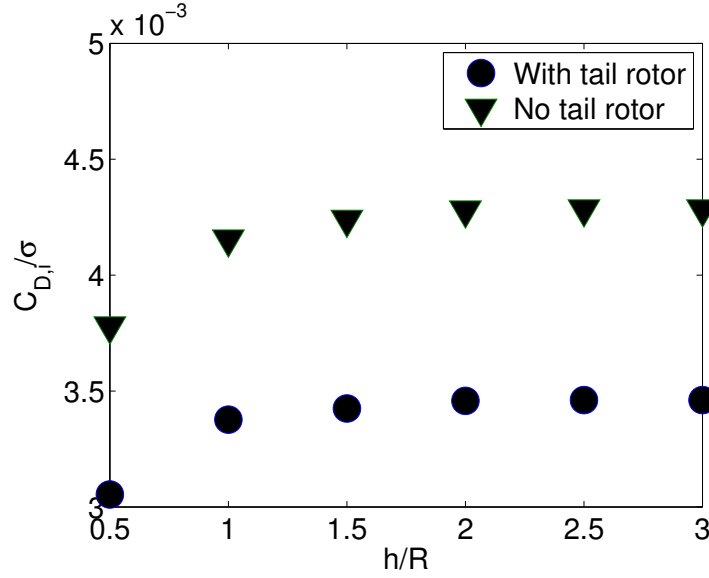


Figure 6.7: Comparison of induced drag coefficient for a two bladed rotor in hover as a function of h/R ratio for a Model without the tail rotor and Model with the tail rotor included; $A = 6$, $\alpha_0=10^\circ$, $h/R = 0.5$.

Figure 6.8 compares the power required to overcome the induced drag plotted as a function of the h/R ratio obtained from the model without the tail rotor included and with the tail rotor included. The trend here is similar to that of the induced drag as expected, with the power requirement increasing as the rotor moves away from the ground. The magnitude of the induced power also is less when the tail rotor is incorporated. With the tail rotor included there is a large increase in the induced power required between h/R values of 0.5 and 1.0. After that the increase is very small and reaches a constant value at $h/R = 2.5$.

Figure 6.9 shows the comparison between the induced power requirements for the models with and without the tail rotor being considered with a two-bladed rotor. The magnitude of the induced power in the model with the tail rotor included is 7.4% lesser compared to

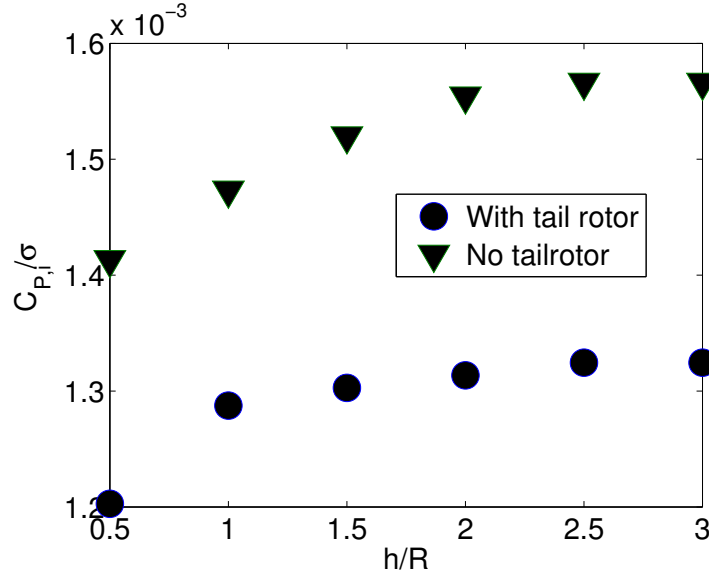


Figure 6.8: Comparison of induced power coefficient for a single bladed rotor in hover as a function of h/R ratio between a model without the tail rotor and a model with the tail rotor included; $A = 6$, $\alpha_0 = 10^\circ$, $h/R = 0.5$.

the model without the tail rotor. The increase in the induced power with increase in ground height is similar to that of the induced drag. With the tail rotor included, the induced power coefficient is around 0.002 at $h/R = 0.5$ and reaches a steady value of 0.00218 at $h/R = 2.5$.

Figure 6.10 compares the induced drag on the rotor in forward flight. The effect of the tail rotor on the induced drag is felt in hover and in low speed forward flight. As can be seen from the figure the magnitude of the induced drag with the tail rotor included is lesser in hover and when $\mu = 0.02$, but with increase in the advance ratio, the induced drag magnitudes are almost the same. They converge to the same value with increase in the advance ratio. Hence it can be inferred that the tail rotor wake has very little effect on the downwash induced on the rotor disk at high advance ratios.

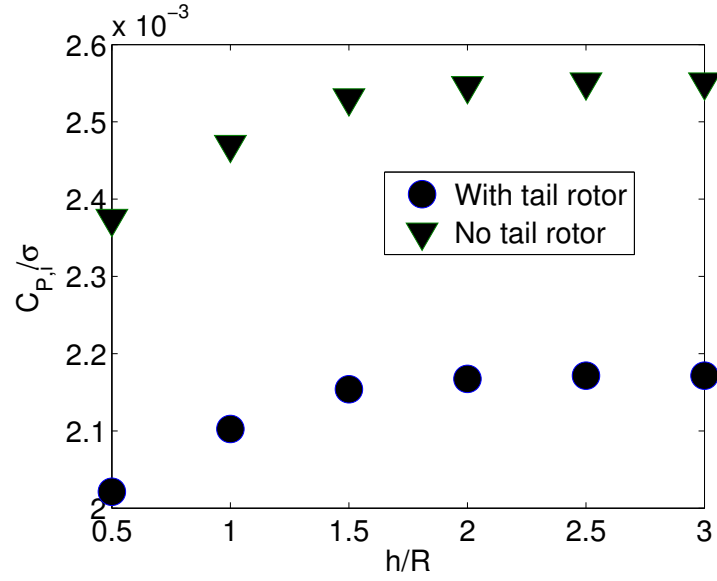


Figure 6.9: Comparison of induced power coefficient for a two bladed rotor in hover as a function of h/R ratio between a model without the tail rotor and a model with the tail rotor included; $A = 6$, $\alpha_0 = 10^\circ$, $h/R = 0.5$.

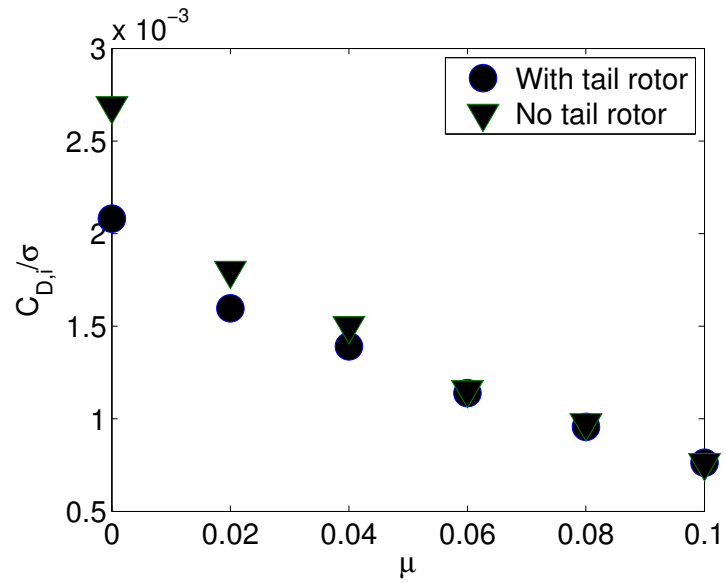


Figure 6.10: Comparison of induced drag coefficient for a single bladed rotor at $h/R = 0.5$ as a function of advance ratio between a model without the tail rotor and a model with the tail rotor included; $A = 6$, $\alpha_0 = 10^\circ$, $h/R = 0.5$.

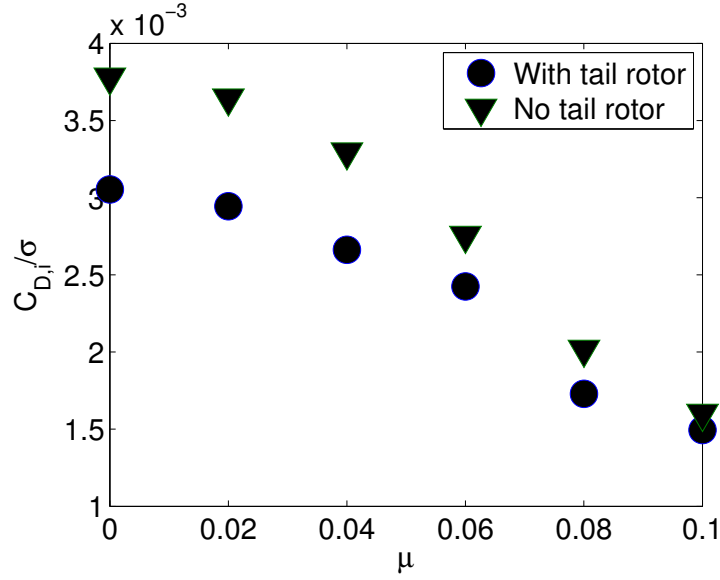


Figure 6.11: Comparison of induced drag coefficient for a two bladed rotor at $h/R = 0.5$ as a function of advance ratio between a model without the tail rotor and a model with the tail rotor included; $A = 6$, $\alpha_0 = 10^\circ$, $h/R = 0.5$.

The comparison for the case of a two-bladed rotor can be seen in Figure 6.11 and it can be noticed that the two figures are similar to each other qualitatively but there is around 9 – 10% difference in magnitude.

The induced power behavior in forward flight is similar to that of the induced drag. It can be noticed that decrease in the induced power in the model without the tail rotor is steeper. The decrease in induced power with advance ratio is almost linear in both the cases. The magnitude of the induced power is around 9-10% lesser with the tail rotor included.

Figure 6.13 compares the power required to overcome the induced drag between the models with and without the tail rotor for a two-bladed main rotor.

Results have also been compared with the experimental results obtained by Empey and Ormiston [8] in Figure 6.14. The behavior of the stagnation point with advance ratio has

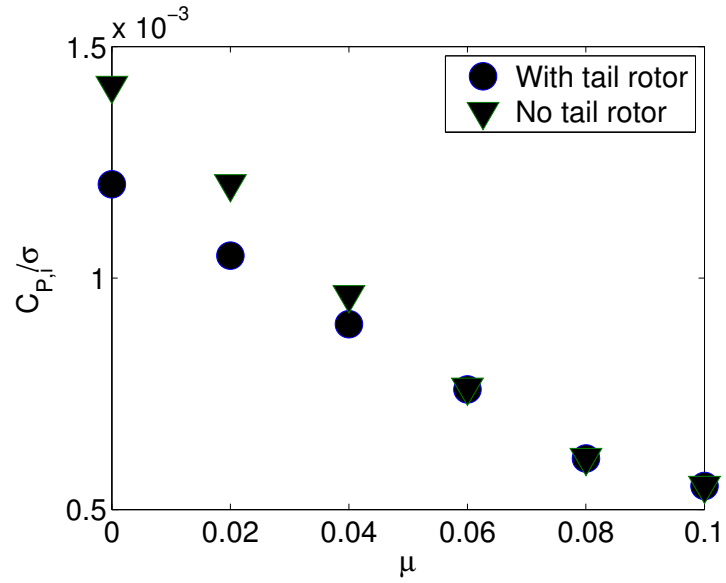


Figure 6.12: Comparison of induced power coefficient for a single bladed rotor at $h/R = 0.5$ as a function of advance ratio between a model without the tail rotor and a model with the tail rotor included; $A = 6$, $\alpha_0 = 10^\circ$, $h/R = 0.5$.

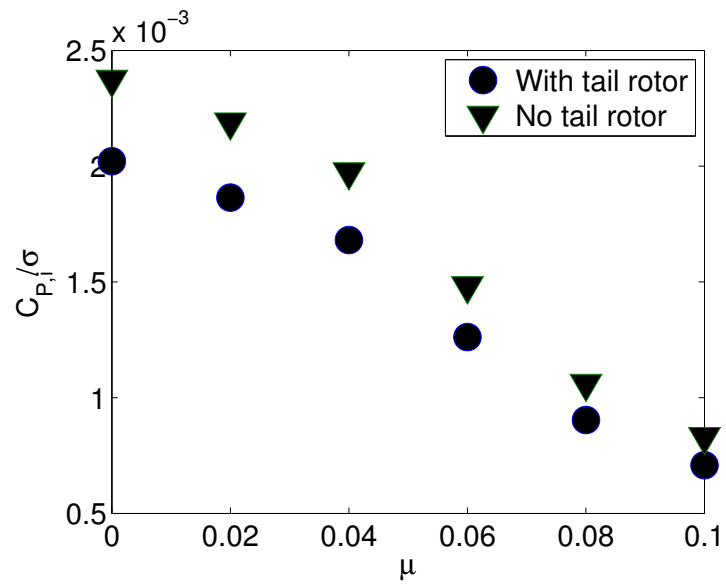


Figure 6.13: Comparison of induced power coefficient for a two bladed rotor at $h/R = 0.5$ as a function of advance ratio between a model without the tail rotor and a model with the tail rotor included; $A = 6$, $\alpha_0 = 10^\circ$, $h/R = 0.5$.

been compared. The stagnation point is the point where the downwash due to the rotor wake becomes zero and it occurs away from the rotor disk center. In the computations, the stagnation point is located by calculating the downwash in the plane of the rotor obtained from Equation (6.1) upstream of the rotor until a zero downwash accurate to three significant digits is attained. The stagnation point is at least near the rotor disk plane since the ground vortex radius is $\sim 2h/R$ as noted in Figure 7 of Empey and Ormiston [8]. In the experiments a two-bladed rotor at a non-dimensional height of 0.53 from the ground with an aspect ratio of 9.78 has been used. In the experiments, a 1/8 scale model of the main rotor-tail rotor configuration of the AH-1G Cobra helicopter is used in a 7-by 10Ft Wind-Tunnel. Teetering hinges and cyclic pitch controls have not been installed and the main and tail rotor blades are rigidly attached to their respective hubs except that pitch changes could be made manually by loosening the hub clamps. It can be seen that the position of the stagnation point moves inboard with the increase in the free stream velocity/advance ratio. The computations simulate the experimental behavior very well qualitatively as well as quantitatively. It can also be noticed that without the tail rotor included the stagnation points are further upstream indicating that the velocity magnitudes are higher.

6.4 Summary

The velocities are over predicted in the model without the tail rotor. The flow field obtained with the tail rotor included in the model is very much different from the flow field obtained without the tail rotor in hover and low advance ratios. At $\mu = 0.03$, the downwash profile obtained with and without the tail rotor is the same but substantial differences in magnitude remain. The effect of tail rotor wake on the loads and power requirements reduces with increase in the advance ratio. With increase in the advance ratio, the tail

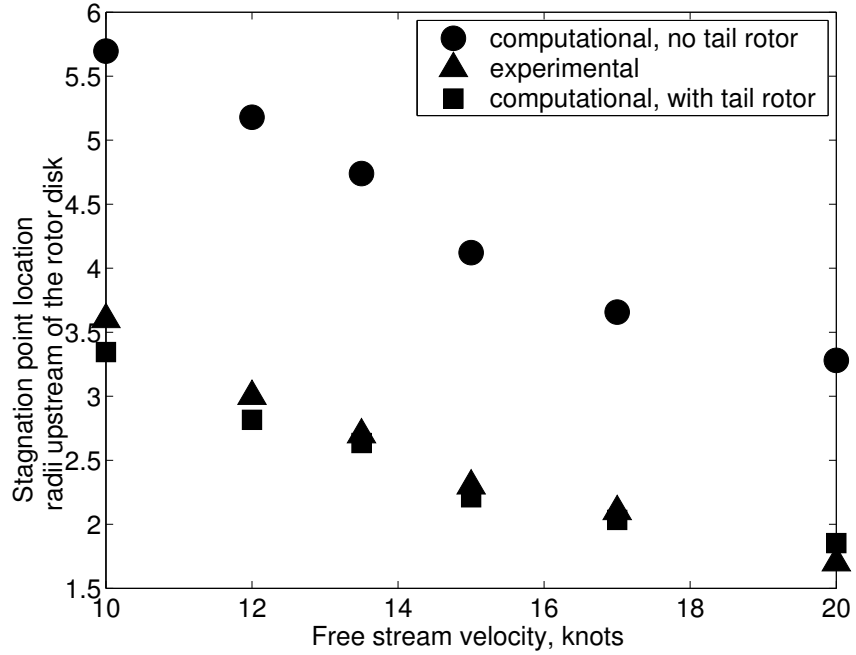


Figure 6.14: Comparison of the variation of the stagnation point position with free stream velocity between computations and experimental results from Empey and Ormiston [8]; $h/R = 0.53$, two-bladed rotor, $A = 9.78$.

rotor wake is swept away and its effect on the flow field significantly reduces. The model has been successfully validated by comparing with experimental results from Empey and Ormiston [8].

CHAPTER 7

Overview and Future Work

7.1 Summary

The current work deals with one of the most complicated problems faced by the rotorcraft industry today. The helicopter wake is among the most complex fluid dynamic structures being three dimensional and in many cases unsteady and the behavior of the rotor wake in the vicinity of the ground is challenging to predict. Under in ground effect(IGE) conditions, the wake collides with the ground and causes a significant perturbation to the flow near the blade. Significant interactions between the main rotor wake and the ground have been associated with the formation and passage of the ground vortex in forward flight.

There has been very little modeling work published in the open literature in the last twenty years. Typically the rotorcraft community has relied on full-scale testing and model scale experiments both of which are time consuming and expensive. The current work is a big step forward towards capturing the physics of the flow features and dynamics of ground-effect flows around rotorcraft and providing an understanding of the rotor wakes/vortices near the ground. The most important contributions of this work to the rotorcraft community have been

- The wake of single and two-bladed rotors has been computed to one hundred rotor revolutions and more revolutions can be performed if needed.
- The computational results have been successfully validated with experimental results obtained from Light [17], Empey and Ormiston [8] and Georgia Institute of Technology [31].
- The formation and structure of the ground vortex has been computed; the results indicate that the ground vortex consists of a more complex version of a Lamb vortex.
- A low frequency component observed in experiments conducted at the Georgia Institute of Technology has been captured by the computations.
- The unsteadiness on a hypothetical tail rotor plane in sideward flight has been studied and it has been determined that the sideward flight at 45 degrees faces maximum unsteadiness in velocities and hence maximum handling problems.
- The thrust generated and the power required for the rotor in ground effect have been determined and it has been observed that the ground has an impact on the loads only when h/R is less than 2.
- The effect of the tail rotor on the flow field has also been studied by incorporating a tail rotor into the model and substantial decrease in the velocities within the ground vortex has been observed.
- The impact of the tail rotor on the flow field decreases with an increase in the forward flight advance ratio
- The drag generated on the rotor is less with the tail rotor incorporated into the model

Due to the rotation of the blade, the lift and the circulation are concentrated at the tip region. Moreover, the zero pressure difference at the rotor tip requires the bound circulation to drop to zero at the wing tip. The bound circulation increases gradually from the root of the blade to near the tip where it suddenly drops to zero. Therefore the rate of spanwise variation in bound circulation near the tip is very high and causes the trailing vortices to quickly roll up into a single strong tip vortex. The tip vortex has a significant effect on the performance and the loads induced on the blade.

The main focus of this work has been in making the flow field IGE to evolve to periodic state. Two different models, lifting line and lifting surface, have been used to achieve this objective. The main drawback in the lifting line model which is not being able to account for the finite aspect ratio blade has been overcome by the lifting surface model. The lifting surface model is very robust in the computation of the circulation. The bound circulation distribution over the entire blade can be computed with the help of this model. It can also account for the shape of the blade. Once the entire flow field has been quantified, its important characteristics have been studied by looking at the wake structure, velocity profiles and the velocity contours. Formation of ground vortex has been observed. The flow field for a single bladed rotor attains periodicity very quickly while that of a two-bladed rotor takes much more time. The wake structure for a two-bladed rotor experiences vortex-vortex interactions close to the ground.

The velocities obtained using the lifting surface model have a slightly smaller magnitude compared to the lifting line counterparts. Also, in low speed forward flight the entire wake structure becomes periodic when the lifting surface model for the blade is used,

while for the lifting line model, the wake structure close to the ground does not attain periodic state. Both lifting line and lifting surface models agree very well qualitatively and in most cases quantitatively with experimental results obtained from Georgia Institute of Technology [31]; quantitatively with the results of Light [17] and Empey and Ormiston [8].

The velocities in the flow field have been used to study the handling qualities problems by looking at the unsteadiness in velocities on and around the tail rotor disk. The unsteadiness in the tail rotor inflow which mainly contributes to the handling problems was observed to be maximum in sideward flight at an angle of 45 degrees.

The thrust produced as well as the induced drag and power on the rotor have been obtained. The presence of the the ground reduces the induced downwash on the rotor disk which in turn increases the thrust on the rotor and helps reduce the induced drag. The presence of the the ground is most felt at $h/R = 0.5$. When $h/R = 1.0$, the influence of the ground becomes almost negligible and the thrust and drag values get close to OGE values.

The presence of a tail rotor reduced the velocities induced in the flow field. With an increase in the advance ratio, the effect of the tail rotor wake on the flow field reduced since the wake is swept away by the forward flight advance ratio. The induced drag and the induced power reduce when the tail rotor is incorporated into the model because of a decrease in the downwash induced at the rotor disk.

7.2 Future Work

There are a number of issues that have not been considered in this work. The effect of the inboard sheet of the vortex has not been taken into account. For most of the cases only single and two-bladed rotors have been considered while the number of blades typically

used in the industry are four to five. Only rectangular blades have been used. This model also does not possess trim capability for the rotor. The model is also not complete in the sense that the fuselage has not been incorporated. Based on these issues I would like to suggest the following future work.

- Rotors containing more than two blades need to be studied since industry typically uses four-five bladed rotors.
- The effect of the inboard sheet can be taken in to account to make the model more complete and this can be done easily since the bound circulation along the entire blade is being computed.
- Since a lifting surface model is being used to model the blade, the effect of blades of different plan-forms can be studied.
- To make the model more realistic, a trim capability needs to be incorporated into the model.
- The side by side configuration of the rotors can be studied which has an important application with respect to the V-22 osprey.
- The effects of the fuselage need to be included in to the model to make it more comprehensive

APPENDIX A

Vortex Ring Computation

In the model for the rotor wake in ground effect, since the wake cannot end in the fluid vortex nodes need to be added after every time step. With increase in the number of rotor revolutions, the number of vortex nodes increases and a large number of vortex nodes accumulate close to the ground. Due to these large number of vortex segments close to the ground, the wake becomes very complex and causes numerical difficulties. This problem is particularly significant in the case of a multi-bladed rotor. Also the computational time increases with increase in the number of vortex nodes. Initially, in the current work, a vortex node was added after every time step. Hence 180 new vortex nodes are added to the tip vortex of each blade during each revolution. If we start with 900 nodes initially, the number of vortex nodes doubles after five revolutions and the wake becomes very difficult to handle by the time the rotor completes ten revolutions. In ground effect, when a rotor with more than one blade is used, ten rotor revolutions is not enough for the flow field to attain periodic state. Also with the wake becoming very complicated due to the increase in the vortex nodes, it becomes difficult to attain periodicity. Hence it is not feasible to increase the number of vortex nodes after every time step and a fixed number of nodes need to be used to model the tip vortex.

Since the ground is modeled by an image wake, the velocity induced by the vortex segments close to the ground is almost canceled by the the corresponding vortex segment in the image wake because the velocity induced by the image wake is in the opposite direction to that of the real wake. By this argument, removing the vortex segment closest to the ground after every time step when a new vortex segment is added at the tip of the blade will not result in a significant change in the flow field. Nevertheless, there will be some effect on the nature of the flow field. To model the removed vortex nodes, since the tip vortex trajectory is almost circular close to the ground, a vortex ring is placed close to the ground and the velocity due to the vortex ring is added to the velocity in the flow field. Another reason behind using the vortex ring to model the removed points is the ease in computing the velocity due to the vortex ring. To satisfy the solid wall boundary condition on the ground, a vortex ring is also introduced in the image wake below the ground.

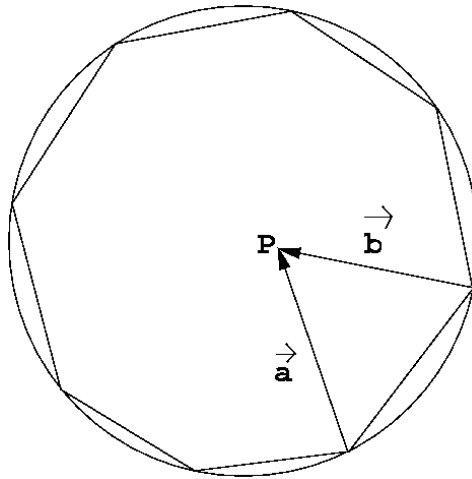


Figure A.1: Discretization of the vortex ring using straight line vortex filaments.

In the current work, the radius of the vortex ring used is one and a half times the radius of the rotor radius. The size of the vortex ring is arrived at by comparing the velocities obtained using this model with the model where vortex nodes are added after every time step. In forward flight the position of the vortex ring is shifted in the direction of the inflow by a non-dimensional distance of ten times the advance ratio. This is based on trial runs. To compute the velocity due to the vortex ring, it is discretized into two hundred equal line vortex segments of piecewise constant circulation. The number of nodes has been numerically verified. The discretization is qualitatively shown in Figure A.1. The velocity due to each vortex segment is computed using the biot savart law. As can be seen from the Figure, the velocity induced by the vortex segment V1 at a point P in the flow field is obtained using the analytical formula given by Conlisk [2],

$$\vec{U}_v = \frac{\Gamma_a}{4\pi} \left\{ \left[\frac{(|\vec{a}| + |\vec{b}|)(|\vec{a}||\vec{b}| - \vec{a} \cdot \vec{b})}{|\vec{a}||\vec{b}||\vec{a} \times \vec{b}|^2} \right] \right\} \quad (\text{A.1})$$

where \vec{b} is the vector connecting the point P and one end of the vortex segment V1b while \vec{a} connects P to the other end of the segment V1a. Γ_a is the value of circulation of the vortex segment connecting V1a and V1b.

BIBLIOGRAPHY

- [1] Caradonna, F.X., "The Application of CFD to Rotary Wing Aircraft", NASA TM 102803, 1992.
- [2] Conlisk, A.T., "Modern Helicopter Aerodynamics", *Annual Review of Fluid Mechanics*, vol. 29, pp. 515-567, 1997.
- [3] Johnson W.R., *Helicopter Theory*, Princeton University Press, New Jersey, 1980.
- [4] Gray, R.B., "An Aerodynamic Analysis of a Single-Bladed Rotor in Hovering and Low-Speed Forward Flight as Determined from Smoke Studies of the Vorticity Distribution in the Wake", Princeton University Aero. Engr. Dept., Report No. 356, Sept. 1956.
- [5] Conlisk, A.T., "Modern Helicopter Rotor Aerodynamics", *Progress in Aerospace Sciences*, to be published 2001.
- [6] Kini, S., and Conlisk, A.T., "On the Nature of Locally Steady Rotor Wakes", submitted to the *Journal of Aircraft*, 2001.
- [7] Yeager, W.T., Jr., Young, W.H., Jr. and Mantay, W.H., "A Wind Tunnel Investigation of Parameters Affecting Helicopter Directional Control in Ground Effect", *NASA TN D-7694*, Nov. 1974.
- [8] [1974] Empey, R.W. and Ormiston, R.A., "Trail Rotor Thrust on a 5.5 Foot Helicopter Model in Ground Effect", American Helicopter Society Preprint No. 802, presented at the Annual National Forum of the AHS May 1974.
- [9] Wiesner, W., and Kohler, G., "Tail Rotor Performance in Presence of Main Rotor, Ground and Winds", Paper presented at the 29th Annual National Forum of the American Helicopter Society, Preprint No.764, May 1973.
- [10] Lynn, R.R., Robinson, F.D., Batra, N.N., and Duhon, J.M., Tail Rotor Design Part I: Aerodynamics, *Journal of the American Helicopter Society*, Vol 15, No.4, October 1970.

- [11] Hayden, J., "The Effect of the Ground on Helicopter Hovering Power Required", *32nd Annual Forum of the American Helicopter Society*, Washington, D.C., May 1976.
- [12] Curtiss, H.C., Jr., Sun, M., Putman, W.F. and Hanker, E.J., Jr., "Rotor aerodynamics in ground effect at low advance ratios", *Journal of the American Helicopter Society* Vol.29 , 1984, pp.48-55.
- [13] Xin, H., Prasad, J.V.R., Peters, D.A, Nagashima,T. and Iboshi, N., "A Finite State Inflow Model for Simulation of Helicopter Hovering in Ground Effect", *54th Annual Forum of the American Helicopter Society*, Washington, D.C., May 1998.
- [14] Hanker, E. J. and Smith, R. P., "Parameters affecting helicopter interactional aerodynamics in ground effect", *Journal of the American Helicopter Society*, 1985.
- [15] Sun, M., "A study of helicopter rotor aerodynamics in ground-effect at low speeds", Ph.D. Thesis, Princeton University, 1983.
- [16] Cimbala, J. M., Gaublumme, D. P., and Oefelein, "Experiments on the unsteadiness associated with a ground vortex", *Journal of Aircraft*, 1991.
- [17] Light, J.S., "Tip Vortex Geometry of a Hovering Helicopter Rotor in Ground Effect," *Journal of American Helicopter Society*, Vol. 38, No. 2, 1993, pp. 34-42.
- [18] Landgrebe, A.J., "The Wake Geometry of a Hovering Rotor and its Influence on Rotor Performance", *Journal of the American Helicopter Society*, vol. 14, no. 4, pp. 3-15, 1972.
- [19] Kucab, J., Moulton, M., Fan, M. and Steinhoff, J., "The prediction of Rotor Flows in Ground Effect with a New Hybrid Method", *AIAA Paper 99-3222*, 17th Applied Aerodynamics Conference, Norfolk, VA, June 28-July 1, 1999.
- [20] Kang, N. and Sun, M., "Prediction of the Flow Field of a Rotor in Ground Effect", *Journal of American Helicopter Society*, Vol.42, 1997, pp. 195-198.
- [21] Kang, N. and Sun, M., "Simulated Flowfields in Near-Ground Operation of Single- and Twin-Rotor Configurations", *J. Aircraft*, Vol.37, 2000, pp. 214-220.
- [22] Landgrebe, A.J., "New Directions in Rotorcraft Computational Aerodynamics Research", US 75th AGARD Fluid Dynamics Panel Meeting on Aerodynamics and Aeroacoustics of Rotorcraft, Berlin, October 1994.
- [23] Srinivasan, G.R. and Sankar, L.N., "Status of Euler and Navier Stokes CFD Methods for Helicopter Applications", Presented at the American Helicopter Society Specialists Meeting on Aeromechanics Technology and Product Design, Bridgeport, CT, 11-13 October 1995.

- [24] Renzoni, P., Alascio, D., Kroll, N., Peshkin, D., Hounjet, M.H.L., Scholl, E. and Kokkalis, A., "EROS-A Common European Euler Code for the Analysis of the Helicopter Rotor Flowfield", *Progress in Aerospace Sciences*, 2000; 36(5-6):437-85.
- [25] Li, H., "The Formation of Rotor Tip Vortices", M.S. Thesis, The Ohio State University, 2000.
- [26] Katz J, Plotkin A., "Low-speed Aerodynamics:from wing theory to panel methods.", New York:Mcgraw-Hill, 1991.
- [27] Betz, A., "Behaviour of Vortex Systems", NACA-TM-713, 1932.
- [28] Schlichting, H., and Thomas, H. H. B. M., "Note on the calculation of lift distribution of swept wings", Royal Aircraft Establishment Rpt., No. Aero. 2236, 1947.
- [29] Affes, H., Conlisk, A.T., Kim, J.M., and Komerath, N.M., "Model for Rotor Tip-Vortex-Airframe Interaction, Part 2: Comparison with experiment", *AIAA Journal*, vol. 31, no. 12, pp. 2274-2282, 1993.
- [30] Jain, R., and Conlisk, A.T., "Interaction of Tip-Vortices in the Wake of a Two-Bladed Rotor in Axial Flight", *Journal of the American Helicopter Society*, Vol. 45, No. 3, pp. 157-164, 2000.
- [31] Ganesh, B., Komerath, N.M., Pulla, D.P., Conlisk, A.T., "Unsteady Aerodynamics of Rotorcraft in Ground Effect", *43rd AIAA Aerospace Sciences Meeting*, Reno, Nevada AIAA 2005-1407, January 10-13 2005.
- [32] Caradonna, F., Hendley, E., Silva, M., Huang, S., Komerath, N., Reddy, U., Mahalingam, R., Funk, R., Ames, R., Darden, L., Villareal, L., Gregory, and Wong, O., "An Experimental Study Of a Rotor in Axial Flight", AHS Specialists' Meeting on Aerodynamics and Aeroacoustics, Williamsburg, VA, Oct. 1997. Also *Journal of the American Helicopter Society*, vol. 44, no. 2, pp. 101-108, 1999.
- [33] Leishman, J.G., "Principles of Helicopter Aerodynamics", Cambridge:Cambridge University Press, 2000.
- [34] Phillips, W.F., and Snyder, D.O., "Modern Adaptation of Prandtl's Lifting Line Theory", *Journal of Aircraft*, 2000 37(4):662-70.